FERMILAB-THESIS-2004-91

A Search for Non-Standard Model W Helicity in Top Quark Decays

by

Benjamin John Kilminster

Submitted in Partial Fulfillment

of the

Requirements for the Degree

Doctor of Philosophy

Supervised by

Professor Kevin McFarland

Department of Physics and Astronomy

The College

Arts and Sciences

University of Rochester

Rochester, New York

2003

This Ph.D. thesis is dedicated to my father,

Dr. Kenneth Kilminster.

Curriculum Vitæ

The author was born in Bletchley, England on December 24th, 1975. He graduated with a Bachelor of Arts degree in Physics from the State University of New York at Geneseo in 1997. He continued his physics education at the University of Rochester in the fall of 1997, receiving his Master of Arts degree in the Spring of 1999, and pursuing high energy physics research under the direction of Professor Kevin McFarland.

Acknowledgements

I am grateful to be on the frontier of particle physics research as we push towards the next great breakthrough. This analysis builds on the work of more than 500 CDF collaborators and Fermilab staff who have devised an extraordinary apparatus for doing measurements that probe the earliest moments of our universe. I would like to acknowledge some people who have made all the difference in my graduate student career.

First of all, thanks to my advisor Kevin McFarland, who is the sharpest physicist I know. His knack for quickly noticing discrepancies and offering solutions is something I shall strive to reproduce. And if there is one person I want in the room as back-up when I am giving talks, it is Kevin. I'd like to thank Ed Thorndike for introducing me to my first particle physics project, and demonstrating how being patient and thorough leads to well understood results. Paul Tipton opened up the world of Fermilab to me with a silicon wafer in one hand when I showed up for orientation, and has been helpful throughout my stay as a practical voice of reason. Thanks to my graduate student class, especially John Janis, who helped get me through the first couple years of classes and exams. And thanks to the university administrative assistants, especially Connie and Barbara, who were always looking out for me.

Mark Kruse, who I shared an office with when I first arrived at Fermilab, showed me the cool scene of Chicago and the way a particle physicist works late into the evening. He also introduced me to a lovely woman who would later become my wife ! My previous officemate Josh Cassada, who may be flying overhead at this very moment, was an example of balance and efficiency, who showed me the way a particle physicist can work in the morning, too. I could always turn (literally) to my next officemate Andrew with my questions about statistics. I appreciate Tim Tait for being able to explain particle physics theory with unusual straightforwardness, especially when I hijacked him at parties with crazy ideas.

Thanks to Jeremy Lys for being the only one who could remember the intricacies of CDF Run I analyses, and Paolo Giromoni for getting me a corroborating plot at the last minute before my analysis was ”blessed”. Thanks to Rene Brun and Suzanne Panacek and the other members of the ROOT analysis software team for fixing bugs in the software and fixing my code when there wasn’t any.

I’d like to thank my parents for opening me up to two worlds on either side of the Atlantic, and for being guides without telling me what to do. Thanks to my brother Tom, and longtime friends Glenn Granzin and Brian Holmes for keeping me out of trouble ;) A word of appreciation for Gala, my little cocker spaniel, who never gives up trying to find the ball. Finally, a gracious thank you to Florencia Canelli, my wonderful wife, who always makes me feel like I am the best.

Abstract

The structure of the tbW vertex is probed by measuring the polarization of the W in $t \rightarrow W + b \rightarrow l + \nu + b$. The invariant mass of the lepton and b quark measures the W decay angle which in turn allows a comparison with polarizations expected from different possible models for the spin properties of the tbW interaction. We measure the fraction by rate of Ws produced with a V+A coupling in lieu of the Standard Model V−A to be $f_{V+A} = -0.21^{+0.42}_{-0.24}$ (stat) $\pm$ 0.21 (sys). We assign a limit of $f_{V+A} <$ 0.80 @ 95% Confidence Level (CL). By combining this result with a complementary observable in the same data, we assign a limit of $f_{V+A} <$ 0.61 @ 95% CL. This corresponds to a constraint on the right-handed helicity component of the W polarization of $f_+ < 0.18$ at 95% CL. This limit is the first significant direct constraint on f_{V+A} in top decay.

Contents

1 The Standard Model of Particle Physics **1**

1.1 Matter in Our Universe 2

1.2 Forces in Our Universe 3

1.3 Standard Model Theory and Predictions 6

1.4 Electromagnetic Processes 8

1.5 Strong Processes 9

1.6 Weak Processes 10

1.7 Fermion Mixing and CP Violation 12

1.8 Electroweak Unification 14

1.9 Limitations and Extensions of the Standard Model 16

2 Producing the Top Quark **19**

2.1 Using Collisions to Study the Structure of Matter 19

2.2 Fermilab Accelerator Complex 21

2.2.1 Protons 21

2.2.2 Antiprotons 24

2.2.3 Collisions 25

2.3 Top Production 26

3 Detecting the Top Quark **31**

3.1 Top Decay 31

3.2 Collider Detector at Fermilab (CDF) 34

3.3 Tracking Detectors 37

3.3.1 Magnetic Field 37

3.3.2 Silicon Vertex Detector (SVX) 37

3.3.3 Vertex Time Projection Chamber (VTX) 39

3.3.4 Central Tracking Chamber (CTC) 40

3.4 Calorimetric Detectors 43

3.4.1 Central, Plug, and Forward Calorimeters 45

3.5 Muon Detectors 47

3.6 Event Trigger System 49

3.6.1 Event Rates 49

3.6.2 Trigger System 50

4 $t\bar{t}$ Event Selection **52**

4.1 The $t\bar{t}$ Signature 52

4.1.1 Monte Carlo 52

4.2 Identifying Electrons in Data 53

4.2.1 Trigger Electrons 53

4.2.2 Primary Electron Selection 56

4.2.3 Secondary Electron Selection 59

4.3 Identifying Muons in Data 59

4.3.1 Trigger Muons 59

4.3.2 Primary Muon Selection 60

4.3.3 Secondary Muon Selection 61

4.4 Identifying W Bosons 63

4.5 Identifying Jets 66
4.5.1 B Jet Selection Criteria 67

5 Search for V+A in Top Decay 71
5.1 Motivation 71
5.2 Introduction to Analysis 74
5.3 Analysis Method 83
5.3.1 Pairing Lepton with B Jet 83
5.4 Event Selection Summary 86
5.5 Signal Modeling 89
5.6 Background Modeling 90
5.6.1 Dilepton Backgrounds 90
5.6.2 SVX Single-Tagged Backgrounds 91
5.6.3 SVX Double-Tagged Backgrounds 91
5.7 Validation of Monte Carlo 101

6 Measurement of V+A Fraction 109
6.1 Likelihood Fit 109
6.1.1 Tests of Fitting Method 111
6.1.2 Statistical Power of Samples 118
6.2 Results of Measurement 121

7 Systematic Uncertainties 143
7.1 Top Mass Uncertainty 143
7.2 Jet Energy Scale Uncertainties 144
7.2.1 Relative Jet Energy Scale 145
7.2.2 Underlying Event and Multiple Interactions 146
7.2.3 Soft Gluon and Splash-Out 146

7.2.4 Absolute Jet Energy Scale 147
7.3 Jet Energy Scale and Top Mass Correlation 147
7.4 Background Shape and Normalization 149
7.5 PDF Uncertainty 150
7.6 B Tag Systematic 151
7.7 Hard Gluon Radiation 154
7.8 Relative Acceptance of V$-$A and V$+$A 158
7.9 Summary of Systematic Uncertainties 159

8 Summary 160
8.1 Measurement of f_{V+A} 160
8.2 Interpretation of Result 160
8.3 Combining with Complementary Observable 165
8.4 Combining M^2_{l+b} and Lepton P_T 167
8.5 Calculation of Statistical Covariance Matrix 168
8.6 Calculation of Systematic Covariance Matrix 170
8.7 Determining Combined Likelihood 172
8.8 Evaluation of Confidence Level 172
8.9 Results of Combined Measurement 173
8.10 Future 174

9 Conclusions 176

A Acronyms and Symbols Used 182

B Units and Prefixes 188

C More information 190

List of Figures

1.1 A general example of a Feynman diagram showing the interaction between two fermions and a boson. Each fermion, boson, and vertex represents mathematical terms that can be combined to determine the probability for the diagrammed process to occur. The probability for this process is dependent on the mass, energy, spin, and momentum of the incoming and outgoing particles. 9

1.2 Feynman diagrams showing electromagnetic processes. (a) The basic diagram of a charged lepton or quark interacting with a photon. (b) An example of a process where an e^+ and an e^- produce a μ^+ and a μ^- through annhilation into a photon. 10

1.3 Feynman diagrams showing QCD interactions. (a) On the left, a quark changes color via interaction with a gluon. The middle diagram shows a gluon fusion process. This is represented on the right in terms of the color flow of the gluons. (b) An example of a QCD interaction where a Δ^{++} decays via a gluon into a proton and a pion. All three of these composite particles are colorless. 11

1.4 Feynman diagrams showing weak interactions of the fermions. (a) A W boson interacts with left-handed fermions and right-handed antifermions. A Z boson interacts with a fermion and antifermion. (b) An example where five weak interactions contribute to a Z boson decay via $\mu^+\mu^-$ into the final state of three left-handed particles and three right-handed antiparticles. A B^0 meson transforms into its own antiparticle by exchanging W^+ and W^- bosons. 12

1.5 The decay of a spin-0 pion must conserve angular momentum, shown by the hollow arrows. Since the neutrinos are the least massive, they are ultra-relativistic, and always left-handed. This forces either the e^+ or μ^+ to be left-handed. The muon is the least relativistic, and therefore, the preferential decay is $\pi^+ \rightarrow \mu + \nu_\mu$ rather than $\pi^+ \rightarrow e^+ + \nu_e$. . . . 13

1.6 Feynman diagrams showing electroweak interactions of the bosons. The diagram on the right demonstrates the photon coupling to the weak boson fields. 16

2.1 An aerial view of Fermilab. Shown are the Linac, Booster, Debuncher, and Accumulator, as well as part of the Main Ring. 20

2.2 Schematic of the Tevatron accelerator complex. 22

2.3 The Cockroft-Walton pre-accelerator. 23

2.4 Feynman diagrams for $t\bar{t}$ production via the strong force. 27

2.5 The structure of the proton as a function of x, the fraction of proton momentum carried by each constituent. The plot is of x f(x,Q^2), the probability density distributions at the given momentum fraction for a given momentum transfer Q^2. The upper distribution compares gluons with valence quarks; the lower compares gluons to sea quarks. 29

2.6 Feynman diagrams for single top quark production by the weak force. . 30

3.1 Feynman diagram for decay modes of $t\bar{t}$ produced by $q\bar{q}$ annihilation. . 32
3.2 The Feynman diagram for W production in association with jets, the dominant background in the $t\bar{t}$ lepton + jets channel. 34
3.3 A view of one quarter of a slice through the center of the CDF II detector. The full detector is recreated by reflecting the image from +z to -z, and rotating about the z-axis. 36
3.4 Diagram of one of the two SVX barrels. 38
3.5 Cross-section of the CTC illustrating the arrangement of 84 layers of drift wires into cells within nine superlayers. 42
3.6 Two views of a wedge of the central calorimeter showing the central electromagnetic (CEM), central hadronic (CHA), and the central muon chamber (CMU) detectors. 46

4.1 The η of generator-level particles from Monte Carlo $t\bar{t}$ lepton+jets events. The upper plot is of the W^+, and W^- daughters: lepton, neutrino, quark, and antiquark. The lower plot is of the b quarks. The arrows denote the extent of coverage for several subdetectors. 54
4.2 The P_T of generator-level particles from Monte Carlo $t\bar{t}$ lepton+jets events. The upper plot is of the W^+, and W^- daughters: lepton, neutrino, quark, and antiquark. The lower plot is of the b quarks. 55
4.3 Distributions of the loose second electron from $Z \rightarrow e^+ + e^-$ sample. The value of the tight electron cuts are denoted with an arrow, indicating the fraction of real electrons kept for the given cut. 58
4.4 Distributions of the loose second muon from the $Z \rightarrow \mu^+ + \mu^-$ sample. The value of tight muon cuts are denoted with an arrow, indicating the fraction of real muons kept for the given cut. 62

4.5 Distributions of the loose second muon from $Z \rightarrow \mu^+ + \mu^-$ sample. In this case, the second muon is a CMI. The value of CMI cuts are denoted with a dotted line, indicating the fraction of real muons kept for the given cut. 64

4.6 Transverse mass of the lepton, P_T, and $\not{E}_{\mathrm{T}}$ vectors for the W sample. The figure on the left is for electrons, and on the right is for muons. . . . 67

4.7 Diagram of a secondary vertex resulting from a b hadron decay. Each track originating from the secondary vertex has an impact parameter, d_0. 69

5.1 The angle $\psi_l^\star$ 75

5.2 The longitudinal helicity distribution is symmetric, while the left-handed and right-handed distributions peak asymmetrically. For instance, $cos\,\psi_l^\star$ = -1 corresponds to the lepton from the W decaying in the same direction as the b quark. 76

5.3 $M_{l+b}^2 = 1/2 \cdot (M_T^2 - M_W^2)(1 + cos\psi_l^\star)$ 77

5.4 W helicity distributions from top decay. The longitudinal component is the largest at 70%. The left-handed coupling causes an asymmetry in the Standard Model distribution. The right-handed component is non-zero when the b mass is considered. 78

5.5 The theoretical distributions for the correct pairings of M_{l+b}^2 comparing V$-$A and V$+$A. Since the V$+$A sample peaks higher, this can be used to discriminate between the two theories. 80

5.6 The left-handed coupling of V$-$A, compared to the right-handed coupling of V$+$A, leads to a lower M_{l+b}^2 distribution for V$-$A than V$+$A. . 81

5.7 The M^2_{l+b} distribution for correct (a) and incorrect (b) pairings of the lepton and the b with V$-$A Herwig generator-level information. The line denotes the cut off from the kinematics of top decay. The last bin is for overflow events. 84
5.8 Background template for dilepton sample (Two entries per event). . . . 92
5.9 Standard Model $t\bar{t}$ template for dilepton sample (Two entries per event). 93
5.10 V$+$A $t\bar{t}$ template for dilepton sample (Two entries per event). 94
5.11 Background template for SVX single-tagged sample (One entry per event). 95
5.12 Standard Model $t\bar{t}$ template for SVX single-tagged sample (One entry per event). 96
5.13 V$+$A $t\bar{t}$ template for SVX single-tagged sample (One entry per event). . 97
5.14 Background template for SVX double-tagged sample (One entry per event). 98
5.15 Standard Model $t\bar{t}$ template for SVX double-tagged sample (One entry per event). 99
5.16 V$+$A $t\bar{t}$ template for SVX double-tagged sample (One entry per event). 100
5.17 Comparison of the Monte Carlo $\not\!\!E_{\rm T}$ distribution in this dilepton analysis with that from the published CDF dilepton cross-section measurement showing the KS probability for agreement. 103
5.18 Comparison of the Monte Carlo H_T distribution in this dilepton analysis with that from the published CDF dilepton cross-section measurement showing the KS probability for agreement. 104
5.19 Comparison of the Monte Carlo $M_{l^+l^-}$ distribution in this dilepton analysis with that from the published CDF dilepton cross-section measurement showing the KS probability for agreement. 105

5.20 Comparison of the Monte Carlo M_{jj} distribution in this dilepton analysis with that from the published CDF dilepton cross-section measurement showing the KS probability for agreement. 106
5.21 Comparison of the Monte Carlo $\phi_{l^+l^-}$ distribution in this dilepton analysis with that from the published CDF dilepton cross-section measurement showing the KS probability for agreement. 107
5.22 Comparison of the Monte Carlo lepton P_T distribution in this dilepton analysis with that from the published CDF dilepton cross-section measurement showing the KS probability for agreement. 108

6.1 With a generated V+A fraction of 0.33, the results of 10,000 pseudo-experiments comparing independent Monte Carlo distributions. The physical region is from 0 to 1. 112
6.2 Pseudo-experiments fit with prediction function for range of V+A inputs. 113
6.3 Mean error for pseudo-experiments fit for range of f^{in}_{V+A}. V−A events have more weight since they are less likely because of the relative efficiency dependence in the fit function. This leads to a slope in the fit error. 114
6.4 Pull distribution is shown fit to a Gaussian. 116
6.5 Theoretical histograms for the integrated probability distribution with non-Gaussian effects. The integration is of a Gaussian probability distribution integrating from the central value to infinity. Pseudo-experiments using the probability distribution from a normal Gaussian produce a flat distribution, but pseudo-experiments with shifted central values and non-standard sigma have well defined effects on the slope and concavity of the distribution, respectively. 117

6.6 Fits to the Monte Carlo are compared with a Gaussian of known shifted parameters to fit for the nature of the non-Gaussian errors from the fit. The slope of the plots is not significant; it is due to the small statistics used in each independent sample. The concavity is significant indicating a shift in sigma such that the prediction function in this analysis underestimates the fit error by a well determined scale factor. 119

6.7 This plot shows a comparison of the leading jet E_T between SVX single-tagged data to Monte Carlo with the KS probability, as well as a side by side comparison to the published run I distribution. 124

6.8 This plot shows a comparison of the second leading jet E_T between SVX single-tagged data and Monte Carlo with the KS probability, as well as a side by side comparison to the published run I distribution. . . 125

6.9 This plot shows a comparison of the second and third leading jet sum E_T between SVX single-tagged data and Monte Carlo with the KS probability, as well as a side by side comparison to the published run I distribution. 126

6.10 This plot shows a comparison of the lepton P_T between SVX single-tagged data and Monte Carlo with the KS probability, as well as a side by side comparison to the published run I distribution. 127

6.11 This plot shows a comparison of the b tagged jet E_T between SVX single-tagged data and Monte Carlo with the KS probability. 128

6.12 This plot shows a comparison of the lepton-b tagged jet angle between SVX single-tagged data and Monte Carlo with the KS probability. . . . 129

6.13 This plot shows a 2D comparison of the b tagged jet E_T vs. lepton E_T between SVX single-tagged data and Monte Carlo with the KS probability. 130

6.14 This plot shows a 2D comparison of the lepton-b tagged jet angle vs. b jet E_T between SVX single-tagged data and Monte Carlo with the KS probability. 131
6.15 This plot shows a 2D comparison of the lepton-b tagged jet angle vs. lepton E_T between SVX single-tagged data and Monte Carlo with the KS probability. 132
6.16 Data and Monte Carlo distributions for dilepton sample with fit value of f_{V+A}. 133
6.17 Data and Monte Carlo distributions for SVX double-tagged sample with fit value of f_{V+A}. 134
6.18 Data and Monte Carlo distributions for SVX single-tagged sample with fit value of f_{V+A}. 135
6.19 Distribution of errors from pseudo-experiments for the dilepton sample, shown with the error from the data marked with an arrow. 136
6.20 Distribution of errors from pseudo-experiments for the SVX single-tagged sample, shown with the error from the data marked with an arrow. 138
6.21 Distribution of errors from pseudo-experiments for the SVX double-tagged sample, shown with the error from the data marked with an arrow. 139
6.22 Distribution of errors from pseudo-experiments for all the samples, shown with the error from the data marked with an arrow. 140
6.23 The log likelihood minima for each sample and the combined minimum shown separately. 141
6.24 The log likelihood minima for each sample and the combined minimum shown overlayed. 142

7.1 Relative contribution of partons from the proton in $t\bar{t}$ production 152

7.2 Distribution in x of $t\bar{t}$ events passing cuts. Two PDFs are chosen which span the most difference in x around the default NLL MRST h-g PDF. . 152

7.3 The SVX b tagging scale factor (data / Monte Carlo) as a function of jet E_T. The systematic uncertainty comes from assuming no Q dependence and a one standard deviation stronger Q dependence in the CTC tracking efficiency. The stars represent the deviation by assuming a one standard deviation stronger Q dependence in the CTC tracking efficiency, and were used to weight the Monte Carlo according to their jet E_T to evaluate the b tagging bias systematic. 155

7.4 Initial state radiation is typically along the beam pipe. If an event has more than 8 GeV transverse initial state radiation in either hemisphere, it is flagged as having hard ISR content. 156

8.1 $\mathcal{L}_{sys+stat}(f_{V+A})$ showing 95% CL for measured result to have an upper limit of 0.82 163

8.2 Distribution of f_{V+A} from 1000 pseudo-experiments such that 95% of pseudo-experiments had a result greater than $f_{measured}$. The arrows indicate the measured value, -0.21, and the "true" value used in the pseudo-experiments, 0.80, which defines the 95% CL upper limit. 164

8.3 The distribution of measured f_{V+A} for the two analysis techniques are shown for 1000 pseudo-experiments. 169

List of Tables

1.1 Fermions of the Standard Model 3

1.2 The bosons of the Standard Model. The coupling constant (α) is the strength of the force, in comparison with the strong force, at a distance scale the size of an atomic nucleus (10^{-13} cm). The range is the distance over which the force interacts in ordinary matter. At this distance scale, the electromagnetic and weak forces have similar strength; however, the strength of the weak force falls off much more rapidly outside the range of 10^{-15} cm. The strong force goes to zero for colorless states above this distance scale and actually increases for colored states. 4

1.3 The properties of fermions in the Standard Model. In the upper left corner are the three generations of leptons and quarks. In the upper right corner are the fermion spins. The next three rows on the left indicate the gauge bosons for each of the Standard Model forces. Next to the gauge bosons are the quantum numbers of the fermions for the given force. The fermions masses in GeV are shown in the last row, alongside the Higgs boson which is responsible for imparting mass to the fermions. Each fermion has an antiparticle (not shown), with the same mass and spin, but opposite quantum numbers. 5

1.4 Weak isospin doublet and singlet. Only left-handed fermions may be transformed by the weak charged current. 8
1.5 The 25 independent parameters of the standard model. 16

3.1 The branching ratios for $t\bar{t}$ decay modes assuming standard model couplings. Here q may be a u, d, c or s quark. 33
3.2 Description of the charged particle tracking chambers. 41
3.3 Absorption properties of materials used in the CDF detector. 43
3.4 Coverage and energy resolution of the calorimeter detectors. $\oplus$ denotes the direct sum. 48

4.1 Tight central electron (TCE) selection criteria. 57
4.2 Differences between tight central electrons (TCE) and loose central electrons (LCE) for top dilepton selection. 59
4.3 Tight muon selection criteria. 61
4.4 Differences between tight central muons (TCM) and loose central muons (LCM) for top dilepton selection. 63
4.5 Loose lepton quality cuts applied to secondary lepton candidates to remove Z boson decays in top lepton+jets events. 65

6.1 Relative efficiency for V$-$A events to pass the top cuts compared to V$+$A. 110
6.2 Statistical power of each sample as measured by the uncertainty of the likelihood fit for 10,000 pseudoexperiments. Shown are the cases when samples are normalized to the same number of M_{lb}^2 combinations, and when samples are normalized to the number of events within the data. In the SVX double-tagged sample, 1.8 % of the fits failed. 120
6.3 Number of events in data and expected background. 121

6.4 The results for each sample, with the combined results. Errors shown are statistical only. 137

7.1 The systematic shift of measurement due to changes in the top mass. "Dependent" refers to the part of a shift in top mass which is correlated to the CDF jet energy scale. "Independent" refers to all other uncertainties in the top mass including statistical uncertainty, and for instance, the $D\emptyset$ jet energy scale. [29] 144

7.2 Approximate size of uncertainties in jet energy corrections. 145

7.3 The percentage of the relative jet energy correction uncertainty for various ranges of $|\eta|$. 146

7.4 The systematic shift of measurement due to uncertainty in jet energy scale from various effects of detector energy repsonse and jet energy corrections. 148

7.5 The systematic shift of measurement due to fluctuating background statistics. 149

7.6 The systematic shift of measurement due to changing background shapes. 150

7.7 The systematic shift of measurement due to different PDFs in comparison with MRSG. 153

7.8 Events are divided into whether the reconstructed particles match the generator level particles or not, according to the ISR and FSR content; "hep fid" means that the generator level particles traversed CDF subdetectors used in this analysis. 157

7.9 The systematic shift of measurement due to removal of hard gluon radiation effects. Uncertainty is taken to be half of the total shift when hard radiation is removed. 158

7.10 Summary of uncertainties in terms of shift in measurement of V+A fraction. The top mass systematic is complementary to the jet energy scale systematic. Shown in parentheses are the systematic errors for top mass and jet energy before accounting for correlation. 159

8.1 Summary of uncertainties in terms of shift in measurement of V+A fraction, and result. 161

8.2 The M^2_{l+b} analysis makes use of the 20 b tagged events from the top mass analysis, while the lepton P_T analysis uses 34 b tagged events from the top cross-section analysis. 168

8.3 The correlated and uncorrelated components of the V$+$A measurement using lepton P_T, as is calculated using the weights from the longitudinal measurement. 171

8.4 Summary of uncertainties in terms of shift in measurement of V$+$A fraction for the two methods. 171

8.5 Systematic uncertainties determined by scaling the systematics of f_{V+A} for the Run I analysis by the factors obtained by comparing the CDF Run I systematic uncertainties of the top mass to those in expected in 2 fb$^{-}1$ of CDF II data. 175

8.6 Statistical uncertainty determined by pseudoexperiments with event samples appropriate to the given luminosty at 1.96 TeV assuming a cross-section of 7.5 pb. Improved systematic uncertainty accounts mainly for better measurements of the jet energy scale and the top mass. 175

B.1 Units. 189

B.2 Prefixes for units. 189

Chapter 1

The Standard Model of Particle Physics

> "If, in some cataclysm, all of scientific knowledge were to be destroyed, and only one sentence passed on to the next generation of creatures, what statement would contain the most information in the fewest words? I believe it is the atomic hypothesis, that all things are made of atoms -- little particles that move around in perpetual motion, attracting each other when they are a little distance apart, but repelling upon being squeezed into one another. In that one sentence, you will see, there is an enormous amount of information about the world, if just a little imagination and thinking are applied."
>
> *Richard Feynman*

Human civilization has greatly advanced its understanding of the composition of the universe since the Greeks first postulated atomic theories 2400 years ago. In 430 B.C., Democritus reasoned that if you divide an object in half repeatedly, eventually

you would arrive at a particle which could not be divided again. He called this particle an “atom”, meaning indivisible. However, what we call the “atom” today is divisible into still smaller particles. Atoms contain a nucleus with fixed numbers of electrically neutral neutrons and positively charged protons. The nucleus is surrounded by a cloud of negatively charged electrons making the atom electrically neutral. Protons and neutrons are composed of two types of “quarks”, called “up” and “down”. A proton has two up quarks and one down quark, while a neutron has two down quarks and an up quark. All matter in our universe is essentially composed of these indivisible particles: up quarks, down quarks, and electrons.

1.1 Matter in Our Universe

The universe would be quite succinct if it were just up quarks, down quarks, and electrons, but a half century of research has led to the discovery of additional particles. There are two other pairs of quarks, identical to the up and down, but more massive. Also, the electron has a light, neutral partner called a “neutrino”. There are two other charged particles like electrons, each with a neutrino partner. Collectively, these three pairs are known as “leptons”. The rich diversity of objects in our universe is made possible by quarks and leptons interacting via a number of forces. As in classical physics, these forces can exchange momentum and energy among particles and lead to formation of bound systems. Quantum mechanically, forces transform particles into other particles, or transform properties of particle into different properties.

The Standard Model of Particle Physics is a theory which categorizes all the fundamental particles of matter and the forces with which they interact [1]. In the Standard Model, the three pairs of quarks and leptons are organized into three generations of matter particles, collectively called fermions (Table 1.1). The first generation of quarks are the up (u) and down (d) quarks, and the first generation of leptons are the electron (e)

Fermions		
Quarks		
$\begin{pmatrix} \mathbf{u} \\ \mathbf{d} \end{pmatrix}$	$\begin{pmatrix} \mathbf{c} \\ \mathbf{s} \end{pmatrix}$	$\begin{pmatrix} \mathbf{t} \\ \mathbf{b} \end{pmatrix}$
Leptons		
$\begin{pmatrix} \mathbf{e} \\ \nu_{\mathbf{e}} \end{pmatrix}$	$\begin{pmatrix} \mu \\ \nu_{\mu} \end{pmatrix}$	$\begin{pmatrix} \tau \\ \nu_{\tau} \end{pmatrix}$

Table 1.1: Fermions of the Standard Model

and the electron neutrino (ν_e) leptons. The second generation of fermions are the charm (c) and strange (s) quarks, and the muon (μ) and muon neutrino (ν_μ) leptons. The third generation are the top (t) and bottom (b) quarks, and the tau (τ) and tau neutrino (ν_τ leptons. The first generation of fermions make up our universe merely because they are the lightest. The heavier second and third generations of quarks and leptons are unstable and decay into the lower mass first generation. Second and third generation particles can be created in high energy laboratories or in atmospheric interactions of cosmic particles. The heaviest known particle is the ”top” quark, discovered in 1995. It has the mass of about 175 protons.

1.2 Forces in Our Universe

The forces of the Standard Model are electromagnetism, the weak force, and the strong force. Electromagnetism is the force which governs electricity, lightning, and light. The weak force causes some radioactive decays, and provides a vital process which allows the sun to burn. The strong force is what holds the proton together. Gravity is also a force, but has not yet been successfully included in the Standard Model.

The Standard Model is a quantum field theory, which has a different view of forces than the classical theories of Newton. In a classical theory, forces arise due to the action

Gauge Bosons	**Force**	**Coupling (α)**	**Range**
Photon (γ)	Electromagnetic	$1/137$	∞
W^+, W^-, Z^0	Weak	10^{-2}	$< 10^{-15}$ cm
Gluon (g)	Strong	1	$< 10^{-13}$ cm
Graviton	Gravity	10^{-38}	∞

Table 1.2: The bosons of the Standard Model. The coupling constant (α) is the strength of the force, in comparison with the strong force, at a distance scale the size of an atomic nucleus (10^{-13} cm). The range is the distance over which the force interacts in ordinary matter. At this distance scale, the electromagnetic and weak forces have similar strength; however, the strength of the weak force falls off much more rapidly outside the range of 10^{-15} cm. The strong force goes to zero for colorless states above this distance scale and actually increases for colored states.

of one particle on another. In a quantum field theory, the forces between particles are interpreted as the exchange of special particles known as “force carriers”.

The force carrying particles of the Standard Model are called “bosons”. The “photon” (γ) is the force carrier of electromagnetism. It has zero mass and interacts with positively and negatively charged objects. Since it is electrically neutral, it does not interact with other photons. Our eyes can observe photons directly in the form of visible light. The photon’s range is infinite, which allows us to see light which has traveled for more than 10 billion light years to reach our most powerful telescopes. The gluon (g) is the force carrier of the strong force, and interacts with all particles that carry a property called “color” which is found in all quarks and the gluons themselves. The gluon is massless. The W^+, W^-, and Z^0 bosons are the force carriers of the weak force. The W bosons have a mass of 80.4 GeV; the Z boson has a 91.2 GeV mass. These bosons interact by coupling to “weak isospin”, the charge of the weak interaction. The bosons are shown in Table 1.2, along with their relative strengths, and their range of interaction.

Table 1.3 shows the properties of the fermions in the Standard Model. Shown are the fermion spins, quantum values, and mass.

Fermions			**Fermion Spins**		
Quarks					
$\begin{pmatrix} \mathbf{u} \\ \mathbf{d} \end{pmatrix}$	$\begin{pmatrix} \mathbf{c} \\ \mathbf{s} \end{pmatrix}$	$\begin{pmatrix} \mathbf{t} \\ \mathbf{b} \end{pmatrix}$	$\begin{pmatrix} \frac{1}{2} \\ \frac{1}{2} \end{pmatrix}$	$\begin{pmatrix} \frac{1}{2} \\ \frac{1}{2} \end{pmatrix}$	$\begin{pmatrix} \frac{1}{2} \\ \frac{1}{2} \end{pmatrix}$
Leptons					
$\begin{pmatrix} \mathbf{e} \\ \nu_{\mathbf{e}} \end{pmatrix}$	$\begin{pmatrix} \mu \\ \nu_{\mu} \end{pmatrix}$	$\begin{pmatrix} \tau \\ \nu_{\tau} \end{pmatrix}$	$\begin{pmatrix} \frac{1}{2} \\ \frac{1}{2} \end{pmatrix}$	$\begin{pmatrix} \frac{1}{2} \\ \frac{1}{2} \end{pmatrix}$	$\begin{pmatrix} \frac{1}{2} \\ \frac{1}{2} \end{pmatrix}$

Gauge Bosons	**Fermion Quantum Numbers**		
	Electric Charge		
Photon	$\begin{pmatrix} +\frac{2}{3} \\ -\frac{1}{3} \end{pmatrix}$	$\begin{pmatrix} +\frac{2}{3} \\ -\frac{1}{3} \end{pmatrix}$	$\begin{pmatrix} +\frac{2}{3} \\ -\frac{1}{3} \end{pmatrix}$
(γ)	$\begin{pmatrix} -1 \\ 0 \end{pmatrix}$	$\begin{pmatrix} -1 \\ 0 \end{pmatrix}$	$\begin{pmatrix} -1 \\ 0 \end{pmatrix}$
	Weak Isospin charge		
Weak Bosons	$\begin{pmatrix} +\frac{1}{2} \\ -\frac{1}{2} \end{pmatrix}$	$\begin{pmatrix} +\frac{1}{2} \\ -\frac{1}{2} \end{pmatrix}$	$\begin{pmatrix} +\frac{1}{2} \\ -\frac{1}{2} \end{pmatrix}$
(W^+, W^-, Z^0)	$\begin{pmatrix} +\frac{1}{2} \\ -\frac{1}{2} \end{pmatrix}$	$\begin{pmatrix} +\frac{1}{2} \\ -\frac{1}{2} \end{pmatrix}$	$\begin{pmatrix} +\frac{1}{2} \\ -\frac{1}{2} \end{pmatrix}$
	Color charge		
8 Gluons	$\begin{pmatrix} R, B, G \\ R, B, G \end{pmatrix}$	$\begin{pmatrix} R, B, G \\ R, B, G \end{pmatrix}$	$\begin{pmatrix} R, B, G \\ R, B, G \end{pmatrix}$
(g)	$\begin{pmatrix} 0 \\ 0 \end{pmatrix}$	$\begin{pmatrix} 0 \\ 0 \end{pmatrix}$	$\begin{pmatrix} 0 \\ 0 \end{pmatrix}$

Scalar Bosons	**Fermion Masses**		
Higgs	$\begin{pmatrix} 0.003 \\ 0.006 \end{pmatrix}$	$\begin{pmatrix} 1.3 \\ 0.1 \end{pmatrix}$	$\begin{pmatrix} 175 \\ 4.3 \end{pmatrix}$
(h)	$\begin{pmatrix} 5 \cdot 10^{-4} \\ < 10^{-5} \end{pmatrix}$	$\begin{pmatrix} 0.8 \\ < 3 \cdot 10^{-6} \end{pmatrix}$	$\begin{pmatrix} 5 \\ < 2 \cdot 10^{-7} \end{pmatrix}$

Table 1.3: The properties of fermions in the Standard Model. In the upper left corner are the three generations of leptons and quarks. In the upper right corner are the fermion spins. The next three rows on the left indicate the gauge bosons for each of the Standard Model forces. Next to the gauge bosons are the quantum numbers of the fermions for the given force. The fermions masses in GeV are shown in the last row, alongside the Higgs boson which is responsible for imparting mass to the fermions. Each fermion has an antiparticle (not shown), with the same mass and spin, but opposite quantum numbers.

1.3 Standard Model Theory and Predictions

The success of the Standard Model is that it provides a terse explanation of particle physics phenomena. The theory describing how the particles behave is formulated by an equation called a "Lagrangian". The Lagrangian is equal to the kinetic energy minus the potential energy of the particles. The kinetic energy terms account for motion of particles. The potential energy terms specify the forces, and account for the fundamental interactions of the theory, including particle production and decay.

The Standard Model Lagrangian incorporates quantum theory, relativity, and local gauge invariance. Quantum theory states that a particle is described by a wave function, and that energy and other quantum numbers are transmitted in discrete quanta. Relativity governs the behavior of interactions or observations extended over space and time. Local gauge invariance means that the phase of the wave function can be chosen arbitrarily at each point in space-time without changing the theory itself. Quantum theory and relativity lead to the interpretation that particle interactions are the exchange of particles. When local gauge invariance is applied, the existence of force mediating "gauge bosons", and the nature of their couplings to other particles in the theory are completely specified.

Each force in the Standard Model is represented by a gauge symmetry transformation. Symmetries lead to the conservation of properties, such as rotational symmetry leading to the conservation of angular momentum. Gauge symmetries require that the physical system is invariant under various shifts in the force charges with respect to shifts in time and space coordinates. A gauge symmetry transformation has the effect of transforming one elementary particle into another. Gauge symmetries are represented by gauge groups: for electromagnetism, it is the U(1) group, for the weak force it is the SU(2) group, and for the strong force it is the SU(3) group.

It has been experimentally found that the weak interaction does not conserve par-

ity (P), the transformation by reflection in space as in the image seen in a mirror. The weak interaction is described by a "polar Vector minus Axial vector" (V$-$A) theory. Polar vectors, like momentum, are vectors which reverse direction under a parity transformation. Axial vectors, like angular momentum or spin, are vectors which do not reverse direction under parity transformation. Since both types of vectors are manifest in the weak interaction, parity is not conserved. This parity violation is biased such that the W^+ and W^- bosons only couple to "left-handed" chiral states of matter and "right-handed" chiral states of antimatter.

Chiral states are related to a more easily visualized measure called helicity $\mathcal{H}$, which is the dot product of the spin and momentum of a particle,

$$\mathcal{H} = J \cdot P. \tag{1.1}$$

Fermions are spin-1/2 particles, having $\mathcal{H}$ = $-$1/2 when the spin is in the opposite direction as the momentum, and $\mathcal{H}$ = $+$1/2 when the spin is in the same direction. Positive helicity states are referred to as "right-handed", similar to the convention of the "right-hand rule" for vector products. Negative helicity states are called "left-handed". Helicity is equal to chirality for particles with no mass. For fermions, chirality is represented by a basis of spinors which have a value of either $+$1/2 or $-$1/2. The $+$1/2 state is referred to as right-handed and denoted by a subscript R, the $-$1/2 state denoted as L.

The V$-$A weak theory is represented by grouping the left-handed chiral states in an "isospin" doublet, and the right-handed chiral states in an "isospin" singlet, as shown in Table 1.4. Weak isospin refers to the charge of the weak current. The upper particle of the doublet in each of the three generations has a weak isospin of $+$1/2, the lower one, a weak isospin of $-$1/2. The gauge symmetry is therefore described by a left-handed $SU(2)$ group, $SU(2)_L$. Incorporating the strong force, electromagnetic force, and the asymmetric weak force, the Standard Model theory is represented by

Doublet			Singlet
$\begin{pmatrix} u \\ d \end{pmatrix}_L$	$\begin{pmatrix} c \\ s \end{pmatrix}_L$	$\begin{pmatrix} t \\ b \end{pmatrix}_L$	u_R, d_R, c_R, s_R, t_R, b_R,
$\begin{pmatrix} e \\ \nu_e \end{pmatrix}_L$	$\begin{pmatrix} \mu \\ \nu_\mu \end{pmatrix}_L$	$\begin{pmatrix} \tau \\ \nu_\tau \end{pmatrix}_L$	$e_R,\ \nu_{eR},\ \nu_{\mu R},\ \mu_R,\ \tau_R,\ \nu_{\tau R}$

Table 1.4: Weak isospin doublet and singlet. Only left-handed fermions may be transformed by the weak charged current.

$SU(3)\ X\ SU(2)_L\ X\ U(1)$.

To predict observable behaviors of particles, the theory must produce finite probabilities for certain processes to occur, and so must define a set of formal rules for the properties of the particles, their propagations, and their interactions. This is often done by constructing Feynman diagrams which visually represent a particle physics process, and also can be used to assist in calculating probabilities. In the diagram, each particle is a represented by a line and each vertex is the interaction of a force. Solid lines with arrows are fermions. Curvy, wavy, or broken lines are bosons. A diagram represents a mathematical term that can be used in a formula. Feynman diagrams can be rotated such that the arrow of time is drawn in any direction. If the particle arrow points opposite to the direction of time, it is considered an antiparticle moving in the direction of time. In Figure 1.1, time moving upward would indicate that the boson decayed producing a particle and antiparticle.

1.4 Electromagnetic Processes

The electromagnetic force is governed by the theory of Quantum Electrodynamics (QED). QED is the exchange of photons by electrically charged particles. All QED calculations can be done in terms of the diagram in Figure 1.2a, which shows a photon interacting

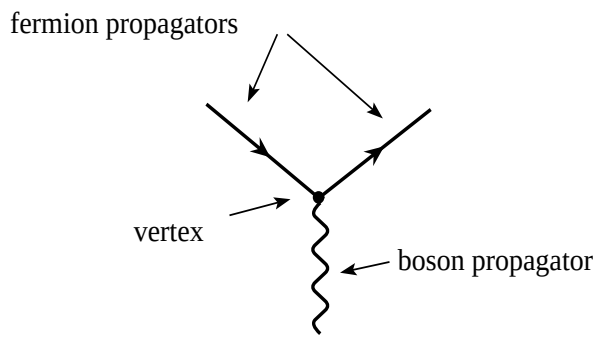

Figure 1.1: A general example of a Feynman diagram showing the interaction between two fermions and a boson. Each fermion, boson, and vertex represents mathematical terms that can be combined to determine the probability for the diagrammed process to occur. The probability for this process is dependent on the mass, energy, spin, and momentum of the incoming and outgoing particles.

with a charged lepton or quark. By means of a photon, an e^+ and e^- may transform into a μ^+ and μ^- (Figure 1.2b).

1.5 Strong Processes

The strong force is governed by the theory of Quantum Chromodynamics (QCD), which is the interaction of gluons with particles having color charge. Quarks can have red (R), blue (B), or green (G) charge. Antiquarks have anticolor, $\bar{R}$, $\bar{B}$, or $\bar{G}$. Gluons are multi-colored, having six color-anticolor combinations of $R\bar{B}$, $R\bar{G}$, $B\bar{G}$, $B\bar{R}$, $G\bar{R}$, $G\bar{B}$, and two multi-color combinations of $1/\sqrt{2}(R\bar{R} - B\bar{B})$, and $1/\sqrt{6}(R\bar{R}$,$B\bar{B}$-2$G\bar{G})$. Quarks exist only in bound states called "hadrons" which are electrically neutral combinations of quarks. Hadrons with two quarks are called "mesons", and with three quarks are called "baryons". The D^- meson $(\bar{c}d)$ and the Ω^- baryon (sss) are examples of each. Since the Pauli exclusion principle prohibits identical spin-1/2 particles from occupying

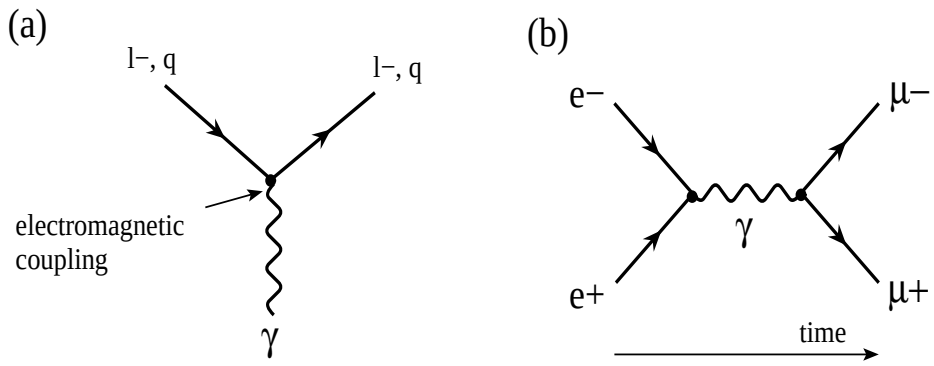

Figure 1.2: Feynman diagrams showing electromagnetic processes. (a) The basic diagram of a charged lepton or quark interacting with a photon. (b) An example of a process where an e^+ and an e^- produce a μ^+ and a μ^- through annhilation into a photon.

the same state, bound states like the Ω^- are explained by each quark having a different color. The name "color" provides a useful analogy since quarks can only be bound in colorless states. Therefore, as in the analogy with light, a combination of $R + B + G$ is colorless, as well as $\bar{R} + \bar{B} + \bar{G}$. When gluons interact with quarks, the color of the quark is transformed. Since gluons carry color, they can interact with themselves. The Feynman diagrams for the interactions of QCD and an example are shown in Figure 1.3.

1.6 Weak Processes

Particles with weak isospin, including all the quarks and leptons, can interact with the weak force. The charged weak interaction is mediated by the W^+ and W^- bosons, and the neutral weak interaction by the Z^0 boson. The W^+ and W^- bosons can change the "flavor" of a lepton or quark, thus transforming an e into a ν_e or a u into a d. A W boson interacts with left-handed fermions and right-handed antifermions. The Z^0 boson

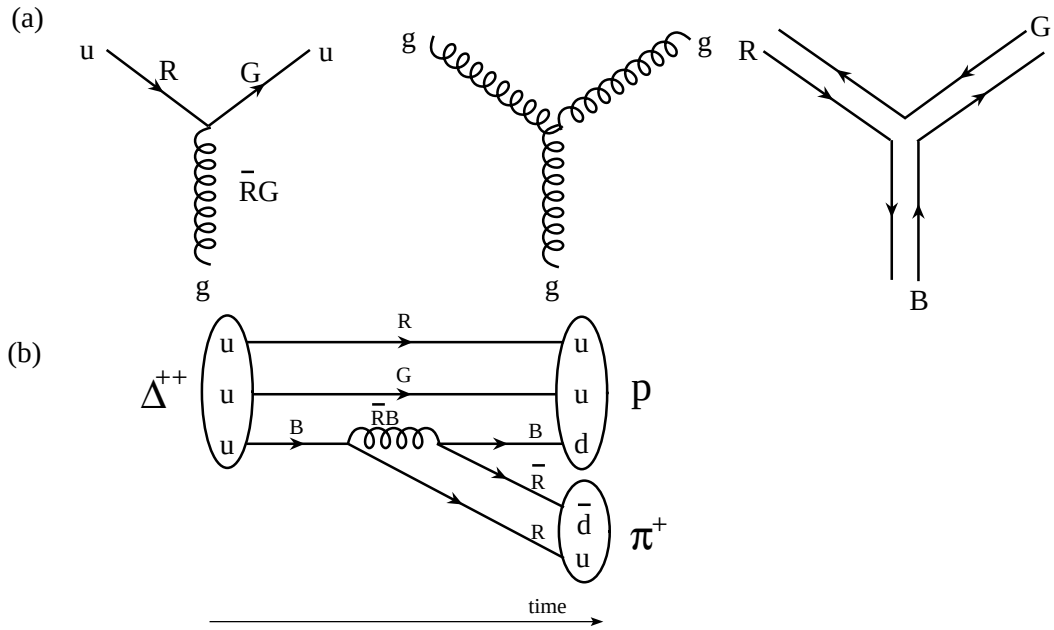

Figure 1.3: Feynman diagrams showing QCD interactions. (a) On the left, a quark changes color via interaction with a gluon. The middle diagram shows a gluon fusion process. This is represented on the right in terms of the color flow of the gluons. (b) An example of a QCD interaction where a Δ^{++} decays via a gluon into a proton and a pion. All three of these composite particles are colorless.

couples to both left-handed and right-handed chiral states, but interacts more strongly with left-handed states. The fermion interactions of the weak theory and an example are shown in Figure 1.4.

The effect of the V$-$A weak interaction can be seen in the decay of the charged pion, shown in Figure 1.5. Because of the left-handed asymmetry in the weak interaction, right-handed fermion and left-handed antifermion interactions are suppressed by the factor of $(1 - v/c)\ m^2/2E^2$ *. Therefore, due to the difference between electron and

*In this case, "handed" refers to helicity rather than chirality. The discussion in Section 1.3 explains the difference.

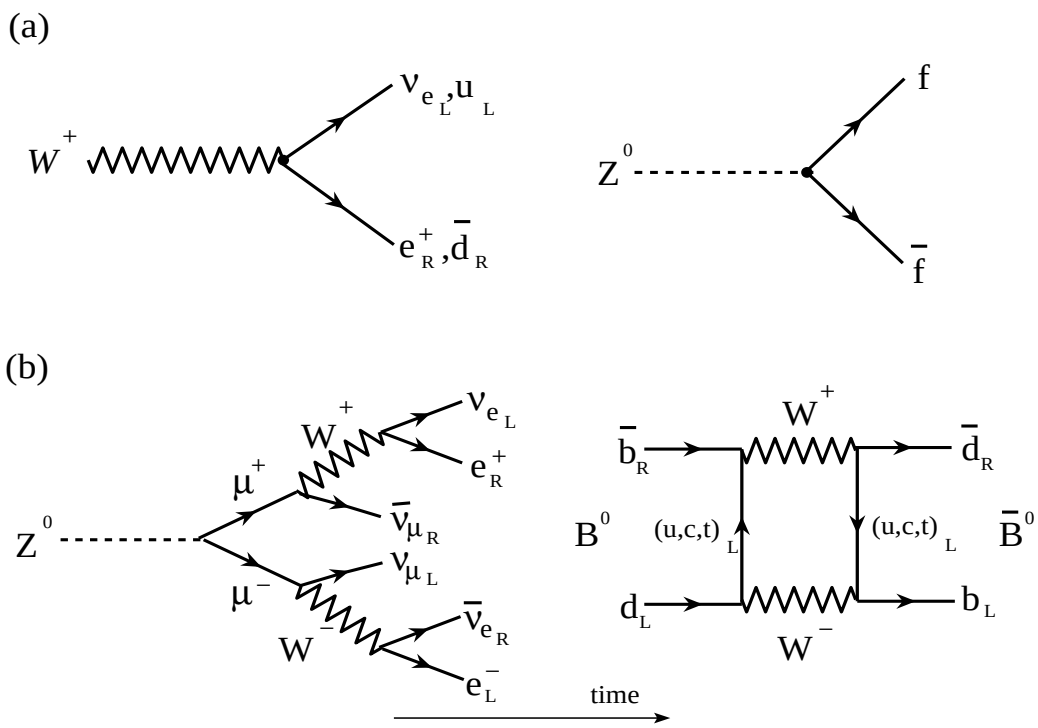

Figure 1.4: Feynman diagrams showing weak interactions of the fermions. (a) A W boson interacts with left-handed fermions and right-handed antifermions. A Z boson interacts with a fermion and antifermion. (b) An example where five weak interactions contribute to a Z boson decay via $\mu^+\mu^-$ into the final state of three left-handed particles and three right-handed antiparticles. A B^0 meson transforms into its own antiparticle by exchanging W^+ and W^- bosons.

muon masses, the rate of $\pi^+ \to e^+ + \nu_e$ is more than ten thousand times less than that of $\pi^+ \to \mu^+ + \nu_\mu$ because the two final state particles in a pion decay must have the same helicity. This effect is called "helicity suppression".

1.7 Fermion Mixing and CP Violation

The weak force maximally violates charge (C) and parity (P) separately, but also violates charge-parity (CP) transformations. This means that left-handed matter does not behave

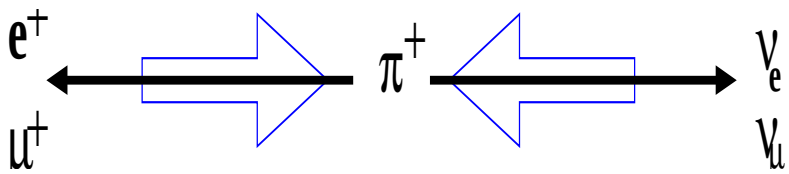

Figure 1.5: The decay of a spin-0 pion must conserve angular momentum, shown by the hollow arrows. Since the neutrinos are the least massive, they are ultra-relativistic, and always left-handed. This forces either the e^+ or μ^+ to be left-handed. The muon is the least relativistic, and therefore, the preferential decay is $\pi^+ \rightarrow \mu + \nu_\mu$ rather than $\pi^+ \rightarrow e^+ + \nu_e$.

exactly like right-handed antimatter, and so the two are distinguishable. The differences are smaller than a percent, but allow us to experimentally quantify the difference between matter and antimatter. The K_L is a linear combination of $d\bar{s}$ and $s\bar{d}$ and its decay $K_L \rightarrow e^+ + \nu_e + \pi^-$ would be expected to have the same rate as $K_L \rightarrow e^- + \bar{\nu}_e + \pi^+$ if there were no CP violation. Because of CP violation, the electron can be defined as the lepton which is produced 0.3% less than the positron in the case of the decay of the K_L meson.

The charged weak interaction can transform a quark of one isospin to a quark of opposite isospin. Primarily this transformation is within the same generation; however, weak interactions allow quarks from different generations to interact. The mixing of quarks between generations is parameterized by the Cabbibo-Kobayashi-Maskawa (CKM) matrix of Equation 1.2. The values in Equation 1.3 are current experimental constraints on the magnitudes of the CKM parameters.

$$\begin{pmatrix} d' \\ s' \\ b' \end{pmatrix} = \begin{pmatrix} V_{ud} & V_{us} & V_{ub} \\ V_{cd} & V_{cs} & V_{cb} \\ V_{td} & V_{ts} & V_{tb} \end{pmatrix} \begin{pmatrix} d \\ s \\ b \end{pmatrix} \tag{1.2}$$

$$= \begin{pmatrix} 0.9741\ to\ 0.9756 & 0.219\ to\ 0.226 & 0.0025\ to\ 0.0048 \\ 0.219\ to\ 0.226 & 0.9732\ to\ 0.9746 & 0.038\ to\ 0.044 \\ 0.004\ to\ 0.014 & 0.037\ to\ 0.044 & 0.9990\ to\ 0.9993 \end{pmatrix} \begin{pmatrix} d \\ s \\ b \end{pmatrix} \tag{1.3}$$

The unitary CKM matrix is often parameterized in terms of three angles, and a complex phase which quantifies the amount of CP violation in the quark sector.

Recent experiments prove that neutrinos have mass, allowing neutrinos to mix between generations. The Maki-Nakagawa-Sakata (MNS) matrix parameterizes the mixing, or oscillation of neutrinos. Each neutrino is viewed as a mixture of three types of neutrinos, ν_1, ν_2, and ν_3. Because of large mixing angles, each ν_i neutrino is not dominantly ν_e, ν_μ, or ν_τ. The MNS matrix has three angles and a CP-violating complex phase.

1.8 Electroweak Unification

Since Coulomb discovered that the electromagnetic force between charges has the same force law as Newton's gravitational force between masses ($charge*charge/distance^2$), physicists have been seeking to unify forces. In the 19th century, Maxwell found that electricity and magnetism were manifestations of the same force. In the 20th century, the electromagnetic force was found to unify with the weak force at high energies, as in the early universe or at particle accelerators. The electroweak unified theory is represented by the gauge group SU(2)$_L$ X U(1), and four massless gauge bosons are necessary to maintain its gauge invariance. Since the W^+, W^-, and Z^0 have been experimentally

observed to have mass while the photon is massless, the electroweak symmetry is necessarily broken.

The Standard Model accounts for breaking of the electroweak symmetry at low energies by introducing an extra term, $\mathcal{L}_{Higgs}$, to the Lagrangian which depends on the weak gauge fields, the electromagnetic gauge field, and a potential V,

$$V = \mu^2|\Phi|^2 + \lambda|\Phi|^4, \tag{1.4}$$

where Φ is a complex scalar field. The minimum of V is non-zero, meaning that there is a non-zero vacuum expectation value (vev) for the Higgs field. There are an infinite number of these non-zero solutions corresponding to the number of points on the circumference of a circle. The symmetry is broken once the minimum is non-zero. The "place on the circle" is the one parameter in the unification theory. Φ is reformulated in terms of a non-zero vacuum expectation value, three scalar fields which have longitudinal degrees of freedom, and a scalar field called H. The weak and electromagnetic fields are redefined such that they are invariant under local SU(2)$_L$ gauge transformations.

Substituting these redefinitions into $\mathcal{L}_{Higgs}$ results in the appearance of three massive vector fields for the Z and W bosons. The Z and W acquire a longitudinal degree of freedom and a mass. The massless photon and the Z boson are defined in such a way that the photon does not participate in the weak interaction. The substitution also results in the appearance of a real scalar Higgs field. The Standard Model accommodates this Higgs field in terms of a massive scalar Higgs boson, another fundamental particle added to the Standard Model. In general, it is possible that the Higgs may be a composite object, although such models are more difficult to reconcile with existing constraints from data.

The combined electroweak theory introduces processes where the photon couples to the charged weak fields as in Figure 1.6.

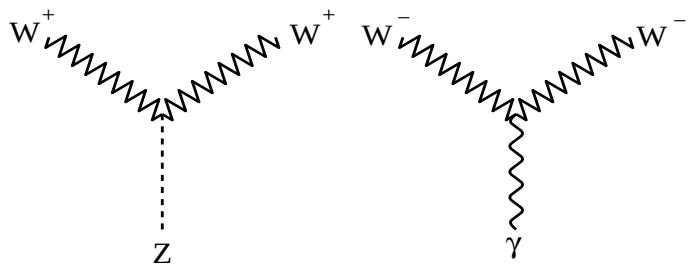

Figure 1.6: Feynman diagrams showing electroweak interactions of the bosons. The diagram on the right demonstrates the photon coupling to the weak boson fields.

Quantity	Number of parameters
Quark masses	6
Lepton masses	6
Coupling constants	3
Independent parameters of CKM matrix	3
Independent parameters of MNS matrix	3
Magnitude of CP violation in quark sector	1
Magnitude of CP violation in lepton sector	1
Fundamental electroweak mass scale	1
Higgs mass	1

Table 1.5: The 25 independent parameters of the standard model.

1.9 Limitations and Extensions of the Standard Model

The Standard Model of Fundamental Particles and Interactions has provided sound predictions which have been repeatedly verified over the last 20 years. Howevever, it has various theoretical flaws.

It fails to predict values like particle masses, realizing them only as empirical parameters entered into the theory. In order to fully specify the Standard Model, one needs to measure 25 independent parameters (Table 1.5).

The Higgs boson, which is integral to the mechanism of electroweak symmetry breaking, has so far escaped discovery. The best fit of the Higgs mass from precision electroweak fits of data has been excluded, and current experimental bounds put the Higgs mass at greater than 114 GeV. To satisy the condition that the sum of various scattering amplitudes for tree-level standard model processes do not exceed unitarity, theory dictates that either the Higgs boson is lighter than about 780 GeV or new physics must appear below an energy scale of 1.2 TeV [2].

It is understood that the Standard Model is likely the low-energy limit of a more global unbroken symmetry which might serve to explain the mechanism for spontaneous electroweak symmetry breaking. One very elegant model, called "Supersymmetry", introduces an additional symmetry to provide a method for electroweak symmetry breaking. This symmetry requires the Standard Model particles to have higher mass supersymmetric partners, thereby almost doubling the number of fundamental particles.

Another theory, called "technicolor", introduces a new strong force to impart mass to the W and Z bosons. This theory is often extended to give special significance to the top quark due to its uniqueness in the Standard Model. It is the most massive quark, and furthermore, it is the only quark with a mass greater than the massive bosons of the weak interaction ($Z^o, W^{\pm}$). Because of its high mass, it is the only fermion to have a Yukawa coupling to the Higgs field of order one. The theory known as "topcolor assisted technicolor" [3] suggests a new strong force preferentially coupling to the third generation of quarks. As a result, a topcolor Z' and two "top gluons" would exist which would decay preferentially to $t\bar{t}$ and $b\bar{b}$.

Theories of extra dimensions, which require some particles to exist in dimensions beyond the three space and one time dimension we see in everyday life, have scenarios where new scalar bosons with couplings preferential to the third generation are predicted. In some extra dimensional scenarios, in which just the bosons exist in extra dimensions, particles very similar to the topcolor Z' are predicted [4].

Beyond the understanding of electroweak symmetry breaking, there are many outstanding problems remaining for the Standard Model. Although there is a very successful classical theory of general relativity describing how gravity behaves on large scales, there is no working theory of the quantum interactions of gravity. The presence of gravity distorts space-time, and so the theory must explain how gravitons not only interact with other quantum particles, but also interact with space-time. The most likely manner of doing this is currently understood to be superstring theory, which has had the most success of any theory in demonstrating that gravity may be properly unified with the other forces.

The Standard Model is remarkably successful, explaining the interactions of matter with forces to a high precision over many orders of magnitude in energy. Perhaps in the next two decades, further developments will explain electroweak symmetry breaking, and unify the electroweak interaction with the strong interaction, or even gravity. The main goal of experimental particle physics today is to conduct measurements which are sensitive to deviations from Standard Model predictions, indicating that there is physics beyond the Standard Model which can solve these puzzles left by our current understanding. This dissertation will focus on the question of whether the top quark is special by searching for a right-handed, or "V+A" interaction, in its decay.

Chapter 2

Producing the Top Quark

The only experimental apparatus capable of producing the 175 GeV top quark is at Fermi National Accelerator Laboratory (Fermilab) [5, 6], located in Batavia, Illinois (Figure 2.1). At Fermilab, the top quark is created in both strong and weak interactions resulting from collisions between 900 GeV protons and anti-protons. This chapter explains the necessity for such high energy collisions, the method of producing them, and the interactions which create top quarks.

2.1 Using Collisions to Study the Structure of Matter

The structure of objects in our universe can be determined by particle collisions. When a 2.4 eV photon from the sun collides with an atom in a blade of grass, a bound electron is temporarily excited to a higher energy level, emitting a photon upon its return. If enough of these resulting photons are absorbed by a human eye, one can see the shape and color of the blade of grass. Visible light has a wavelength of $5 \cdot 10^{-7}$ m, allowing the lens of a microscope to bring into focus an object as small as a $1.7 \cdot 10^{-6}$ m human cell. The fundamental particles of the Standard Model are smaller than a proton, radius $1 \cdot 10^{-15}$

Figure 2.1: An aerial view of Fermilab. Shown are the Linac, Booster, Debuncher, and Accumulator, as well as part of the Main Ring.

m (1 fm), making it necessary to use energies 100 billion times greater to determine its structure. At high energies, the proton structure is a combination of quarks and gluons called partons. In addition to the three quintessential "valence" quarks (u, u, and d), the gluons give rise to virtual quark-antiquark pairs called "sea" quarks.

2.2 Fermilab Accelerator Complex

Inside the four-mile-circumference Tevatron tunnel circulates a clockwise-running beam of 900 GeV protons, and a counterclockwise-running beam of 900 GeV anti-protons. To achieve such energies, the protons and antiprotons are driven through a progression of accelerators (Figure 2.2). The speed of the particles is increased by accelerating them in electric fields. The direction of particles is controlled using magnetic fields to constrain them in circles and to focus them at the interaction points. The beams collide in the center of the Collider Detector at Fermilab (CDF) and the $D\emptyset$ detector.

2.2.1 Protons

The protons are obtained by heating hydrogen gas (H_2) so that H^+ ions are produced. A small electric field accelerates the H^+ ions into a metal surface with a high cesium content. Because the metal contains free electrons and the cesium has a low work function, high numbers of loosely held electrons gather around the H^+ ions. When an H^+ collects two electrons and is dislodged by another proton hitting the surface, the H^- ion will accelerate away from the metal surface. An electrostatic field accelerates these H^- ions to kinetic energies of 18 KeV. The H^- ions then approach the Cockroft-Walton pre-accelerator (Figure 2.3) which uses a series of voltage multiplier ladders to create a large electrostatic potential between the huge dome and a grounded column. The H^- beam is accelerated in the resulting field to 750 keV.

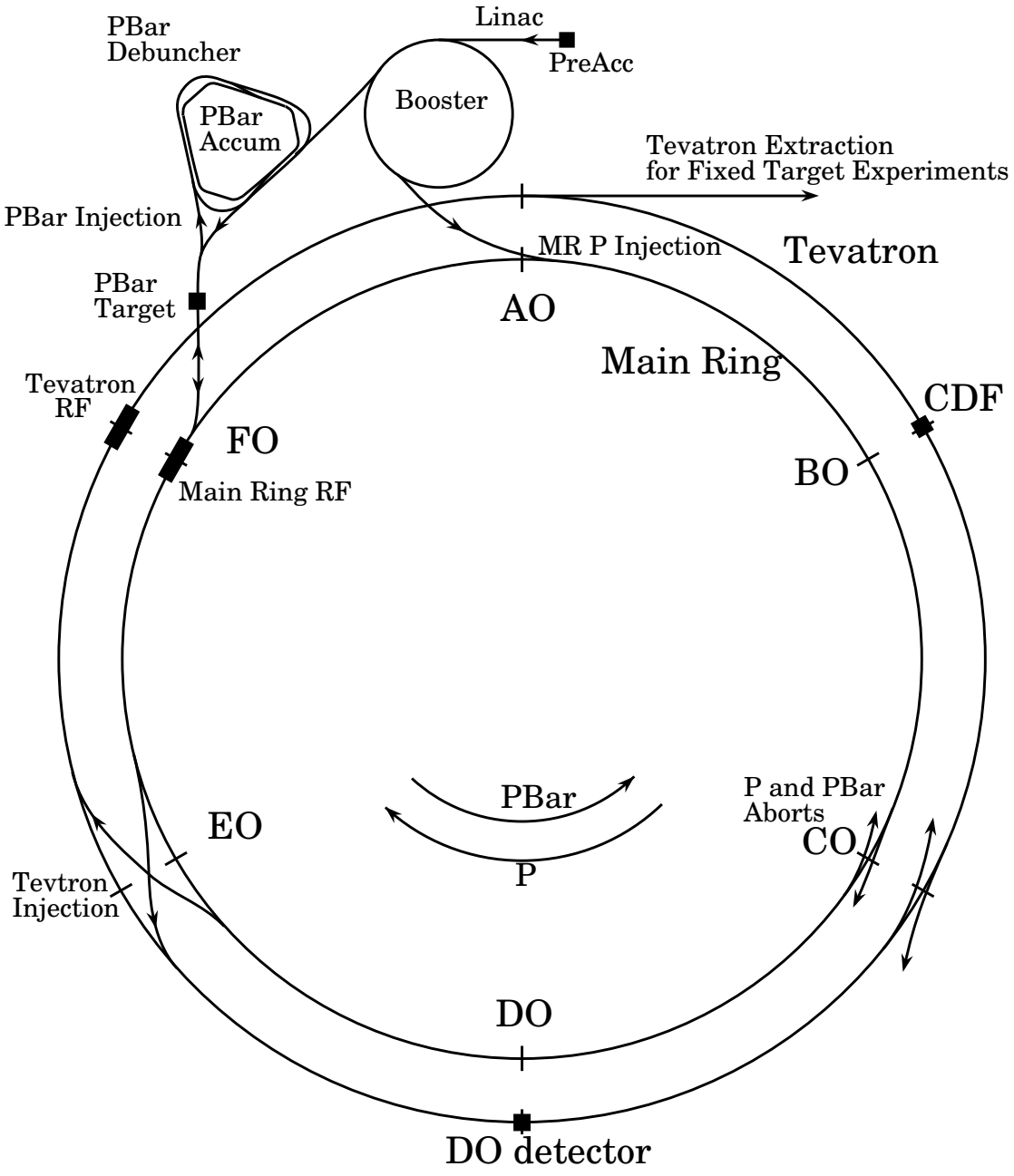

Figure 2.2: Schematic of the Tevatron accelerator complex.

Figure 2.3: The Cockroft-Walton pre-accelerator.

The H^- ions are next accelerated in the Linac, which is a series of fourteen cylindrical radio-frequency (RF) cavities. In an RF cavity, the electric field's frequency is tuned so that incoming ions are given coherent kicks of acceleration. The first five cavities are drift tube linacs which use high-gradient electric fields (2 MV/m) to synchronously kick the H^- ions to 116 MeV. The last nine cavities resonate with standing RF waves to accelerate the moving H^- ions to 400 MeV.

On the way into the Booster, the H^- ions pass through a carbon foil which strips off the electrons, leaving H^+ ions. These protons travel in orbit for 20,000 rotations around the 75 m radius Booster, and are accelerated from 400 MeV to 8 GeV by these many passes through a series of alternating gradient RF cavities.

The 8 GeV protons are then extracted from the booster and injected into the Main Ring, a circular accelerator which shares the Tevatron tunnel. The Main Ring consists of 774 dipole magnets for bending, 240 quadrupole magnets for focusing, and 18 RF cavities for particle acceleration. Protons are accelerated from 8 GeV to 150 GeV in this apparatus once every 2.4 seconds.

The 150 GeV protons are injected into the Tevatron, an alternating gradient synchrotron contained in the same tunnel as the Main Ring and mounted just below it. Its eight RF cavities accelerate the protons to 900 GeV. To keep such high energy particles in orbit, the Tevatron utilizes about 1000 superconducting magnets whose Nb-Sn conductors are cooled to liquid helium temperatures.

2.2.2 Antiprotons

Antiprotons ($\bar{p}$) bend in the opposite direction as protons in a magnetic field. The Fermilab accelerator complex makes use of this by transporting $\bar{p}$ in much of the same apparatus, but in the opposite direction and in two different orbits that only overlap at collision points.

Antiprotons are produced when 120 GeV protons extracted from the Main Ring collide with a nickel target. For every 10^{12} protons converging upon the target, 10^7 antiprotons are created. Charged particles from the collision are rendered nearly parallel by a lithium lens, and dipole magnets are used to select $\bar{p}$ with 8 GeV momentum. Antiprotons are directed through the Debuncher, which reduces their momentum spread in the longitudinal and transverse directions, allowing them to be collected in the Accumulator. With this procedure, 10^{10} $\bar{p}$ can be collected in one hour. After 10^{11} $\bar{p}$ have been collected, they are accelerated from 8 to 150 GeV in the Main Ring. The $\bar{p}$ beam is then added to a p beam already circulating in the Tevatron at 150 GeV where they are then accelerated to 900 GeV simultaneously.

2.2.3 Collisions

Inside the Tevatron, beams of $2{\cdot}10^{11}$ protons and $6{\cdot}10^{10}$ antiprotons are each divided into six bunches. The beams travel in the same beam pipe in double helical orbits, thereby intersecting only in two locations, the CDF and $D\emptyset$ detectors. At the interaction points, the beams are focused to a transverse diameter of about 35 μ m, creating an average of 2.5 interactions per bunch crossing (every 3.5 μ s).

The performance of the Tevatron is measured in terms of instantaneous luminosity $\mathcal{L}$ which is proportional to the number of protons N_p and antiprotons $N_{\bar{p}}$ per bunch, the number of bunches B in either beam, the frequency of bunch revolution f, and inversely proportional to the area of the intersection between the bunches, A.

$$\mathcal{L} = \frac{N_p N_{\bar{p}} B f}{4\pi A} \tag{2.1}$$

$\mathcal{L}$ typically decreases by a factor of two in ten hours due to transverse spreading of A and losses of N_p and $N_{\bar{p}}$ from collisions or interactions with residual gas or from strays which fall out of a focused orbit. To consistently maintain high $\mathcal{L}$, the beams are then

jettisoned, and new protons and antiprotons are injected.

The goal of the accelerator complex is to operate continuously, producing high integrated luminosity $\int \mathcal{L}dt$. The data evaluated for this analysis was collected in two periods: Run IA (August 1992 to May 1993) and Run IB (January 1994 to July 1995). In Run IA, the peak instantaneous luminosity was 9.2 $\cdot 10^{30}$cm^{-2}s^{-1}, while typical values were 5.4 $\cdot 10^{30}$cm$^{-2}s^{-1}$. The total integrated luminosity was 31.7$\cdot 10^{36}$cm^{-2}, or 31.7 pb^{-1} (p = pico = 10^{-12}, b = barn = 10^{-24}cm^2).

In Run IB, the peak instantaneous luminosity increased to 27 $\cdot 10^{30}$cm^{-2}s^{-1}, with typical values of 16 $\cdot 10^{30}$cm^{-2}s^{-1}, for a total integrated luminosity of 100.8 pb^{-1}.

In total, the Tevatron delivered a total integrated luminosity of 132.5 pb^{-1} to CDF in Run I, providing 106 pb^{-1} of usable data for top physics analysis.

The integrated luminosity, $\int \mathcal{L}dt$, is related to the number of events N expected for a given physics process by

$$N = \int \mathcal{L}dt \cdot \sigma, \tag{2.2}$$

where σ is the cross-section for the process to occur.

The $p\bar{p}$ inelastic scattering cross-section is about 50 mb, thus producing approximately 6.5 trillion inelastic scattering events in Run I.

2.3 Top Production

In contrast to the high inelastic scattering cross-section, the predicted cross-section for producing 175 GeV top quarks at $\sqrt{s}$ = 1.8 TeV is ten billion times less. Thus only a thousand of these events were delivered to the CDF detector in Run I.

The top quark is mainly produced in association with an antitop quark via the strong interaction. This $t\bar{t}$ production mechanism has a predicted cross-section of 5.1 pb [37], 90% coming from annihilation of initial state quarks on antiquarks, and 10% from col-

lisions of gluons. The $q\bar{q}$ production processes dominate gg since quarks tend to carry

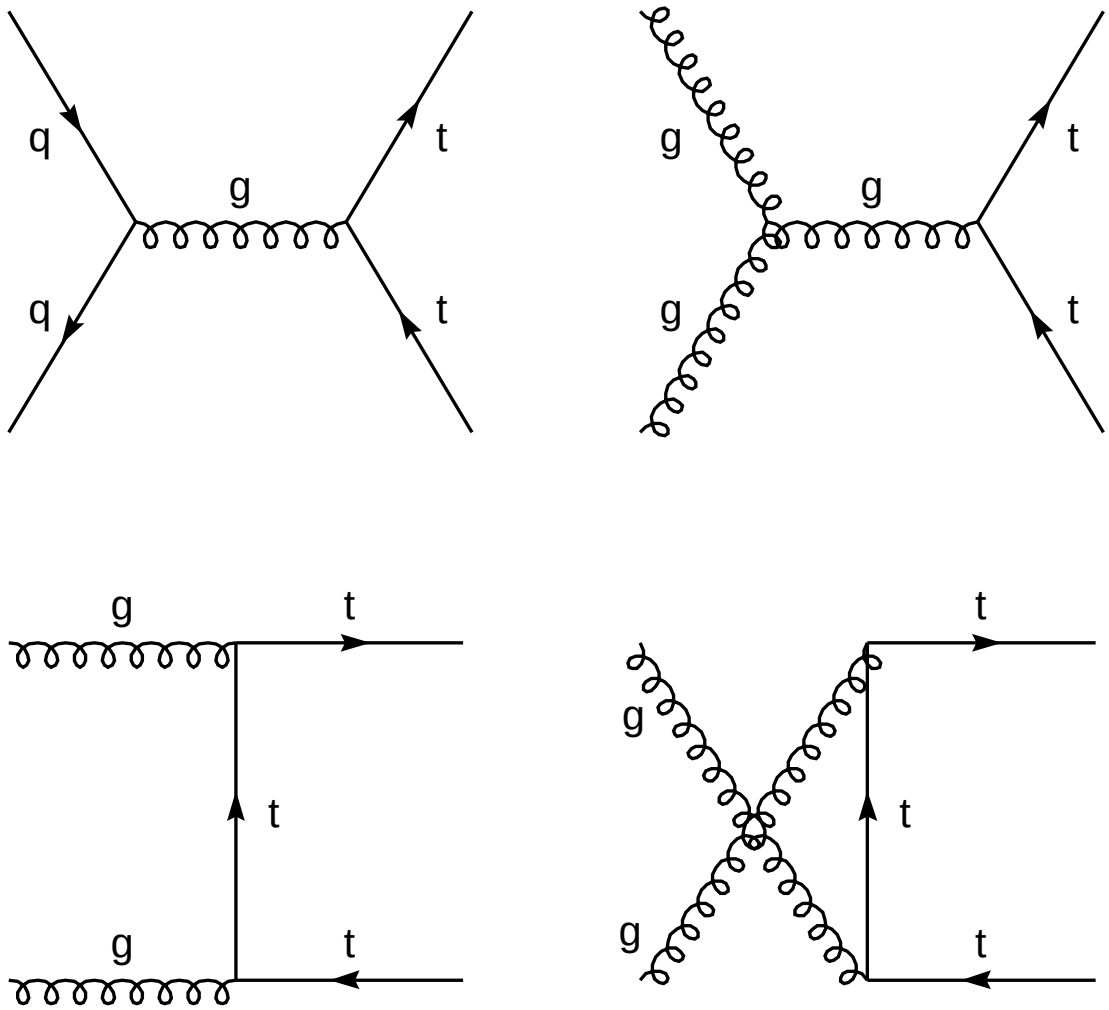

Figure 2.4: Feynman diagrams for $t\bar{t}$ production via the strong force.

more momentum within the proton than the gluons. To create $t\bar{t}$, the incoming partons must have at least 20% of the 900 GeV p and $\bar{p}$ momentum. The probability for a parton to have a given momentum fraction is specified by its parton distribution function (PDF). At these high momentum fractions, the number of u quarks is greater than the d

quarks and gluons, and is much higher than the number of sea quarks (Figure 2.5).

The top quark can also be produced via the weak interaction when a virtual W boson decays into a single top quark as in Figure 2.6. Since the cross-section for this process is about a third of $t\bar{t}$ production and has lower experimental sensitivity, the observation of top quarks at Fermilab has so far been restricted to $t\bar{t}$ production.

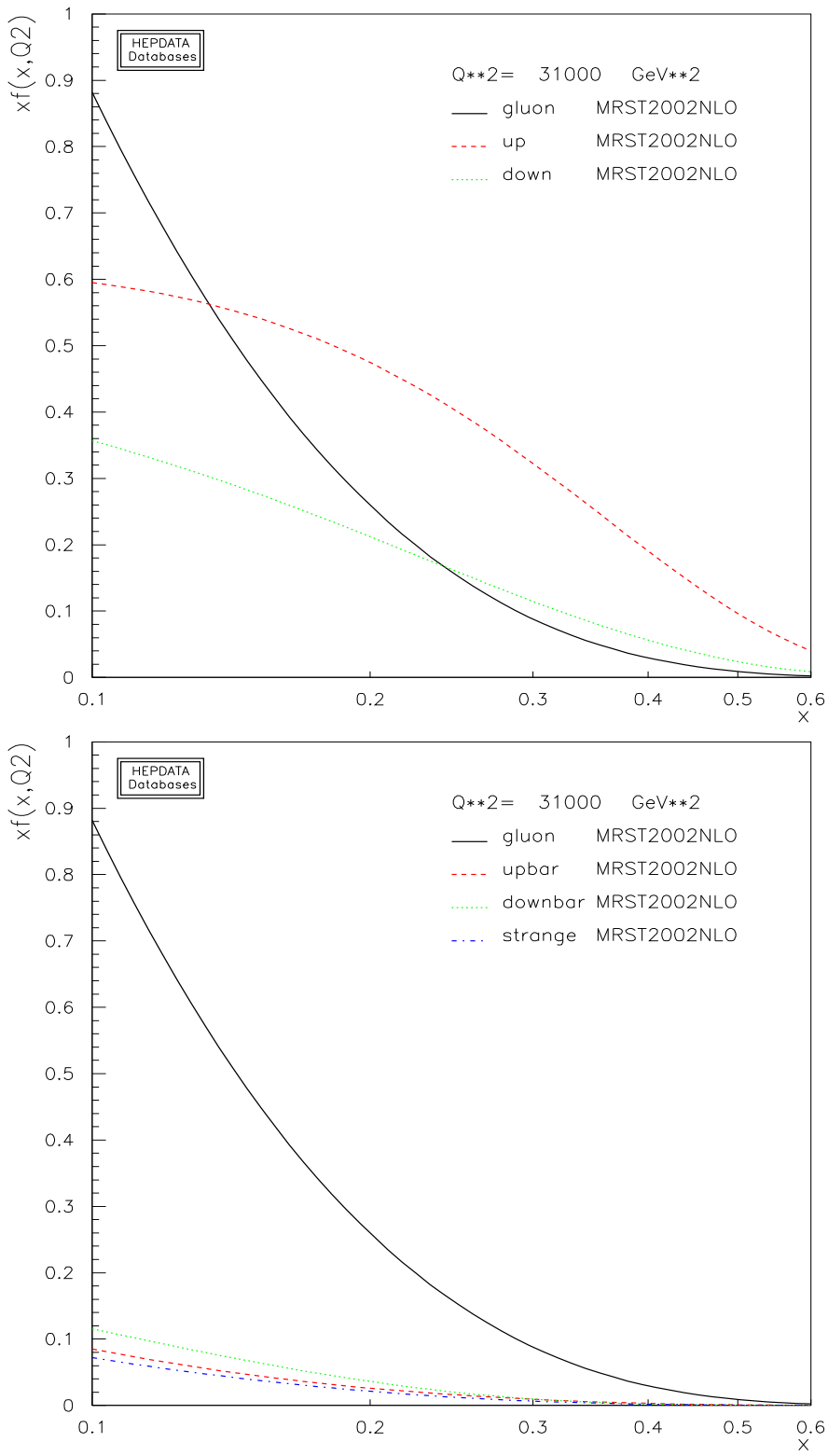

Figure 2.5: The structure of the proton as a function of x, the fraction of proton momentum carried by each constituent. The plot is of x f(x,Q^2), the probability density distributions at the given momentum fraction for a given momentum transfer Q^2. The upper distribution compares gluons with valence quarks; the lower compares gluons to sea quarks.

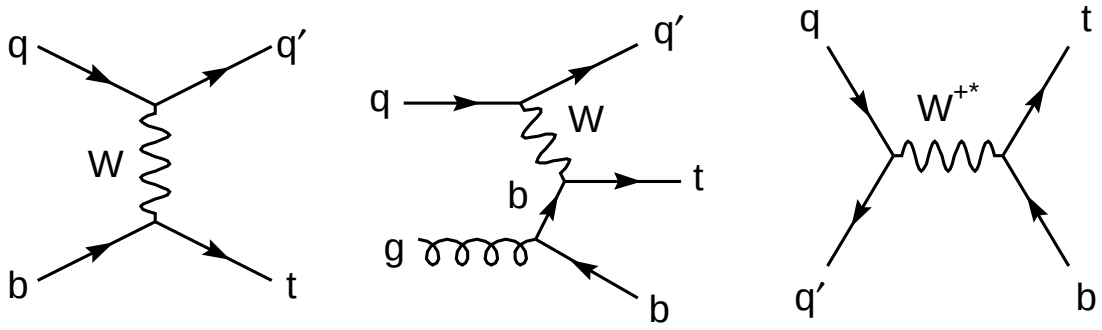

Figure 2.6: Feynman diagrams for single top quark production by the weak force.

Chapter 3

Detecting the Top Quark

After the bottom quark was discovered in 1977, physicists began searching for its partner, the top quark. In 1994, CDF found evidence for a 174 $\pm$ 10 (stat.) $^{+13}_{-12}$ (syst.) GeV top quark using 19.3 pb^{-1} data from Run IA [8]. In 1996, CDF and $D\emptyset$ simultaneously announced the observation of the top quark with a mass of 176 $\pm$ 8 (stat.) $\pm$ 10 (syst.) GeV and 199 $^{+19}_{-21}$ (stat.) $\pm$ 22 (syst.) GeV, respectively [9, 10]. By 1999, the joint CDF/$D\emptyset$ top mass was determined to be 174.3 $\pm$ 5.1 GeV [29].

3.1 Top Decay

The top quark is unique due to its heavy mass. Since its lifetime is approximately 10^{-24} s, and the time for a free quark to form a bound state is approximately 10^{-23} s, the top quark decays as a free quark. The top quark decays almost 100% of the time to a real W boson by $t \rightarrow W^+ + b$. The W boson decays either leptonically into a charged lepton and its neutrino partner such as $W^+ \rightarrow \mu^+ + \nu_\mu$, or hadronically into a quark and its opposite isospin antiquark such as $W^+ \rightarrow u + \bar{d}$. The Feynman diagram for $t\bar{t}$ decay, where there are two W bosons, is shown in Figure 3.1. The branching ratios for the $t\bar{t}$

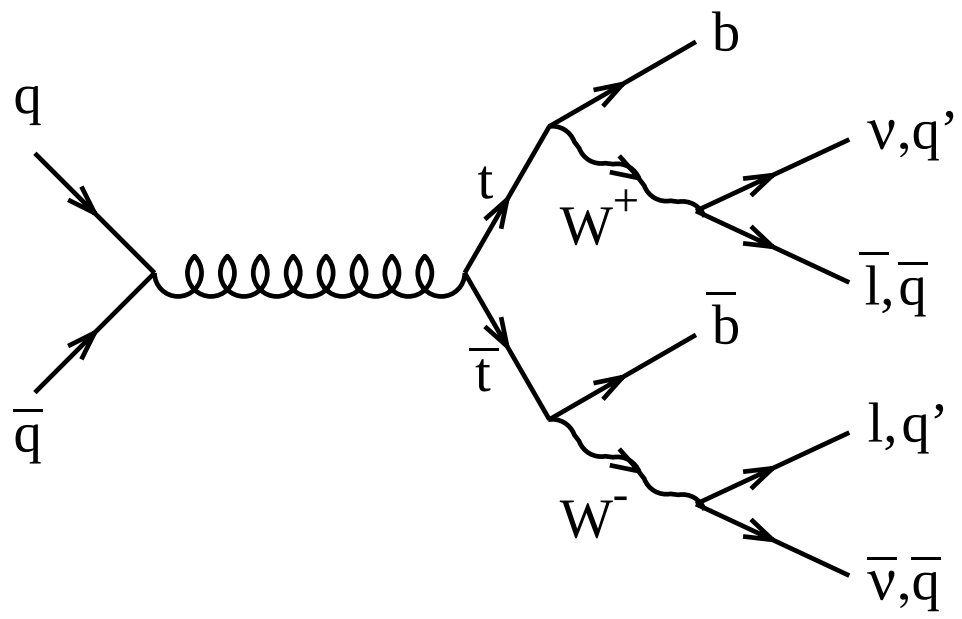

Figure 3.1: Feynman diagram for decay modes of $t\bar{t}$ produced by $q\bar{q}$ annihilation.

decay modes appear in Table 3.1.

$t\bar{t}$ decays are classified into channels by number of final state charged leptons. Events are referred to as "all-hadronic" when both Ws decay to quarks, "dilepton" when both Ws decay to either electrons or muons, and "lepton + jets" when one W decays to an electron or muon while the other decays to quarks. Tau leptons are not explicitly included in the $t\bar{t}$ decay channels because their observed final states, either hadrons plus a neutrino or a softer momentum electron or muon plus two neutrinos, are difficult to identify in the detector. However, their subsequent decay into electrons or muons may cause them to be included in the other channels. For each decay mode, there are non-$t\bar{t}$ physics "backgrounds" which can imitate the $t\bar{t}$ signal, decreasing measurement sensitivity. The effect of these backgrounds can be reduced by discarding events with kinematics inconsistent with $t\bar{t}$ decay. However, improvements in signal purity must be weighed against diminution of real $t\bar{t}$ events.

Decay Mode	Branching Ratio
$t\bar{t} \rightarrow (q'\bar{q})(q'\bar{q})b\bar{b}$	36/81
$t\bar{t} \rightarrow (q'\bar{q})(e\nu)b\bar{b}$	12/81
$t\bar{t} \rightarrow (q'\bar{q})(\mu\nu)b\bar{b}$	12/81
$t\bar{t} \rightarrow (q'\bar{q})(\tau\nu)b\bar{b}$	12/81
$t\bar{t} \rightarrow (e\nu)(\mu\nu)b\bar{b}$	2/81
$t\bar{t} \rightarrow (e\nu)(\tau\nu)b\bar{b}$	2/81
$t\bar{t} \rightarrow (\mu\nu)(\tau\nu)b\bar{b}$	2/81
$t\bar{t} \rightarrow (e\nu)(e\nu)b\bar{b}$	1/81
$t\bar{t} \rightarrow (\mu\nu)(\mu\nu)b\bar{b}$	1/81
$t\bar{t} \rightarrow (\tau\nu)(\tau\nu)b\bar{b}$	1/81

Table 3.1: The branching ratios for $t\bar{t}$ decay modes assuming standard model couplings. Here q may be a u, d, c or s quark.

The branching fraction to the all-hadronic channel is 44%. This mode is characterized by six or more "jets" which are collimated sprays of particles resulting from gluon radiation and hadronization of the quarks. The main background for this mode is inelastic scattering where multiple jets are created through gluon radiation. Although this background is significantly more abundant than $t\bar{t}$ in this channel, it can be reduced by requiring one or two jets to be "b tagged" or identified as coming from a b quark. One disadvantage of this channel is that in $W \rightarrow q' + \bar{q}$, the quark and antiquark jets cannot be easily distinguished. The measurement of this thesis requires differentiation of W decay products, so the all-hadronic channel is not considered.

The branching fraction to the lepton + jets mode is 30%. Its signature is an electron or muon, four jets, and missing energy due to the unmeasured neutrino. The backgrounds in this channel are mainly from electroweak processes which produce a weak boson in association with jets. A Feynman diagram for the dominant background called "W + jets" is shown in Figure 3.2. By requiring one or two of the jets to be b tagged, backgrounds are reduced considerably. The lepton + jets sample of data provides the

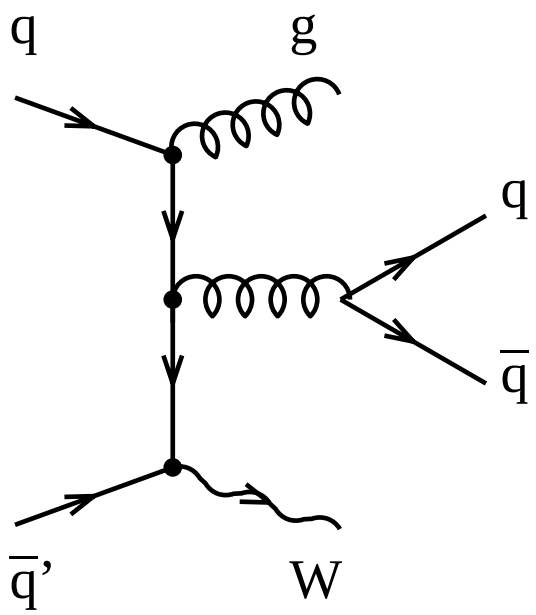

Figure 3.2: The Feynman diagram for W production in association with jets, the dominant background in the $t\bar{t}$ lepton + jets channel.

best measurements of the top quark cross-section and mass due to its small background and large signal rate.

The branching fraction to the dilepton channel is 5%. Its signature is two leptons (μ or e), two jets from the b quarks, and missing energy from the two unmeasured neutrinos. The largest backgrounds are from Drell Yan processes in which quarks interact producing a Z or a virtual photon (γ^*), and then decay into leptons. This background can be reduced by requiring the leptons to be of different flavor, thereby rejecting all except $Z \rightarrow \tau^+\tau^- \rightarrow e^+ + \nu_e + \mu^- + \nu_\mu$.

3.2 Collider Detector at Fermilab (CDF)

CDF is a multi-component detector equipped to detect the top quark by identifying electrons, muons, jets, and missing energy due to neutrinos. The detector surrounds the

collision region with azimuthal and forward-backward symmetry. Tracking detectors measure the momentum (P) of charged particles such as electron and muons, and also are used to identify jets from b quark decay. Calorimeter detectors measure the energy (E) of electrons, photons, hadronic particles, as well as the minimum ionization energy of muons. Muon detectors surround the calorimeters, providing additional muon tracking. A diagram of CDF is shown in Figure 3.3. More detailed descriptions of CDF can be found elsewhere [7].

It is useful to define detector coordinates and detection variables. θ is the angle between the proton direction +z and a vector in the $\hat{y} - \hat{z}$ plane. Rapidity, defined as $-\ln[(E+P)/(E-P)]$, is a Lorentz invariant quantity such that particle multiplicity from inelastic collisions is constant per unit rapidity. For highly relativistic particles which have $E \gg M$ this is approximated by pseudorapidity η,

$$\eta = -\frac{1}{2}\ln(\tan(\theta/2), \tag{3.1}$$

which measures the forward direction of particles produced in collisions. Particles are also specified by their "transverse energy" E_T, defined by

$$E_T = E \cdot \sin\theta. \tag{3.2}$$

Similarly, transverse momentum,

$$P_T = P \cdot \sin\theta. \tag{3.3}$$

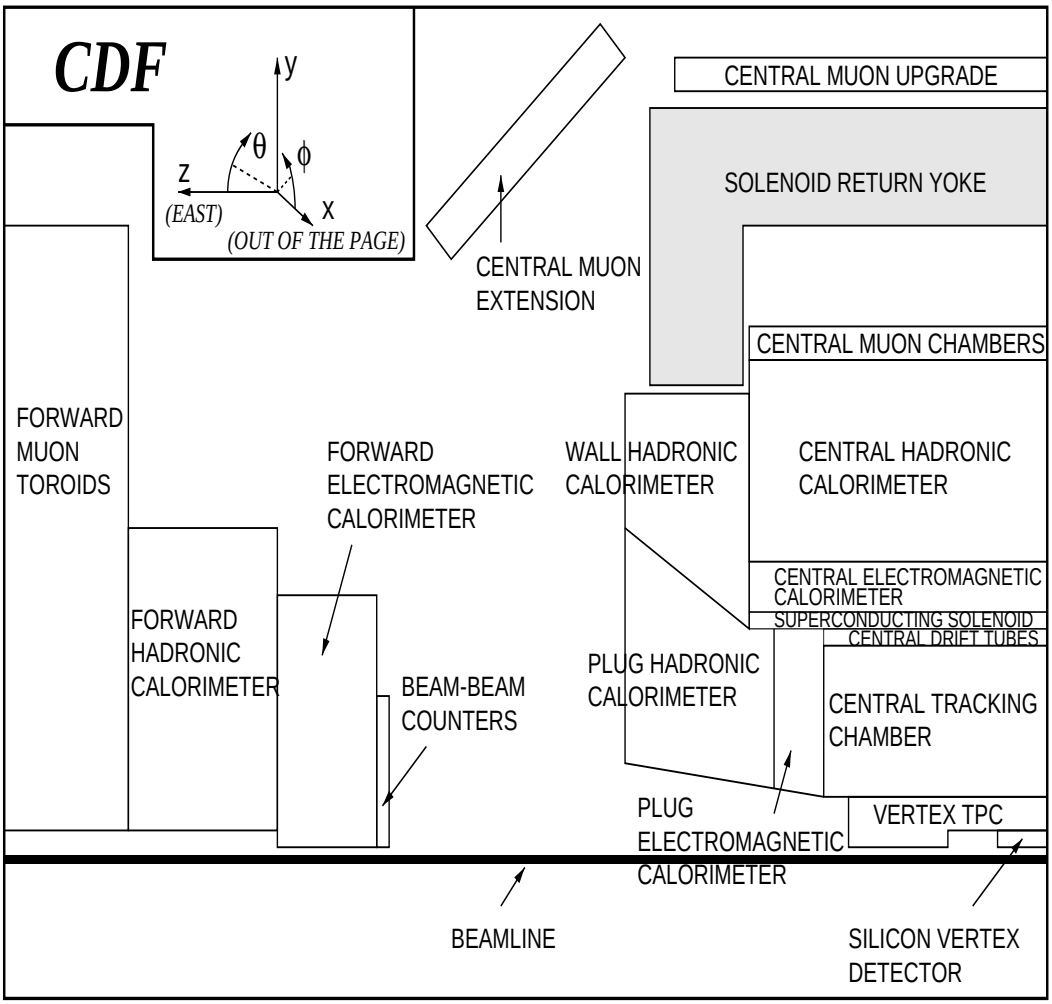

Figure 3.3: A view of one quarter of a slice through the center of the CDF II detector. The full detector is recreated by reflecting the image from +z to -z, and rotating about the z-axis.

3.3 Tracking Detectors

3.3.1 Magnetic Field

Charged particles entering the central detector volume pass through a series of three tracking detectors enclosed in a 1.4 T magnetic field, created by a 1.5 meter radius, 4.8 meter long super conducting toroidal magnet. The magnetic field B is aligned with the direction of the proton beam, bending charged particles to curve in the $\hat{x} - \hat{y}$ plane with radius

$$R = \frac{P_T}{q * B} \tag{3.4}$$

where q is the sign of the electric charge, and B is the strength of the magnetic field.

3.3.2 Silicon Vertex Detector (SVX)

Immediately surrounding the beryllium beam pipe is the Silicon Vertex Detector (SVX) shown in Figure 3.4, which provides coverage for $|\eta| < 1.9$, and has a single hit resolution per layer of 13 μm with a 96% hit efficiency. The 54 cm long SVX encompasses most of the $p\bar{p}$ interactions which are centered at z = 0 and have a 30 cm Gaussian width. Silicon does not conduct electricity because there is a ~ 1 eV potential gap between its valence band of electrons and its conduction band. A charged particle traveling through 300 μm thick silicon produces 24,000 electrons, but this signal cannot be distinguished above the 10^8 free charge carriers typically being excited from the valence to the conduction band at thermal equilibrium. By substituting some phosphorus for silicon, extra electrons are added to the conduction band, making the silicon “n-type”. Similarly, substituting boron for silicon removes electrons from the valence band, making the silicon “p-type”. Applying a bias voltage to a junction of “n-type” and “p-type” silicon creates a depleted region that minimizes the number of free electrons being thermally excited from the valence band to the conduction band, allowing a 24,000 electron signal to be

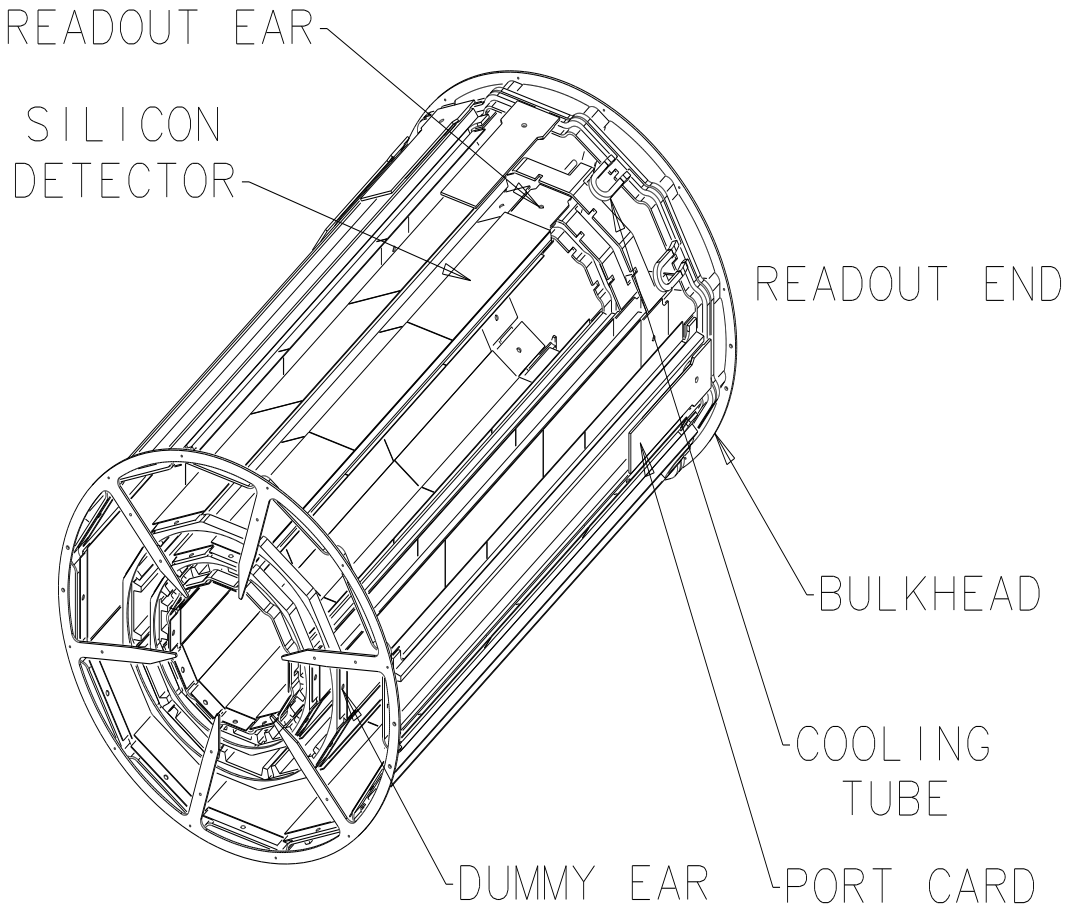

Figure 3.4: Diagram of one of the two SVX barrels.

detected.

The basic unit of the SVX is a wafer composed of a junction of strips of “p-type” silicon on an “n-type” silicon substrate. A “ladder” is composed of three 8.5 cm long silicon wafers electrically bonded end to end with aluminum read-out strips running parallel to the beam line. Ladders are read out on one side by readout chips handling 128 strips (channels) each. A “wedge” is 4 layers of increasingly wider ladders at radii of 2.861 cm, 4.256 cm, 5.687 cm, and 7.866 cm from the beam axis. Twelve wedges equally spaced in ϕ are mounted onto a barrel running parallel to the beam. Two 25.5 cm barrels separated by a 2.15 cm gap at z = 0 compose the SVX detector, for a total of 96 ladders. To minimize data readout of the 46,080 channels, only channels which register a hit are read out. In this sparse mode, only 5% of the channels are read out on an average event. The time it takes to read out all twelve wedges in parallel is 2 ms.

Between Run IA and Run IB, the SVX was replaced with an SVX’ detector, identical in structure but incorporating radiation resistant readout chips, and utilizing AC rather than DC currents.

The SVX provides precise $r-\phi$ tracking and a mechanism for discerning secondary vertices in the $\hat{r}-\hat{\phi}$ plane. Combined with the other tracking detectors, the SVX provides a measurement with approximately 15 μm resolution of the impact parameter of a track, which is defined as the distance of closest approach to the primary vertex of an event. A non-zero impact parameter is a signature of secondary vertices from the b hadron.

3.3.3 Vertex Time Projection Chamber (VTX)

Surrounding the SVX, the Vertex Time Projection Chamber (VTX) provides z vertex information which distinguishes between vertices from multiple interactions occurring in a single bunch crossing. The VTX extends radially from 8 cm to 22 cm, and is comprised lengthwise by eight octagonal modules containing an equal mixture of argon

and ethane gas. Each module holds 192 sense wires which run radially outward and serve to collect free charge carriers that are created when charged particles ionize the gas.

The wire position of the signal gives a radial coordinate, and the timing of the hits at each wire determines the z position. In events with multiple tracks, the VTX provides the z position of the primary vertex with an uncertainty of less than 1 mm, allowing a track to be associated with the correct vertex. The 2.8 m length of the VTX provides tracking information for $|\eta| < 3.25$.

3.3.4 Central Tracking Chamber (CTC)

Beyond the VTX from a radius of 0.3 m out to 1.3 m is the Central Tracking Chamber (CTC) which measures the transverse momentum of charged particles, using their curvature inside the 1.4 T magnetic field. The CTC accommodates 84 layers of sense wires grouped into nine superlayers running the 3.2 m length of the chamber, as shown in Figure 3.5. Field wires in the chamber generate a 1350 V/m drift field. The superlayers alternate between "axial", which run parallel to the beam direction and provide $r - \phi$ tracking, and "stereo", which are offset from the beam axis by 3° and together with the axial layers can therefore resolve positions in the $\hat{r} - \hat{z}$ plane. Together, these layers provide 3-D tracking. The superlayers contain cells of sense wires in an argon-ethane-ethanol gas mixture. Axial cells hold twelve sense wires, while stereo cells have six. The cells are tilted 45° relative to the radial direction to account for the azimuthal direction of drift electrons in the crossed electric and magnetic fields. By fitting hits in the CTC to a helical path, the CTC provides tracking coverage over the range $|\eta| < 1.0$, and gives a transverse momentum resolution of $\delta P_T/P_T < 0.002\ P_T$. Combined with the SVX, this resolution improves to $\delta P_T/P_T < 0.001\ P_T$ because of the precision of the SVX and the increased path length for the measurement.

	Central Tracking Chamber (CTC)	Vertex Tracking Chamber(VTX)	Silicon Vertex Detector (SVX)
Polar Angle Coverage	$\|\eta\| < 1.5$	$\|\eta\| < 3.25$	$\|\eta\| < 1.2$
Inner, Outer Radii (cm)	30.9, 132.0	8, 22	2.7, 7.9
Length (cm)	320	280	26
Layers	60 axial, 24 stereo	24	4
Strip/Wire Spacing	10 mm	6.3 mm	60 μm (inner 3 layers) 55 μm (outer layer)
Spatial Resolution	200μm $(r-\phi)$ 4 mm $(r-z)$	200-500 μm $(r-z)$	15 μm $(r-\phi)$
Momentum Resolution	$\delta P_T/P_T =$ 0.002 P_T		$\delta P_T/P_T =$ 0.001 P_T
Thickness in Radiation Lengths (X_0)	$\approx$ 0.015 X_0	$\approx$ 0.0045 X_0	$\approx$ 0.035 X_0

Table 3.2: Description of the charged particle tracking chambers.

The parameters of the tracking detectors are summarized in Table 3.2. Charged particles with energy greater than 350 MeV and neutral particles escape the magnetic field in the tracking volume and enter the calorimeters.

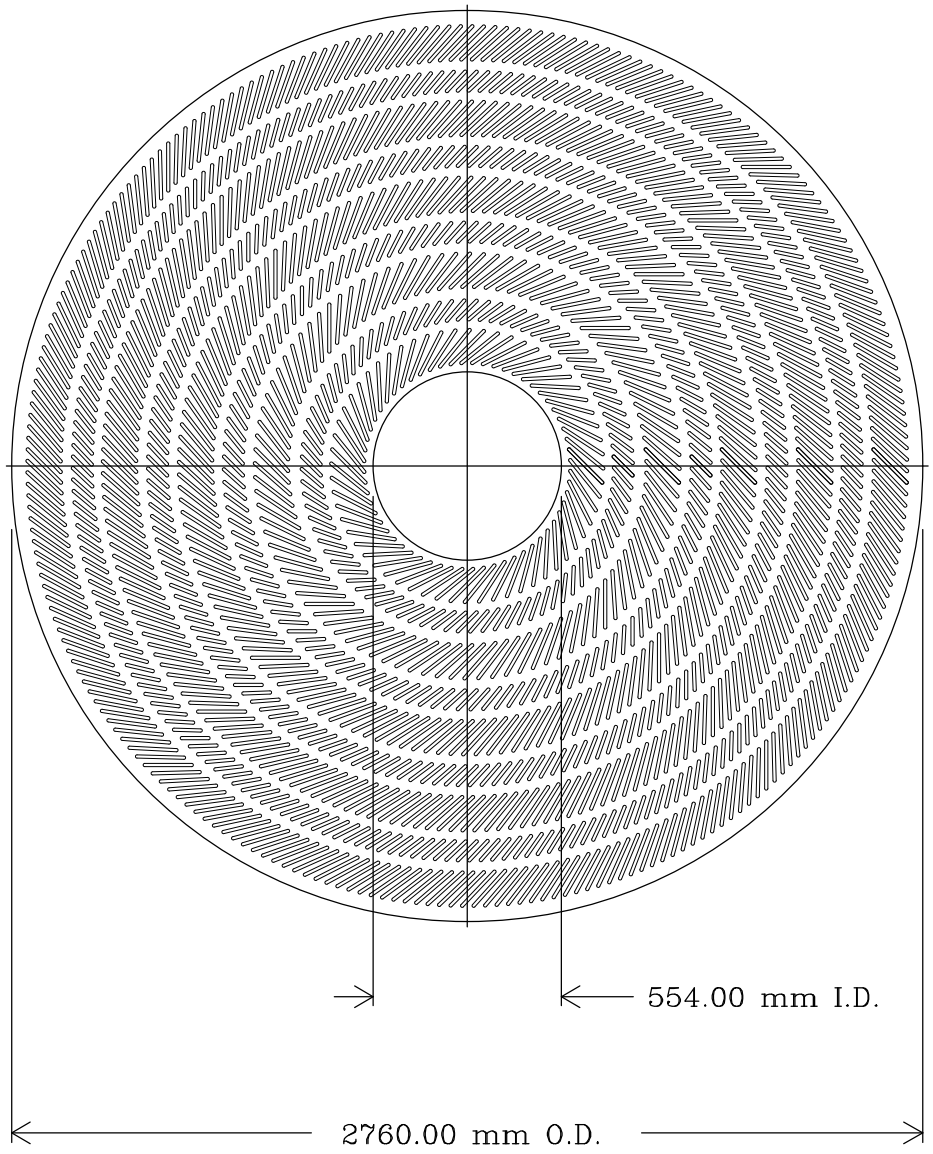

Figure 3.5: Cross-section of the CTC illustrating the arrangement of 84 layers of drift wires into cells within nine superlayers.

Material	Atomic Mass (g/mol)	Atomic Number	Density (g/cm^3)	Radiation Length λ_0 (cm)	Absorption Length X_0 (cm)
Aluminum	26.98	13	2.70	8.90	37.2
Iron	55.85	26	7.87	1.76	17.1
Lead	207.19	82	11.35	0.56	18.5

Table 3.3: Absorption properties of materials used in the CDF detector.

3.4 Calorimetric Detectors

Surrounding the tracking detectors are calorimeters which measure the deposited energy of incident electrons, hadrons, and photons by causing them to cascade into a shower of lower energy particles.

The calorimeters encompass the beam axis with 2π symmetry, extending to $|\eta| < 4.2$. They are composed of alternating layers of an absorption material and an active collection medium. There are two types of calorimeters, electromagnetic (EM) and hadronic (HA), each with different absorption materials.

Electromagnetic calorimeters mainly measure electrons, positrons, and photons. When an electron passes through the dense absorption layers, it is deflected by the electric field of the atoms in the material, producing bremsstrahlung photons to conserve momentum. The photons will compton scatter in the medium, and if the photons have sufficient energy ($>$ 3 MeV in lead) they will produce electron-positron pairs in the field of the nucleus. These three particles travel in almost the same direction, and the process of photon, electron, and positron creation repeats creating a cascade of particles which first grows and then diminishes as shower particles lose energy. This electromagnetic shower of particles is detected as a signal in the active collection medium. Electromagnetic absorption layers are classified in terms of radiation length X_0, the distance over which an electron loses all but $1/e$ of its total energy by bremsstrahlung. With its high nuclear

charge of +82, lead has an X_0 of 0.56 cm, and is used as the absorption material in the EM calorimeters.

Hadronic calorimeters provide additional material to measure the showers of hadrons. Hadrons mainly shower due to inelastic nuclear collisions rather than electromagnetic deflections. These collisions produce additional particles, such as pions. Neutral pions produced by the showers result in electromagnetic cascades. Since the effective target area of a nuclei is 100,000,000 times smaller than that of an atom, hadronic showers develop over a longer distance. The hadronic calorimeters are therefore located outside the electromagnetic calorimeters. Hadronic absorption materials are classified by their interaction length λ_0, the mean free path of a particle before undergoing an inelastic collision. Iron has a λ_0 of 17.1 cm, compared with 18.5 cm for lead, making it the choice for the HA calorimeters. A comparison of absorption materials is shown in Table 3.3.

Both types of calorimeters sample the energy of the randomly fluctuating shower, leading to an uncertainty in the energy measurement. In electromagnetic cascades, the primary energy loss mechanism is ionization, which provides a detectable signal in the active layers. Hadronic cascades however lose 30% of their incident energy through the breakup of nuclei. Since this does not yield a signal, energy resolution in the HA calorimeters is worse than in the EM calorimeter.

The active collection layers in the EM and HA calorimeters detect a fraction of the energy produced in the shower by returning a signal proportional to the ionization loss of shower particles. Two types of active layers are used in the CDF detector. Plastic scintillating counters contain organic molecules which become excited by the passage of charged particles, and produce photons. This luminescence is transmitted by light guides, and amplified by a photo-multiplier. Proportional counters contain gas-filled tubes with an electric field created between a high voltage anode wire in the tube and copper planes surrounding the tubes. As charged particles penetrate the tubes, the gas is ionized, and free electrons are accelerated to the wire, creating an avalanche of sec-

ondary electrons which are collected and amplified.

To determine the position of incoming particles, the detectors are segmented into towers in $\eta - \phi$ space which project to the nominal interaction point. Each tower has a constant size of $\Delta\eta \sim 0.1$, resulting in increasingly smaller towers as a function of η. The extent of the shower, in terms of the number of towers and the progression of the shower through the layers, helps distinguish electrons and photons from jets.

In addition to measuring the energy and direction of particle showers, the calorimeters also detect a small amount of "minimum ionizing energy" from muons, which are not easily deflected by the absorption material due to their high mass and do not produce showers. Neutrinos do not interact with the CDF detector but are inferred by summing the energy deposited as a function of ϕ and calculating the transverse missing energy ($\not{E}_{\mathrm{T}}$) and its ϕ direction.

The calorimeter is divided into three pseudorapidity regions: Central (C) with $|\eta| < 1.1$, Plug (P) with $1.1 < |\eta| < 2.4$, and Forward (F) with $2.4 < |\eta| < 4.2$.

3.4.1 Central, Plug, and Forward Calorimeters

The central calorimeter is composed of the Central Electromagnetic Calorimeter (CEM), the Central Hadronic Calorimeter (CHA), and the Wall Hadronic Calorimeter (WHA). The collection medium is plastic scintillating counters; polystyrene is used in the CEM, and acrylic is used in the CHA and WHA.

There are 24 ϕ wedges of CEM and CHA pointing to r = 0, each covering 15° of the circle. Each wedge has ten towers extending in the z direction and segmented with $\Delta\eta$ = 0.11, as shown in Figure 3.6. This geometry is duplicated at -z with 24 additional wedges, for a total EM coverage of $|\eta| < 1.1$. The WHA calorimeter augments the coverage of hadronic showers to a range of $|\eta| < 1.3$.

The Central Electromagnetic Shower Detector (CES) is embedded a third of the

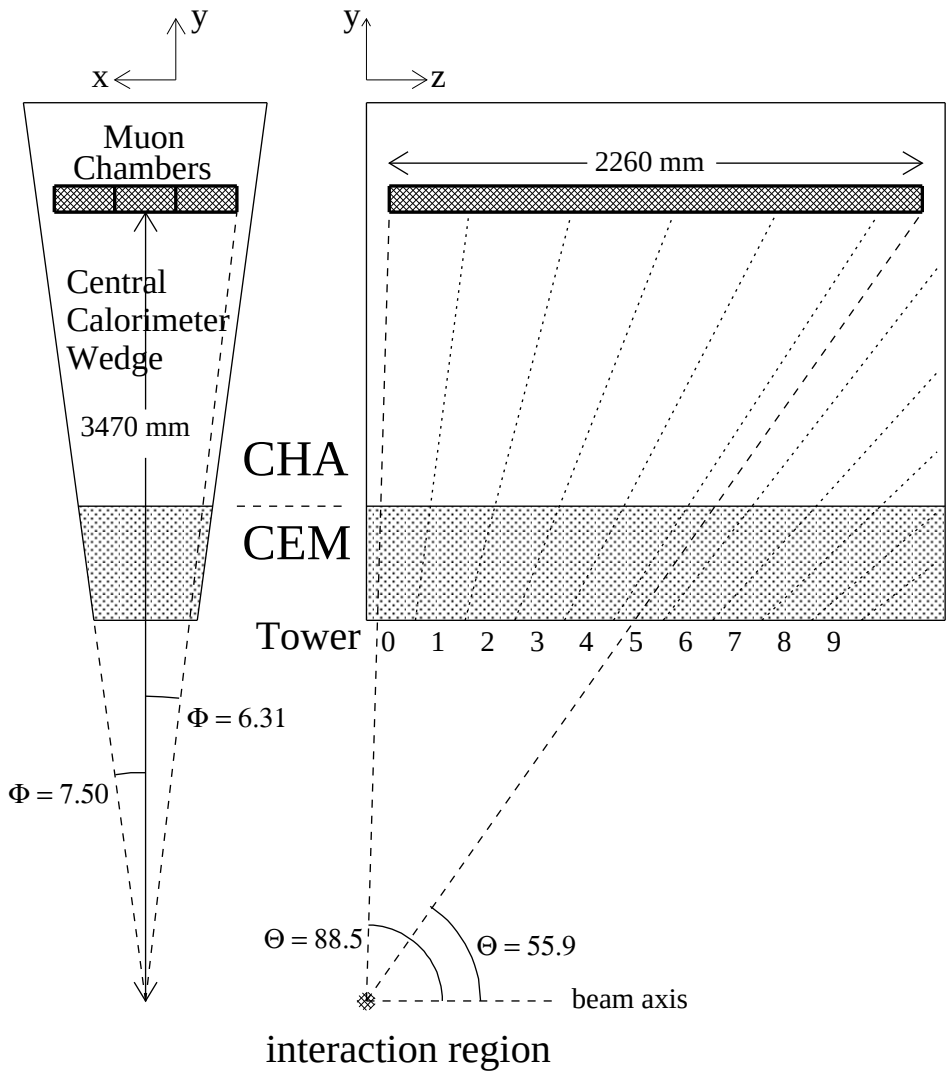

Figure 3.6: Two views of a wedge of the central calorimeter showing the central electromagnetic (CEM), central hadronic (CHA), and the central muon chamber (CMU) detectors.

way into the CEM at 5.9 X_0, which is the point of maximum shower development for 50 GeV electrons. The CES is a a proportional strip and wire chamber which measures the transverse profile of the shower in the ϕ direction using anode wires running along the z-axis, and in the z-direction using radial cathode strips. The CES can identify the position of a 50 GeV electron with 2 mm resolution.

A set of proportional tubes called the Central Preshower Detector (CPR) is located between the solenoid and the CEM. Electrons typically interact with the solenoid coil and deposit energy in the CPR, whereas hadrons are much less likely to interact, leaving little or no energy.

The Plug Electromagnetic Calorimeter (PEM) is 34 disk-shaped, alternating layers of lead (PEM) and proportional tube counters. The Plug Hadronic Calorimeters (PHA) contain 20 alternating layers of iron and proportional tube counters. The Forward Calorimeters, FEM and FHA, extend the η range to 4.2. At such high η, there is high particle activity and little spatial discrimination between nearby jets or electrons. The plug region is used to find jets, but the forward region is only used for the $\not{E}_{\mathrm{T}}$ calculation.

The CEM, PEM, FEM, and FHA were calibrated using test-beam electrons to understand the characteristic particle showers and measure the energy resolution. The CHA and PHA were calibrated with test-beam pions. The central calorimeter is regularly calibrated with ^{137}Cs sources to check for change in response over time.

The energy resolution, coverage, and segmentation of the different calorimeters is specified in Table 3.4.

3.5 Muon Detectors

Muons have exactly the same interactions as electrons. However, since their mass is 200 times more than that of electrons, their deflection in the absorption material of calorime-

System	Range	Segmentation	Energy Resolution	Total Thickness	Thickness Per Layer
	($\|\eta\|$)	($\|\Delta\eta\| \times \|\Delta\phi\|$)	(GeV)		(cm)
CEM	< 1.1	0.11 $\times$ 15°	$13.7\%\sqrt{E_T} \oplus 2\%$	18 X_0	0.32
CHA	< 0.9	0.11 $\times$ 15°	$50\%\sqrt{E_T} \oplus 3\%$	4.5 λ_0	2.5
WHA	0.7 - 1.3	0.1 $\times$ 15°	$75\%\sqrt{E_T} \oplus 4\%$	4.5λ_0	5.0
PEM	1.1 - 2.4	0.09 $\times$ 5°	$22\%\sqrt{E_T} \oplus 2\%$	18 - 21 X_0	0.27
PHA	1.3 - 2.4	0.09 $\times$ 5°	$106\%\sqrt{E_T} \oplus 6\%$	5.7 λ_0	5.0
FEM	2.2 - 4.2	0.1 $\times$ 5°	$26\%\sqrt{E_T} \oplus 2\%$	25 X_0	0.45
FHA	2.4 - 4.2	0.1 $\times$ 5°	$137\%\sqrt{E_T} \oplus 3\%$	7.7 λ_0	5.0

Table 3.4: Coverage and energy resolution of the calorimeter detectors. $\oplus$ denotes the direct sum.

ters produces little radiation, and therefore they lose energy very slowly when passing through matter. Muons are identified using arrays of proportional drift tubes located outside of the calorimeter. To ensure that hadrons whose showers extend through the calorimeter do not reach the muon detectors, 60 cm of absorbing steel was added beyond the central calorimeter before Run IB. Muons are identified by a track in the CTC, a failure to shower in the calorimeter, and an ionization signal in the muon detectors.

The central muon detection system is comprised of the Central Muon Chambers (CMU), the Central Muon Upgrade (CMP), and the Central Muon Extension (CMX). The CMU and CMP extend to $|\eta| < 0.6$, and the CMX provides coverage to $|\eta| < 1.0$.

A CMU chamber contains three modules filled with an argon/ethane/ethanol gas mixture. Each module holds four layers of four single-wire, rectangular drift cells. The sense wires are offset in ϕ by $\pm$ 2 mm in alternating layers to remove ambiguity as to which side of the wire the particle traversed. Each CMU chamber covers 12.6° in ϕ. Between Run IA and Run IB, four layers of staggered drift chambers called the CMP were added outside the solenoid return yoke to provide more muon coverage and hadron rejection. The CMU encompasses 85% of the solid angle in the region $|\eta| < 0.6$, the

CMP encompasses 63%; the intersection of CMU and CMP is 53 % of the solid angle.

The CMX is two hollow, truncated cones at either end of the detector in z. Each cone is composed of two free-standing arches housing eight staggered layers of rectangular drift tubes. Sandwiching the CMX are the two layers of the Central Muon Extension Scintillators (CSX), which serve as timing counters for identifying muons. The CMX system covers 71% of the solid angle in the $0.6 < |\eta| < 1.0$ region. The Forward Muon Detector (FMU) covers the region $2.0 < |\eta| < 3.6$ using a toroidal muon spectrometer, but is not used in this analysis.

3.6 Event Trigger System

3.6.1 Event Rates

The rate of bunch crossings at CDF during Run I was 280 kHz, or every 3.5 μs. Inelastic scattering event rates are used to determine the instantaneous luminosity, which determines the number of events expected for predicted physics processes. Inelastic processes, selected in a data sample at CDF referred to as "minimum bias", generate particles uniformly in η, and therefore mainly at small angles relative to the beam axis.

The Beam Beam Counters (BBC) are scintillating detectors used to count minimum bias interactions. The BBC covers an angular region between 0.32° and 4.47°. In this small region, where $3.2 < |\eta| < 5.9$, as many particles are expected in inelastic collisions as in the entire central and plug sections of the detector. The BBC counters look for at least one track on each side of the detector to identify inelastic interactions. Using the BBC and the VTX, an average of one interaction per beam crossing was measured in Run IA, and three interactions per crossing in Run IB.

3.6.2 Trigger System

The event rate due to inelastic scattering is nearly 280 kHz. With each event generating 130 kilobytes of digitized data, this is beyond data handling capabilities. CDF manages incoming data by using a trigger system which searches for specific physics processes while rejecting undesirable events.

This three level trigger system reduces the event rate to approximately 5 interesting events per second, while minimizing "dead-time", the amount of time that the detector does not register new interactions. At each step, events are selected which satisfy increasingly more sophisticated algorithms. The Level 1 and Level 2 triggers select events by implementing gate logic with signals received from the detector readout channels. The Level 3 trigger uses software reconstruction to choose events.

The Level 1 trigger has no dead-time since its decision time is less than the bunch-crossing time. Its decision is based on whether significant energy is deposited in the calorimeters, or whether muons are identified in the muon chambers. Trigger towers in the calorimeter are defined with $|\Delta\eta| \times |\Delta\phi|$ = 0.2 $\times$ 15°. Electrons and jets are found by searching trigger towers for deposited energy above a threshold. The muon trigger requires a pair of hits in two parallel muon drift tubes, sometimes called a "stub". Events with potential neutrinos are selected by searching for a large $\not{E}_{\mathrm{T}}$ in the calorimeter. Level 1 reduces the event rate from 280 kHz to 1 kHz.

The Level 2 trigger combines tracking and calorimetry information to make a decision in 20 μs, resulting in a few percent of dead-time. The central fast tracker (CFT) is a digital processor that uses hits in the CTC to reconstruct the P_T of high momentum tracks with a resolution of $\Delta P_T/{P_T}^2$ =3.5%. Jet candidates are identified by combining the energy from Level 1 trigger towers with that of neighboring towers. Electron candidates are found using the E_T and ϕ of trigger towers in conjunction with two dimensional CTC track trajectories. Muon candidates are detected by matching CTC

tracks with track segments in the CMU, CMP, and CMX. The Level 2 trigger reduces the event rate from 1 kHz to about 20 to 35 Hz.

The Level 3 trigger is a software reconstruction program running on a farm of four Silicon Graphics processors. The software executes a two dimensional CTC tracking algorithm that accounts for 50% of the $\frac{4}{7}$ of a second processing time per event. These CTC Tracks are matched to energy clusters or muon segments, further reducing the event rate from about 30 Hz to 3-5 Hz for Run IA and almost 8 Hz in Run IB. The surviving events are written to tape for a more comprehensive reconstruction of the event.

Chapter 4

$t\bar{t}$ Event Selection

4.1 The $t\bar{t}$ Signature

4.1.1 Monte Carlo

We determine the signature of $t\bar{t}$ events in the CDF detector using a Monte Carlo generator. To generate $t\bar{t}$, the Monte Carlo must model its production and decay. The Monte Carlo uses parton distribution functions (Figure 2.5) and calculated cross-sections for parton-level production processes (Section 2.3) to determine the momenta distributions of the produced t and $\bar{t}$. Next, the t and $\bar{t}$ are decayed according to the branching ratios from Table 3.1 with angular distributions and momenta consistent with those predicted by the electroweak theory.

The two most important kinematic properties are the η of the particles which determines the subdetectors that can provide measurements, and the P_T which determines the ability of the trigger and analysis to distinguish particles produced in top decay from background. Using the Herwig Monte Carlo program [23], we generate a sample of 8,000 $t\bar{t}$ lepton+jets events. The η distribution of the particles from these decays is shown in Figure 4.1, with the coverage of the subdetectors. The particles mainly traverse

the central detectors, allowing us to limit our search window and reduce backgrounds which produce particles at high η. Shown in Figure 4.2 are the P_T distributions of these particles. Note that few of the particles have $P_T < 10$ GeV.

These distributions do not take into account the effects of quark fragmentation and radiation, nor the ability of the detector to measure the energy and direction of the resulting particles. The selection criteria will finally depend on the efficiency for finding objects in each detector region, and also on $t\bar{t}$ background rejection. However, Monte Carlo information provides us with the subdetectors and energy ranges necessary to find the $t\bar{t}$ decay products.

This analysis focuses on the dilepton and lepton+jets $t\bar{t}$ channels where we require a sample of events with at least one high P_T electron or muon. From this sample, events with final state neutrinos are selected by requiring $\not\!\!E_{\mathrm{T}}$. After requiring jets, possibly with b tags, the $t\bar{t}$ selection is complete. The selection criteria for these objects remove or "cut" background events.

4.2 Identifying Electrons in Data

4.2.1 Trigger Electrons

The Level 1 trigger requires electrons to have a CEM cluster with $E_T > 8$ GeV. The Level 2 trigger imposes electrons to have a CFT track of $P_T > 12$ GeV pointing to a CEM cluster of $E_T > 16$ GeV. Since this cut removes 10% of real electrons, there is an additional trigger which requires a CEM cluster of at least 16 GeV and $\not\!\!E_{\mathrm{T}}$ greater than 20 GeV which helps regain events with both an electrons and neutrino (e.g., $W \rightarrow e + \nu_e$ events).

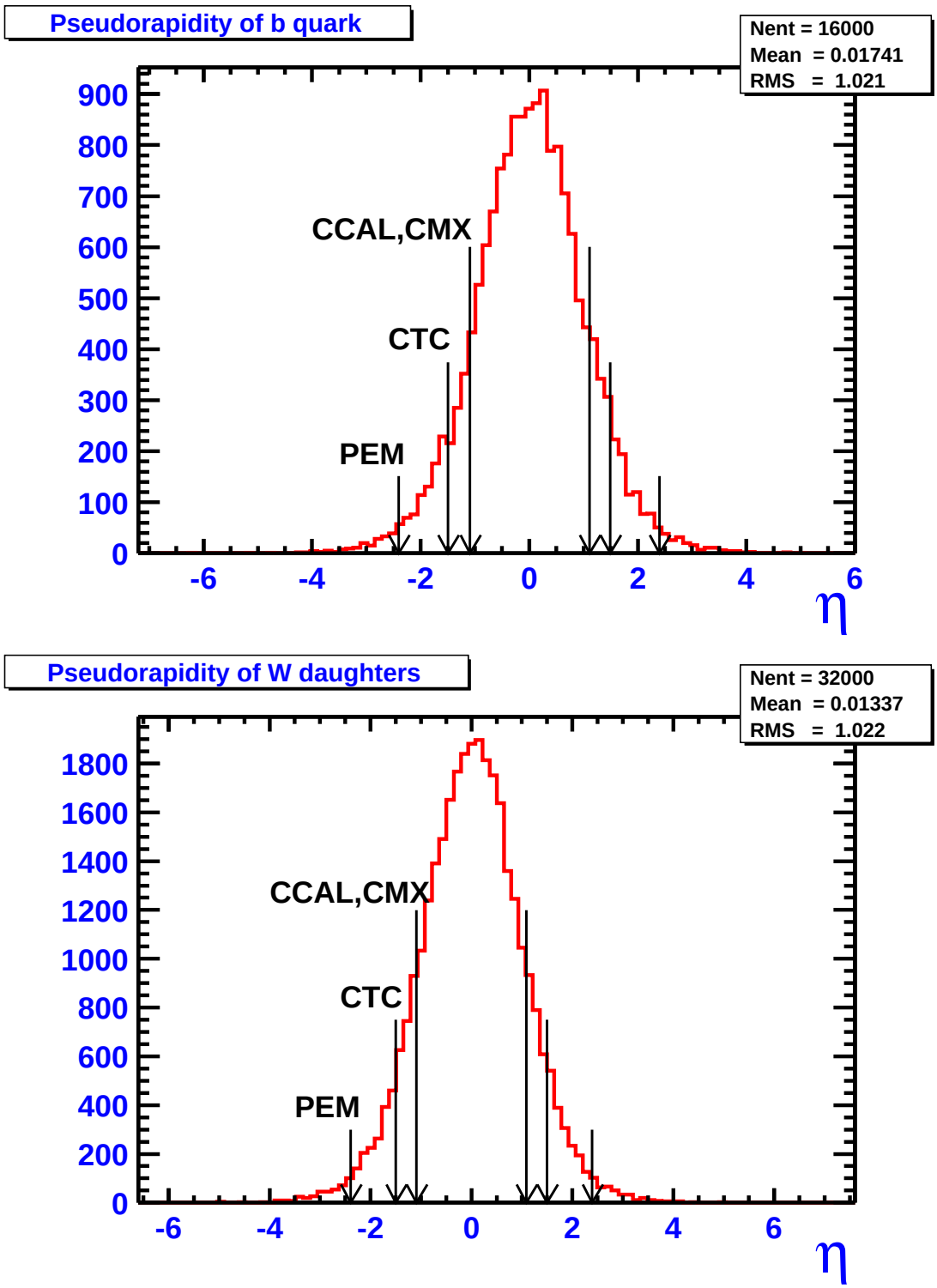

Figure 4.1: The η of generator-level particles from Monte Carlo $t\bar{t}$ lepton+jets events. The upper plot is of the W^+, and W^- daughters: lepton, neutrino, quark, and antiquark. The lower plot is of the b quarks. The arrows denote the extent of coverage for several subdetectors.

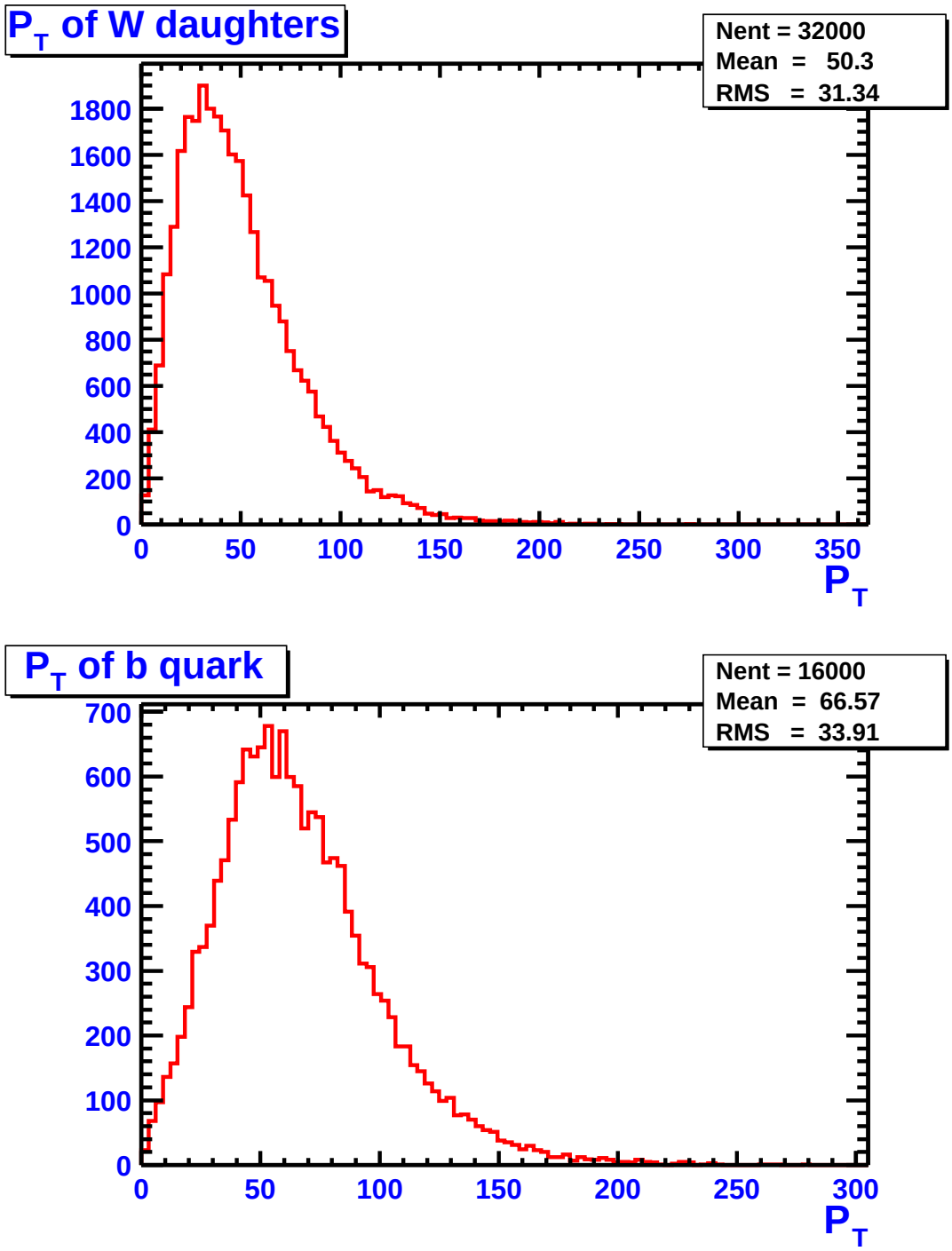

Figure 4.2: The P_T of generator-level particles from Monte Carlo $t\bar{t}$ lepton+jets events. The upper plot is of the W^+, and W^- daughters: lepton, neutrino, quark, and antiquark. The lower plot is of the b quarks.

4.2.2 Primary Electron Selection

Electron quality cuts remove electrons produced from secondary decays of hadrons in jets, photon pair production of e^+e^-, and fake electrons. Electrons are required to have $E_T > 20$ GeV in the CEM to stay above the trigger threshold. The energy (E) of the CEM cluster is compared to the CTC track momentum (P) of a matched track, and candidates with $|E/P| > 1.8$ are eliminated since their energy deposits do not likely come from the track. As mentioned in Section 3.4, electrons shower mainly in the electromagnetic calorimeter, whereas hadrons leave a large fraction of energy in the hadronic calorimeter. To remove hadrons, E_{had}/E_{em} is required to be less than 0.05. The lateral shower profile variable, L_{shr}, is required to be consistent with real testbeam electrons. L_{shr} is defined by

$$L_{shr} = 0.14 \sum_i \frac{E_i^{obs} - E_i^{pred}}{\sqrt{(0.14\sqrt{E})^2 + \sigma_{pred}^2}}$$

where for each tower i adjacent to the central tower, E_i^{obs} and $0.14\sqrt{E}$ are the observed energy and uncertainty, E_i^{pred} and σ_{pred}^2 are the predicted energy and uncertainty. The extrapolation of the CTC track and the shower position in the CES must match within a few centimeters, both in $r - \phi$ distance, Δx, and in z distance, Δz. The profile of the electron shower shape in the CES is also compared to testbeam electrons (χ^2_{strip}). The z position of the electron vertex ($Z_{electron}$) must match to the z position of the primary vertex as measured in the VTX (Z_{vertex}). This Z_{vertex} value also must be within about two standard deviations (60 cm) from the nominal interaction point. The last condition requires that the energy cluster not be at the boundaries of gaps in the detector, where there is potential for mismeasurement. These cuts are summarized in Table 4.1 and define the tight central electron criteria (TCE).

The efficiency for keeping real electrons with these cuts is evaluated using a data

$E_T > 20$ GeV
$E/P < 1.8$
$E_{had}/E_{em} < 0.05$
$L_{shr} < 0.2$
CES requirements :
$\Delta x < 1.5$ cm
$\Delta z < 3.0$ cm
$\chi^2_{strip} < 10$
$\lvert Z_{electron} - Z_{vertex} \rvert < 5$ cm
$\lvert Z_{vertex} \rvert < 60$ cm
Fiducial cuts at boundaries

Table 4.1: Tight central electron (TCE) selection criteria.

sample of $Z \rightarrow e^+ + e^-$ events. In this sample, one electron satisfies tight electron requirements. A second electron passing "loose" requirements must combine with the tight electron to form an invariant mass of between 75 and 105 GeV. This creates a relatively pure sample of Z events, and therefore a pure sample of secondary electrons. Since these electrons have not been subjected to the trigger requirements or the electron selection criteria, they can be used to study the efficiency of the tight cuts. The distributions for the second electron are shown in Figure 4.3. The overall efficiency for retaining electrons after imposing the cuts in Table 4.1 is 81.9 $\pm$ 0.7 %.

After these cuts, 30 to 40% of the selected electrons originate from "photon conversions", collisions between photons and detector material resulting in electron-positron pairs. These conversions are not interesting to most analyses, and can be eliminated. Since conversion electrons are tangential to each other but with opposite sign curvature, tracks which are closer than 0.2 cm in $x - y$ space when they are parallel or closer in θ than $|\Delta cot\ \theta| = 0.06$ are removed. Any track that does not extrapolate fully through the VTX is considered a conversion. Finally, the invariant mass of the electron track with any other CTC track must be greater than 0.5 GeV since photons are massless. The

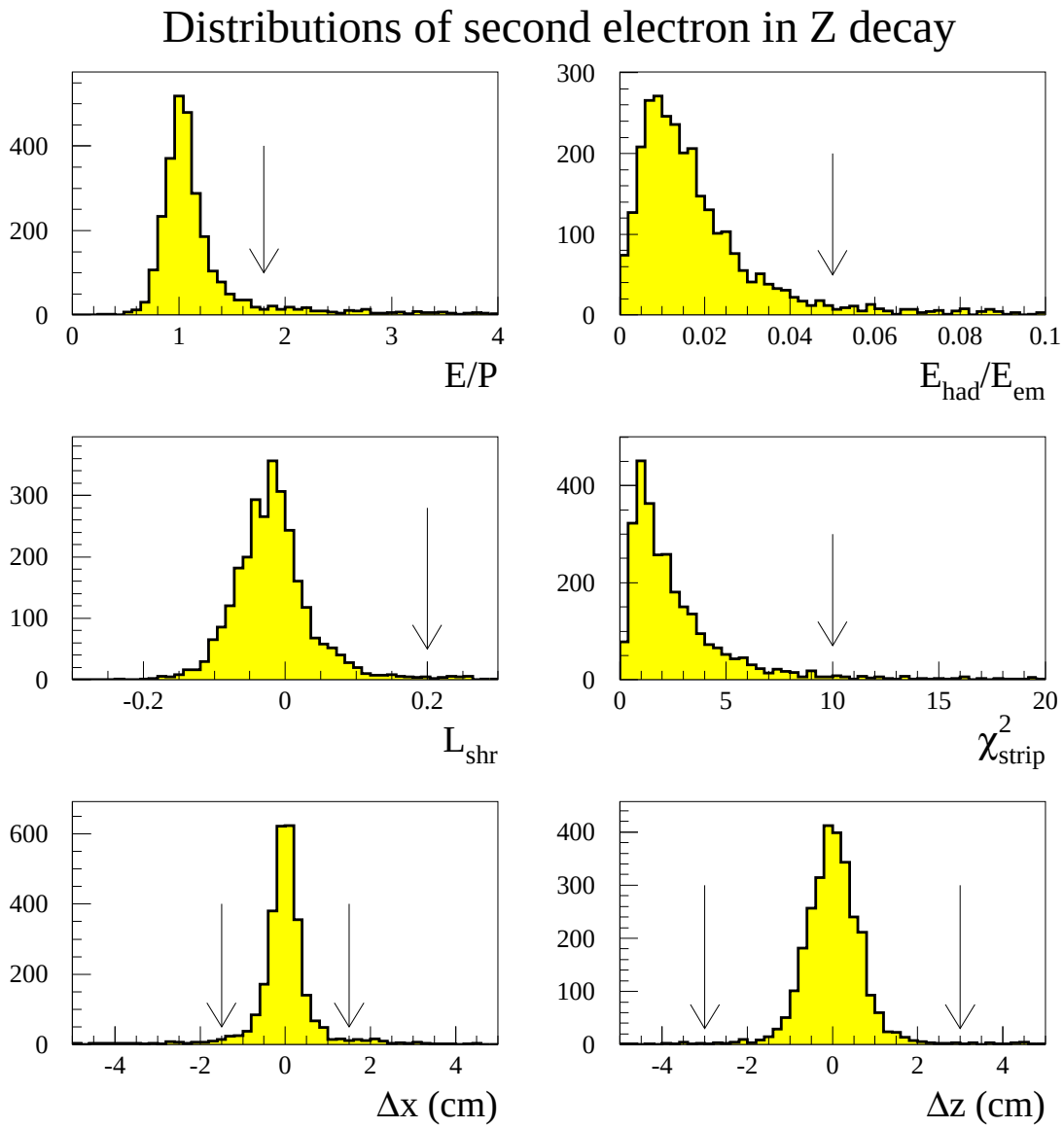

Figure 4.3: Distributions of the loose second electron from $Z \rightarrow e^+ + e^-$ sample. The value of the tight electron cuts are denoted with an arrow, indicating the fraction of real electrons kept for the given cut.

Variable	TCE requirement	LCE requirement
E/P	< 1.8	< 4.0
E_{had}/E_{em}	< 0.05	$< 0.055 + \frac{0.045 \times E}{100}$
χ^2_{strip}	< 10	no requirement

Table 4.2: Differences between tight central electrons (TCE) and loose central electrons (LCE) for top dilepton selection.

overall efficiency for keeping electrons after conversion removal is 88 $\pm$ 4%.

4.2.3 Secondary Electron Selection

In $t\bar{t}$ dilepton events, an additional lepton is required. To increase electron detection efficiency, the second electron is subjected to loose central electron (LCE) criteria which balance the gain in $t\bar{t}$ efficiency against the loss in purity of the sample.

To select an LCE, the E/P cut, E_{had}/E_{em}, and χ^2_{strip} requirements are loosened. Table 4.2 outlines the difference between the TCE and LCE classes. The efficiency of the LCE requirements is determined from $Z \rightarrow e^+ + e^-$ events to be 89.7 $\pm$ 0.005 %.

4.3 Identifying Muons in Data

4.3.1 Trigger Muons

The Level 2 muon trigger accepts events with a CTC track of $P_T > 12$ GeV pointing to a Level 1 muon chamber stub. Since there are more muon events passing the Level 2 trigger than can be handled by the data acquisition system, a prescale procedure is applied which keeps only a specified fraction of events. To prevent top events from being lost, an additional trigger keeps high P_T muon events if there is a calorimeter cluster with $E_T > 15$ GeV matching the CTC track, a possible signature for the semi-

leptonic decay of a b hadron. Muons which pass through only the CMP (called "CMP-only" as distinguished from "CMU-only" and the intersection of both "CMUP") are also kept for events with two additional jets and at least 35 GeV of $\not\!\!E_{\mathrm{T}}'$.

4.3.2 Primary Muon Selection

Quality cuts are applied to the muon candidates to remove hadrons and cosmic ray muons. The cuts ensure that the CTC track, calorimeter energy deposit, and muon stub are aligned. The first cut, motivated by Figure 4.2, is the requirement that a CTC track must have $P_T > 20$ GeV, after refitting the track to pass through the calculated beam position (a "beam-constrained" track). This track should also extrapolate to its muon stubs, to within a few centimeters in the $r - \phi$ plane, $|\Delta X|$. The $|\Delta X|_{CMX}$ and $|\Delta X|_{CMP}$ requirements are looser than $|\Delta X|_{CMU}$ due to the multiple scattering from additional detector material. The muon should only deposit a small amount of energy in the calorimeters, and therefore the electromagnetic and hadronic calorimeter energy deposits (E_{em} and E_{had}) must be small but non-negligible. The impact parameter of a track, d_0, is defined as the distance between the extrapolated track and the beam line. Cosmic ray backgrounds are reduced by requiring d_0 to be less than a few millimeters, and the z position at the beam line Z_{muon} to be close to the z position of the vertex Z_{vertex}. The Z_{vertex} should also be located near the nominal interaction point. The cuts are outlined in detail in Table 4.3.

The efficiency of the tight muon cuts is determined using the second muon in a sample of $Z \rightarrow \mu^+ + \mu^-$ events. This sample is extremely pure; only one of 2500 dimuon events selected prior to a 75 GeV $< M_{ee} <$ 105 GeV cut has same-sign muons. The second muon is required to have $P_T > 20$ GeV to remove any P_T dependence from the efficiency calculation. The efficiency for the combined set of cuts is 91.4 $\pm$ 1.0% for CMX muons, 90 $\pm$ 2% for CMU-only muons, 88 $\pm$ 2% for CMP-only muons, and 93.6

For $P_T > 20$ GeV/c
Track-Stub Matching :
$\lvert\Delta X\rvert_{CMU} < 2.0$ cm
OR
$\lvert\Delta X\rvert_{CMP} < 5.0$ cm
OR
$\lvert\Delta X\rvert_{CMX} < 5.0$ cm
E_{em} in Tower < 2.0 GeV
E_{had} in Tower < 6.0 GeV
$E_{had} + E_{em}$ in Tower > 0.1 GeV
Impact Parameter < 3 mm
$\lvert Z_{muon} - Z_{vertex}\rvert < 5$ cm
$\lvert Z_{vertex}\rvert < 60$ cm

Table 4.3: Tight muon selection criteria.

$\pm$ 0.7% for CMUP muons. Figure 4.4 shows the distributions of selection variables for the second muon in the $Z \rightarrow \mu^+ + \mu^-$ sample. Tight muons in the $t\bar{t}$ dilepton sample are required to be CMUP, CMP-only, CMU-only, or CMX as defined above.

4.3.3 Secondary Muon Selection

For $t\bar{t}$ dilepton events, the efficiency is increased by requiring additional muons in the event to satisfy somewhat looser criteria.

Central minimum ionizing muons (CMI) are added to the loose muon selection. These muon candidates do not pass through the fiducial volume of the muon chambers, and therefore satisfy all of the tight muon criteria except the requirement of matching a muon stub in the CMX. To reduce fakes, CMI muons are required to be well separated from surrounding tracks and energy deposits. To quantify this, the variables I_{cal} and I_{track} are defined as

$$I_{cal} = \frac{E_T^{cone} - E_T}{P_T^{muon}} \tag{4.1}$$

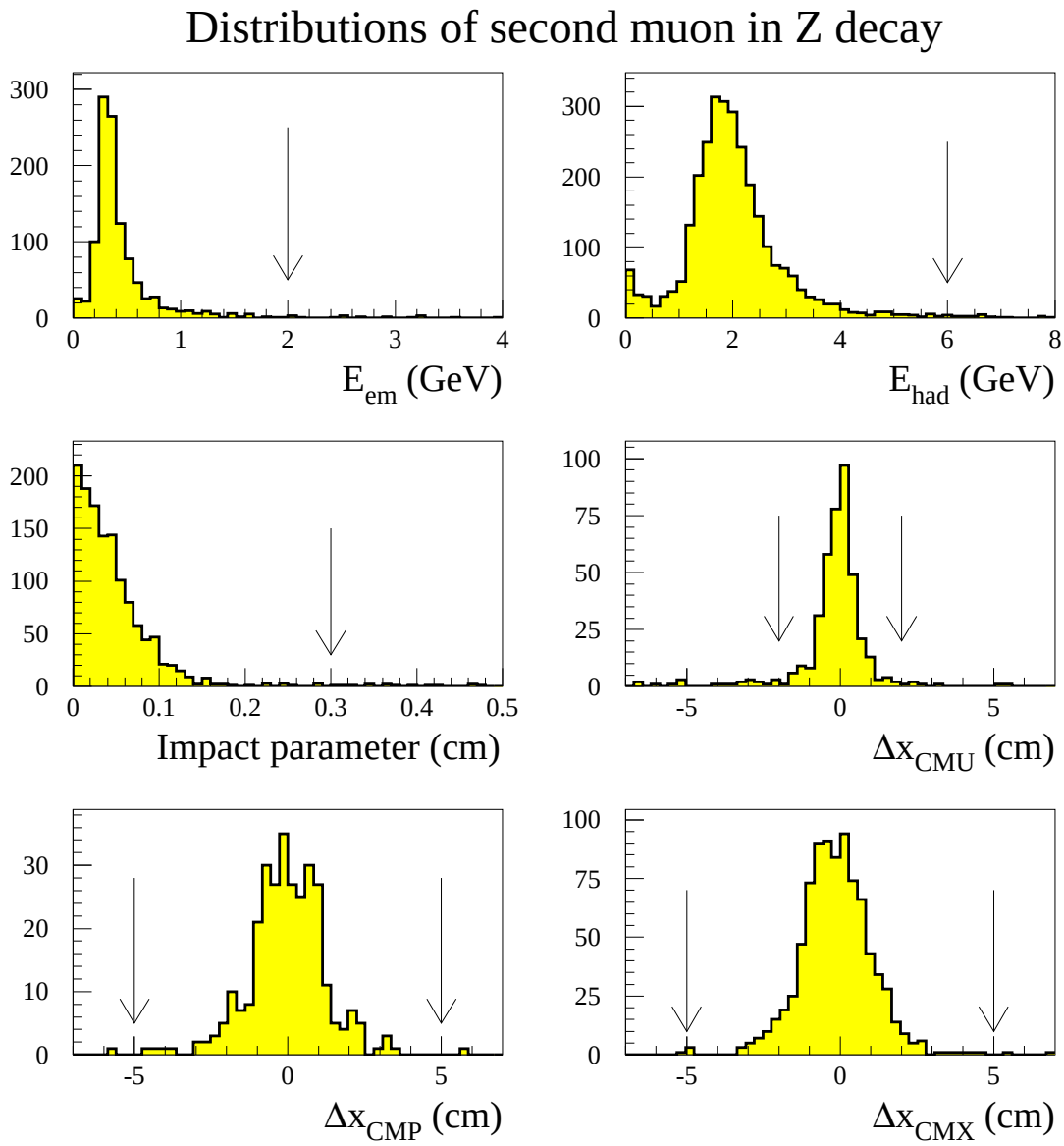

Figure 4.4: Distributions of the loose second muon from the $Z \rightarrow \mu^+ + \mu^-$ sample. The value of tight muon cuts are denoted with an arrow, indicating the fraction of real muons kept for the given cut.

Type	TCM requirement	LCM requirement
	Track-Stub Matching :	
CMU	$\lvert\Delta X\rvert_{CMU} < 2.0$ cm	No $\lvert\Delta X\rvert$ requirement
CMP	$\lvert\Delta X\rvert_{CMP} < 5.0$ cm	No $\lvert\Delta X\rvert$ requirement
CMX	$\lvert\Delta X\rvert_{CMX} < 5.0$ cm	Not defined
CMI	Not defined	$I_{cal}, I_{track} < 0.1$

Table 4.4: Differences between tight central muons (TCM) and loose central muons (LCM) for top dilepton selection.

and

$$I_{track} = \frac{P_T^{cone} - P_T^{muon}}{P_T^{muon}} \tag{4.2}$$

where E_T^{cone} is the sum of all transverse energy in a cone of radius $\Delta R = \sqrt{\Delta\phi^2 + \Delta\eta^2}$ = 0.4 centered around the muon, P_T^{cone} is the transverse sum of all track momenta in the cone, E_T is the transverse energy in the muon tower, and P_T^{muon} is the P_T of the muon refit using the $r - \phi$ of the beam position. Both I_{cal} and I_{track} are required to be less than 0.1 for CMI muons. The efficiency for CMI muons from $Z \rightarrow \mu^+ + \mu^-$ data where the first muon is a TCM is found to be 91.6 $\pm$ 0.012. The differences between LCM's and TCM's for the dilepton sample are outlined in Table 4.4. The distributions for these criteria are shown in Figure 4.5.

4.4 Identifying W Bosons

Further criteria are demanded for lepton+jets events to be consistent with W decay. The electron or muon must be well separated from jets to remove events with leptons originating from semi-leptonic b decays. Events with an additional lepton consistent with Z decay are removed. Also, $\not\!\!E_{\mathrm{T}}$ is required to indicate the presence of a neutrino.

The separation of leptons from other jet activity is done using the isolation variable,

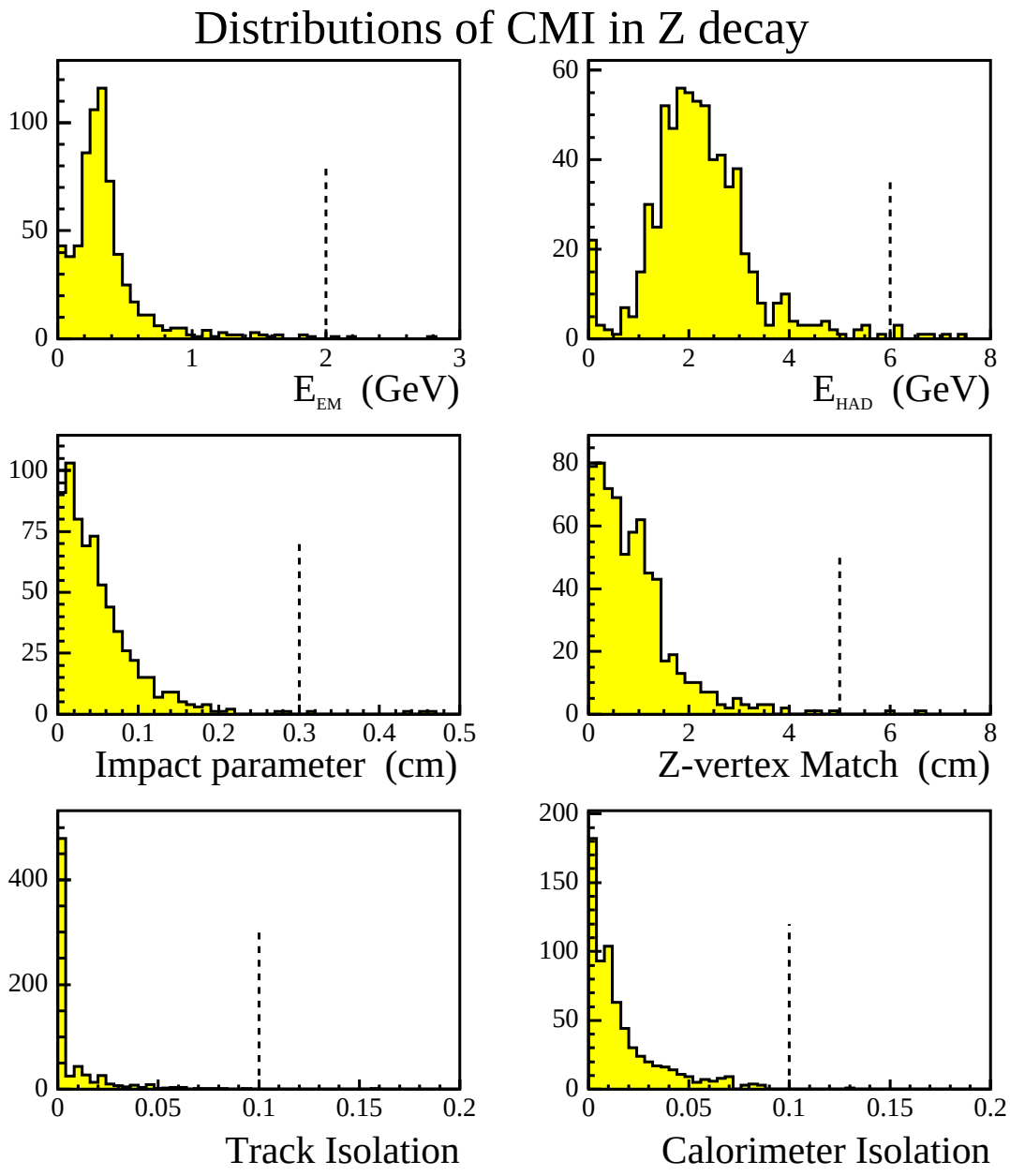

Figure 4.5: Distributions of the loose second muon from $Z \rightarrow \mu^+ + \mu^-$ sample. In this case, the second muon is a CMI. The value of CMI cuts are denoted with a dotted line, indicating the fraction of real muons kept for the given cut.

Electron Cuts:
$E_T > 10$ GeV
$E_{had}/E_{em} < 0.12$
$E/P < 2.0$ (if in CEM)
$I_{cal} < 0.2$
Muon Cuts:
$P_T > 10$ GeV/c
If Associated With a Stub
E_{em} energy in tower < 5.0 GeV
E_{had} energy in tower < 10.0 GeV
$\|\Delta X\|_{CMU,CMPorCMX} < 5.0$ cm
$I_{cal} < 0.1$
If No Stub
E_{em} in tower < 2.0 GeV
E_{had} in tower < 6.0 GeV
$\|\eta\| < 1.1$
$I_{cal} < 0.2$

Table 4.5: Loose lepton quality cuts applied to secondary lepton candidates to remove Z boson decays in top lepton+jets events.

I. For muons I_{cal} is defined by Equation 4.1. For electrons :

$$I_{cal} = \frac{E_T^{cone} - E_T}{E_T^{ele}} \tag{4.3}$$

where E_T^{cone} is the transverse energy in a cone of radius ΔR = 0.4 centered around the electron, and E_T is its transverse energy. Primary electrons and muons must have $I_{cal} <$ 0.1 to be considered for the W sample.

To create a pure sample of W events, $Z \rightarrow e^+ + e^-$ and $Z \rightarrow \mu^+ + \mu-$ events must be removed. After identifying an isolated lepton, a loose set of criteria are applied to any additional lepton candidates in the event to classify them as a Z boson and reject them from the W sample. These cuts are defined in Table 4.5.

Neutrinos do not interact with the detector, so their presence is inferred through $\not\!\!E_{\mathrm{T}}$.

$\not{E}_{\rm T}$ is calculated by first taking the vector sum of all the towers within $\eta < 3.6$. Next, the P_T of tight and loose muons with $P_T > 10$ GeV is added in, since their energy was not deposited in the detector. Requiring $\not{E}_{\rm T} > 20$ GeV is 83.0 $\pm$ 0.1 % efficient for $t\bar{t}$ events.

After the isolation requirement, Z removal, and $\not{E}_{\rm T}$ cut, there are 38,602 muon events, and 57,675 electron events of quality data, coming from "good runs" where there are no known detector problems.

To establish the remaining events contain real Ws, a measurement of the W mass from these events should agree with the accepted value. A precise determination of the z-axis component of the missing energy cannot be made in $p\bar{p}$ events due to uncertainty in the z component of the initial partons in the interaction. Instead, a transverse mass M_T is computed:

$$M_T = \sqrt{(|P_T^{lep}| + \not{E}_{\rm T})^2 - (\vec{P_T^{lep}} + \vec{\not{E}}_{\rm T})^2} \tag{4.4}$$

where P_T is measured from the track momentum for muons, and from the calorimeter energy deposit for electrons. This is plotted in Figure 4.6 for both the electron and muon events. As is expected, there is a peak at about 80 GeV indicating the W mass. The asymmetric shape is a smeared Jacobian peak due to the missing z momentum component. A complete study of the W sample provides a measurement of the W boson mass; M_W = 80.433 $\pm$ 0.079 GeV. This agrees with the world average as of March 2003 of M_W = 80.425 $\pm$ 0.038 GeV. Note that currently, the CDF Run I W mass is the third most precise out of six measurements used to compute this world top mass.

4.5 Identifying Jets

The energy deposited in both the EM and HA calorimeter towers within a cone size of ΔR of 0.4 is used to determine jet energy E. Combined with the location of the primary

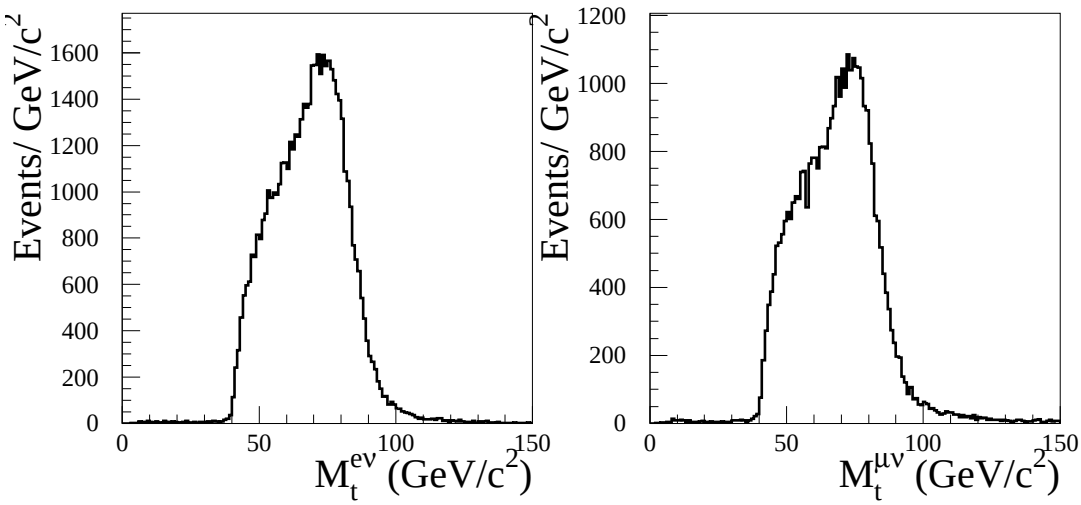

Figure 4.6: Transverse mass of the lepton, P_T, and $\not{E}_T$ vectors for the W sample. The figure on the left is for electrons, and on the right is for muons.

vertex and the location of the center of the jet cone, the θ of the jet can be determined. Jets in the plug calorimeter region are included to improve acceptance of $t\bar{t}$ events. A "tight jet" is defined as a jet with $E_T > 10$ GeV and $|\eta| < 2.0$. "Loose jets" must have $E_T > 8$ GeV, and $|\eta| < 2.0$. For dilepton events, two tight jets are required. For lepton+jets events, only three tight jets and a fourth loose jet are required. This improves acceptance without adding significant background. Because of jet fragmentation and gluon radiation, there is a strong likelihood of extra jets in both types of $t\bar{t}$ events, and these events are not rejected.

4.5.1 B Jet Selection Criteria

In dilepton events, the two highest E_T jets in the event are assumed to be b jets. Any additional jets from gluon radiation are typically lower energy.

For lepton+jets events, there are at least four jets, only two of which are real b jets. The main background to $t\bar{t}$ lepton+jets is W+jets, in which the jets have only about a

1% probability of being a b jet. Therefore, identifying at least one b jet in the event greatly reduces this background.

The method used for identifying b jets in this analysis is called the secondary-vertex (SECVTX) algorithm. The lifetime of the b is about 1.5 ps. Since the b typically has a P_T of 65 GeV (see Figure 4.2) and a typical b hadron mass of 5 GeV, the relativistic boost $\gamma = E/m$ causes the b to travel about 5 mm in the radial direction before decaying into charged tracks creating a secondary vertex. Since the SVX detector can resolve displaced vertices to roughly 130 μm, it can be used to identify b jets. Figure 4.7 is an illustration of such a vertex showing the impact parameter, d_0, or distance in $r - \phi$ of closest approach of a track to the primary vertex. The signed displacement L_{xy} is useful for determining fake rates of the b tagging algorithm, since if L_{xy} were negative, it would indicate that the secondary vertex occured before the primary vertex, and therefore is not likely a real b jet.

The primary vertex is found using a weighted fit of the z-position of the vertex given by the VTX detector, and the SVX tracks not consistent with a secondary vertex. In events with multiple interactions, the primary vertex is defined as the one with the largest scalar sum of transverse momentum of its associated tracks. The beam is not completely parallel and coaxial with the CDF z-axis. The slope was found to be about 5 μm/cm in the transverse direction with an uncertainty of 1 μm/cm. The displacement between the beam axis and the detector axis varied by as much as 2 mm. The beam locations were measured on a run-by-run basis and found with accuracies of 0.4 μm/cm for the slope and 10 μm for the displacement. The overall uncertainty in the determination of the primary vertex for one event in the transverse direction ranges from 6 to 36 μm depending on the number of tracks and the event topology.

Secondary vertices are found by looping over tracks, calculating their impact parameter, and determining whether they are in the proximity to a jet. Displaced tracks are required to have $|d_0|/\sigma_{d_0} < 3$, where σ_{d_0} is the uncertainty on the d_0 measurement. The

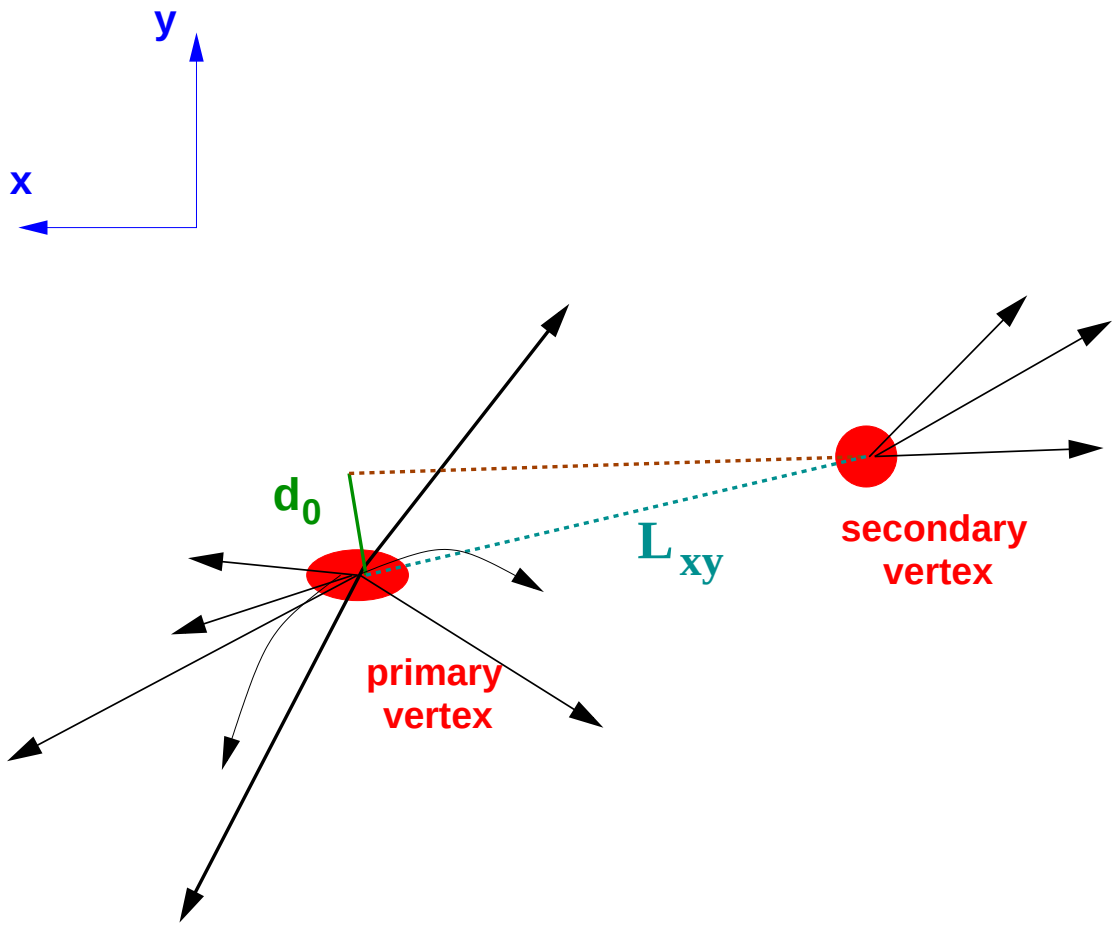

Figure 4.7: Diagram of a secondary vertex resulting from a b hadron decay. Each track originating from the secondary vertex has an impact parameter, d_0.

tracks must match a jet with $E_T > 15$ GeV and $|\eta| < 2.0$ to within 35 $^\circ$ in the transverse plane. If two such tracks exist for a given jet, the vertex is defined to be displaced.

67% of $t\bar{t}$ events have at least one b jet in the fiducial range of the SVX detector. The efficiency for tagging at least one b jet in $t\bar{t}$ events is measured to be 39 $\pm$ 3%.

Chapter 5

Search for V+A in Top Decay

5.1 Motivation

The ability of physics to characterize properties of nature and the universe is often related to the understanding of a symmetry. Conservation of energy, momentum, and angular momentum are all associated with symmetries and allow us to predict the behavior of particles in certain situations.

Asymmetries in the universe are particularly worthy of study. The weak force violates the symmetries of Parity (P), Charge (C), and Time (T). Our current understanding of the Standard Model is that nature seems to have arbitrarily chosen the weak force carrier to couple to left-handed matter. This is highly unsatisfying, yet may have paved the way for our universe, consisting of matter, to exist.

The top quark is also an oddity of nature. Its high measured mass means that unlike all other quarks, it decays before hadronizing passing its spin information to its decay products. Also, unlike other quarks, it can decay to a real W boson.

The heavy top mass leads to a Yukawa coupling to the Higgs field of

$$g(top) = \sqrt{2} \cdot 174.3\, GeV/246\, GeV = 1.00. \tag{5.1}$$

This means that the top quark has the only large coupling with the Higgs field, and is the factor which dominates many higher order calculations to predicted low energy phenomenon. “From an Electroweak Symmetry Breaking point of view, top is the only natural quark” [11].

Because of its close relationship with the Higgs field, it is often argued that the top quark may play a unique non-Standard Model role in electroweak symmetry breaking. This has led to a wide development of extensions to the Standard Model.

Top-condensate models argue that similar to a condensate of Cooper Pairs forming in a super conductor giving rise to a photon mass, top-antitop pairs may form a condensate, giving rise to the masses of the W^+, W^-, and Z. This condensate would then be the Higgs particle [12]. Another model introduces a charged scalar called a top-pion, which in contrast to the W boson, couples only to the right-handed top quark [13]. There are also extended standard models with a new $SU(2)_R$ gauge group and mirror fermions that cause anomalous right-handed weak couplings of the top and bottom quarks [14]. It is certainly an appealing solution to the asymmetry of $SU(2)_L\ X\ U(1)$ to assume that is merely part of a bigger group with right-handed couplings as well: $SU(2)_L\ X\ SU(2)_R\ X\ U(1)$. The beautiful mirror theory predicts a non-standard fourth generation with unbiased weak interactions may impact the W helicity in top quark decays since the predicted fourth generation particles will mix with the top quark. Also if this new fourth generation particle has a mass sufficiently similar to the top quark, it may contaminate the top event sample causing the properties of the top quark, including W helicity, to be mismeasured [15].

V+A admixtures with a mirror fermion X may grow with quark mass with terms

like $\sqrt{M_q/M_X}$, therefore providing the largest mixing with the top quark.

Indirect limits of right-handed $t \rightarrow b$ currents have been assigned using the process $b \rightarrow s + \gamma$, which proceeds via W emission to a top quark followed by W absorption to a strange quark, thereby sensitive to the tbW vertex. These limits are stringent, but scenarios can be envisaged where other contributions to $b \rightarrow s+\gamma$ lead to an invalidation of these bounds [16].

It is necessary to check the chirality of the tbW decay current directly to validate or invalidate the Standard Model expectations of top. It is therefore the topic of this thesis to verify that the electroweak coupling of the top quark is a standard V$-$A coupling predicted by electroweak theory in the context of searching for a V$+$A component to the coupling.

5.2 Introduction to Analysis

The electroweak coupling of the top quark can be studied via the decay of the top quark to a W boson and b quark.

The spin one W has three possible spin orientations: +1, 0, or -1. This leads to three W helicities (dot product of spin and momentum) : for W^+ it is right-handed when the spin is in line with the momentum, left-handed when it is anti-aligned, and longitudinal when it it perpendicular to the momentum. The handedness is opposite for the W^-.

$$H_{W^+,W^-} = \bar{J} \cdot \hat{P} = \begin{cases} -1 & left - handed, right - handed \\ 0 & longitudinal \\ +1 & right - handed, left - handed \end{cases}$$

The helicity of the W is reflected in the different angular distributions of the lepton coming from W decay. For the $W^+ \rightarrow l^+ + \nu$, the lepton will tend to decay in the direction of the W spin. For $W^- \rightarrow l^- + \bar{\nu}$, the lepton will tend to decay in the opposite direction. The measurement of W helicity in t $\rightarrow l + \nu + b$ is often done in terms of the cosine of $\psi_l^\star$ [17], the angle between the lepton in the W rest frame and the boost vector from the top to the W rest frame (Figure 5.1).

Longitudinal Ws produce a symmetric distribution about $cos\ \psi_l^\star$. Left-handed Ws have their spin anti-aligned with the momentum, causing the lepton to decay opposite the W momentum, with a peak at $cos\ \psi_l^\star$ = -1, in the b quark direction. Right-handed Ws give leptons an extra kick in the direction of the W momentum, causing them to point in the opposite direction of the b quark, $cos\ \psi_l^\star$ = +1 (Figure 5.2).

A measurement of the angle $\psi_l^\star$ requires a knowledge of the top and W rest frames, which are difficult to obtain because of the uncertainty in the neutrino direction. In dilepton events, two neutrinos means that these reference frames are even more difficult to obtain.

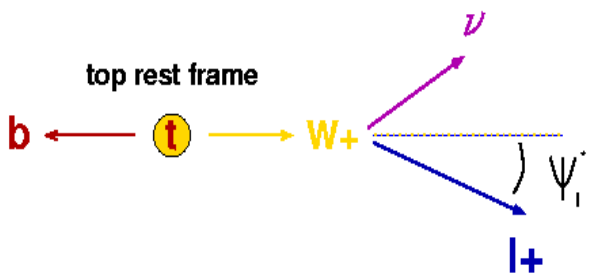

Figure 5.1: The angle $\psi_l^\star$

This analysis exploits the relationship between the angle $\psi_l^\star$ and the $l - b$ invariant mass combination,

$$M_{l+b}^2 = 1/2 \cdot (M_T^2 - M_W^2)(1 + cos\psi_l^\star). \tag{5.2}$$

$M_{l+b}^2 = (P_l + P_b)^2$ (Figure 5.3) is invariant under boost and since it is a direct measure of the $cos\ \psi_l^\star$ distribution, it can be used to determine the relative proportions of left-handed, right-handed, and longitudinal Ws in top data.

V$-$A theory predicts the probability of each W helicity distribution in top decay. Because of the large top mass relative to the W, 70% of Ws will be polarized in the longitudinal direction according to

$$f_0 = \frac{M_t^2/M_W^2}{(M_t^2/M_W^2 + 2)} \ , \tag{5.3}$$

for $M_t = 174.3$ GeV and $M_W = 80.4$ GeV. Due to maximal parity violation in the weak interaction, the remaining 30% of Ws must be either right-handed or left-handed. Since nature is biased so that the $W^+(W^-)$ couples to left-handed (right-handed) matter, this 30% is left-handed (right-handed) (Figure 5.4).

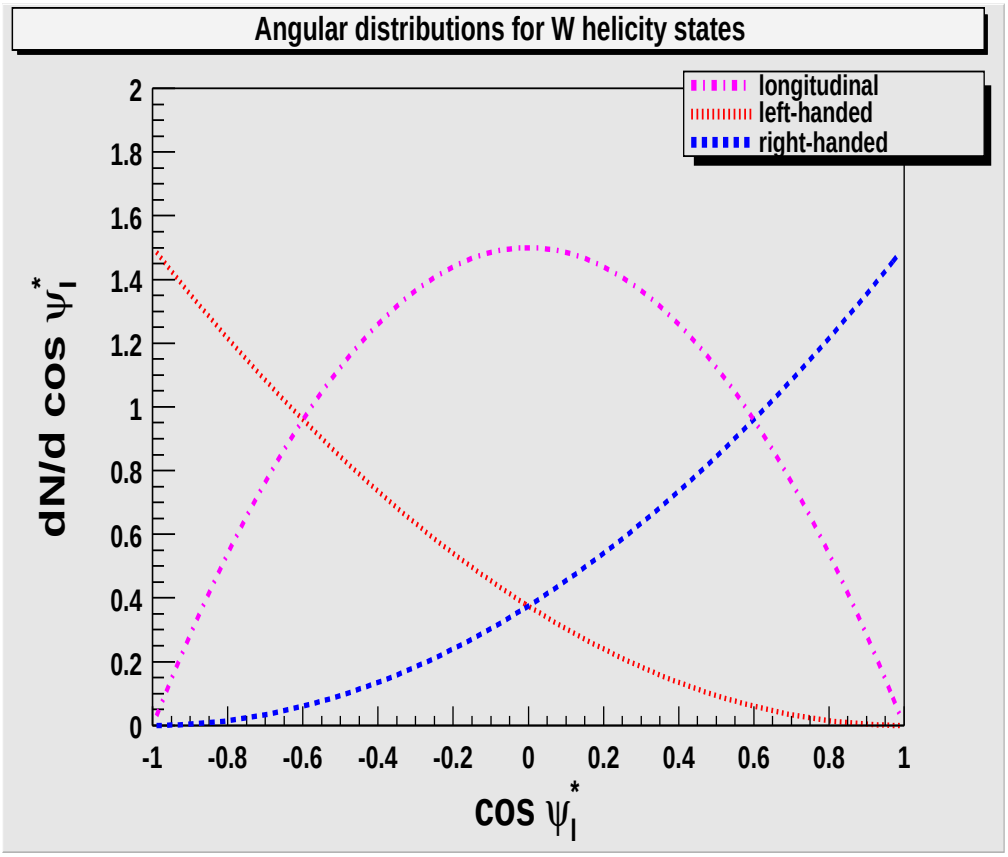

Figure 5.2: The longitudinal helicity distribution is symmetric, while the left-handed and right-handed distributions peak asymmetrically. For instance, $cos\ \psi_l^\star$ = -1 corresponds to the lepton from the W decaying in the same direction as the b quark.

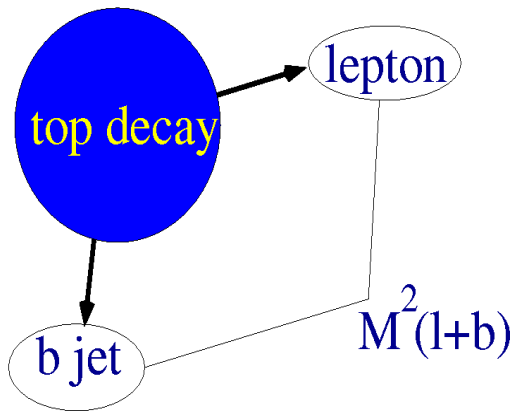

Figure 5.3: $M^2_{l+b} = 1/2 \cdot (M^2_T - M^2_W)(1 + cos\psi^\star_l)$

If there were right-handed decays, it would not decrease the branching ratio to longitudinal Ws, it would instead decrease the branching ratio to left-handed Ws. If the asymmetry of the weak theory were instead right-handed, a V+A interaction, the W helicity would stay 70% longitudinal, and the remaining portion would be right-handed. For a very nice calculation of the helicity amplitudes see reference [18].

This analysis compares the data from leptonic decays of top quarks produced in $t\bar{t}$ pairs to MC distributions representing V−A and V+A theories in order to extract a measurement for the fraction of tbW couplings which exhibit a V+A interaction, f_{V+A}. In terms of the branching ratios Γ to right-handed and left-handed Ws,

$$f_{V+A} = \frac{\Gamma(t \to W^+_{RH} b)}{\Gamma(t \to W^+_{RH} b) + \Gamma(t \to W^+_{LH} b)}. \tag{5.4}$$

Theoretical distributions of M^2_{l+b} are shown in Figure 5.5. The reason for the different M^2_{l+b} distributions can be understood in terms of $\psi^\star_l$. A 30% right-handed, as opposed

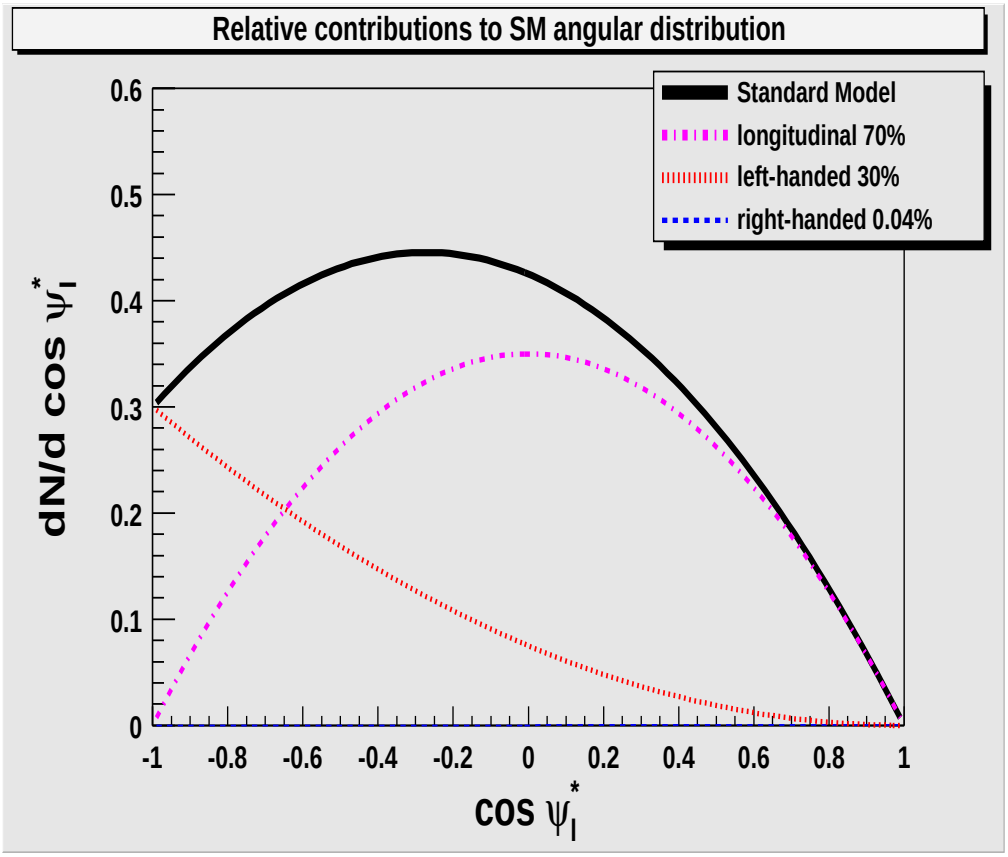

Figure 5.4: W helicity distributions from top decay. The longitudinal component is the largest at 70%. The left-handed coupling causes an asymmetry in the Standard Model distribution. The right-handed component is non-zero when the b mass is considered.

to left-handed, coupling causes there to be more events where the lepton boost in the W rest frame is in the same direction as the W momentum in the lab. This results in a higher invariant $l - b$ invariant mass (Figure 5.6).

With detector acceptance effects, these distributions will change slightly. For instance, since the lepton must be outside of the cone of the jet, the distribution will be cut off at small angles between the lepton and the b jet, leading to reduced contributions at low M^2_{l+b}. This affects the V$-$A distribution since it peaks at low M^2_{l+b}, but does not reduce the sensitivity for finding V$+$A since the V$+$A M^2_{l+b} distribution peaks higher.

The interference between identical final states of V$+$A and V$-$A is not considered in this analysis, as is the case when the b mass is neglected in matrix element calculations. With no b mass, the chirality and helicity would be the same, and there would be no interference between V$+$A and V$-$A. The largest effect this could have is if the non-standard theory being searched for contained equal couplings of V$+$A and V$-$A for the tbW vertex. In this case, leading interference terms of the order of the mass of the b quark divided by its energy would enter in to the matrix element calculation, of order approximately 6%. This 6% is an estimate of how much of the matrix element is being failed to be calculated by ignoring the interference effects as is the case when using calculating the V$+$A and V$-$A amplitudes separately. The 6% is an overestimate since it considers the maximal case of equal V$-$A and V$+$A components, and also since the actual effect of this interference on the relative polarizations of the W bosons is expected to be smaller. For pure V$-$A theory, the interference term is almost zero, since there is only a tiny right-handed component from the b mass with contribution on the order of M_b^2/M_t^2. Since a $<$6% effect, pales in comparison with the statistical and systematic effects in this analysis, this effect can safely be ignored, but may need to be revisited for Run II if statistical and systematic uncertainty reaches this level of precision. [19]

f_{V+A} will be a value from zero to one, and is not the same as f_{RH}, the fraction of right-handed Ws. These two are related simply by f_{V+A} = f_{RH}/(1-f_0). f_{RH} has

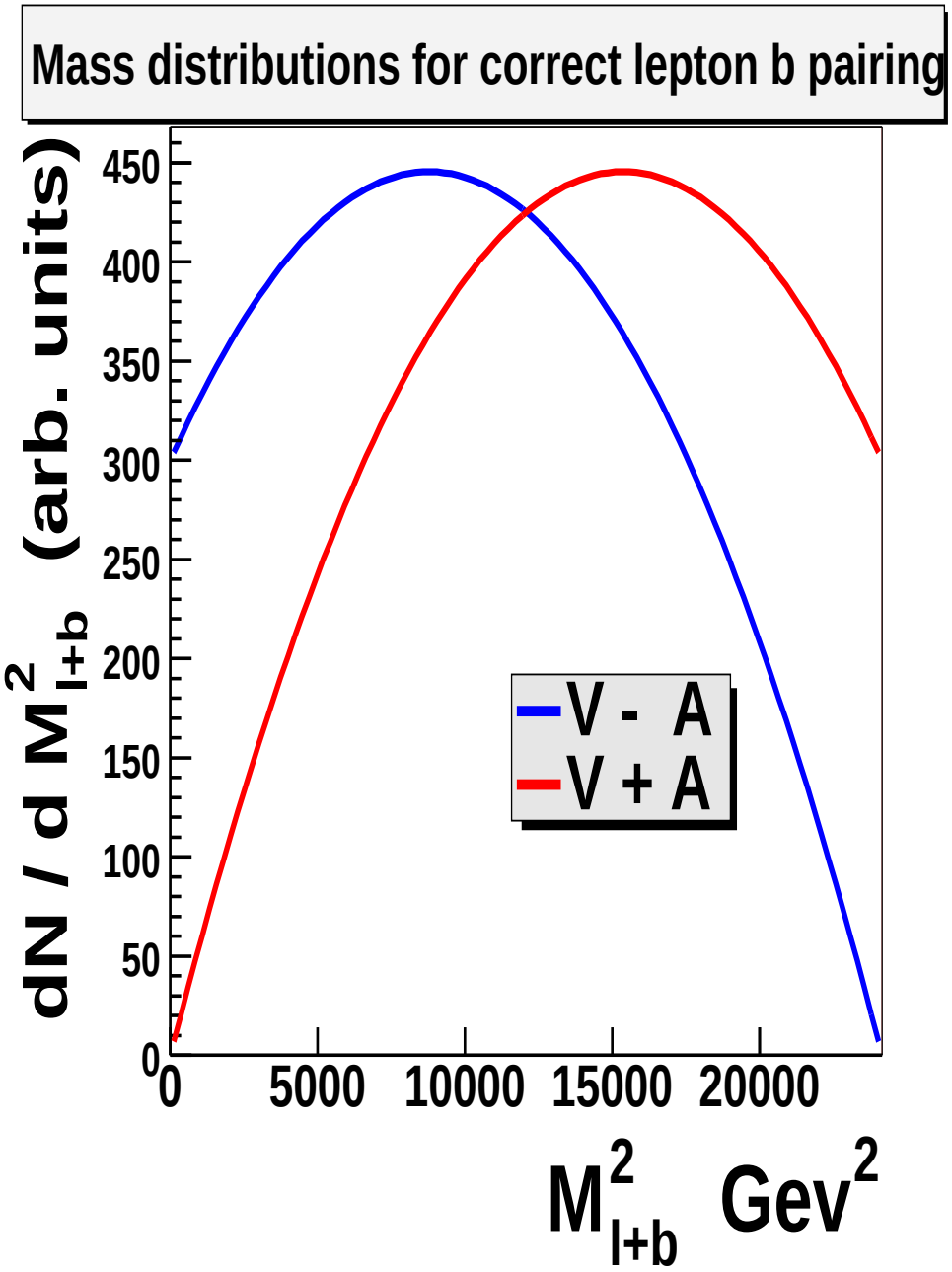

Figure 5.5: The theoretical distributions for the correct pairings of M^2_{l+b} comparing V$-$A and V$+$A. Since the V$+$A sample peaks higher, this can be used to discriminate between the two theories.

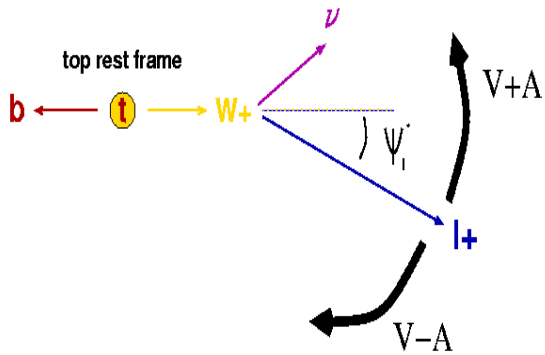

Figure 5.6: The left-handed coupling of V−A, compared to the right-handed coupling of V+A, leads to a lower M^2_{l+b} distribution for V−A than V+A.

been previously measured at CDF to be f_{RH} = 0.11 ± 0.15 (stat.) ± 0.06 (sys.) [20]. In terms of V+A, this corresponds to f_{V+A} = 0.37 ± 0.50 (stat.) ± 0.2 (sys.). This previous analysis uses the difference in lepton P_T spectrum between lower P_T left-handed Ws verses higher P_T right-handed Ws. The lepton P_T technique has the benefit of being dependent only on the well-measured lepton P_T, allowing looser $t\bar{t}$ lepton+jets and dilepton sample requirements, without regard to matching the lepton to the t or $\bar{t}$, and without the uncertainties associated with reconstructing the jets in the event. As will be shown later, the latter is not significant, since systematic uncertainties associated with jet energy scale are anti-correlated with top mass uncertainties, and so jet energy scale uncertainties largely cancel out in the M^2_{l+b} analysis. The main advantage of the M^2_{l+b} analysis is that it is reference frame invariant. Since it takes into account the top P_T, it is more sensitive to $cos\ \psi^\star_l$ than the lepton P_T method.

Indirect limits of right-handed top decay from analyzing $b \rightarrow s + \gamma$ data from CLEO are strong, limiting the contribution to less than a few percent [16]. However, there

is an assumption that the top-quark loop, rather than new physics, gives the dominant contribution to the process. A direct method for measuring the $cos\ \psi_l^\star$ distribution and therefore determining the nature of the tbW vertex is still the only definitive answer.

5.3 Analysis Method

5.3.1 Pairing Lepton with B Jet

This analysis seeks to measure M^2_{l+b} in the $t\bar{t}$ dilepton and lepton+jets channels.

The calculation of M^2_{l+b} is complicated by lack of knowledge about which is the correct jet to match with the lepton in the event. Even when two jets in the event can be identified as b jets, there is still an ambiguity about which one belongs with the lepton.

Only correct pairings of leptons and bs are sensitive to $cos\ \psi^\star_l$. Incorrect pairings produce a different distribution, with a large tail beyond the physical limit from top decay of $M^2_{l+b} < (M^2_t - M^2_W)$ (Figure 5.7).

Kinematic fitting to determine the correct $l-b$ pairing from top decay was considered but since the M^2_{l+b} distributions are different between V+A and V−A, fit methods would be biased toward solutions which favored more V−A like distributions. Comparison of sensitivity was done with pseudo-experiments between only correct pairings and all pairings, and the result of including correct pairings was less than a 10% decrease in statistical uncertainty. Some of this gain is probably due to the fact that when events were deemed correctly paired to generator level partons, this eliminated much of the effect of initial and final state gluon radiation in these events. Therefore, we decided against using kinematic constraints to discriminate correct pairings in this analysis.

Tagging the charge of b jets by doing a P_T weighted sum of the track charges within the jet was also considered, and is unbiased to event kinematics. Since the ability of this technique to discriminate between b and $\bar{b}$ is small, and not well measured due to limited statistics in the data, it was not utilized, but may be useful with more statistics in Run II.

Every lepton and b pairing in the event is considered in this analysis. The possible pairings for each lepton are correlated since when one possible lepton pairing is unphysical, the other is more likely to be physical. This adds more information than

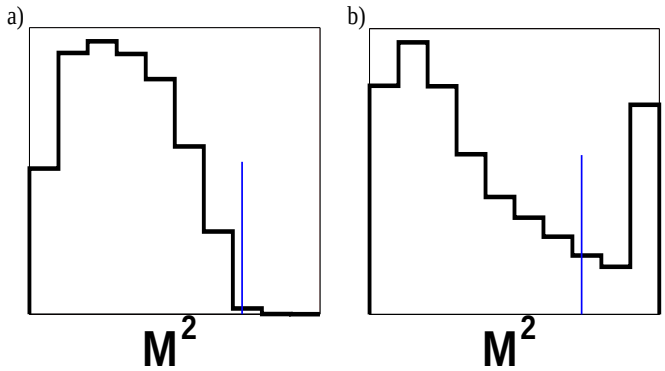

Figure 5.7: The M^2_{l+b} distribution for correct (a) and incorrect (b) pairings of the lepton and the b with V$-$A Herwig generator-level information. The line denotes the cut off from the kinematics of top decay. The last bin is for overflow events.

taking the pairings all independently, so wherever possible the possible lepton pairings are considered simultaneously in the fit.

Depending on the type of $t\bar{t}$ event, several techniques are used to maximize the sensitivity to correct pairings.

For dilepton $t\bar{t}$ events, the two leptons are paired with the highest two corrected E_T jets. For each lepton, there are two possible pairings, one of which is likely to be correct (barring possibilities of extra jets in the event from gluon radiation), and one which is a mismatch to the b jet of the opposite charged top in the event. A 2-D distribution can be made plotting M^2_{l+b1} vs. M^2_{l+b2} for each lepton: 2 entries per event. Instead of removing incorrect pairings, this approach uses the correlation between correct and incorrect pairings to gain more information. For instance, if both the incorrect pairing and correct pairing were both high in M^2_{l+b}, the event would have a greater weight for being right-handed than if only one pairing was high in M^2_{l+b}.

For lepton+jets events, a sub-sample is chosen in which events have jets that pass

the SECVTX b tag criteria outlined in Section 4.5.1. Since the jets are b tagged rather than chosen by assumption of highest E_T jets as in the dilepton case, one would expect these samples to be more correctly paired than in the dilepton case. The lepton+jets sub-sample is divided into events with a single b tagged jet and events with two b tagged jets. In the double- tagged sample, the situation is similar to that in the dilepton sample: for each lepton, there is a correct and an incorrect pairing. The M^2_{l+b} values in this sub-sample can be arranged in a 2-D distribution of M^2_{l+b1} vs. M^2_{l+b2} demonstrating the possible pairings for the lepton.

For the single-tagged sample, there is only one lepton and one b jet, and therefore only one possible pairing, thus this pairing will be correct only half the time. With only one b jet and one lepton, a 1-D distribution of M^2_{l+b} must be used.

5.4 Event Selection Summary

The $t\bar{t}$ samples chosen for this analysis are chosen with the CDF Run I dilepton criteria [21], and the CDF Run I top mass sample for SVX single-tagged and SVX double-tagged events [22]. The $t\bar{t}$ samples used in this analysis were chosen to contain low background fractions in order to minimize dependence on the ability of Monte Carlo generators to produce the correct jet distributions, as well as to improve signal to background. These samples minimize combinatorics because the b jets are explicitly identified by tagging or by the absence of light quark jets from W decay. Also, since they have been well studied in Run I, the backgrounds are well understood, as well as the necessary systematics. A more complete description of the electron, muon, and jet identification variables is described in Chapter 4.

- **Dilepton selection criteria**
  - Event selection
    - A high P_T electron
    - An oppositely charged high P_T muon
    - 2 high E_T jets
    - Large $\not{E}_{\mathrm{T}}$
    - Conversion electrons and cosmic ray contamination removed
  - Electron and muon selection
    - $P_T > 20$ GeV
    - $|\eta| < 1.0$
    - Track and calorimeter isolation < 0.1
  - Jet selection
    - measured $E_T > 10$ GeV

    - $|\eta| < 2.0$

  - $\not\!\!E_{\mathrm{T}}$ selection
    - $\not\!\!E_{\mathrm{T}} > 25$ GeV
    - if $\Delta\phi(\not\!\!E_{\mathrm{T}}, l\ or\ j) < 20\ ^{\circ}$, then $\not\!\!E_{\mathrm{T}} > 50$ GeV

- **SVX single-tagged selection criteria**
  - Event selection
    - A good quality high $E_T(P_T)$ electron or muon
    - Four high E_T jets
    - Large $\not\!\!E_{\mathrm{T}}$
    - Conversion electrons and cosmic ray contamination removed
  - Electron and muon selection
    - $E_T > 20\ GeV$
    - $|\eta| < 1.0$
    - Track and calorimeter isolation < 0.1
  - Jet selection
    - Three jets $E_T > 15$ GeV, $|\eta| < 2.0$
    - Fourth jet $E_T > 8$ GeV, $|\eta| < 2.4$
    - One jet is SECVTX tagged
  - $\not\!\!E_{\mathrm{T}}$ selection
    - $\not\!\!E_{\mathrm{T}} > 20$ GeV
  - Other contamination removed
    - Candidate dilepton events (defined above) removed
    - Z removal of $75 < M_{e^+e^-or\ \ \mu^+\mu^-} < 105$

    - Mass reconstruction goodness-of-fit, $\chi^2 < 10.0$

- **SVX double-tagged selection criteria**
  - Event selection
    - A good quality high $E_T(P_T)$ electron or muon
    - Four high E_T jets
    - Large $\not\!\!E_{\mathrm{T}}$
    - Conversion electrons and cosmic ray contamination removed
  - Electron and muon selection
    - $E_T > 20$ GeV
    - $|\eta| < 1.0$
    - Track and calorimeter isolation < 0.1
  - Jet selection
    - Three jets $E_T > 15$ GeV, $|\eta| < 2.0$
    - Fourth jet $E_T > 8$ GeV, $|\eta| < 2.4$
    - Two jets are SECVTX tagged
  - $\not\!\!E_{\mathrm{T}}$ selection
    - $\not\!\!E_{\mathrm{T}} > 20$ GeV
  - Other contamination removed
    - Candidate dilepton events (defined above) removed
    - Z removal of $75 < M_{e^+e^- or \mu^+\mu^-} < 105$
    - Mass reconstruction goodness-of-fit, $\chi^2 < 10.0$

5.5 Signal Modeling

Since no prior data set had uncovered the top quark prior to Run I at the Tevatron, there were no experimental measurements of the top quark on which to create templates for the M_{l+b} distributions in $t\bar{t}$ events. Additionally, the V+A model is non-standard, and isn't predicted to exist in nature. Therefore, it is necessary to simulate these samples in the CDF detector to determine their shapes. Monte Carlo is used for this purpose, as was used to sketch the $t\bar{t}$ signature in the detector in Section 4.1.1.

To generate the $t\bar{t}$ Monte Carlo, Herwig 6.2.0 [23] was used in association with a CDF tool which allows one to specify the relative left-handed, right-handed, and longitudinal W helicity fractions used in top decay. For the V$-$A sample, the W^+ (W^-) bosons were set to have a relative contribution of 70% longitudinal and 30% left-handed (right-handed) angular distributions. For the V+A sample, the W^+ (W^-) bosons were set to have a relative contribution of 70% longitudinal and 30% right-handed (left-handed) angular distributions.

Events were then input into the CDF Fast Detector Simulation (QFL) software which simulates the signals the detector would read out. The events are then fully reconstructed to translate these signals into energy, momenta, and position. The information from each detector is linked together to form candidate physics objects, which then must pass the trigger simulation. Finally, many corrected quantities are calculated, such as the $\not\!\!E_{\mathrm{T}}$ re-fit with corrected jet energies and muon momenta. Primary and secondary vertices are reconstructed, and tracks are fit with all available constraints. This simulation software has been finely tuned to output the same detector response as that of real data. Reconstructed Monte Carlo is only as good as its ability to represent data, and so the process of obtaining agreement between reconstructed Monte Carlo and reconstructed data is painstaking.

Herwig $t\bar{t}$ Monte Carlo events were fully reconstructed and subjected to the same

selection criteria as the data. After event selection, the $t\bar{t}$ dilepton and lepton+jets Monte Carlo samples had on the order of 50,000 events each, representing a significant wealth of statistics.

Non-overlapping sets of these distributions were used in pseudo-experiments and compared to independent templates to determine the statistical error of the Monte Carlo distributions in terms of the measurement of f_{V+A} to be 0.01.

5.6 Background Modeling

The event selection criteria was chosen to have a small background contribution. The background samples also tend to have the peak of the M^2_{l+b} distribution well separated from the signal region of V+A and V−A $t\bar{t}$.

5.6.1 Dilepton Backgrounds

The background types and expected contribution was determined from published CDF Run I top dilepton analyses to determine the top mass [21]. The main background for the dilepton $e - \mu$ sample is $Z \rightarrow \tau^+ + \tau-$, where one τ decays to an electron and one τ decays to a muon. Other backgrounds are W^+W^- where one W decays to an electron, and one decays to a muon, and the fake lepton background which comes from W+jets events where one of the jets fakes an electron. The $Z \rightarrow \tau^+ + \tau^-$ sample was generated using Pythia Monte Carlo [24] and the W^+W^- samples were created from ISAJET Monte Carlo [25]. The fake lepton background was created by using VECBOS [26] Monte Carlo to create a W+jets sample, where the highest E_T jet was purposely misidentified as the lepton. The M^2_{l+b} background distribution normalized to the contribution in the data for the event selection outlined is shown in Figure 5.8, and can be compared to the $t\bar{t}$ V−A (Figure 5.9) and V+A (Figure 5.10) distributions. For

each distribution, there are two entries per event. One entry is the M^2_{l1+b1} vs. M^2_{l1+b2} where the b jets are chosen by E_T ordering. The other entry is for the second lepton M^2_{l2+b1} vs. M^2_{l2+b2}. The b jets are E_T-ordered in all distributions, and therefore the distributions have a higher peak on the x-axis where the b jet has higher E_T.

5.6.2 SVX Single-Tagged Backgrounds

There are many backgrounds considered for the SVX single-tagged sample, including W and Z processes with extra jets, di-boson production, and single top. For a complete list, see [22]. It was decided in top mass analyses based on KS tests, that with reasonable certainty, W+jets background could represent the shape of the other backgrounds and therefore is used here as the only background for the SVX single-tagged sample. The W+jets background is, however, normalized to the total contribution of all the backgrounds in this channel. The M^2_{l+b} background distribution normalized to the contribution in the data for the event selection outlined is shown in Figure 5.11 compared to the $t\bar{t}$ V$-$A (Figure 5.12) and V$+$A (Figure 5.13) distributions. These distributions are one dimensional since the only entry is M^2_{l1+b1}.

5.6.3 SVX Double-Tagged Backgrounds

Requiring two SVX tagged jets greatly reduces the background in this sample. The background is very small, and the only non-negligible part comes from W+jets production [22]. The M^2_{l+b} background distribution normalized to the contribution in the data for the event selection outlined is shown in Figure 5.14 compared to the $t\bar{t}$ V$-$A (Figure 5.15) and V$+$A (Figure 5.16) distributions. For each distribution, there is one entry per event: M^2_{l1+b1} vs. M^2_{l1+b2} where the b tagged jets are chosen by E_T ordering.

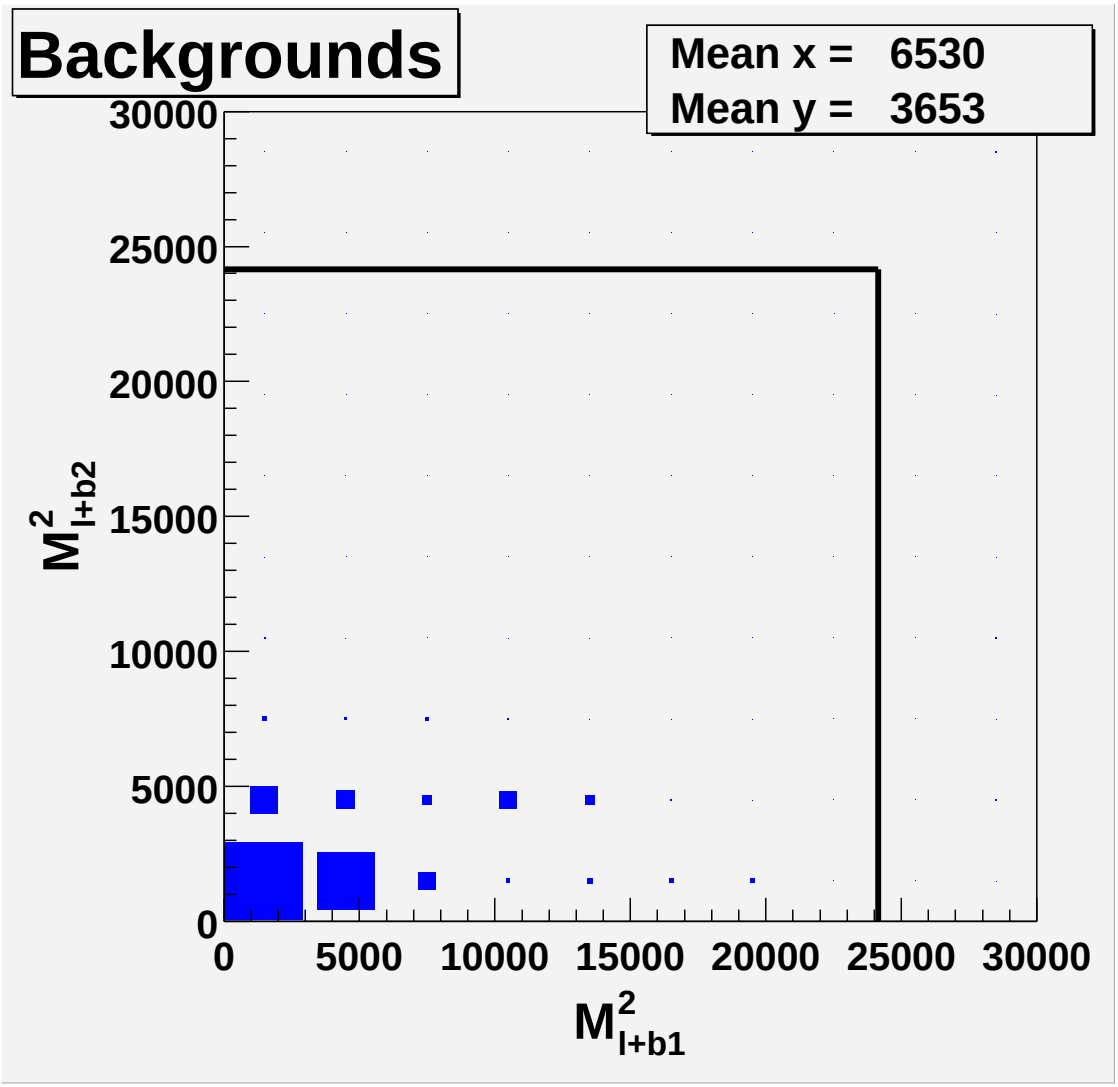

Figure 5.8: Background template for dilepton sample (Two entries per event).

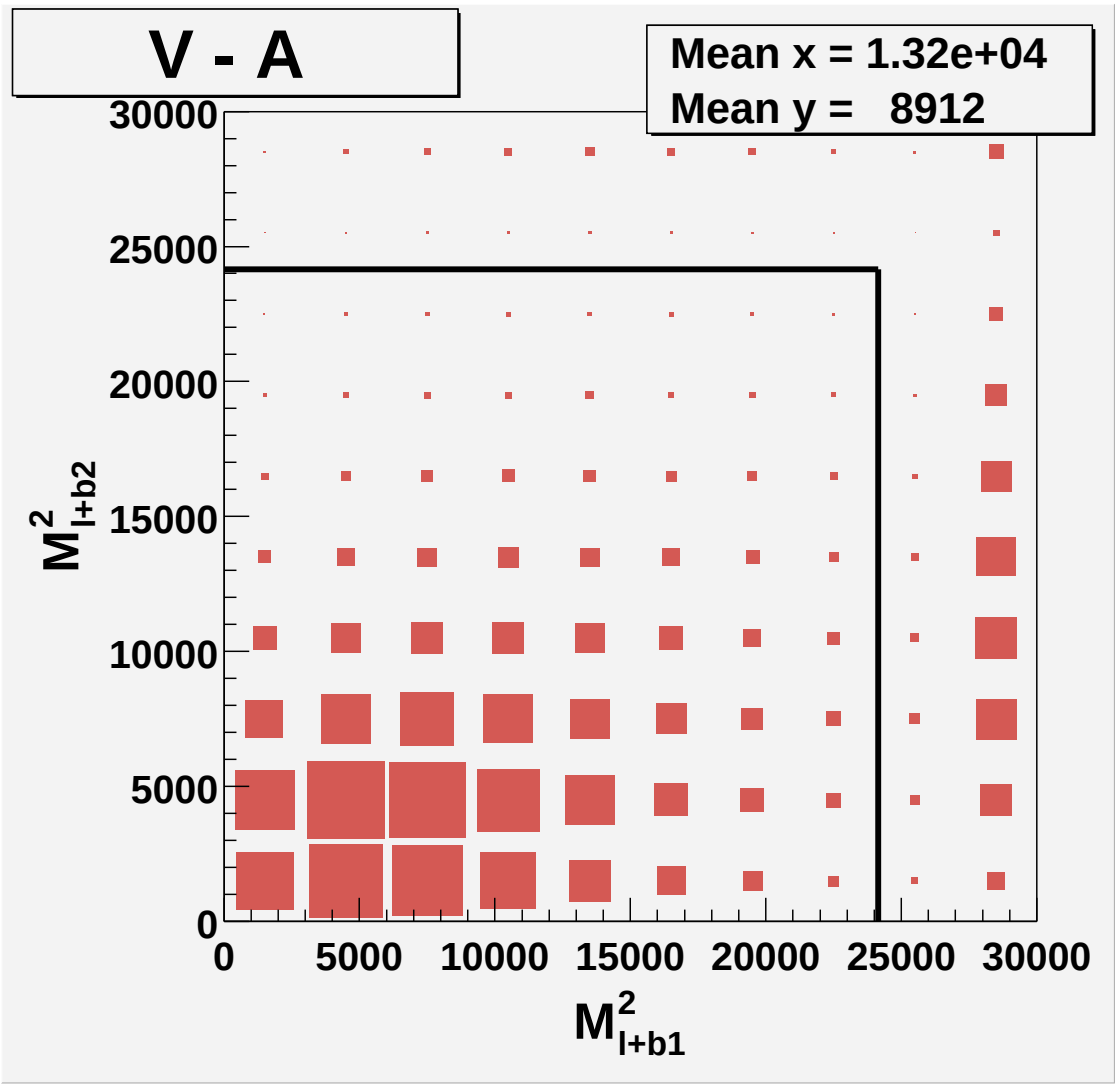

Figure 5.9: Standard Model $t\bar{t}$ template for dilepton sample (Two entries per event).

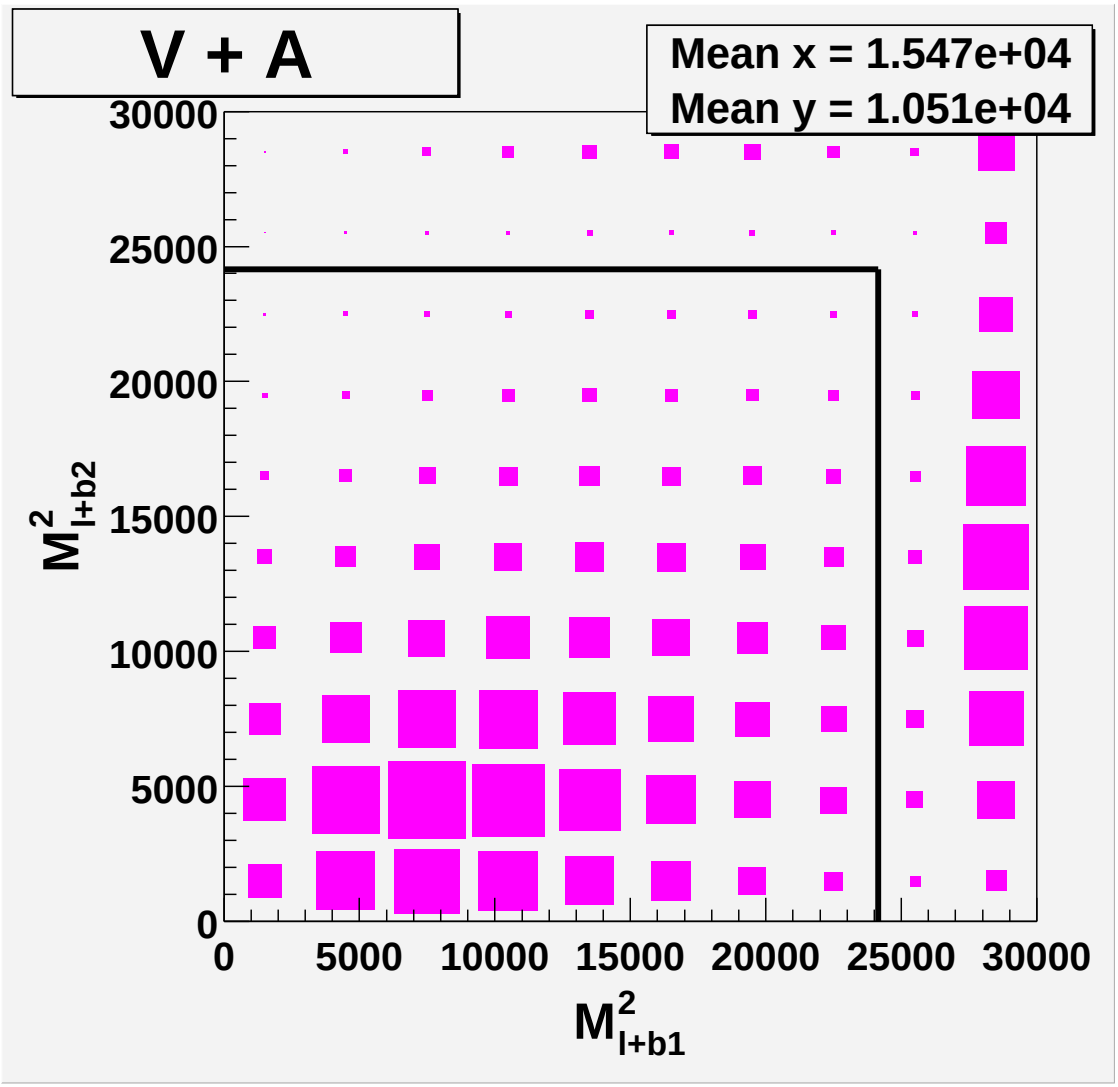

Figure 5.10: V+A $t\bar{t}$ template for dilepton sample (Two entries per event).

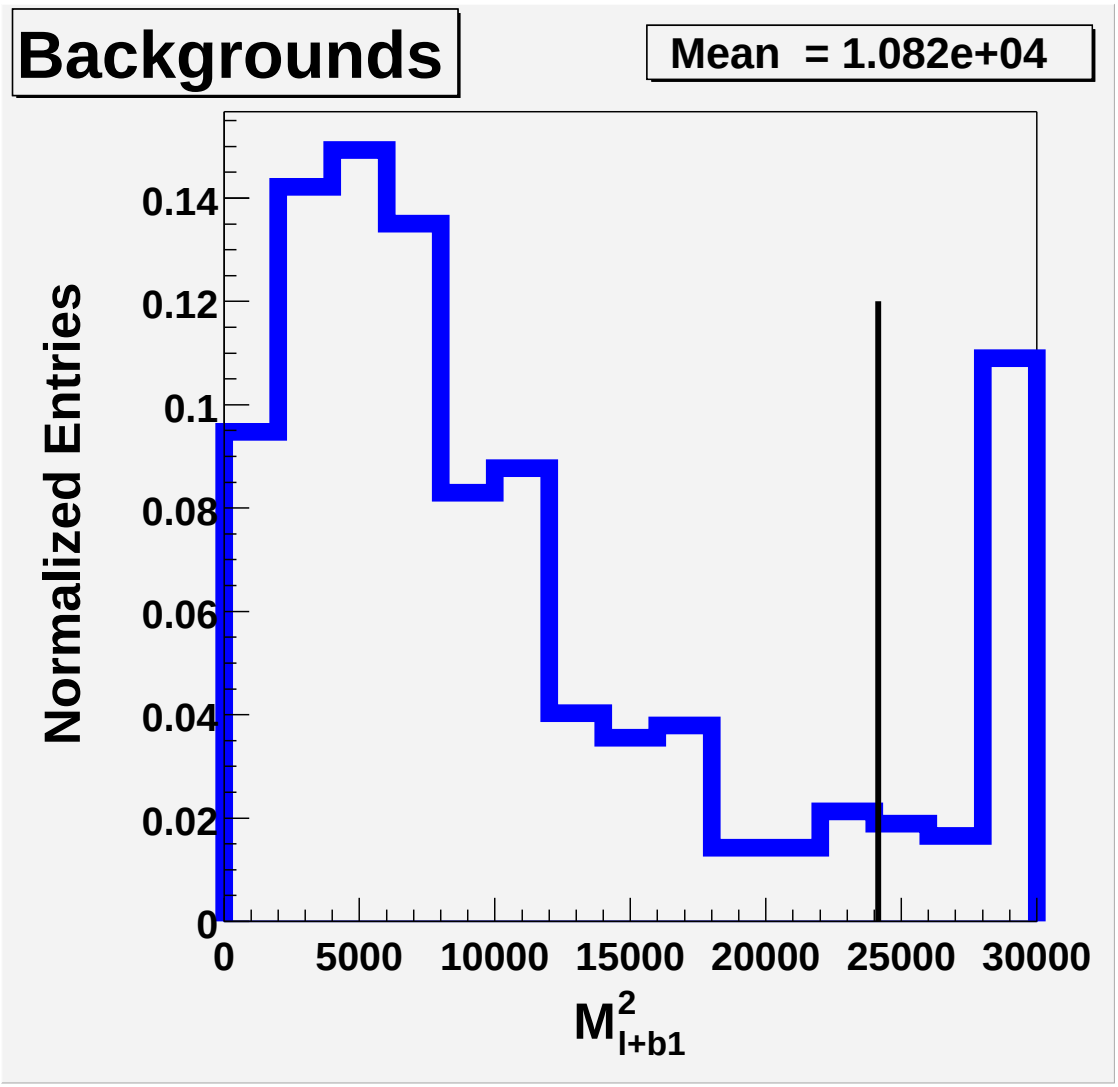

Figure 5.11: Background template for SVX single-tagged sample (One entry per event).

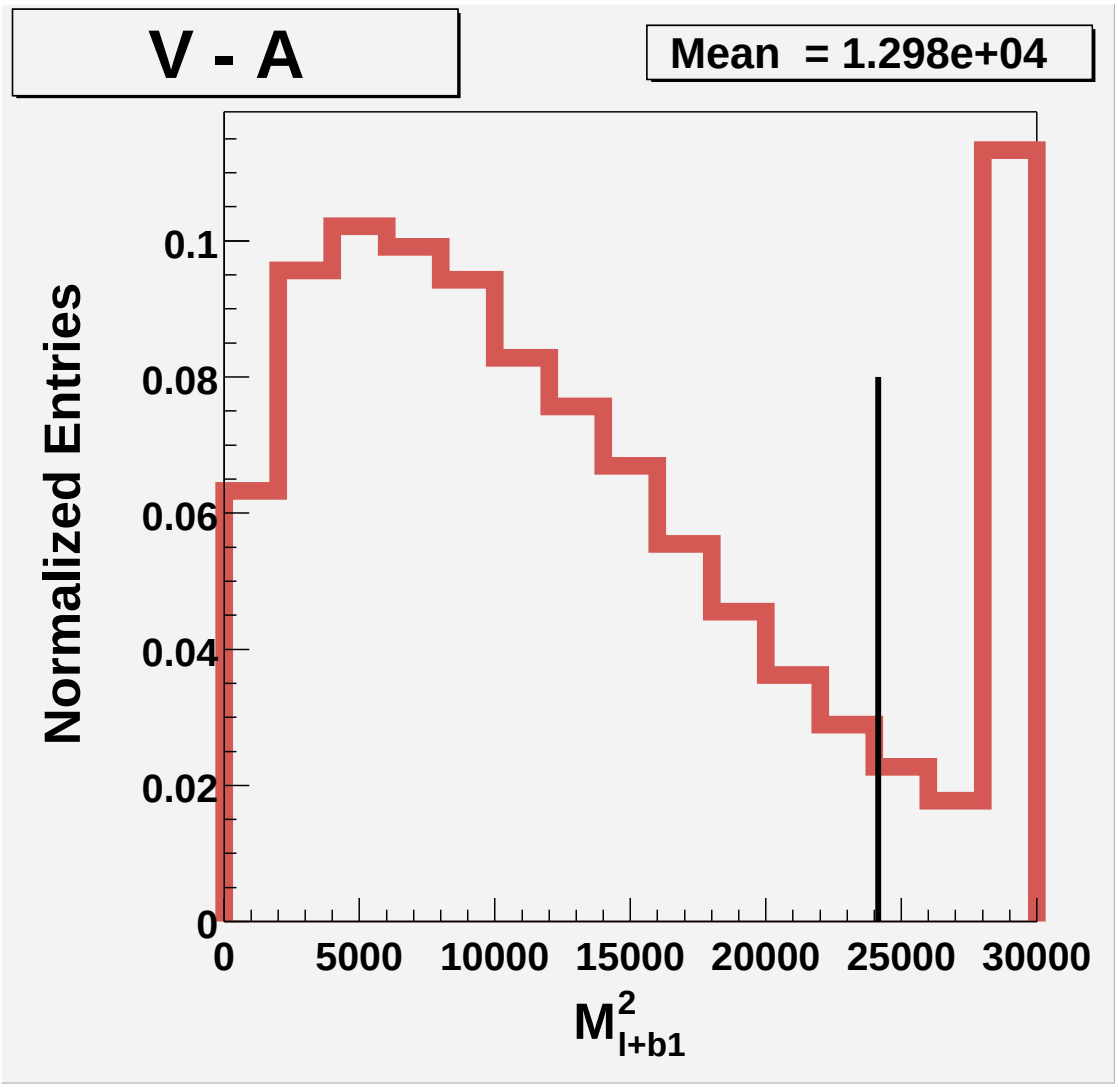

Figure 5.12: Standard Model $t\bar{t}$ template for SVX single-tagged sample (One entry per event).

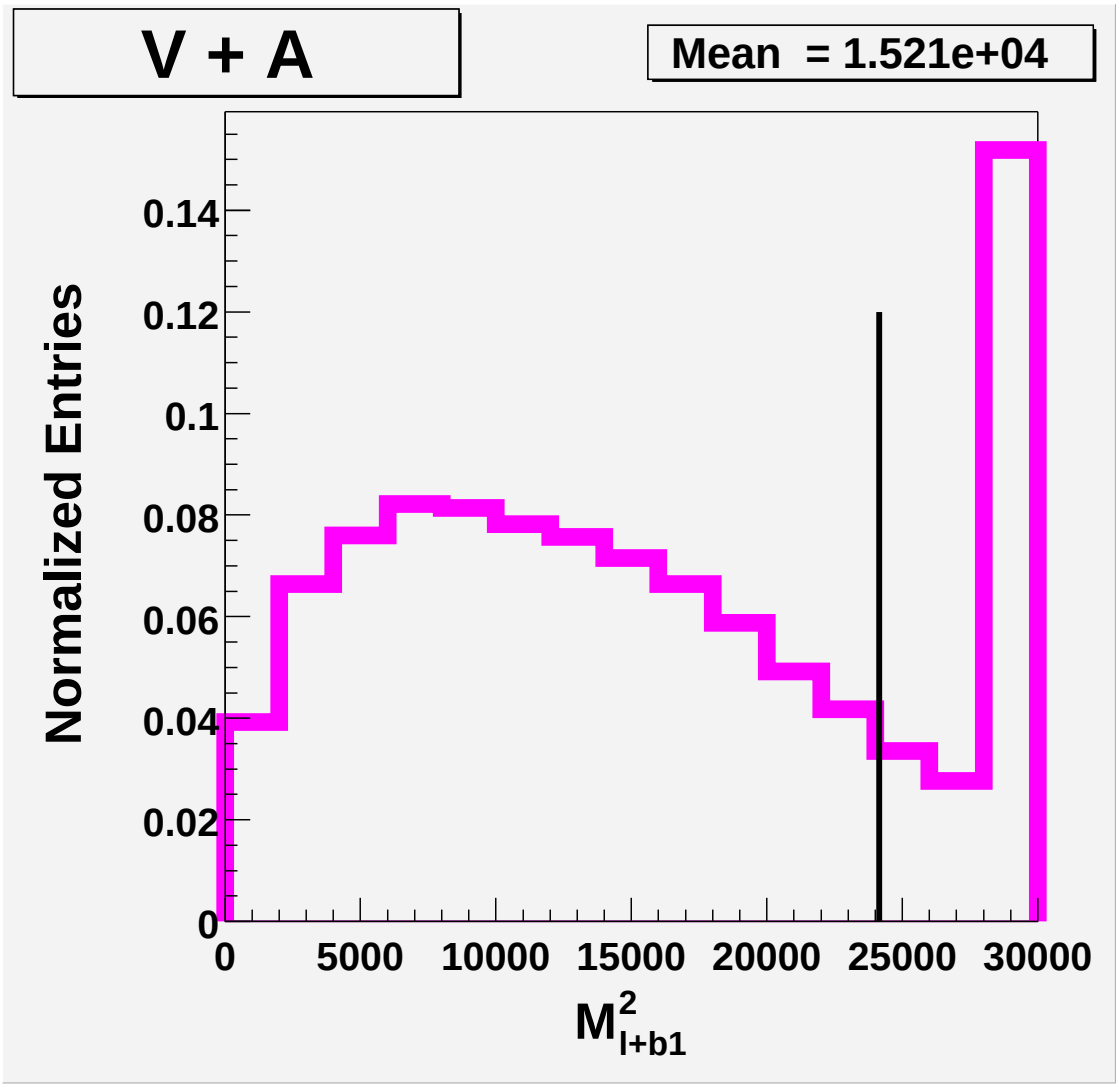

Figure 5.13: V+A $t\bar{t}$ template for SVX single-tagged sample (One entry per event).

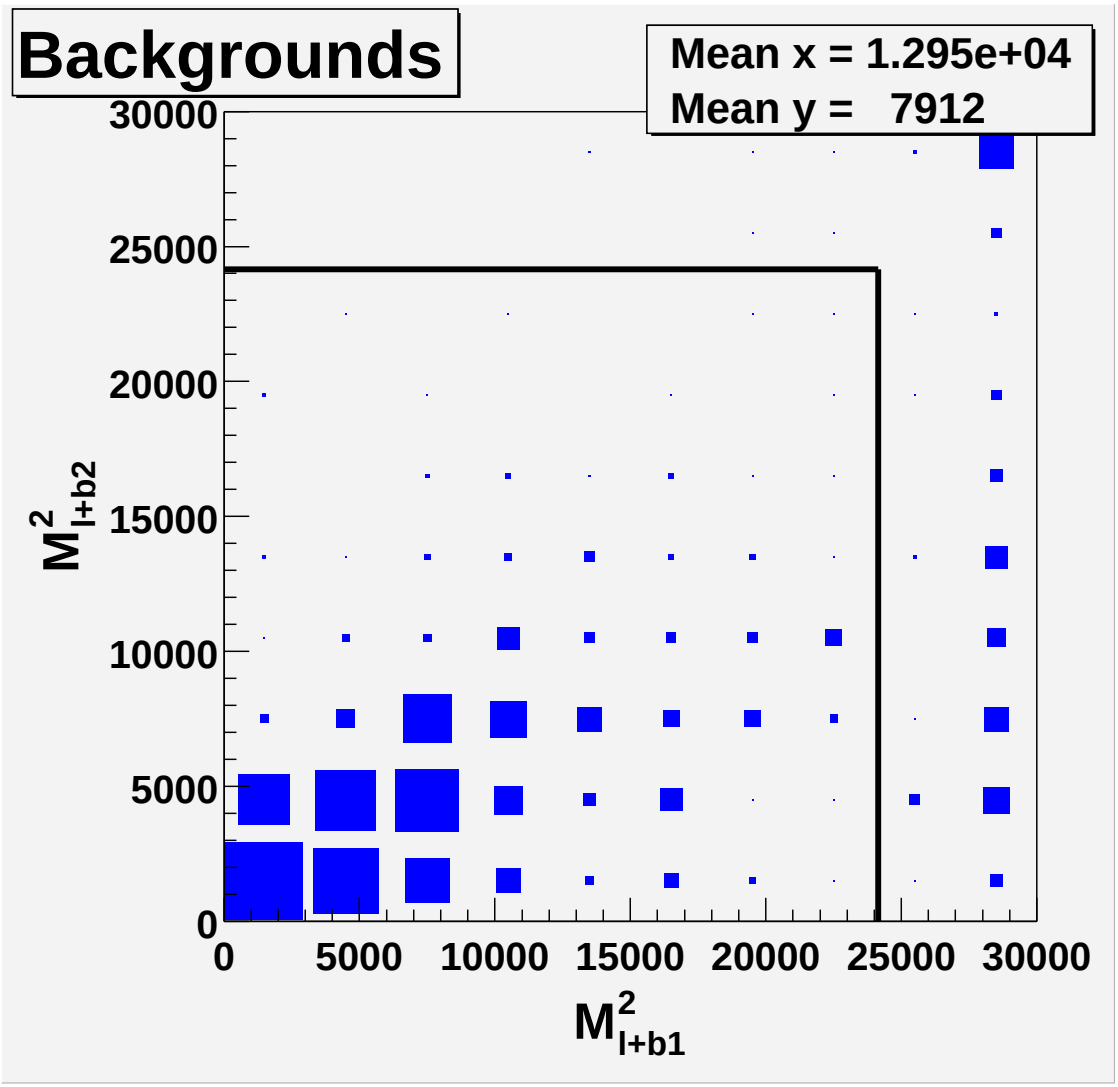

Figure 5.14: Background template for SVX double-tagged sample (One entry per event).

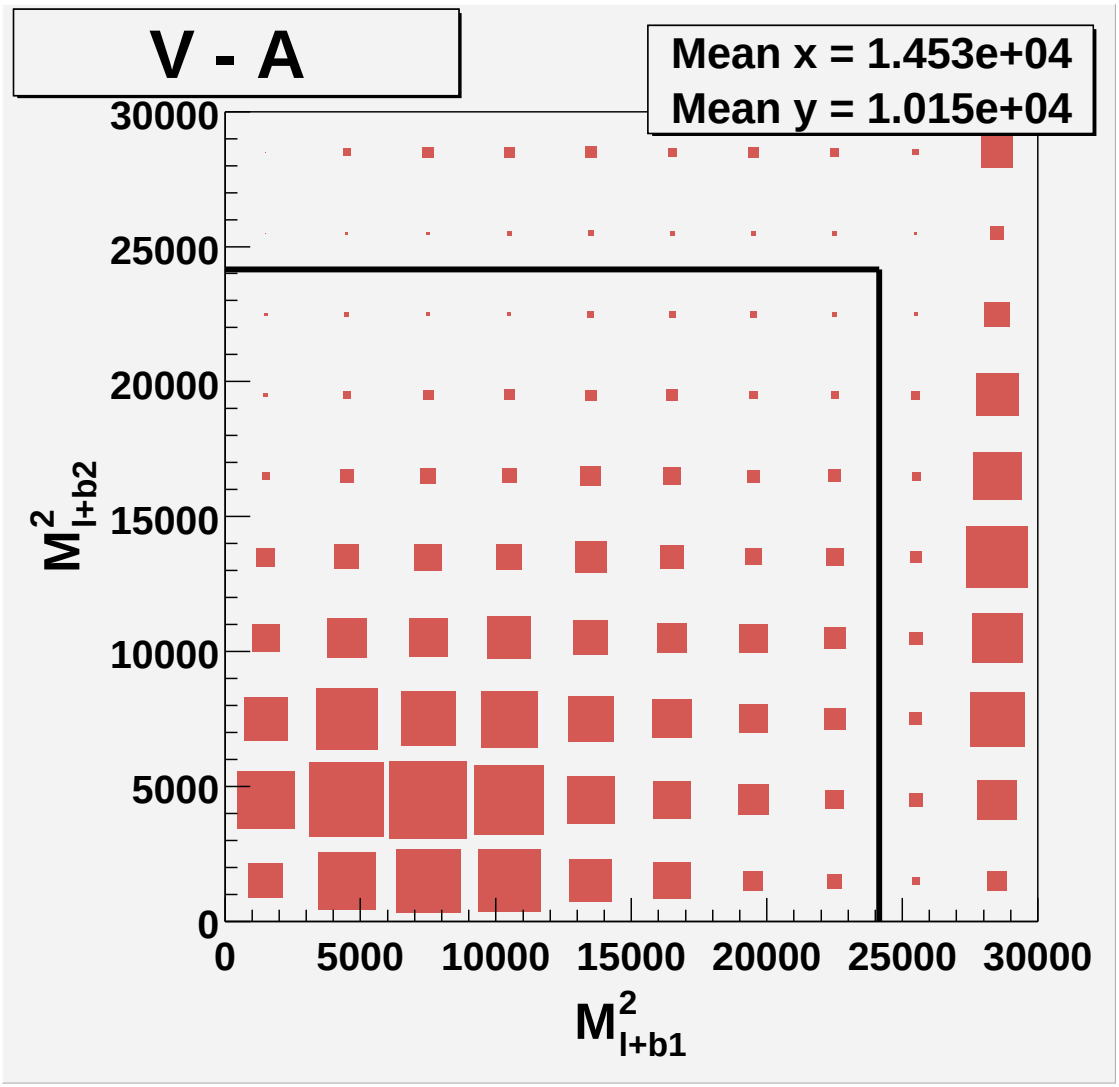

Figure 5.15: Standard Model $t\bar{t}$ template for SVX double-tagged sample (One entry per event).

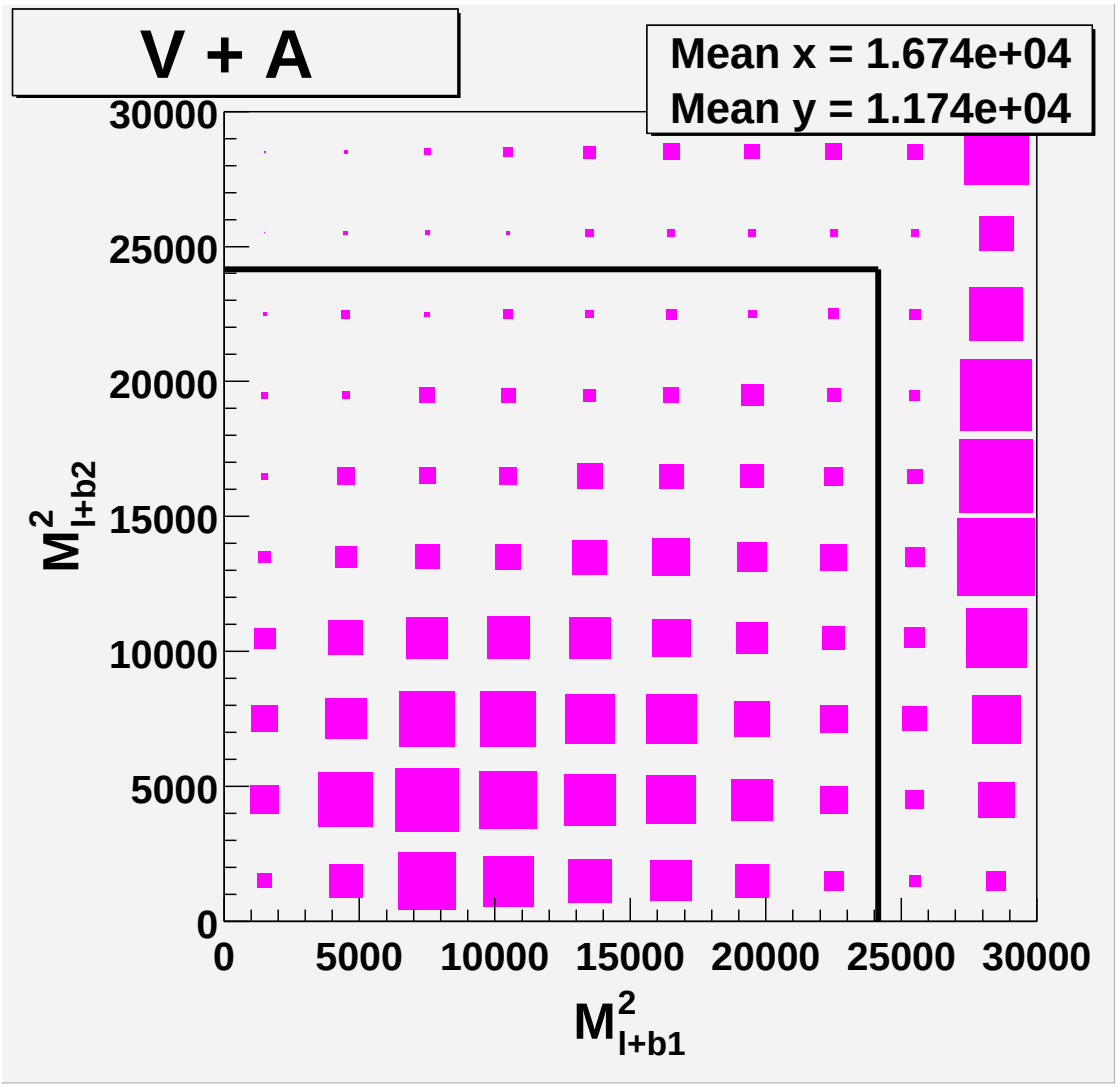

Figure 5.16: V+A $t\bar{t}$ template for SVX double-tagged sample (One entry per event).

5.7 Validation of Monte Carlo

Reconstructed Monte Carlo must accurately represent the data. The original CDF detector simulation and reconstruction software was written in FORTRAN on VAX operating systems. It was then ported to a central UNIX operating system, where several analyses were conducted. Finally, it was ported to the LINUX operating system, allowing the possibility of individual users to maintain a complete copy of the entire CDF software package. This analysis was done using a copy of the LINUX CDF software distribution maintained and debugged by the author. Bugs were found on a variety of levels including simulation issues where Monte Carlo τ particless were treated as stable particles, coding issues such as bank formats not being translated properly, and more subtle issues such as the improper definition of $\not{E}_{\mathrm{T}\phi}$ being stored by the reconstruction. In addition, the author adapted much of the code specifically for this analysis, including the top candidate analysis software.

Since there are many possible errors in creating reconstructed MC, care was taken to validate Monte Carlo distributions with those from the original CDF software distribution used for the published top cross-section and mass analyses [21].

To do this, the Standard Model $t\bar{t}$ dilepton Monte Carlo created for this analysis was compared to an extracted set of Run I distributions from a previous Run I analysis which examined the consistency of the Run I top dilepton MC distributions. The distributions examined include $\not{E}_{\mathrm{T}}$ (Figure 5.17), H_T (Figure 5.18), M_{ll} (Figure 5.19), M_{jj} (Figure 5.20), $\Delta\phi_{ll}$ (Figure 5.21), and P_T^{j1} (Figure 5.22). Kolmogorov-Smyrnov probability tests were used and show a high level of agreement between the samples previously used and the samples generated for this analysis. Besides validating the reconstruction of these quantities, this also demonstrates good agreement between the Herwig 6.2 Monte Carlo used in this analysis, and the Herwig 5.6 Monte Carlo used in the published top analyses. This agreement is crucial in order to maintain published

assumptions about top event finding efficiencies and variable shapes that feed in to the M^2_{l+b} distributions. Additional comparisons of Monte Carlo distributions with data are shown later in Section 6.2.

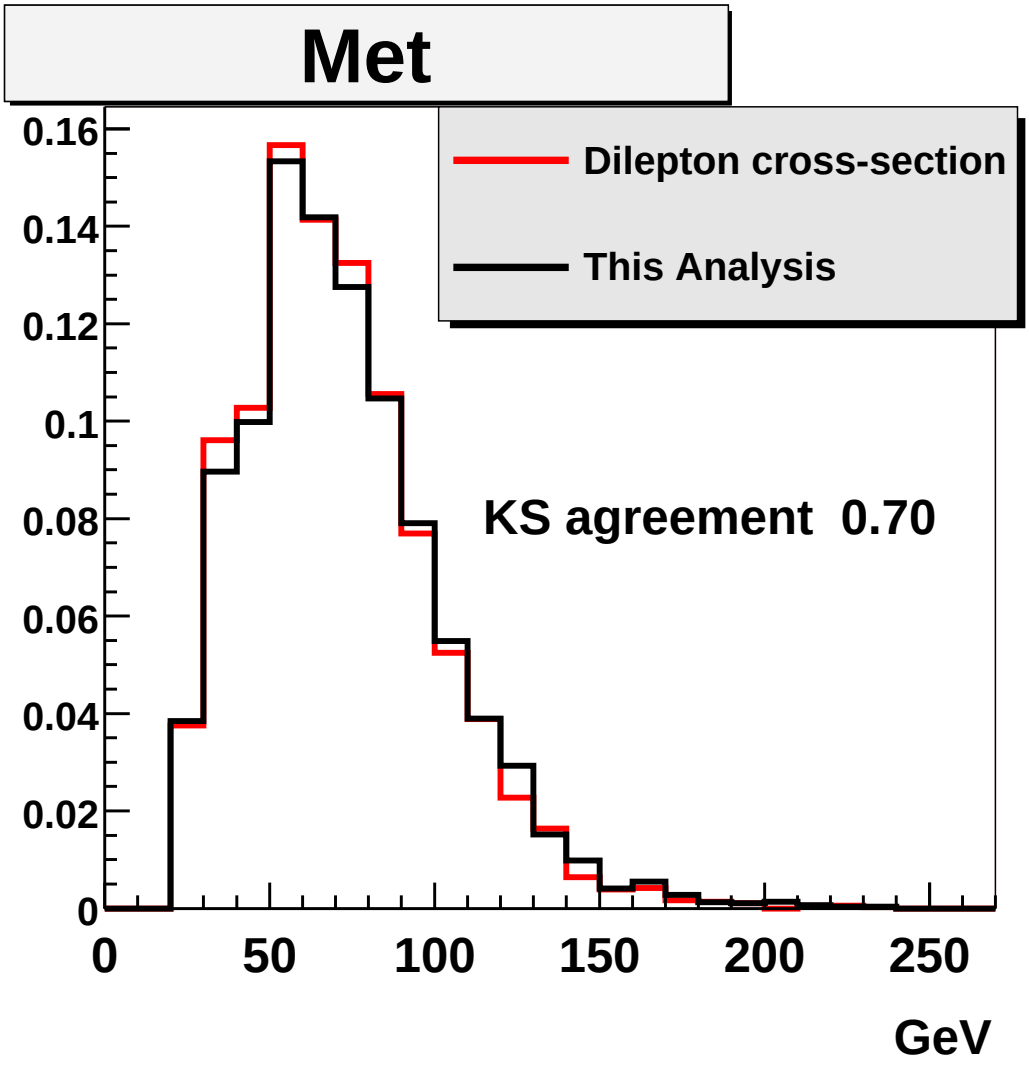

Figure 5.17: Comparison of the Monte Carlo $\not\!\!E_T$ distribution in this dilepton analysis with that from the published CDF dilepton cross-section measurement showing the KS probability for agreement.

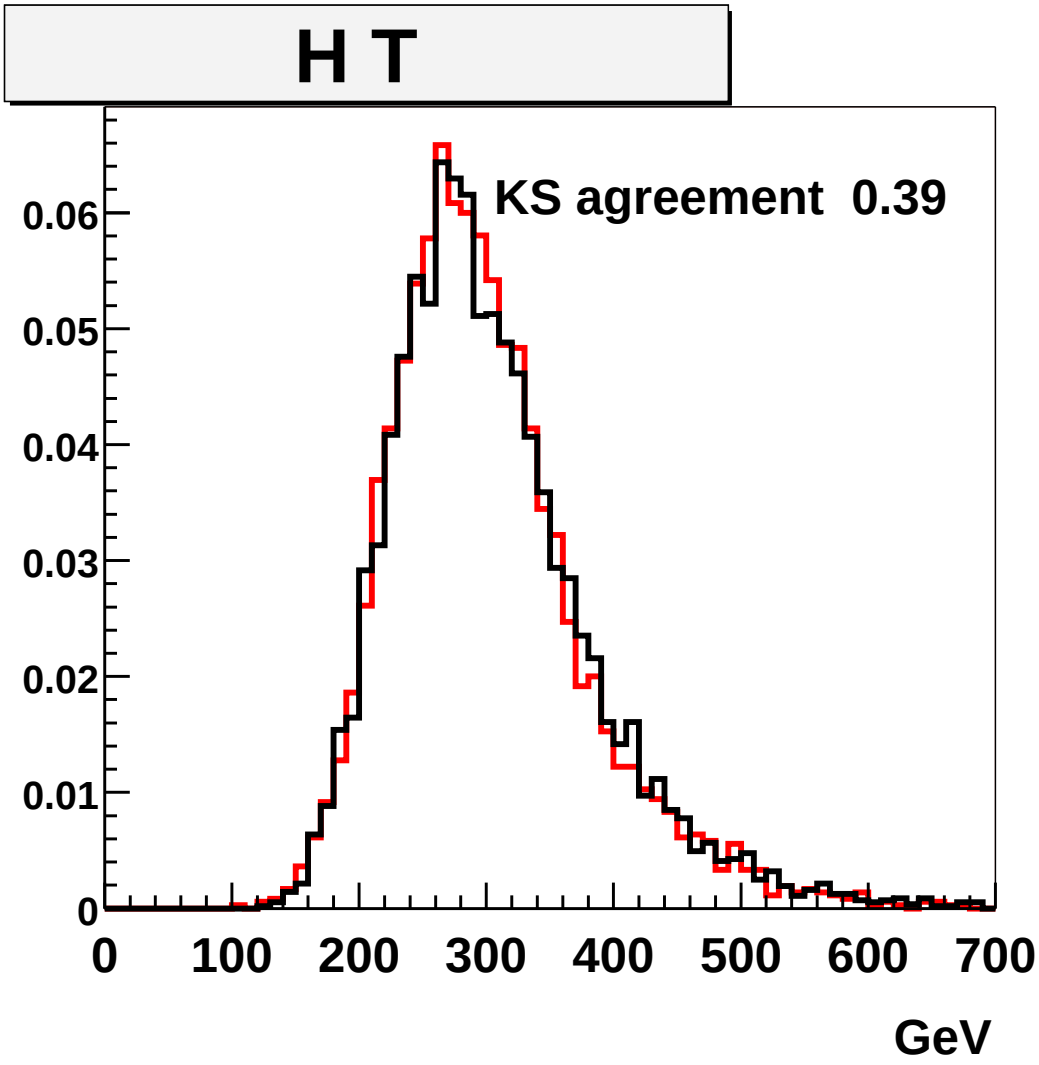

Figure 5.18: Comparison of the Monte Carlo H_T distribution in this dilepton analysis with that from the published CDF dilepton cross-section measurement showing the KS probability for agreement.

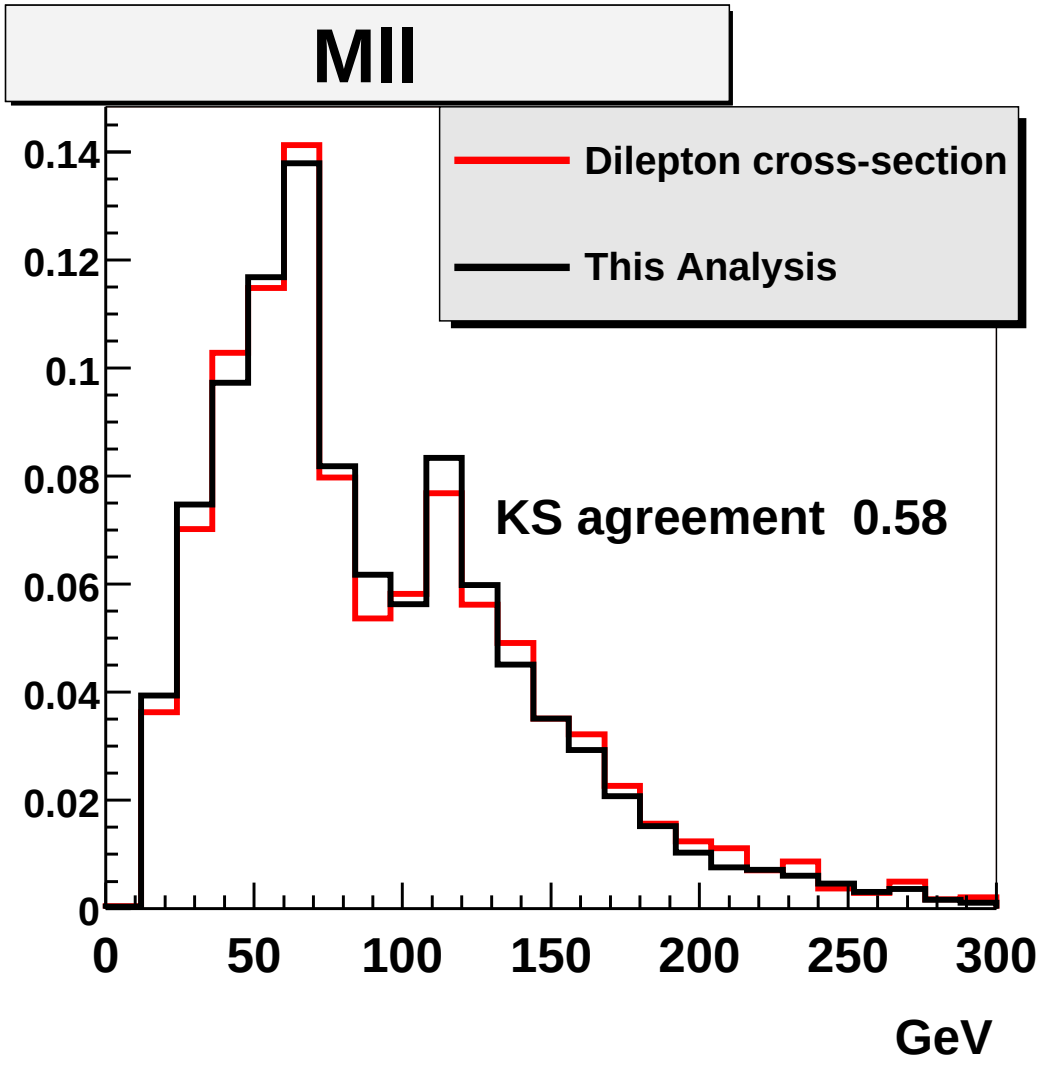

Figure 5.19: Comparison of the Monte Carlo $M_{l^+l^-}$ distribution in this dilepton analysis with that from the published CDF dilepton cross-section measurement showing the KS probability for agreement.

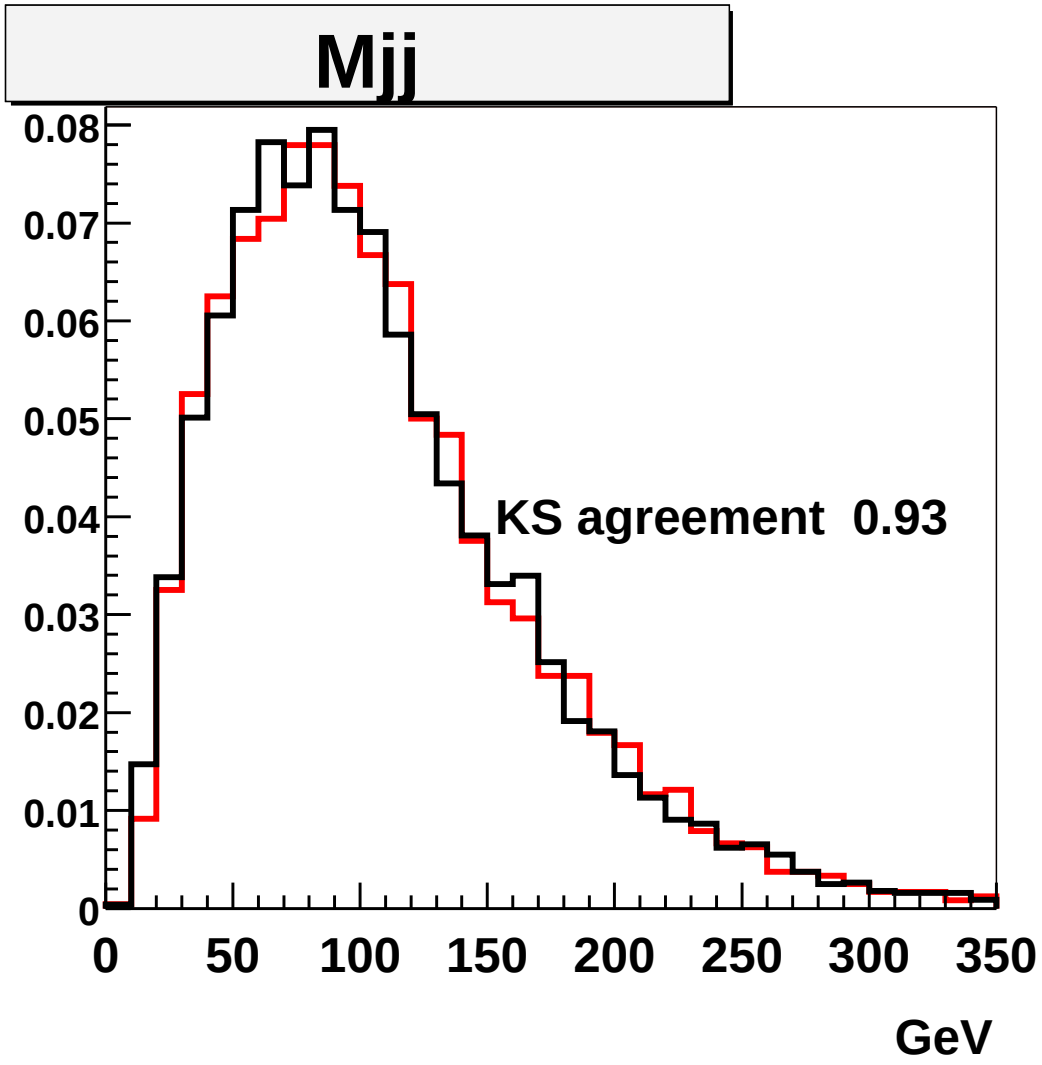

Figure 5.20: Comparison of the Monte Carlo M_{jj} distribution in this dilepton analysis with that from the published CDF dilepton cross-section measurement showing the KS probability for agreement.

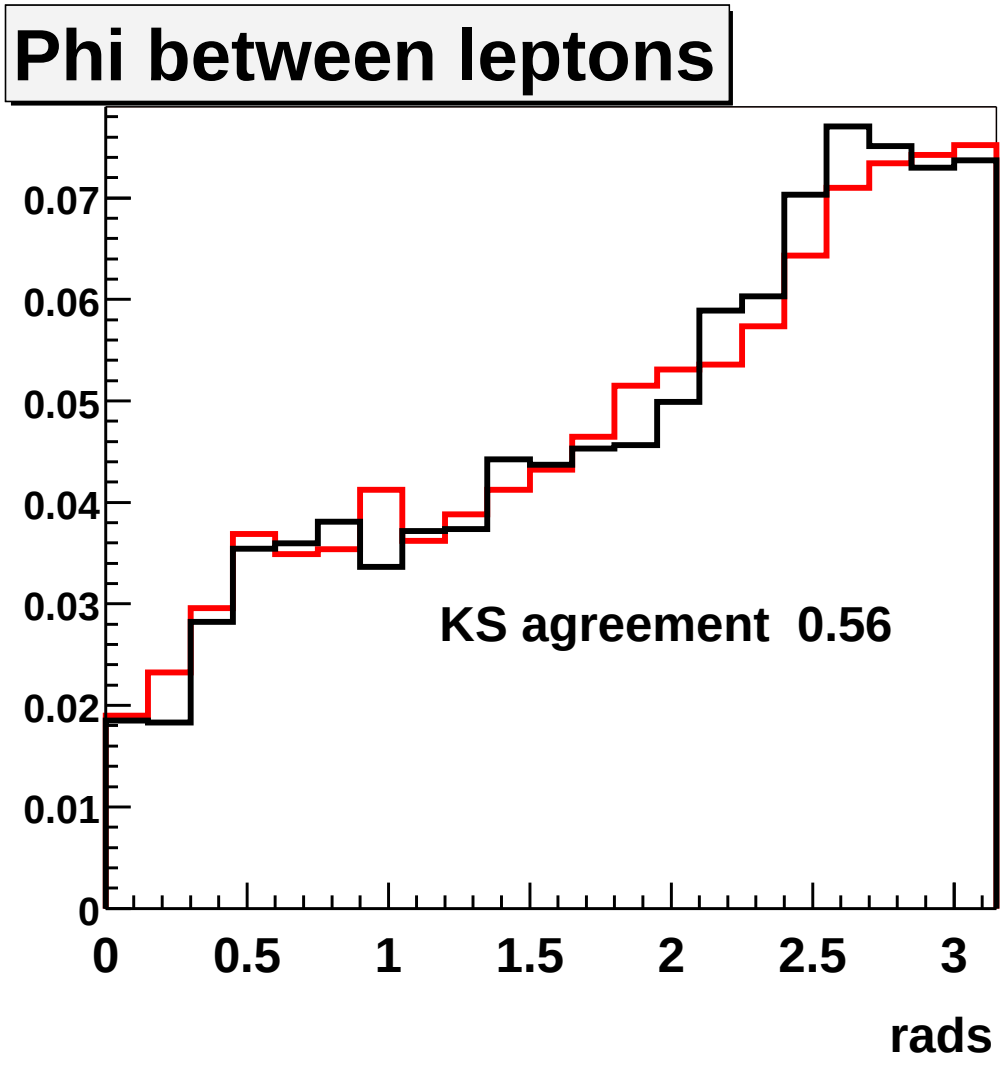

Figure 5.21: Comparison of the Monte Carlo $\phi_{l^+l^-}$ distribution in this dilepton analysis with that from the published CDF dilepton cross-section measurement showing the KS probability for agreement.

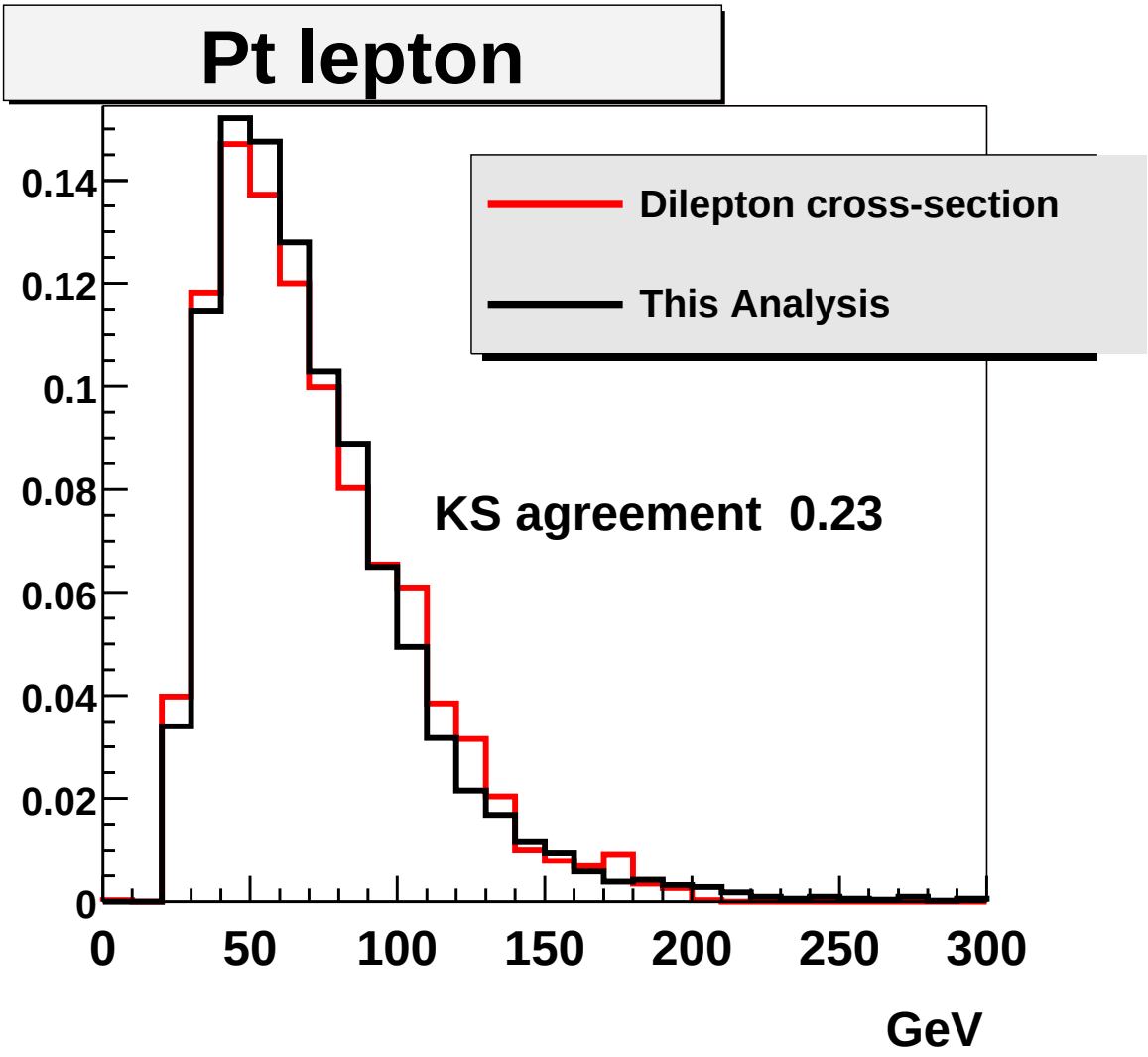

Figure 5.22: Comparison of the Monte Carlo lepton P_T distribution in this dilepton analysis with that from the published CDF dilepton cross-section measurement showing the KS probability for agreement.

Chapter 6

Measurement of V+A Fraction

6.1 Likelihood Fit

A binned log likelihood fit is used to extract the V+A fraction from the data samples by comparing them to Monte Carlo templates of V+A, V−A, and background. A combined log likelihood fit for f_{V+A} is done to fit each sample simultaneously while constraining to the background normalization determined in the standard top analyses.

Since the lepton P_T spectrum is higher for right-handed Ws as compared to left-handed Ws, right-handed Ws are more likely to pass the lepton P_T requirements, leading to a higher efficiency for finding V+A events. For each sub-sample, the efficiency for V−A events passing all cuts compared to that of V+A was calculated, and used to determine a relative acceptance factor

$$R = \epsilon_{V-A}/\epsilon_{V+A} \tag{6.1}$$

for the fitting procedure (Table 6.1).

The prediction function is expressed in terms of a combined likelihood for the dilep-

Sub-sample	Relative efficiency
Dilepton	0.909 ± 0.005
SVX double	0.936 ± 0.004
SVX single	0.945 ± 0.01

Table 6.1: Relative efficiency for V$-$A events to pass the top cuts compared to V$+$A.

ton, SVX double-tagged, and SVX single-tagged samples.

$$\mathcal{L}_{combined} = \mathcal{L}_{dilepton} \cdot \mathcal{L}_{svx2} \cdot \mathcal{L}_{svx1} \tag{6.2}$$

$\mathcal{L}$ for each sample is the product of the Poisson probabilities when comparing prediction to experiment, multiplied by a Gaussian constraint on the background.

$$\mathcal{L}_{sample} = \prod_{i=1}^{H} \frac{\mu_i^{x_i} \cdot e^{-\mu_i}}{x_i!} \frac{1}{\sqrt{2\pi\sigma_b}} e^{-\frac{(n_b - N_b)^2}{2{\sigma_b}^2}} \tag{6.3}$$

The prediction $\mu_i = \mu_i(f_{V+A}, n_b)$ is the bin content obtained for a given V$+$A fraction, f_{V+A}, and background per event, n_b. N_b is the expected background fraction per event, σ_b is the uncertainty on N_b, and x_i is the data for bin i. N_b and σ_b are the same values used in the published CDF top mass analyses. μ_i is calculated as :

$$\mu_i = N \cdot \frac{f_{V+A} \cdot P_i + R \cdot [(1 - f_{V+A}) \cdot M_i + B_i \cdot n_B]}{f_{V+A} + R \cdot [(1 - f_{V+A}) + n_B]} \tag{6.4}$$

where P_i, M_i, and B_i are the contents of bin i for the MC templates of V$+$A, V$-$A, and background, respectively. The fraction of background expected per event in the data is

n_B. R is the relative efficiency of $\frac{\epsilon_{V-A}}{\epsilon_{V+A}}$, N is the number of events in the sample, and f_{V+A} is the fraction of V+A.

Some additional conditions were applied in the fit function to ensure that the likelihood was well-defined. When the prediction function for a given bin gets too close to zero (i.e., $\mu_i \rightarrow \epsilon$), it levels off at ϵ to ensure that minima are not chosen for $\mu_i < 0$.

$-2 \cdot \log \mathcal{L}_{combined}$ is minimized to determine the most likely values of f_{V+A} and n_B for a given experiment. The statistical uncertainty is found by measuring the spread of f_{V+A} when $-2 \cdot \log \mathcal{L}$ is increased by one unit with respect to the minimum. The MINUIT package of ROOT [27] is used to determine the fit minimum using the MIGRAD algorithm. The HESSE algorithm then determines the error matrix at the point of the minimum, and the MINOS algorithm, which takes into account non-parabolic shape, calculates the positive and negative errors of the fit. The fit is not constrained to the physical region [0,1], and so one would expect for the Standard Model $f_{V+A} = 0$ to have as many unphysical solutions less than zero as physical solutions above zero.

6.1.1 Tests of Fitting Method

The fitting method was tested extensively using "pseudo-experiments". While many experiments cannot be done, with the benefit of Monte Carlo, pseudo-experiments of data-sized event samples can accomplish this task. V+A, V−A, and background templates were created for each sub-sample using $2/3$ of the reconstructed Monte Carlo events which passed the cuts. The remaining $1/3$ of events were used to make pseudo-experiments to simulate the possible results of the fit.

The distribution of 10,000 fit values of f_{V+A} is shown in Figure 6.1 for the case when the input fraction f^{in}_{V+A} was a Poisson fluctuated fraction centered at 0.33.

The fit function was checked to make sure that the sensitivity to the measurement was not dependent on the true value of f^{in}_{V+A}. The fit value was found to be constant as

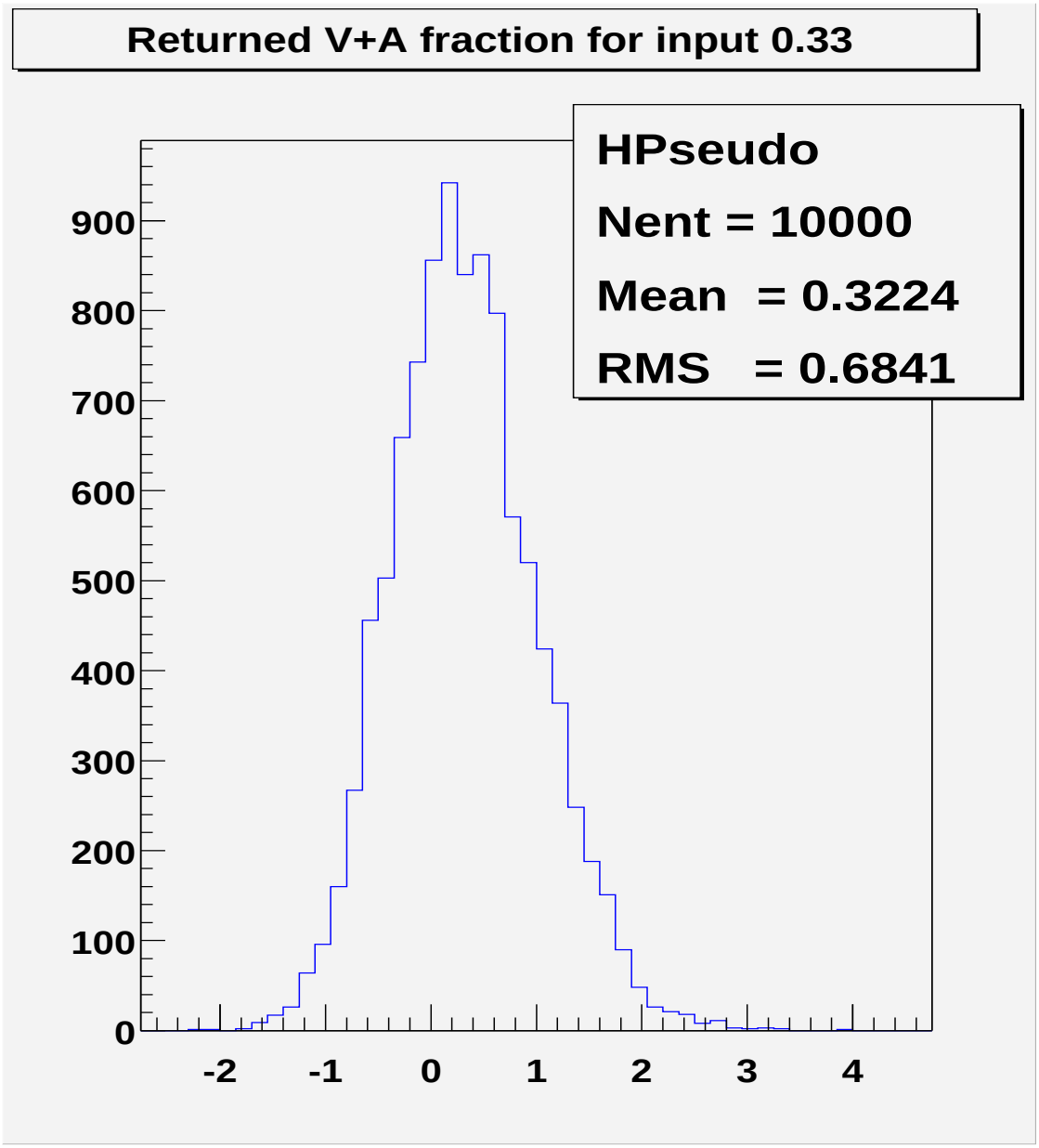

Figure 6.1: With a generated V+A fraction of 0.33, the results of 10,000 pseudo-experiments comparing independent Monte Carlo distributions. The physical region is from 0 to 1.

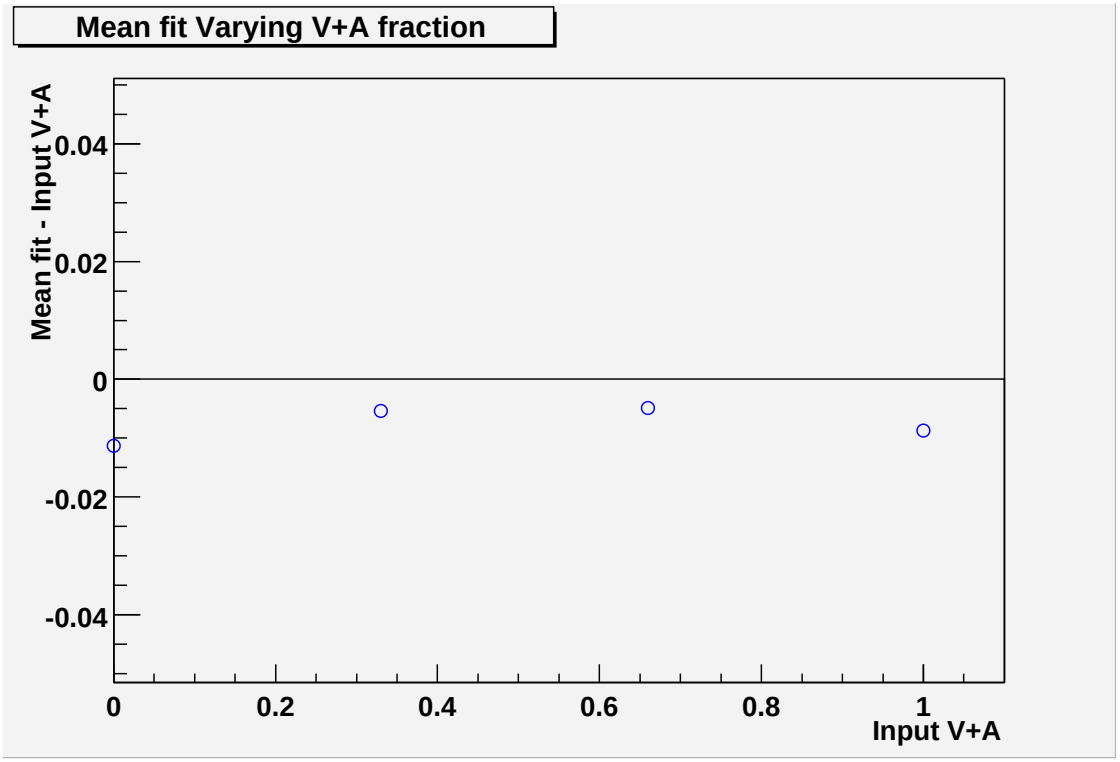

Figure 6.2: Pseudo-experiments fit with prediction function for range of V+A inputs.

a function of input value, so that there is no bias in the likelihood minima for different f^{in}_{V+A} values (Figure 6.2). The offset from zero is consistent with the expected statistical uncertainty from between the template events and the independent events used for the pseudo-experiments.

The error is also studied as a function of f^{in}_{V+A} in Figure 6.3, it can be seen that the error increases as f^{in}_{V+A} increases. This is to be expected since the R parameter, defined in Equation 6.1, causes the likelihood to give higher statistical significance to V−A-like events, since they are relatively less likely to be in a given pseudo-experiment. The slope of the mean returned error is defined by the value of R. Since R is relatively high, 0.9 or greater for each sample, it is only a small effect. However, one expects the error for V+A-like distributions to be higher than if the distribution is distinctly V−A-like due

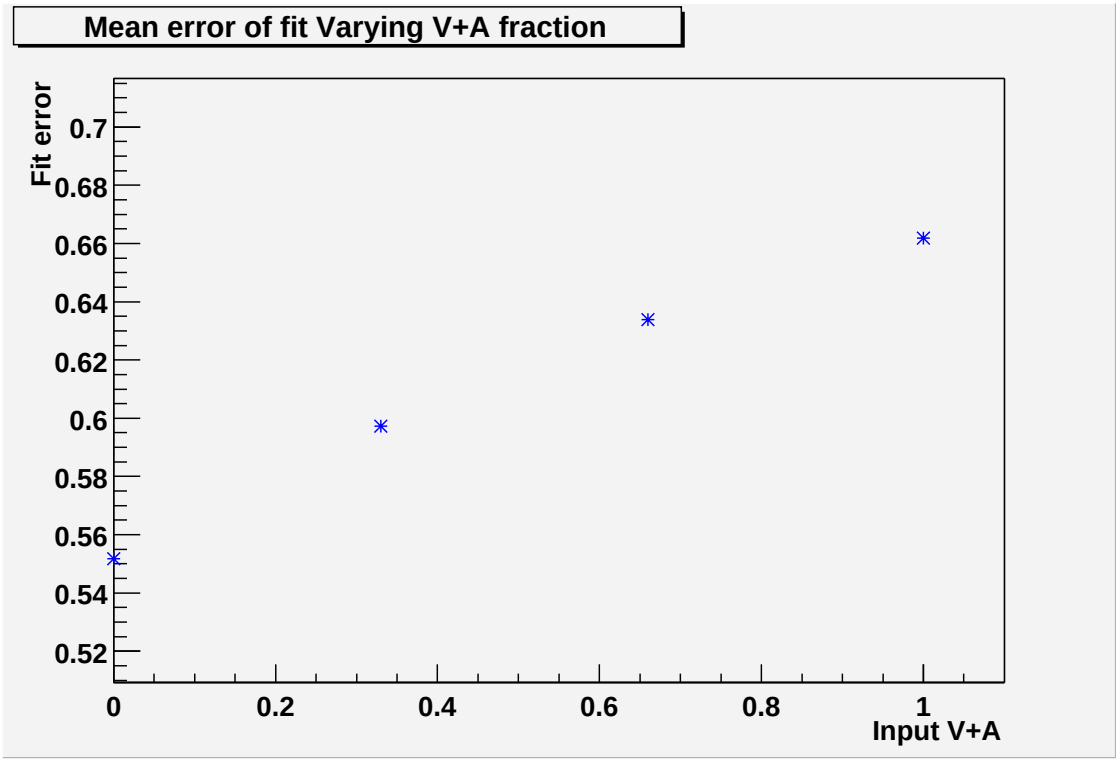

Figure 6.3: Mean error for pseudo-experiments fit for range of f^{in}_{V+A}. V$-$A events have more weight since they are less likely because of the relative efficiency dependence in the fit function. This leads to a slope in the fit error.

to this effect of different detection efficiencies for V$-$A and V$+$A events.

The fit value and errors of the fit were tested using the figure of merit known as the "pull" which is in general defined as :

$$pull = \frac{Measured - Expected}{Error} \tag{6.5}$$

When many experiments are done, the distribution of pull values should be consistent with a unit Gaussian of mean 0 and width 1. If the width is other than 1, it could mean that the errors are being miscalculated. If the mean is not 0, then the fit function is biasing the return value in one direction. The proper mean and width signify that the

prediction function correctly represent the sample, and that the fitting algorithm does not have mistakes.

The pull in the case of this analysis is defined as

$$pull = \begin{cases} \frac{f^{in}_{V+A} - f_{V+A}}{\sigma^{+}_{f_{V+A}}} & \text{when } f_{V+A} < f^{in}_{V+A} \\ \frac{f_{V+A} - f^{in}_{V+A}}{\sigma^{-}_{f_{V+A}}} & \text{when } f_{V+A} > f^{in}_{V+A} \end{cases} \tag{6.6}$$

where $\sigma^{+}_{f_{V+A}}$ is the positive error returned by the fit, and $\sigma^{+}_{f_{V+A}}$ is the negative error. It was found that positive and negative errors provided better pull distributions than a single Gaussian error due to asymmetric fit errors. Figure 6.4 demonstrates that the mean of the pull is consistent with zero although the width of the distribution indicates the errors may be slightly small.

To study the fit error in more detail, a technique is used to extract the degree to which the fit mean and uncertainty values are non-Gaussian. Independent samples are used to draw pseudo-experiments with a Poisson-fluctuating input value of f^{in}_{V+A}. For each pseudo-experiment, the integrated probability distribution (IPD) of the likelihood is calculated from the input f^{in}_{V+A} value to infinity. This calculation can be written in terms of the Error function, Erf(x).

$$IPD(x) = \int_{f^{in}_{V+A}}^{\infty} \frac{1}{\sqrt{2\pi}} \exp^{-x^2/2} dx = \frac{1}{2} - \frac{1}{2} Erf(\frac{f^{in}_{V+A}}{\sqrt{2}}) \tag{6.7}$$

For a normal Gaussian distribution, this should produce a flat distribution from zero to one. However, if the errors are not Gaussian, this distribution will not be flat. By changing the parameters of a normal Gaussian, mainly the offset and the sigma, one can alter the IPD in well-defined ways (Figure 6.5).

The IPD distribution from pseudo-experiments is then fit to a Gaussian with varying

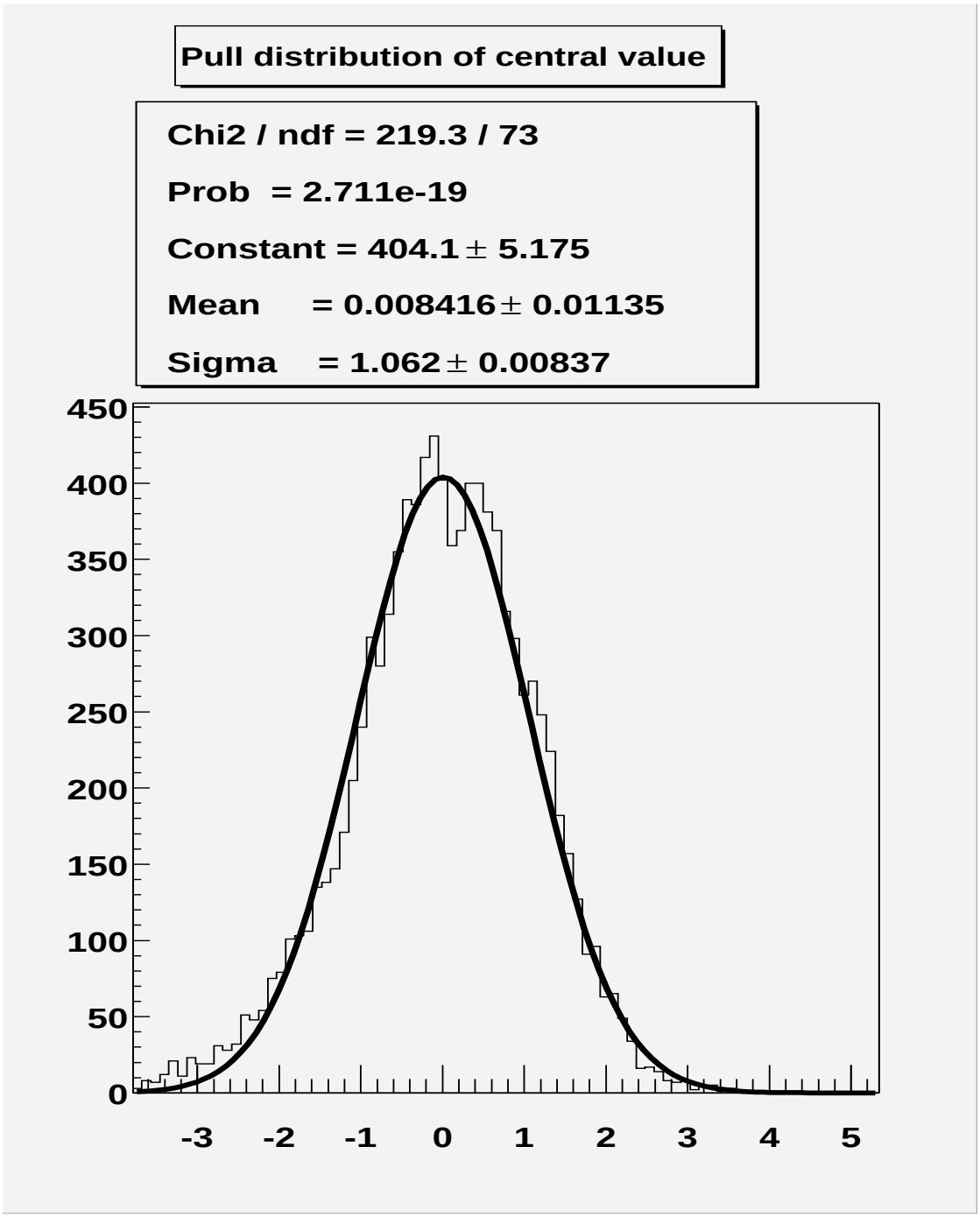

Figure 6.4: Pull distribution is shown fit to a Gaussian.

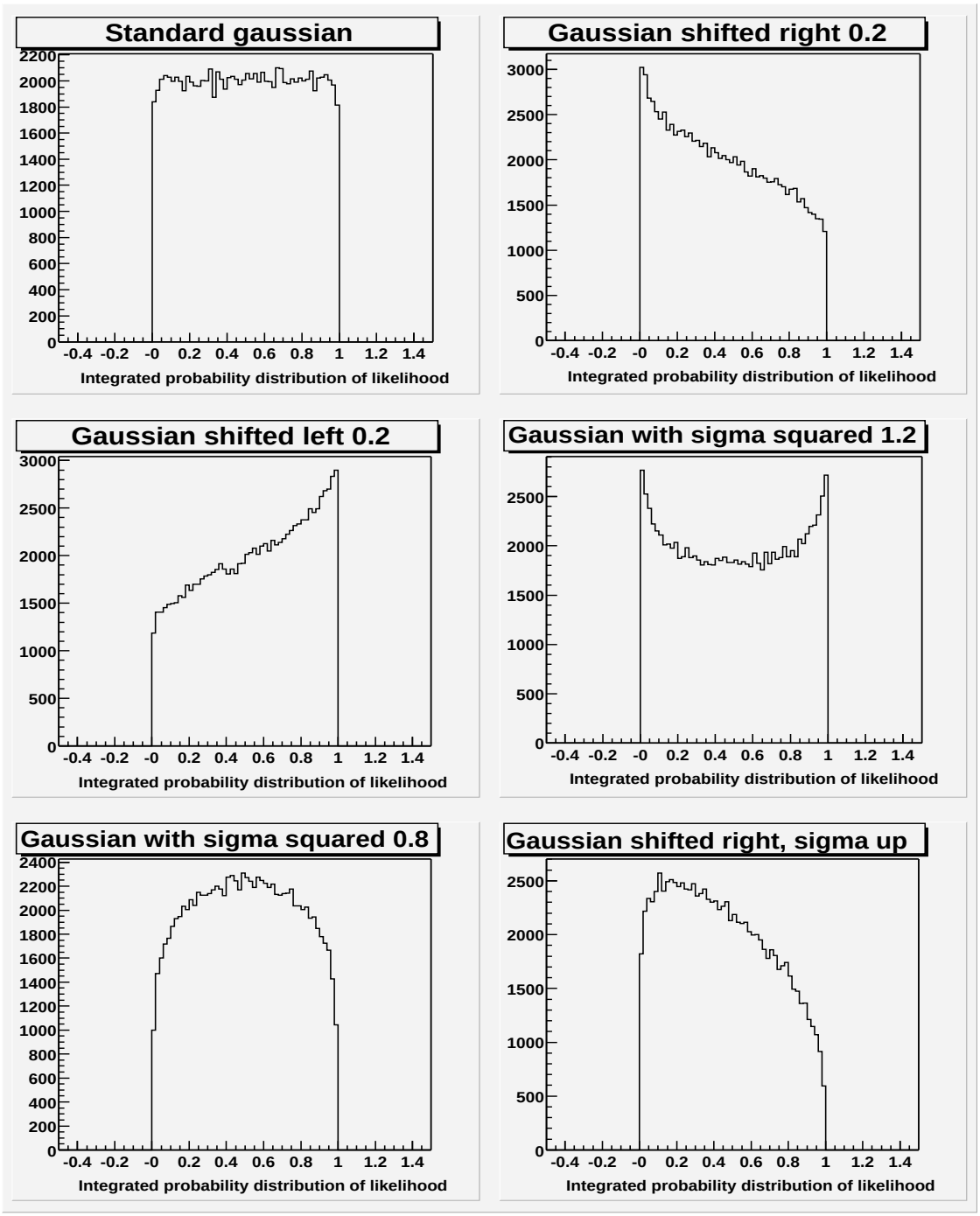

Figure 6.5: Theoretical histograms for the integrated probability distribution with non-Gaussian effects. The integration is of a Gaussian probability distribution integrating from the central value to infinity. Pseudo-experiments using the probability distribution from a normal Gaussian produce a flat distribution, but pseudo-experiments with shifted central values and non-standard sigma have well defined effects on the slope and concavity of the distribution, respectively.

sigma and offset, to determine the variation of the IPD distribution from a standard Gaussian. Nine independent samples are used to determine the parameters; the results for some fits are shown in Figure 6.6, and used to determine the sigma of the likelihood fit.

The result is that there is an upward scale factor of 1.04 necessary to make the error returned by the fit consistent with that of a Gaussian spread of measurements around the true mean value.

The scale factor of 1.04 will be applied to the fit error when the data is fit. With this slight alteration of the fit error, it is determined that the likelihood fitting procedure behaves as expected and will reliably determine f_{V+A}.

6.1.2 Statistical Power of Samples

The statistical power for each sample improves with the number of M^2_{l+b} measurements in the sample. Since the dilepton sample has two leptons, and two b jets, there are four M^2_{l+b} values in each dilepton event, two of which are mainly correctly paired, and two of which are incorrect. In the SVX double-tagged sample, there is one lepton and two b jets, meaning there are two M^2_{l+b} values per event, one which is correctly paired, and one which is mispaired. The SVX single-tagged sample has one lepton and one b jet, meaning it has only one M^2_{l+b} pairing, which may or may not be the correct one. The relative sensitivity for each sample in measuring f_{V+A} is shown in Table 6.2 using the average likelihood error for 10,000 pseudo-experiments. The first part shows the sensitivity of each sample normalized arbitrarily to 100 M^2_{l+b} values per sample. The second part shows the sensitivity expected in the data for each of the sub-samples and the combined sensitivity.

The SVX double-tagged sample shows the greatest sensitivity per number of M^2_{l+b}. The improvement between the double-tagged sample over the single-tagged sample are

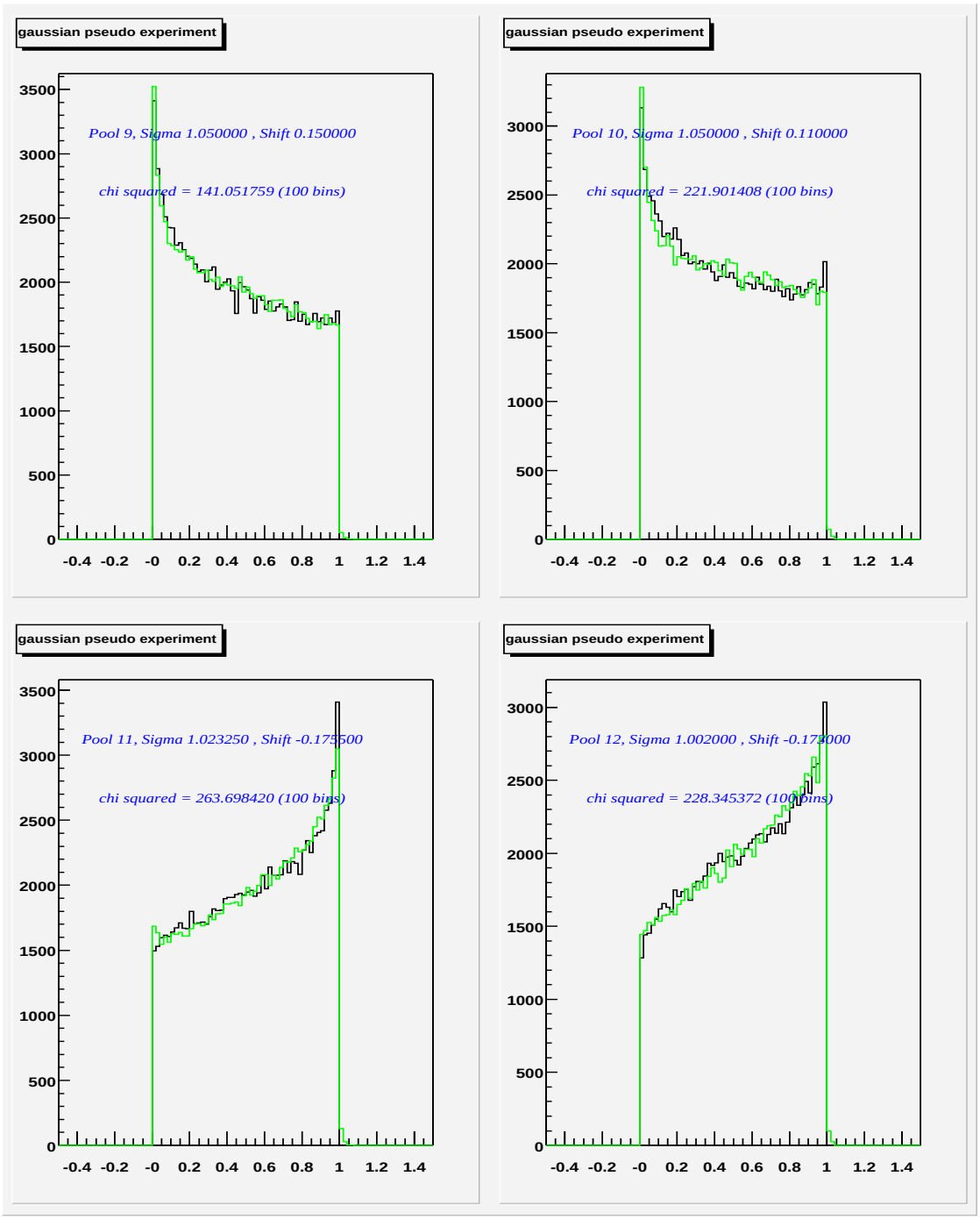

Figure 6.6: Fits to the Monte Carlo are compared with a Gaussian of known shifted parameters to fit for the nature of the non-Gaussian errors from the fit. The slope of the plots is not significant; it is due to the small statistics used in each independent sample. The concavity is significant indicating a shift in sigma such that the prediction function in this analysis underestimates the fit error by a well determined scale factor.

Normalized to number of M^2_{Lb}			
Sample	# Events	# of M^2_{Lb}	Average fit error
Dilepton	25	100	0.45
SVX double	50	100	0.38
SVX single	100	100	0.43
Normalized to fraction of data			
Sample	# Events	# of M^2_{Lb}	Average fit error
Dilepton	7	28	0.87
SVX double	5	10	1.24
SVX single	15	15	1.06
Total	27	53	0.59

Table 6.2: Statistical power of each sample as measured by the uncertainty of the likelihood fit for 10,000 pseudoexperiments. Shown are the cases when samples are normalized to the same number of M^2_{lb} combinations, and when samples are normalized to the number of events within the data. In the SVX double-tagged sample, 1.8 % of the fits failed.

due to smaller backgrounds and the use of a two dimensional fit.

The dilepton sample, with 28 M^2_{l+b} values, provides the most statistical power of the Run I data samples.

Sub-sample	Number of events	Expected background
Dilepton	7	0.76 ± 0.2
SVX double	5	0.2 ± 0.1
SVX single	15	2.4 ± 0.8

Table 6.3: Number of events in data and expected background.

6.2 Results of Measurement

"you've got to ask yourself one question:
Do I feel lucky? *Well, do ya punk?"*
Clint Eastwood

The dilepton data samples were made by running through the inclusive high P_T electron and high P_T muon data sets from Run IA and Run IB using the selection criteria outlined in this note. The SVX lepton+jets data samples were found similarly in both the inclusive high P_T lepton samples and the samples used for the CDF lepton+jets top mass measurement. Run and event numbers were carefully cross-checked for agreement with those used in the published Run I analyses. The data sample sizes and background contribution are shown in Table 6.3.

As a final check of the consistency of the Monte Carlo with data, the distributions were compared using a statistic from the Kolmogorov Smyrnov (KS) test. Since the KS test is generally valid only for high statistics samples, a more thorough analysis was done using pseudo-experiments. 10,000 data-sized pseudo-experiments were created from the $t\bar{t}$ plus normalized backgrounds mixture. For each pseudo-experiment, the KS distance, which is a measure of the integrated total difference between all the

bins between two distributions, was taken between the pseudo-experiment and the parent Monte Carlo distribution. The KS distances for all the pseudo-experiments were binned, and the fraction of all KS distances greater than that produced from the comparison of the data with the Monte Carlo distribution was taken to be the KS probability. This KS probability corresponds to the fraction of data-sized distributions which would produce a KS distance less consistent with the Monte Carlo distribution than the data. This technique was found to be more reliable than the standard analytical approach of calculating the KS probability, and was offered and incorporated into the official version of ROOT [34].

The distributions compared include a selection of pertinent kinematic distributions used in the CDF analysis of kinematic distributions of top decays [35]: leading jet E_T (Figure 6.7), second jet E_T (Figure 6.8), sum of second and third jet E_T (Figure 6.9), and lepton P_T (Figure 6.10). These distributions are shown side by side with the plots extracted from [35]. Both the $t\bar{t}$ and $t\bar{t}$ + background distributions are normalized to the number of events in the data. The Monte Carlo distributions show excellent agreement with those from the top kinematic distributions analysis. The top mass cuts produce 15 SVX single-tagged and 5 SVX double-tagged events, whereas the kinematics distributions analysis uses the 34 SVX tagged event sample. Since the selection criteria used for the top mass analysis are more stringent than those in the top cross-section analysis, the data points are not directly comparable.

Also shown are distributions more pertinent to this analysis for which no comparison to documentation could be found. The SVX single tagged sample is highlighted here because the backgrounds are the largest of the three sub-samples, and because this sub-sample turns out to be the least consistent with that expected from V$-$A $t\bar{t}$ + background Monte Carlo. The distributions include E_T of the b tagged jet (Figure 6.11), angle between the lepton and b jet (Figure 6.12), and 2-D correlation plots of b jet E_T vs. lepton E_T (Figure 6.13), angle vs. b jet E_T (Figure 6.14), and angle vs. lepton P_T

(Figure 6.15).

The distribution with the lowest KS probability, the angle between the lepton and the b jet, shows that the data reflect a smaller angle than that expected in the Monte Carlo distributions. This shape does not indicate a preference for more or less background since the Monte Carlo distributions for $t\bar{t}$ and backgrounds are similar. Since 11% of pseudo-experiments have a higher KS distance, the result is not inconsistent. As a test which encompasses many stages of the analysis process, this distribution was also validated independently by a collaborator and found to be the same. Looking at this distribution in greater detail, one can see from the 2-D plots that the higher E_T b jets and leptons tend to correspond with these smaller angles. Since M^2_{l+b} is dependent on the angle between lepton and b, one might expect that the M^2_{l+b} distribution for the SVX single-tagged sample may be lower than expected from the Monte Carlo, leading to a smaller measured V+A fraction in the data.

The results of the f_{V+A} measurement for the dilepton (Figure 6.16), SVX double-tagged (Figure 6.17), and SVX single-tagged (Figure 6.18) samples are shown along with their data and Monte Carlo distributions. The likelihood curves are presented separately in Figure 6.23, and together in Figure 6.24, both showing the result of the combined fit for f_{V+A}. The results are shown in table 6.4. The average error for each sample is compared to the distribution of errors from pseudo-experiments in Figures 6.19, 6.20, and 6.21, and for the combined set of samples in Figure 6.22.

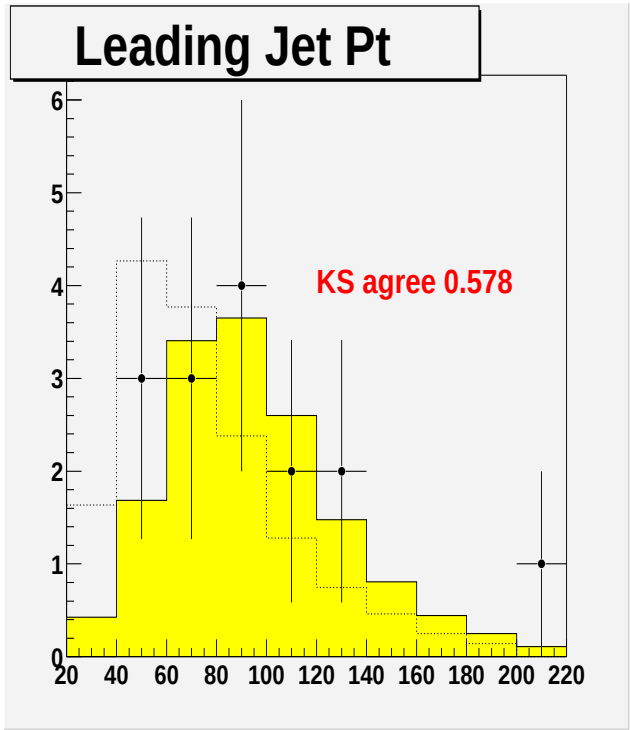

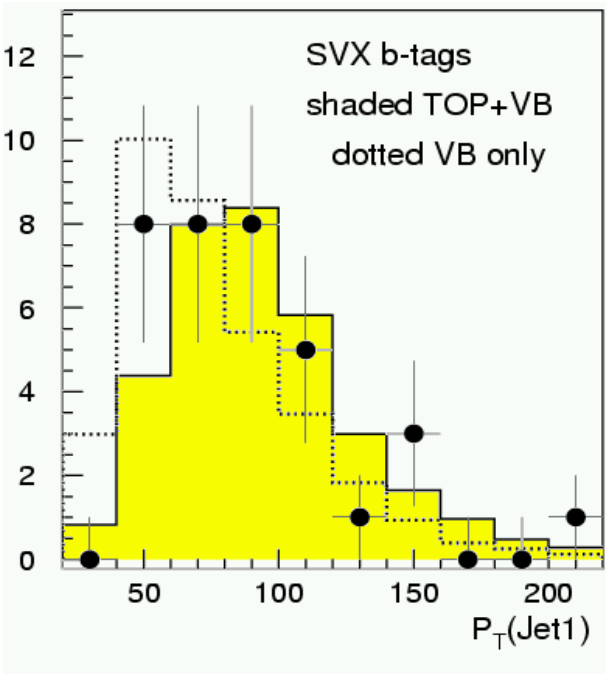

Figure 6.7: This plot shows a comparison of the leading jet E_T between SVX single-tagged data to Monte Carlo with the KS probability, as well as a side by side comparison to the published run I distribution.

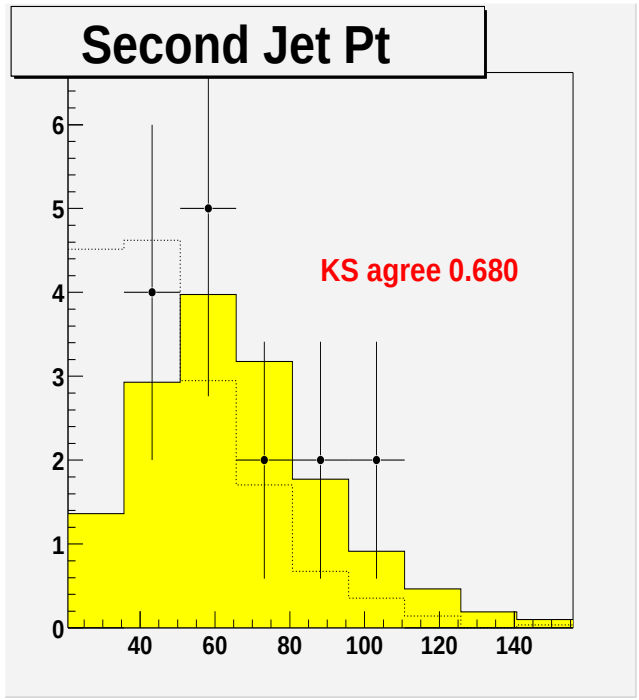

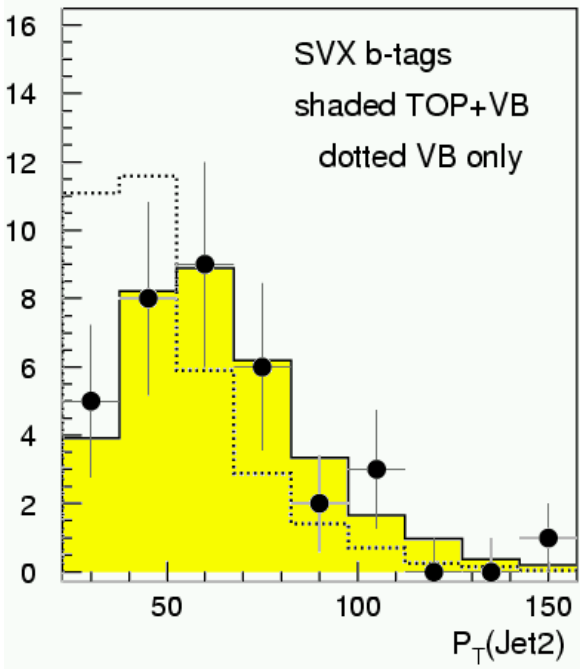

Figure 6.8: This plot shows a comparison of the second leading jet E_T between SVX single-tagged data and Monte Carlo with the KS probability, as well as a side by side comparison to the published run I distribution.

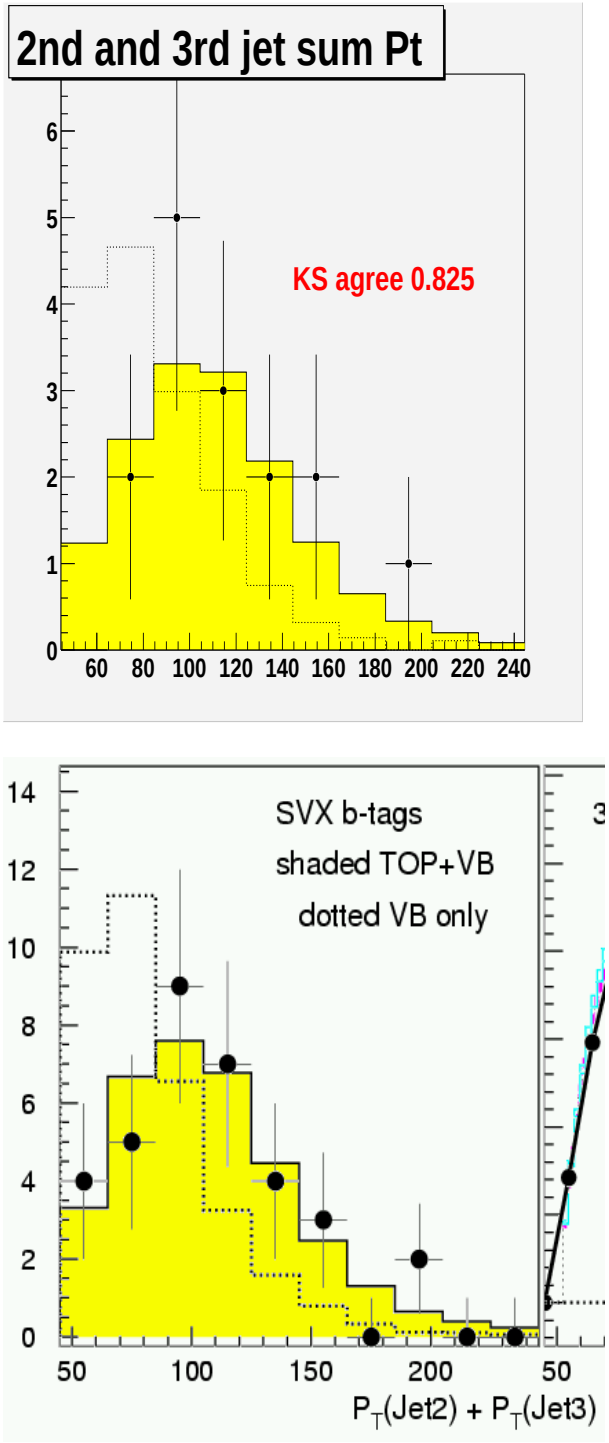

Figure 6.9: This plot shows a comparison of the second and third leading jet sum E_T between SVX single-tagged data and Monte Carlo with the KS probability, as well as a side by side comparison to the published run I distribution.

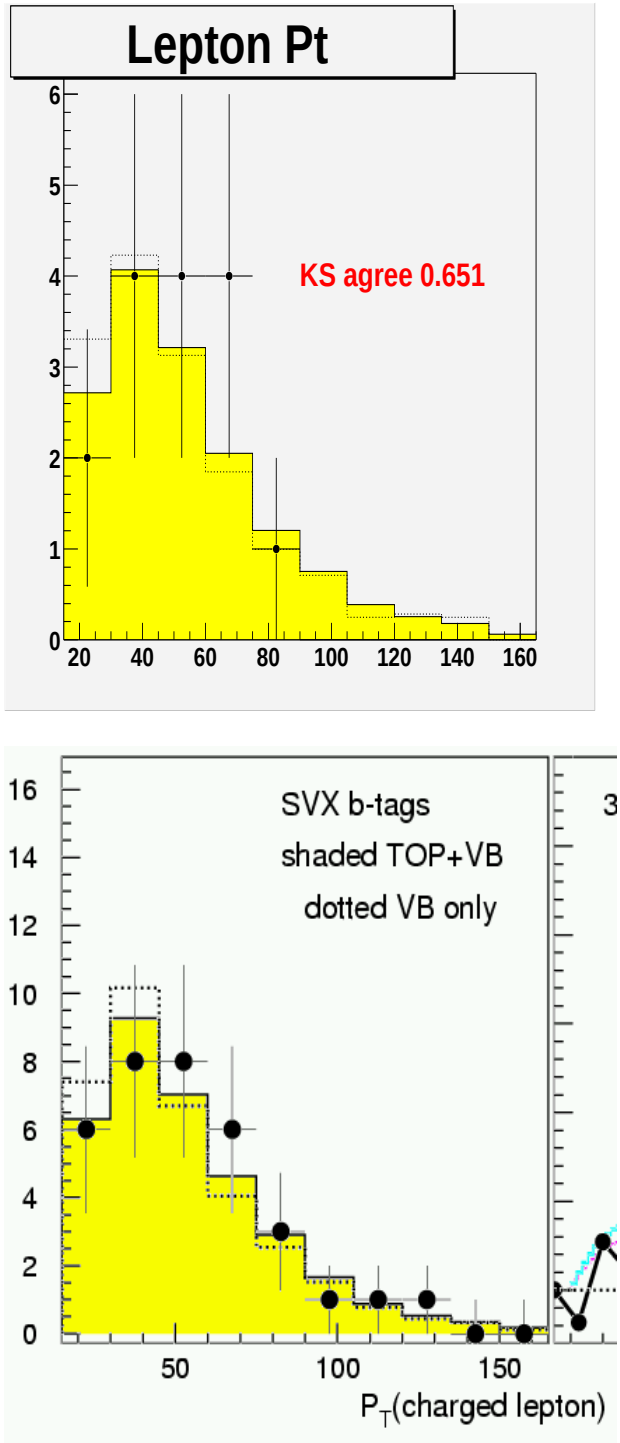

Figure 6.10: This plot shows a comparison of the lepton P_T between SVX single-tagged data and Monte Carlo with the KS probability, as well as a side by side comparison to the published run I distribution.

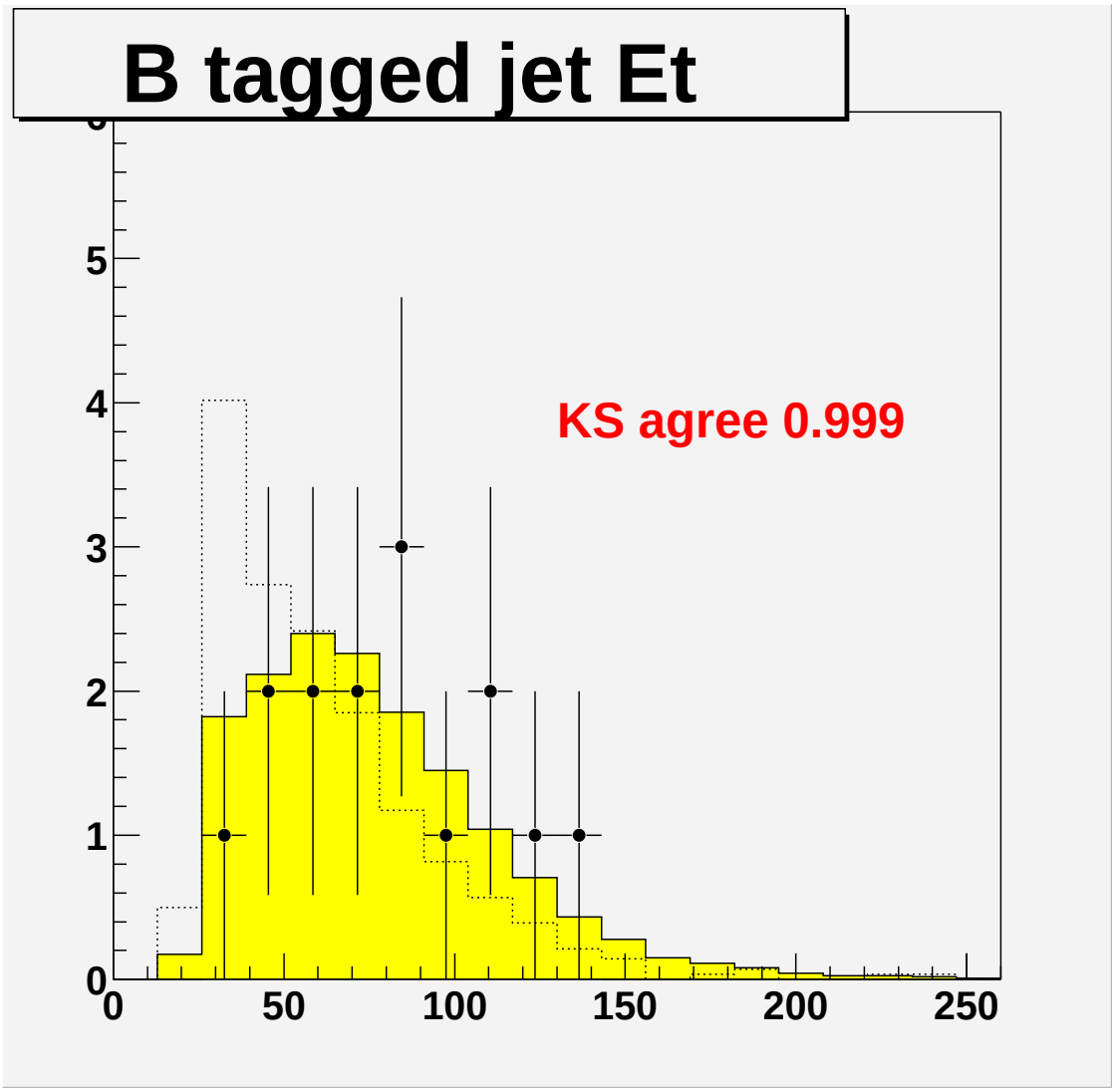

Figure 6.11: This plot shows a comparison of the b tagged jet E_T between SVX single-tagged data and Monte Carlo with the KS probability.

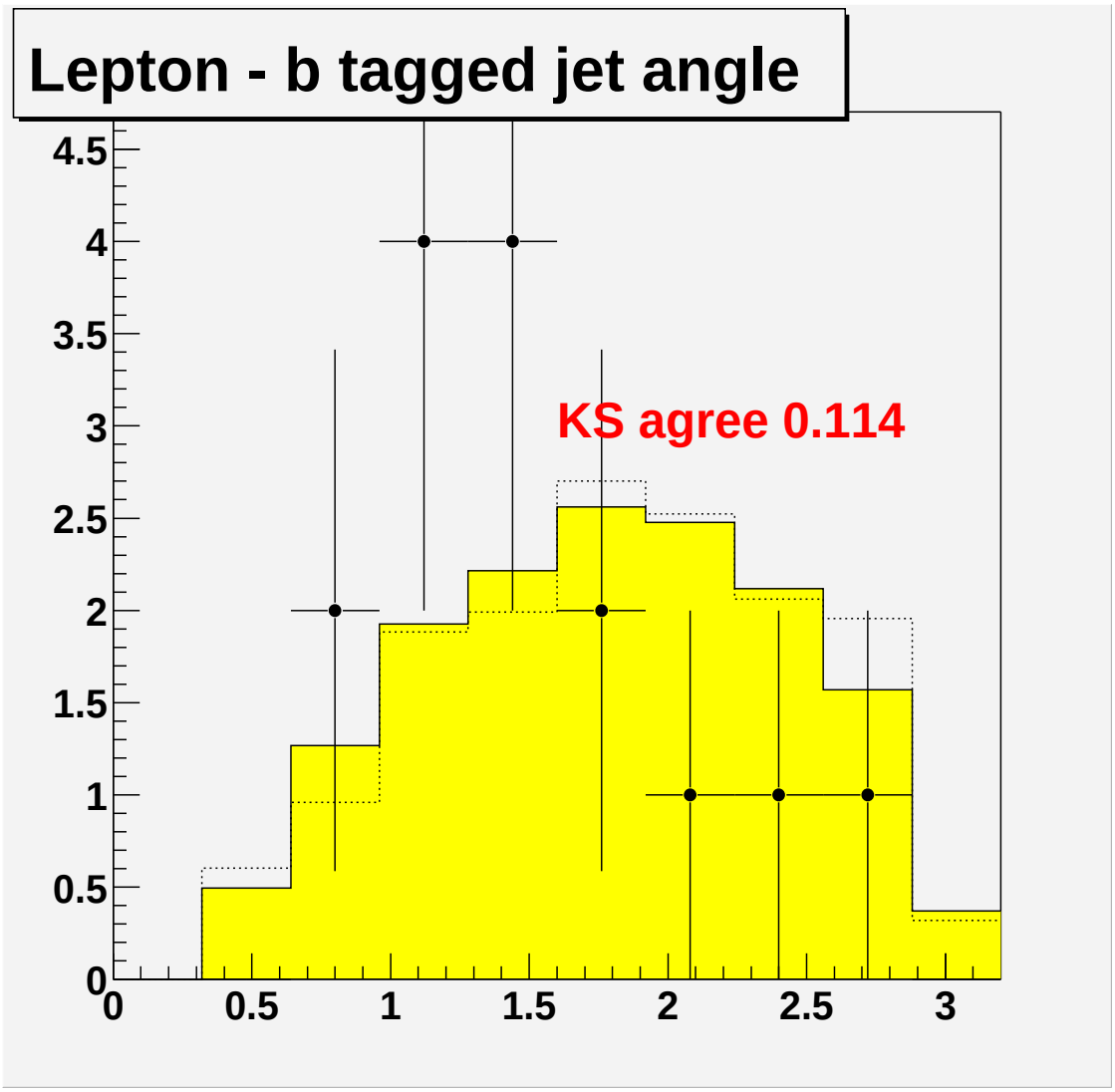

Figure 6.12: This plot shows a comparison of the lepton-b tagged jet angle between SVX single-tagged data and Monte Carlo with the KS probability.

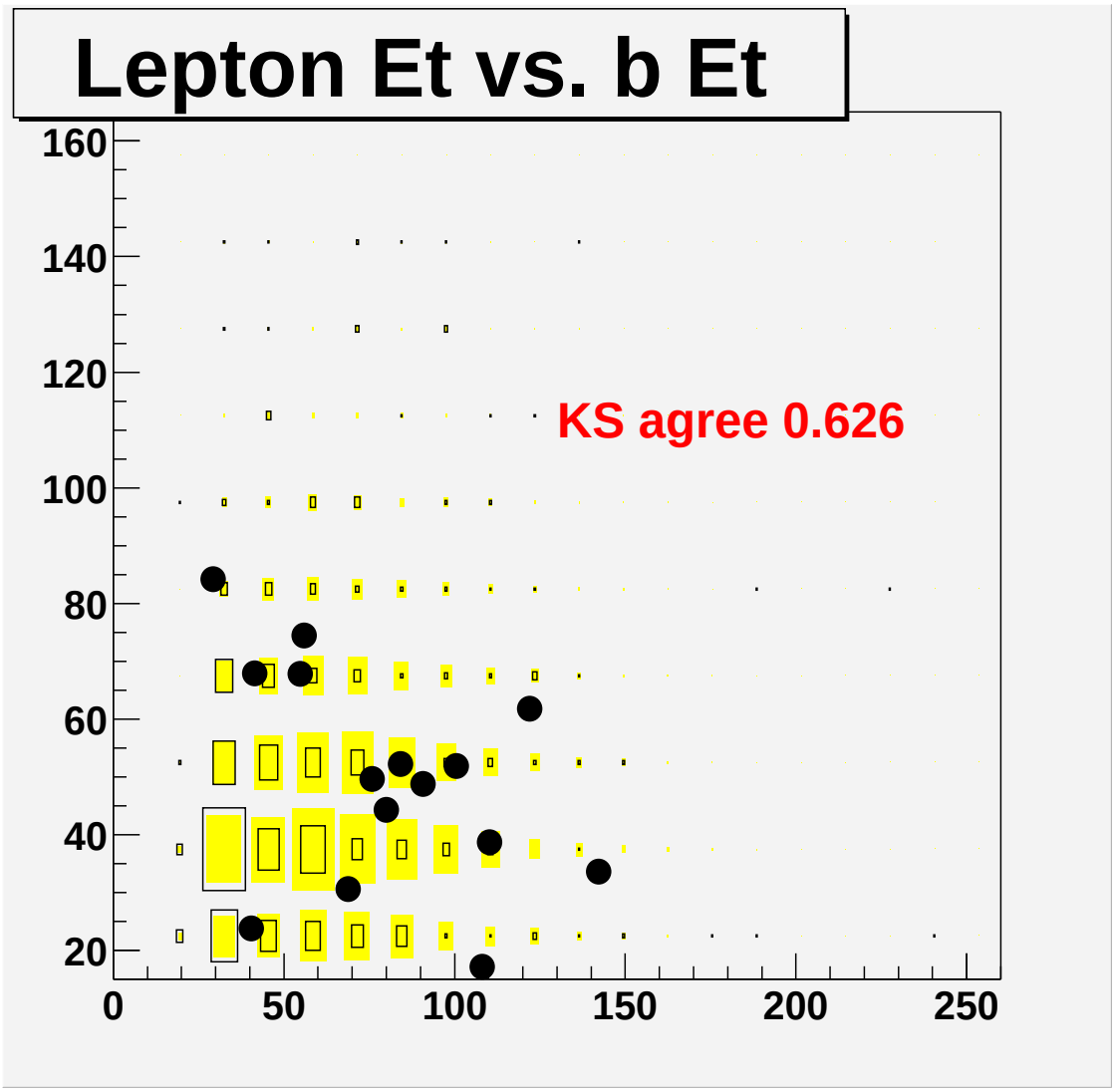

Figure 6.13: This plot shows a 2D comparison of the b tagged jet E_T vs. lepton E_T between SVX single-tagged data and Monte Carlo with the KS probability.

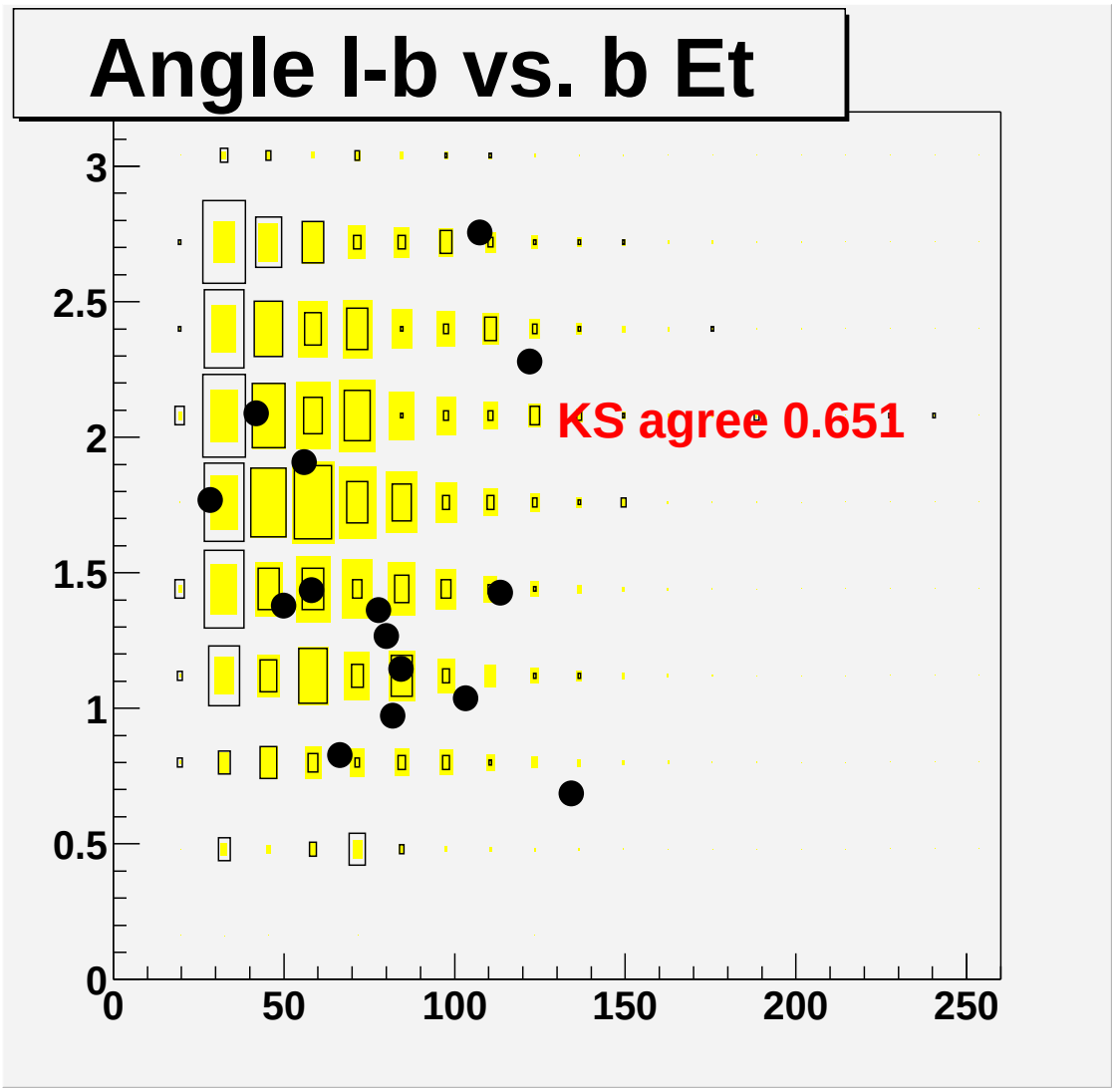

Figure 6.14: This plot shows a 2D comparison of the lepton-b tagged jet angle vs. b jet E_T between SVX single-tagged data and Monte Carlo with the KS probability.

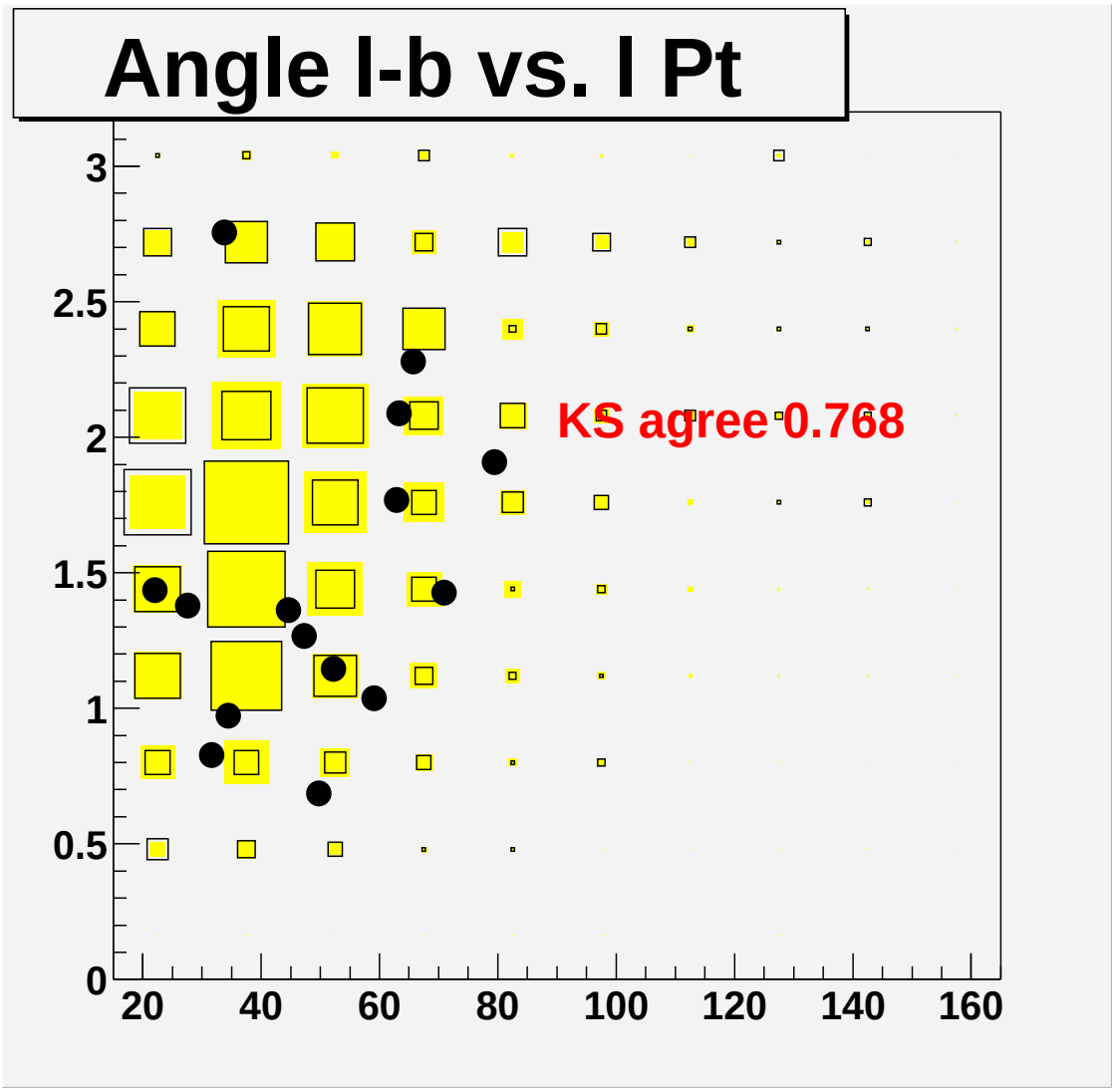

Figure 6.15: This plot shows a 2D comparison of the lepton-b tagged jet angle vs. lepton E_T between SVX single-tagged data and Monte Carlo with the KS probability.

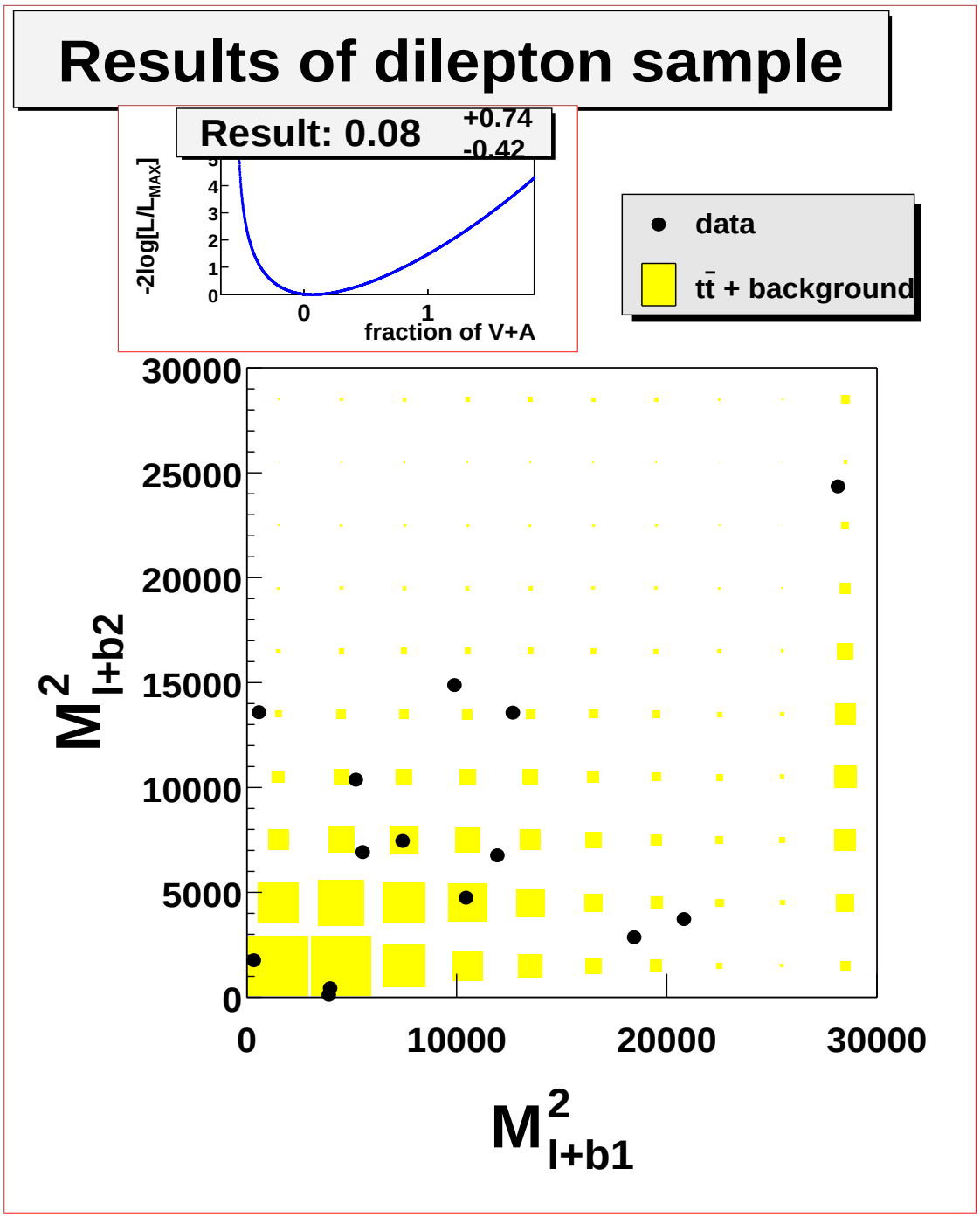

Figure 6.16: Data and Monte Carlo distributions for dilepton sample with fit value of f_{V+A}.

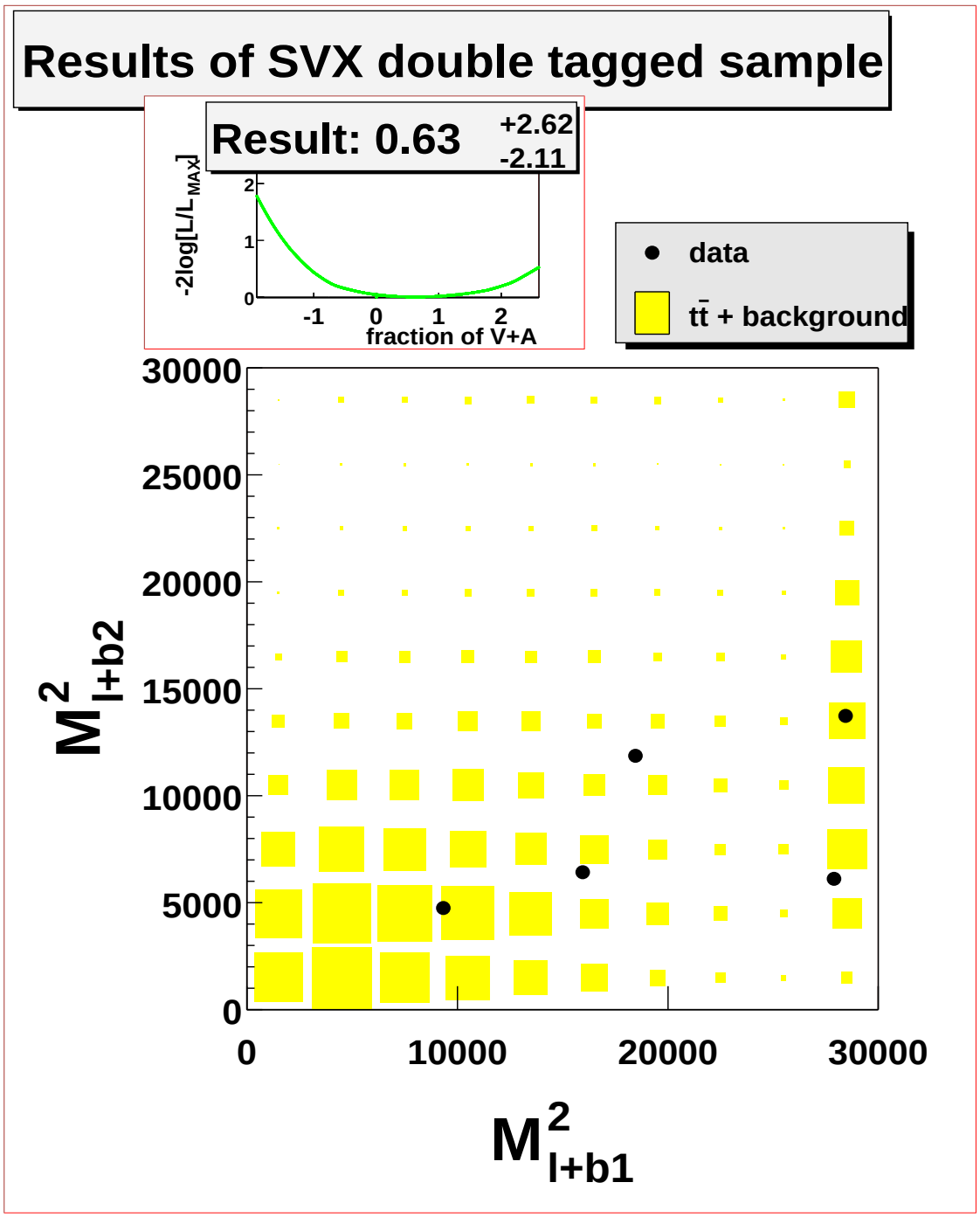

Figure 6.17: Data and Monte Carlo distributions for SVX double-tagged sample with fit value of f_{V+A}.

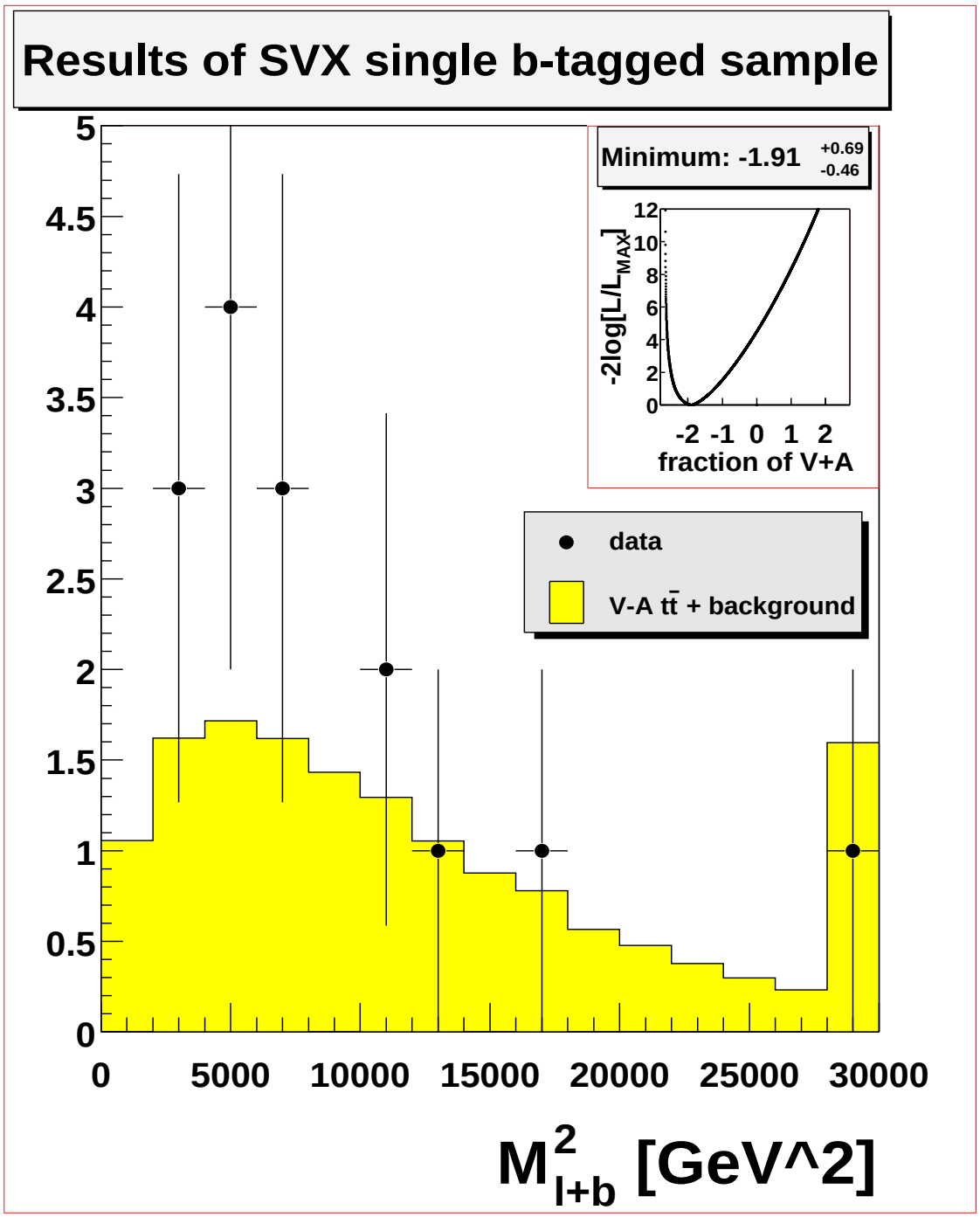

Figure 6.18: Data and Monte Carlo distributions for SVX single-tagged sample with fit value of f_{V+A}.

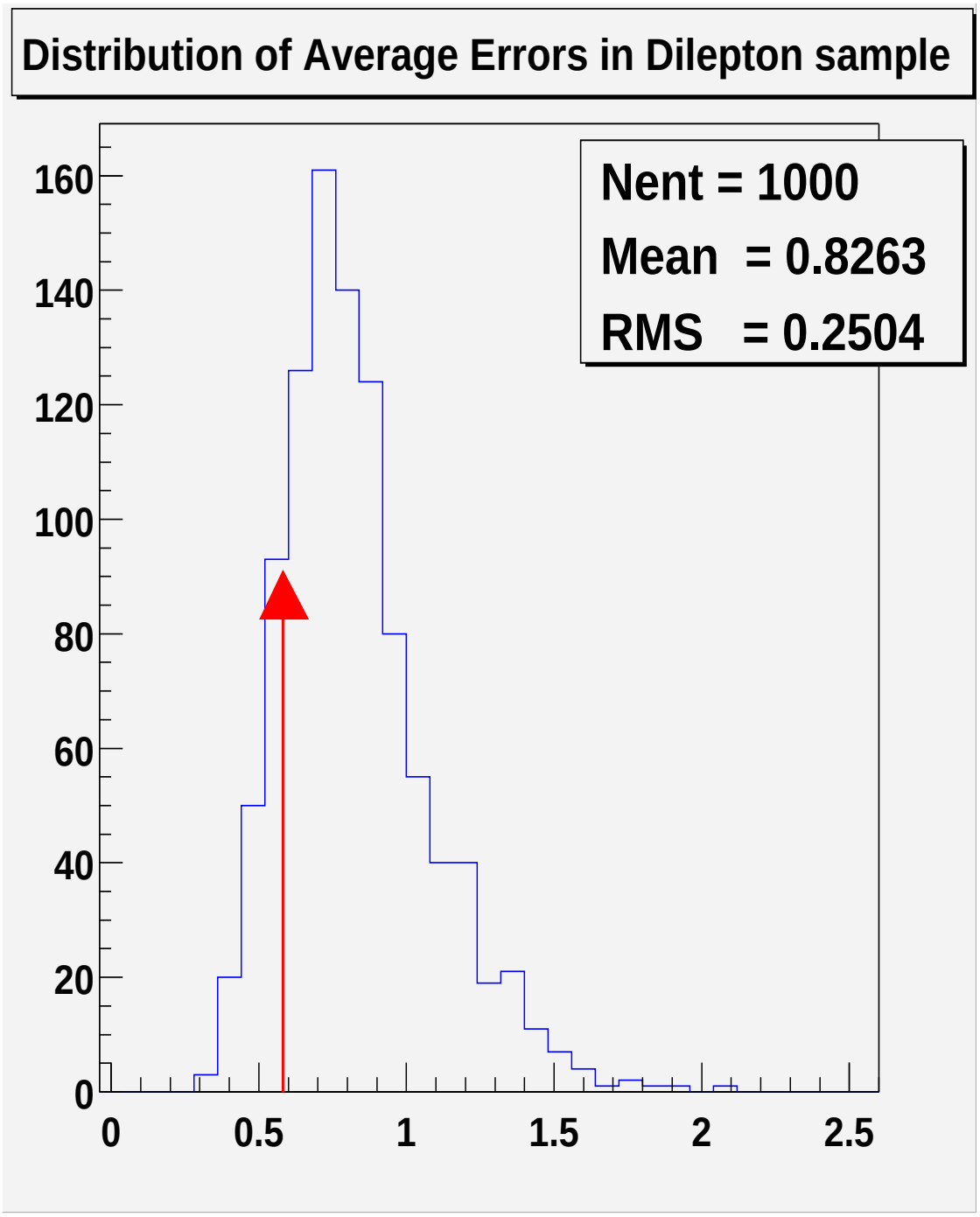

Figure 6.19: Distribution of errors from pseudo-experiments for the dilepton sample, shown with the error from the data marked with an arrow.

Sample	Measurement
dilepton	$0.08^{+0.74}_{-0.42}$
SVX double tagged	$0.63^{+2.62}_{-2.11}$
SVX single-tagged	$-1.92^{+0.69}_{-0.48}$
combined	$-0.21^{+0.41}_{-0.23}$
combined with non-gaussian correction	$-0.21^{+0.42}_{-0.24}$

Table 6.4: The results for each sample, with the combined results. Errors shown are statistical only.

It is clear that the likelihood shape, although asymmetric, is well-formed throughout the physically allowed region, and for at least eight units of log likelihood on either side of the minimum.

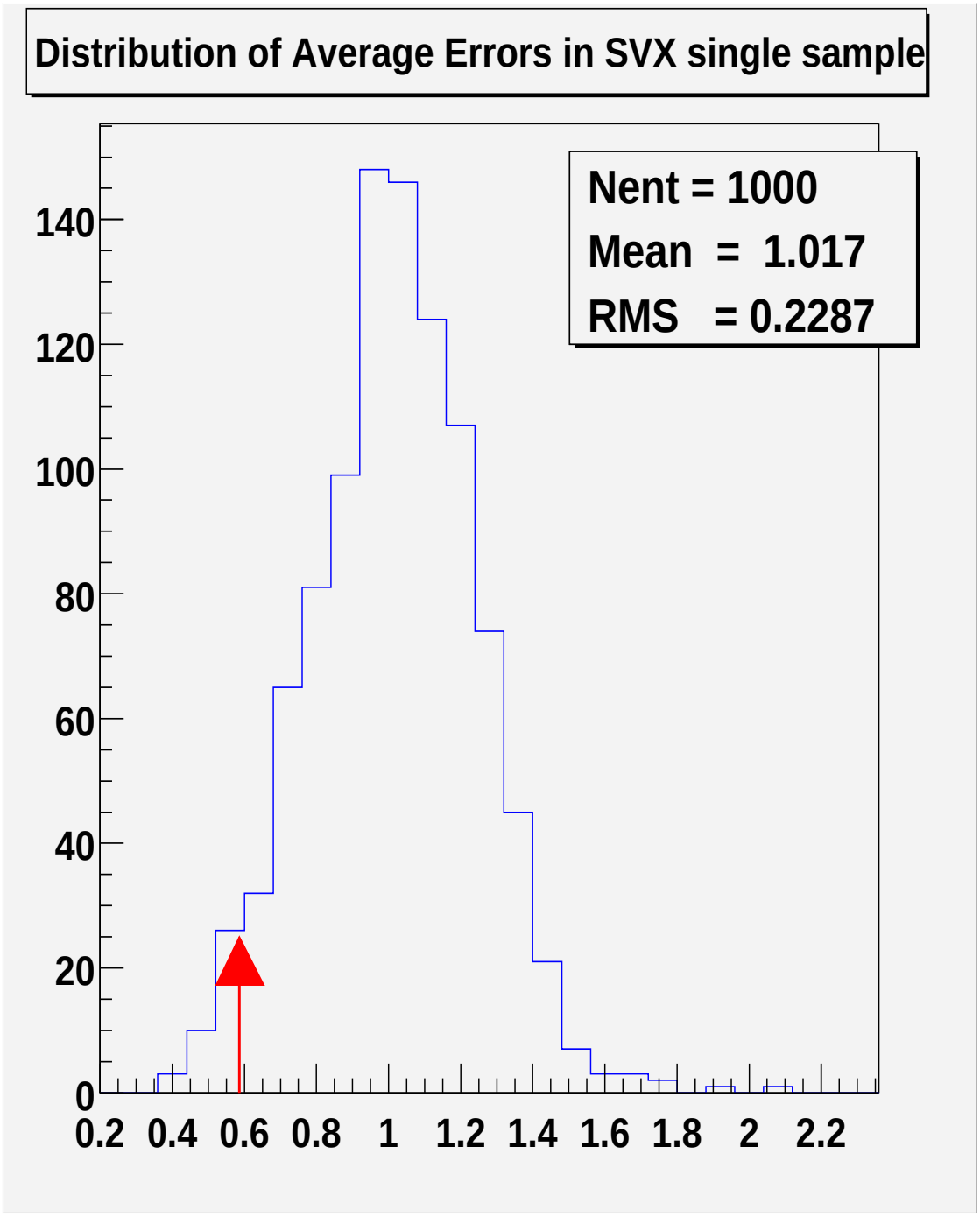

Figure 6.20: Distribution of errors from pseudo-experiments for the SVX single-tagged sample, shown with the error from the data marked with an arrow.

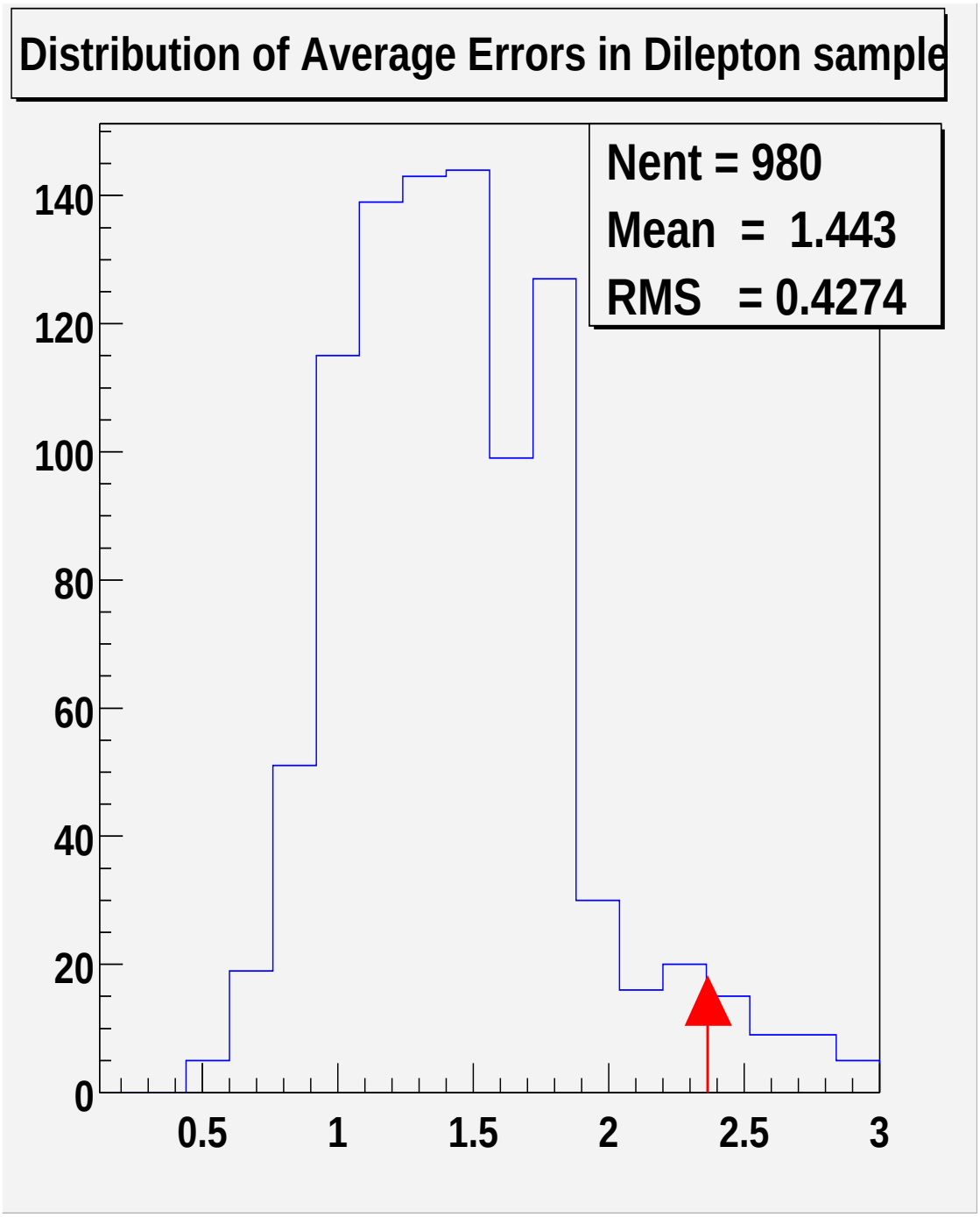

Figure 6.21: Distribution of errors from pseudo-experiments for the SVX double-tagged sample, shown with the error from the data marked with an arrow.

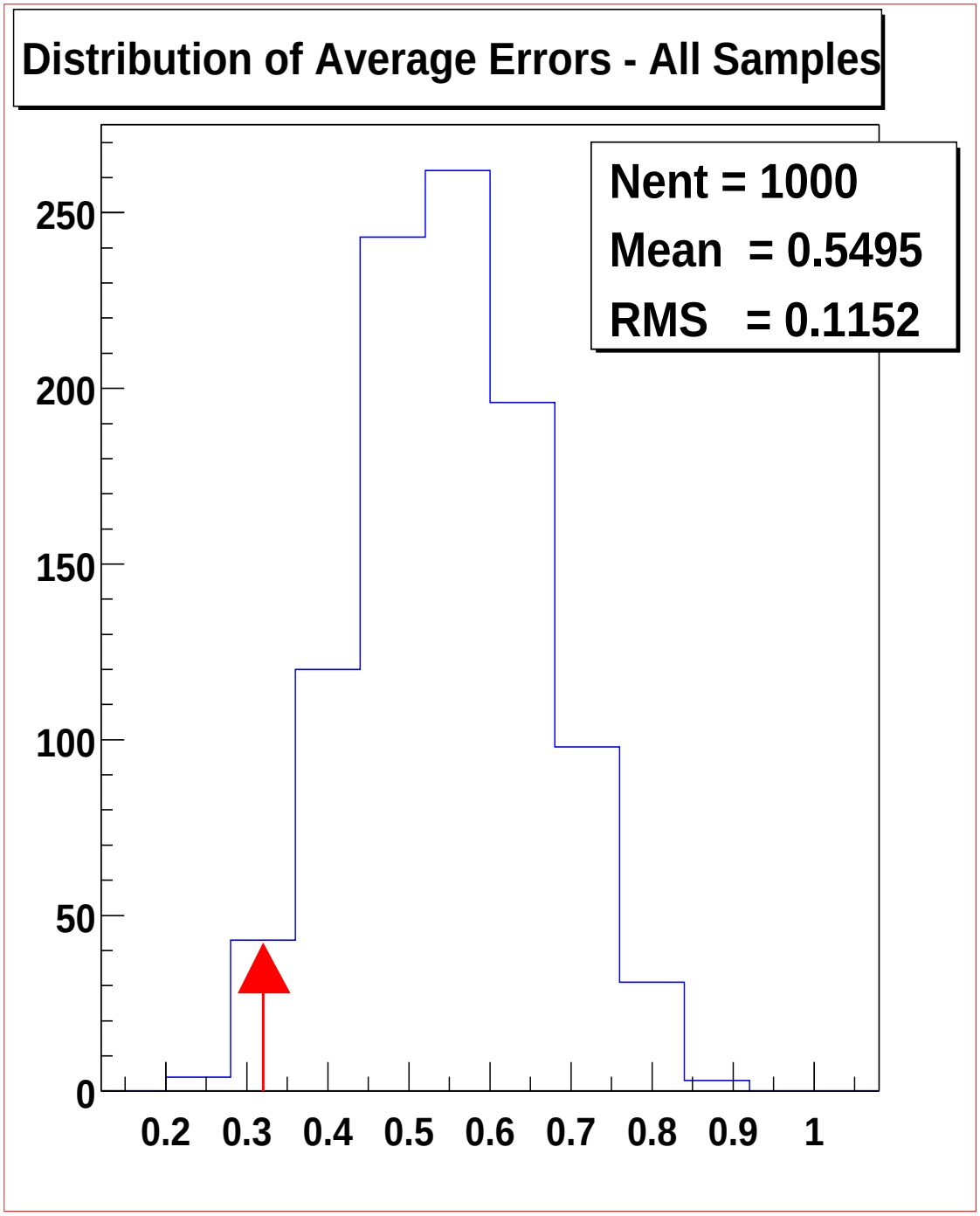

Figure 6.22: Distribution of errors from pseudo-experiments for all the samples, shown with the error from the data marked with an arrow.

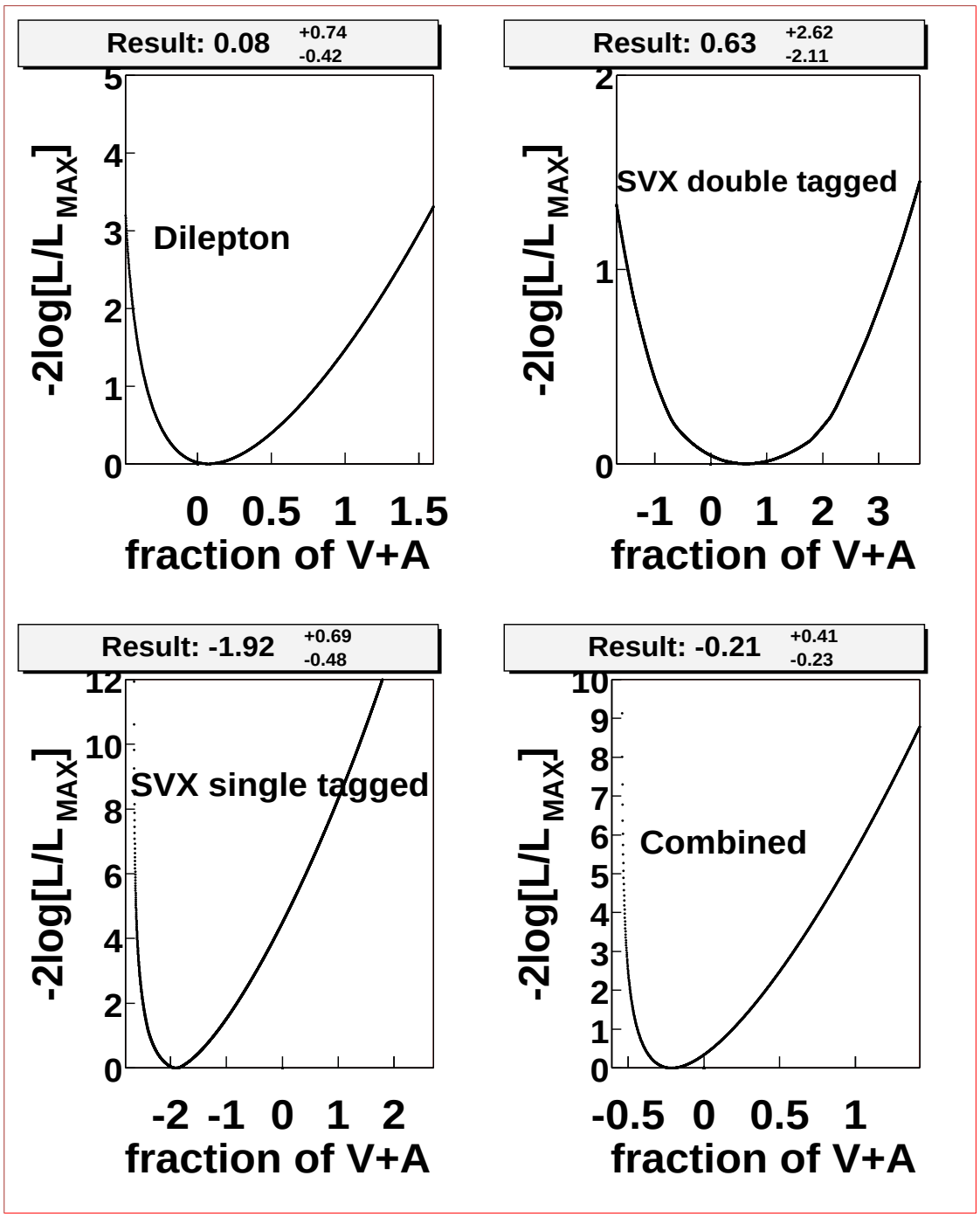

Figure 6.23: The log likelihood minima for each sample and the combined minimum shown separately.

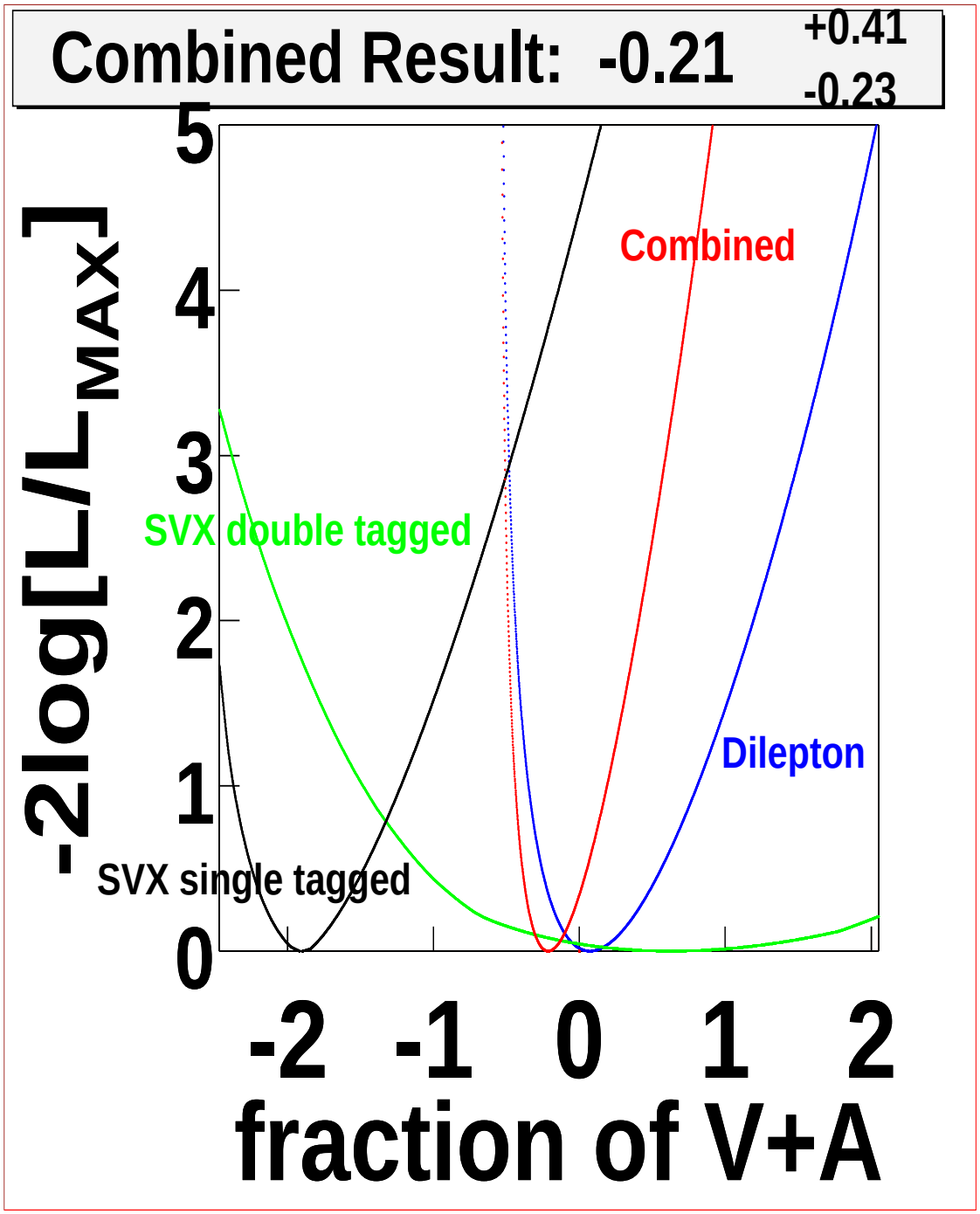

Figure 6.24: The log likelihood minima for each sample and the combined minimum shown overlayed.

Chapter 7

Systematic Uncertainties

Systematic uncertainties indicate by how much the measurement would be different from the expected value if the input assumptions were allowed to fluctuate within their uncertainties. In this analysis, this is calculated by measuring the f_{V+A} parameter for sets of events in which an assumption of the analysis has been altered within its uncertainty at the one sigma level. The mean change in the measurement of f_{V+A} in pseudo-experiments (Section 6.1.1) between the default assumptions and the altered assumptions is determined to be the systematic uncertainty due to the given effect.

7.1 Top Mass Uncertainty

The top mass has great bearing on precision electroweak tests of the standard model, and its precise measurement is the cornerstone of the prediction of a light Higgs boson from the electroweak data [28]. An accurate measurement of the top mass is being enthusiastically sought after in the Run II physics program at CDF and $D\emptyset$.

In addition to increasing the energies of the top decay products and therefore M^2_{l+b}, a higher top mass also increases the true value of f_0, the fraction of Ws that have a

Top mass uncertainty	shift
5 GeV shift	0.21
Jet energy dependent (2.4 GeV)	0.10
Jet energy independent (4.5 GeV)	0.19

Table 7.1: The systematic shift of measurement due to changes in the top mass. "Dependent" refers to the part of a shift in top mass which is correlated to the CDF jet energy scale. "Independent" refers to all other uncertainties in the top mass including statistical uncertainty, and for instance, the $D\emptyset$ jet energy scale. [29]

longitudinal polarization distribution. Although this is not a large effect, an increase in f_0 means that there is a smaller percentage of events which have left-handed (or right-handed) distributions, effectively decreasing the pool of significant events which the fitter uses to extract the V+A fraction.

To evaluate these effects, first the total uncertainty in f_{V+A} due to a top mass shift of 5 GeV is considered by measuring f_{V+A} using standard templates, but with pseudo-experiments generated with a top mass at 180 GeV. Then the CDF jet-energy dependent and CDF jet-energy independent components of the world top mass uncertainty (see Section 7.3) are used to calculate the relative shift of f_{V+A} for each component.

7.2 Jet Energy Scale Uncertainties

By calculating M^2_{l+b} of b jets and leptons, this analysis is able to infer the $cos\psi^\star_l$ distribution. However, since $M^2_{l+b} \sim (E_l * E_b - |E_l| * |E_b| \cdot cos\psi^{lab}_l)$, there is clearly a strong dependence on the jet energy scale. Each of the jet corrections applied to the energy scale of the b jet has an associated uncertainty.

Correction	Systematic Uncertainty
Absolute Jet Energy (includes primary vertex UE)	≈2.5%
Calorimeter Stability	1.0%
Underlying Event (multiple vertexes)	100 MeV/vertex
Relative Jet Energy	0.2-4% of f_{rel}
Soft Gluon (dR 0.4 to 1.0)	6-1.4%
Splash-out beyond dR>1.0	1 GeV

Table 7.2: Approximate size of uncertainties in jet energy corrections.

If the jet energy scale applied in the correction was too high, this would lead to a higher mean M^2_{l+b} value, and would shift the measurement toward V+A, since V+A events have a higher mean M^2_{l+b} value.

A summary of the relative size of each uncertainty in the jet energy scale is noted in Table 7.2, and is discussed in more detail in [22]. Each source of systematic error in jet scale is considered independently. The 4-vectors of all jets in the events are shifted or scaled up and down according to the uncertainty of one particular jet correction. The up and down systematic shifts for each correction are then averaged and then all combined in quadrature to obtain the complete systematic due to all jet energy scale uncertainties.

7.2.1 Relative Jet Energy Scale

The relative jet energy scale correction accounts for the different detector response as a function of η as compared to the central region where jets are best measured 0.2< $|\eta|$ <0.7. The varying corrections take into account features of the detector such as

$\|\eta\|$ interval	% Uncertainty on Relative Correction
0.0 - 0.1	2%
0.1 - 1.0	0.2%
1.0 - 1.4	4%
1.4 - 2.2	0.2%
2.2 - 2.6	4%

Table 7.3: The percentage of the relative jet energy correction uncertainty for various ranges of $|\eta|$.

cracks where there is no calorimeter coverage. The uncertainty ranges from 0.2% to 4% of the actual correction factor (Table 7.3).

7.2.2 Underlying Event and Multiple Interactions

The underlying event correction corrects the event for extra energy due to the remnant pieces of the $p\bar{p}$ not involved in the hard process, and also corrects for multiple interactions in the same beam crossing. It has a correction for the primary vertex and one for each additional vertex to take into account the multiple interactions. The primary vertex uncertainty is approximately 30% of itself, while multiple interactions have an uncertainty of 100 MeV per vertex.

7.2.3 Soft Gluon and Splash-Out

Energy outside of the jet cone due to differences between the fragmentation modeling of Monte Carlo and data is considered in two parts. Soft gluon radiation is the energy between the jet of cone 0.4 used in top analyses and the larger cone of 1.0 surrounding it. An additional splash-out correction is applied for jet energy outside a cone of 1.0. These uncertainties are taken into account separately.

7.2.4 Absolute Jet Energy Scale

The uncertainty has two components: detector response, including uncertainty in the calorimeter calibration and its stability, and fragmentation effects, which have an uncertainty due to particle detection efficiency and relative response. To relate the energy of the initial parton with the energy of the observable jet, an absolute jet energy scale correction is applied. Electron and pion test beam data from various energies was used to tune the CDF simulation to reproduce the particle response in the calorimeter. This test beam data, combined with isolated pion data in minimum bias events, was used to determine the detector response.

7.3 Jet Energy Scale and Top Mass Correlation

A complication with the jet energy is that it is the dominant source of systematic uncertainty in the CDF top mass measurement. Since the measured top mass is an input parameter in this analysis, and only CDF and $D\emptyset$ have measured the top mass directly, both effects must be taken into account when determining systematic uncertainties in these quantities.

If the CDF jet energy scale was high, the measured top mass would also be high, meaning that the true top mass is lower than what was measured. A systematically shifted up jet energy scale results in a higher measurement of f_{V+A}. However, this high jet energy scale would have also meant that the CDF-measured top mass would be too high, meaning the real top mass is lower. If the top mass is lower, it would result in a lower measurement of V+A. Therefore these two effects are anti-correlated.

It is therefore important to determination the correlation between the jet energy scale systematic and that of the top mass. The uncertainty on the top mass is divided into two parts: one which is from the CDF jet energy scale uncertainty, and one which is all other

Type	shift
Detector response	0.04
Underlying event	0.01
Relative correction	0.03
Absolute correction	0.09
Soft gluon radiation	0.07
Out of cone correction	0.07
Total	0.14
With top mass correlation	0.04

Table 7.4: The systematic shift of measurement due to uncertainty in jet energy scale from various effects of detector energy repsonse and jet energy corrections.

systematic and statistical sources of error (Table 7.1). The jet energy systematic is then determined by adding the positive shift of f_{V+A} from the increased jet energy scale with the negative shift due to the mismeasurement of the top mass.

The $D\emptyset$ and CDF combined top mass measurement [29] was used to get the correlation between the CDF jet energy scale and the world top mass average. For each of the channels: CDF dilepton, CDF lepton+jets, CDF all-hadronic, $D\emptyset$ dilepton, $D\emptyset$ lepton+jets, the effect of a 1-sigma change in the CDF jet energy scale uncertainty was calculated. This contribution (2.4 GeV) can then be considered separately from all other errors (4.5 GeV).

The effect of the jet energy scale systematic uncertainties on the measurement of f_{V+A} is shown in Table 7.4.

The positive (negative) shift results are then combined to form an overall positive (negative) shift of the measurement. As is expected, if the jet energy scale is higher than was calculated, the true V+A fraction must be smaller than is nominally measured.

Background type	Shift
Dilepton	
WW	-0.016
$Z->\tau\tau$	-0.022
Fake lepton	-0.024
SVX double tagged	
W+jets	-0.006
SVX single tagged	
W/Z and non W/Z	-0.027
Total	0.045

Table 7.5: The systematic shift of measurement due to fluctuating background statistics.

7.4 Background Shape and Normalization

The amount of background within a pseudo-experiment is set to be higher or lower (according to its uncertainty) than that in the prediction function. The shift of the measurement is taken to be the systematic error due to fluctuations in the background normalization (Table 7.5).

The background shape uncertainty is also taken into account. For the dilepton sample, nominal templates of the backgrounds are compared to pseudo-experiments where all the background is assumed to be of one type (i.e., all $Z \rightarrow \tau^+\tau-$). The largest shift is determined to be the systematic uncertainty due to the background shape for the dilepton sample [21].

For the single-tagged lepton plus jets sample, pseudo-experiments using W+jets Monte Carlo with $Q^2 = M_W^2$ are compared with templates using $Q^2 = P_T^2$ [22]. This different q^2 scale changes the gluon emission in the Monte Carlo leading to different

Background type	shift
Dilepton sample	
All WW	-0.028
All $Z->\tau\tau$	0.005
All W+j w/ fake	0.047
SVX single tagged	
W+jets $Q^2 = m_W^2$	0.03
Total	0.06

Table 7.6: The systematic shift of measurement due to changing background shapes.

E_t and jet multiplicity distributions. The background shape uncertainties are shown in Table 7.6.

7.5 PDF Uncertainty

The probability for producing $t\bar{t}$ pairs is dependent on which initial partons interact, the momentum transferred between them (Q^2), and whether the fraction of the total proton and anti-proton momentum they are carrying, $x = P_z/E_{beam}$, is enough to create the massive $t\bar{t}$ state. At high x, the proton consists mainly of its three valence quarks, although there are small contributions from gluons and sea quarks, mainly $u\bar{u}$, and $d\bar{d}$ (Figure 7.1).

The contributions of these partons ($u, \bar{u}, d, \bar{d}, s, c, b, g$) are modeled at a given x by parton distribution functions, $F(x, Q^2)$. These functions are determined experimentally, mainly from deep inelastic scattering experiments, and the results are parameterized by various models, with slight differences between their shapes. Since these functions are

input to the Monte Carlo used to simulate $t\bar{t}$ events, the uncertainty in f_{V+A} due to the effect of using different parton distribution functions (PDF) needs to be considered. The x distributions for initial partons in $t\bar{t}$ production for events passing the top dilepton selection criteria are shown in Figure 7.2 for selected PDFs. Since there is open debate about whether it is appropriate to use Leading Order (LO) structure functions with parton showering Monte Carlo like Herwig, an assortment of LO structure functions are considered as well as the more appropriate Next-to-Leading-Log (NLL) structure functions.

The systematic uncertainty due to structure function modeling is evaluated by reweighting the Monte Carlo according to the probability distributions of different models as a function of x. The PDF's called LO CTEQ5L [30] and NLL $M\overline{S}$ MRS d0' [31] provide a diverse span of systematic difference from the MRSG PDF used in the MC. NLL $M\overline{S}$ MRST h-g is chosen as the mid-range default structure function for this analysis. The systematic shifts of the measurement for each structure function is shown in Table 7.7.

7.6 B Tag Systematic

Although the E_T distribution for b jets is not different for V+A and V−A, it is important to determine if the SVX tagging efficiency has any effect on the measurement.

For top analyses, the SVX b tagging efficiency was assumed to be flat as a function of jet E_T. Using CTC tracking studies, the variation from this assumption was measured. In Figure 7.3 the scale factor relating b tagging in Monte Carlo to data is shown with statistical and systematic uncertainties [32]. The systematic uncertainties are determined by varying the track quality variable, Q, which is a measure of the hit density in the area immediately surrounding the track. By assuming a one standard deviation stronger Q dependence than for the standard CTC tracking efficiency, an E_T dependent scale factor is determined. This scale factor is used to weight the Monte Carlo distributions

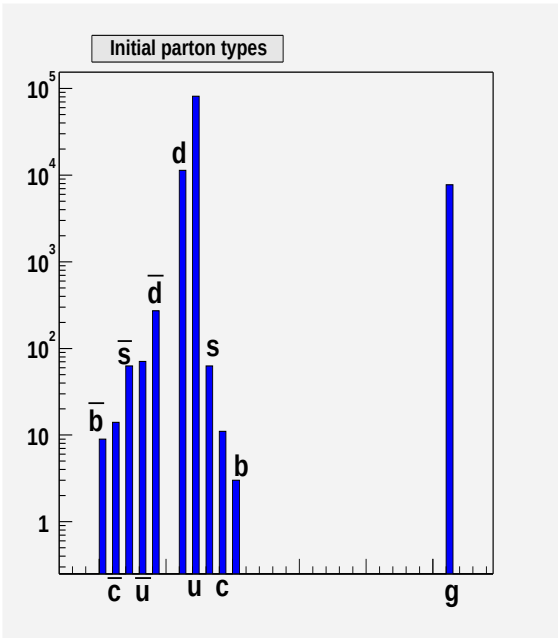

Figure 7.1: Relative contribution of partons from the proton in $t\bar{t}$ production .

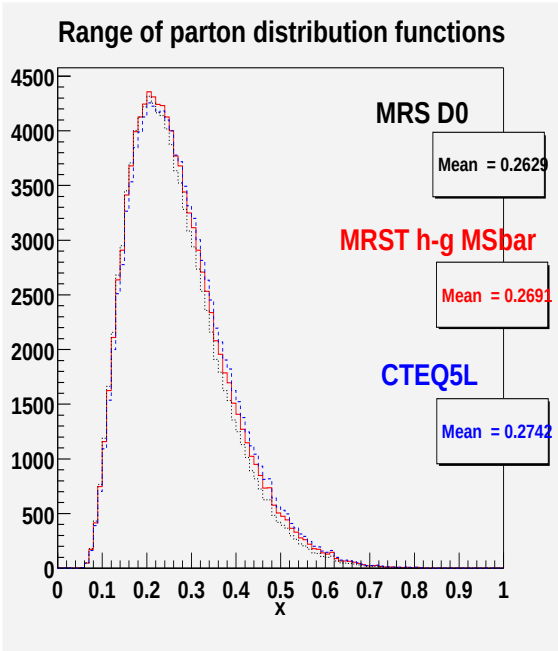

Figure 7.2: Distribution in x of $t\bar{t}$ events passing cuts. Two PDFs are chosen which span the most difference in x around the default NLL MRST h-g PDF.

PDF type	shift
LO	
CTEQ4L	0.018
CTEQ5L	0.038
MRST h-g	0.039
MRST c-g	0.037
NLL, $\overline{MS}$	
CTEQ4M	-0.001
CTEQ5M	0.010
MRS d0'	-0.005
MRST h-g	0.020
MRST c-g	0.020
Using MRST h-g NLL	
Maximum uncertainty	0.02

Table 7.7: The systematic shift of measurement due to different PDFs in comparison with MRSG.

according to the E_T of the tagged b jets. The effect of this is found by comparing the shift of f_{V+A} when pseudo-experiments with weighted events are fit to the nominal templates.

7.7 Hard Gluon Radiation

Hard gluon radiation effects enter into this analysis in two ways. Initial state radiation occurs before the $t\bar{t}$ state is produced and is therefore uncorrelated with any $t\bar{t}$ decay products. There is a small probability, mainly in the dilepton case which does not require a b tag, that a high P_T initial state gluon could have enough energy to be mistaken for the b jet. Hard final state radiation can cause the direction and energy of the b jet to be mismeasured, or to be identified as the b jet.

Traditional top analyses have estimated the effect of ISR uncertainties by making altered $t\bar{t}$ samples using Pythia Monte Carlo with the ISR option turned off. FSR is evaluated similarly by using ISR off and requiring jet matching so that all jets can be related to their parent partons. These altered samples are analyzed with the standard analysis, and a systematic uncertainty is determined from half the difference of each in terms of the measurement.

In this analysis, a new approach is used which does not simply turn off radiation in the Monte Carlo. Instead, since ISR/FSR jets originate from within the Monte Carlo itself, one can attempt to flag these events by examining the generator-level information.

Initial state radiation tends to be along the beam axis in each hemisphere of the detector. One can loop through the generator level banks, find all unique gluons emitted from the initial state that are fiducial in eta, and sum up the P_T in each hemisphere. If the P_T in an individual hemisphere is above 8 GeV, the event is flagged as having hard ISR content, and may cause a misinterpretation of the event such as being identified as a b jet (Figure 7.4).

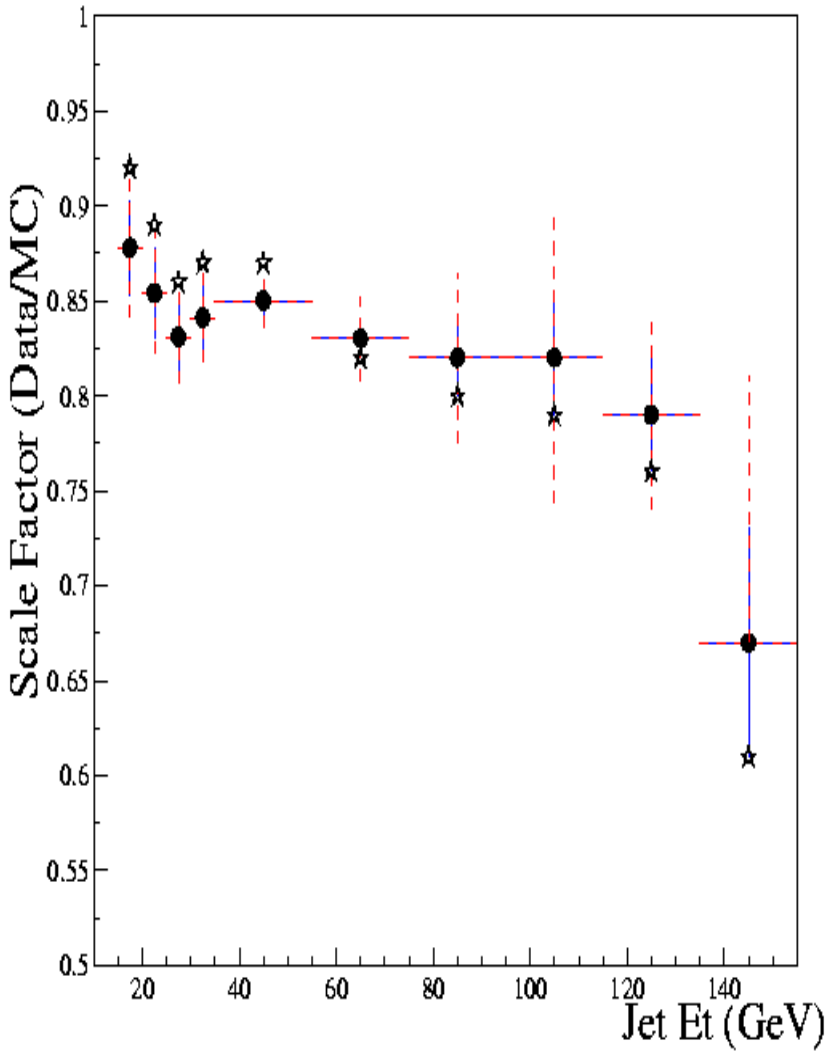

Figure 7.3: The SVX b tagging scale factor (data / Monte Carlo) as a function of jet E_T. The systematic uncertainty comes from assuming no Q dependence and a one standard deviation stronger Q dependence in the CTC tracking efficiency. The stars represent the deviation by assuming a one standard deviation stronger Q dependence in the CTC tracking efficiency, and were used to weight the Monte Carlo according to their jet E_T to evaluate the b tagging bias systematic.

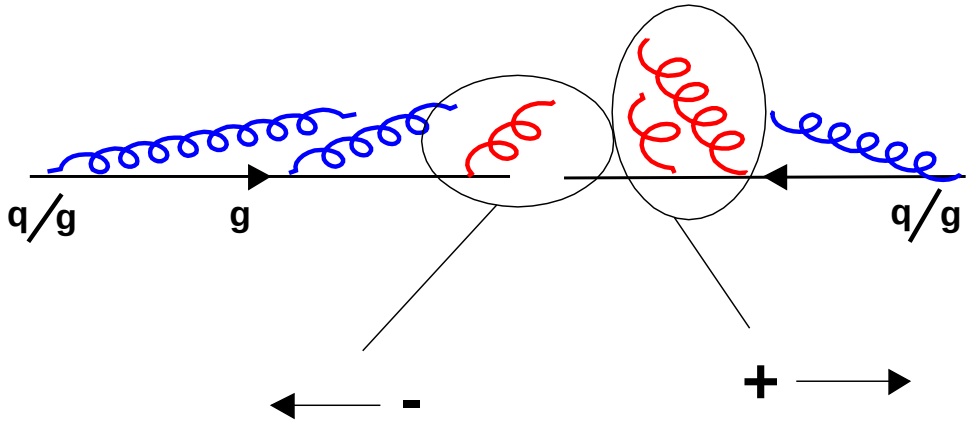

Figure 7.4: Initial state radiation is typically along the beam pipe. If an event has more than 8 GeV transverse initial state radiation in either hemisphere, it is flagged as having hard ISR content.

Matched: 73,185				Not Matched: 19,397			
	# ISR	# FSR	#ISR ‖ FSR		# ISR	# FSR	#ISR ‖ FSR
hep fid	26,048	19,044	38,224	hep fid	11,694	7,737	14,926
(fraction)	0.36	0.26	0.52	(fraction)	0.60	0.40	0.77
not hep fid	342	252	498	not hep fid	1,912	1,248	2,466
(fraction)	0.005	0.003	0.007	(fraction)	0.10	0.06	0.13

Table 7.8: Events are divided into whether the reconstructed particles match the generator level particles or not, according to the ISR and FSR content; "hep fid" means that the generator level particles traversed CDF subdetectors used in this analysis.

Final state radiation tends to be along the direction of the b jet and is mostly included within the b jet cone. When final state radiation is hard enough to escape the cone, it can be misidentified as a b jet or cause the b jet to be mismeasured. Therefore, the procedure for final state radiation is to loop through unique final state gluon radiation emissions and sum up the portion in each hemisphere that is outside $dR = \sqrt{d\eta^2 + d\phi^2}$ = 0.4 of the real b partons in the event and within the detector. When an event has more than 8 GeV worth of this FSR E_T, it is flagged an having hard FSR radiation.

A good measure of the ability of tagging these events is to look at the generator level partons and determine how well they match the reconstructed jets in the cases when the event passed the reconstruction cuts, but was flagged as having ISR and/or FSR. Table 7.8 is divided into whether the event was matched or not and whether its generator level partons were fiducial. The number of ISR, FSR, and (ISR ‖ FSR) events in each category is tabulated. One can see that there are many more unmatched events that are tagged as having hard gluon radiation than matched events. Also, the presence of gluon radiation can cause events which are not matched, and have non-fiducial partons to pass the cuts.

Gluon radiation type	shift
ISR removed	-0.04
FSR removed	0.03

Table 7.9: The systematic shift of measurement due to removal of hard gluon radiation effects. Uncertainty is taken to be half of the total shift when hard radiation is removed.

By removing ISR or FSR flagged events from consideration in pseudo-experiments, and fitting to the standard templates, a systematic shift for each can be measured. One would expect FSR to result in a positive shift since one is removing events in which much of the b parton energy was radiated outside its jet cone. Therefore, the remaining events would have higher E_T and have a higher M^2_{l+b}, appearing more like V+A.

For the ISR systematic, there are two effects. One is that ISR gluons may be mistaken for b jets, the other is that although the direction of the summed ISR gluon vector is uncorrelated to the lepton, its energy can be associated with b jets. The more significant effect is the addition of extra energy to the b jets. Therefore, when ISR events are removed, there is a tendency for lower b jet energies, causing the events to look more like V−A events (Table 7.9).

7.8 Relative Acceptance of V−A and V+A

As mentioned in Section 6.1, a relative acceptance factor, R, is used in the likelihood to account for the different efficiencies for V−A and V+A events to pass the selection criteria. The R value is shifted in pseudoexperiments within its statistical uncertainty to determine a systematic shift of f_{V+A}.

Summary of uncertainties and effect on f_{V+A}	
Top mass	0.19 *(0.21 w/out jet energy correlation)*
Jet energy scale	0.04 *(0.14 w/out top mass correlation)*
Background shape	0.05
Background normalization	0.05
ISR gluon radiation	0.04
FSR gluon radiation	0.03
B-tagging efficiency	0.03
Parton distribution functions	0.02
Monte Carlo statistics	0.01
Relative acceptance	0.005
Total systematic	0.21

Table 7.10: Summary of uncertainties in terms of shift in measurement of V+A fraction. The top mass systematic is complementary to the jet energy scale systematic. Shown in parentheses are the systematic errors for top mass and jet energy before accounting for correlation.

7.9 Summary of Systematic Uncertainties

The largest systematic uncertainty is the top mass. Fortunately it is correlated and complementary with the jet energy scale, and therefore both effects are reduced. This is an important reason this analysis makes sense in Run II, since a better measurement of the top mass will lead to a lower jet energy scale systematic, and vice-versa (Table 7.10).

Chapter 8

Summary

8.1 Measurement of f_{V+A}

The final results are shown in Table 8.1 with an explanation of uncertainties. The final value of $-0.21^{+0.42}_{-0.24}$ (stat.) $\pm$ 0.21 (sys) is consistent with a pure V$-$A theory, and strongly disfavors a large V$+$A component. The prediction from the dilepton and SVX single-tagged samples dominate the combined result, the strong V$-$A result from the SVX single-tagged sample having the effect of shifting the combined result slightly to an unphysical V$+$A fraction.

If the true top mass were 180 GeV (170 GeV) instead of the 175 GeV assumed in the Monte Carlo, the most likely value would shift from -0.21 to -0.02 (-0.40).

8.2 Interpretation of Result

The final result of this measurement is a value less than those of the physical region. For the Standard Model value of f_{V+A} = 0, one expects half of the values to be less than zero, so this is not a surprise. The degree to which f_{V+A} is less than zero is important

Result and Summary of Uncertainties	
Systematic effects	
Top mass Uncertainty	0.19 *(0.21 w/out jet energy correlation)*
Jet energy Scale	0.04 *(0.14 w/out top mass correlation)*
Background shape uncertainty	0.05
Background normalization	0.05
ISR Gluon radiation	0.04
FSR Gluon radiation	0.03
B tagging efficiency	0.03
Parton distribution Functions	0.02
Monte Carlo Statistics	0.01
Relative acceptance uncertainty	0.005
Total systematic	0.21
Statistical uncertainty	
Likelihood error from minimization	+0.40 -0.23
Likelihood error with non-gaussian correction	+0.42 -0.25
Result	$-0.21^{+0.42}_{-0.25}$ (stat) +- 0.21 (syst)

Table 8.1: Summary of uncertainties in terms of shift in measurement of V+A fraction, and result.

since it makes values with high f_{V+A} less probable. This can be quantified by assigning a confidence level to which the true value of f_{V+A} is most probable.

In order to evaluate the confidence level of the result from data, two different techniques were chosen.

A Bayesian approach is used in which the area under the likelihood is calculated in the physical region [0,1], and then the value of f_{V+A} is found such that 95% of the area of the likelihood is between 0 and f_{V+A}. To incorporate systematic uncertainty into this likelihood, the statistical likelihood is convoluted with a Gaussian $G_{sys}(x)$ of width equal to the total systematic uncertainty of the measurement, so that

$$\mathcal{L}_{sys+stat}(f_{V+A}) = \int_{-\infty}^{+\infty} \mathcal{L}_{stat}(f_{V+A} + x) G_{sys}(x) dx \tag{8.1}$$

is the likelihood used to evaluate the Bayesian confidence level. In practice, the limits of integration used were $\pm$ 5 sigma of $G_{sys}(x)$. Using this approach, the Bayesian 95% Confidence Level for the true value was determined to be $f_{V+A} <$ 0.82 @ 95% CL (see Figure 8.1). If instead of the full likelihood function, we use a Gaussian approximation, the result becomes $f_{V+A} < 0.74$ @ 95% CL.

A Frequentist approach, the Neyman confidence band, was also used to assign an upper limit on f_{V+A} ([33]). Pseudo-experiments were generated with a fixed fraction of f_{V+A} between 0 and 1. The measurements from each pseudo-experiment were then smeared with a random value from a Gaussian with width equal to the total systematic uncertainty, and the distribution of resulting pseudo-measurements was recorded. The input fraction f_{V+A} was systematically increased in each set of pseudo-experiments until only 5% of pseudo-experiments yielded a return value of f_{V+A} which was less than or equal to that measured in the data. This corresponds to a 95% upper limit confidence level of $f_{V+A} = 0.80$ (Figure 8.2). If the likelihood function were purely Gaussian, an analytical calculation yields $f_{V+A} < 0.56$ @ 95% CL.

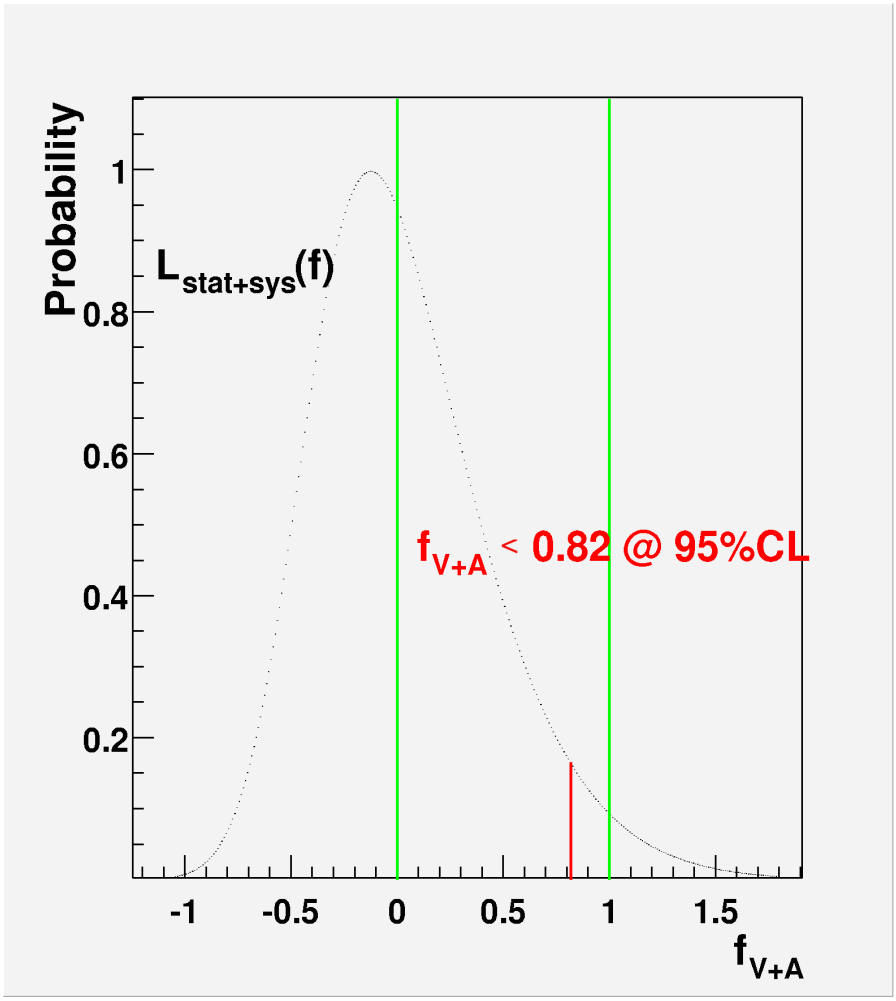

Figure 8.1: $\mathcal{L}_{sys+stat}(f_{V+A})$ showing 95% CL for measured result to have an upper limit of 0.82

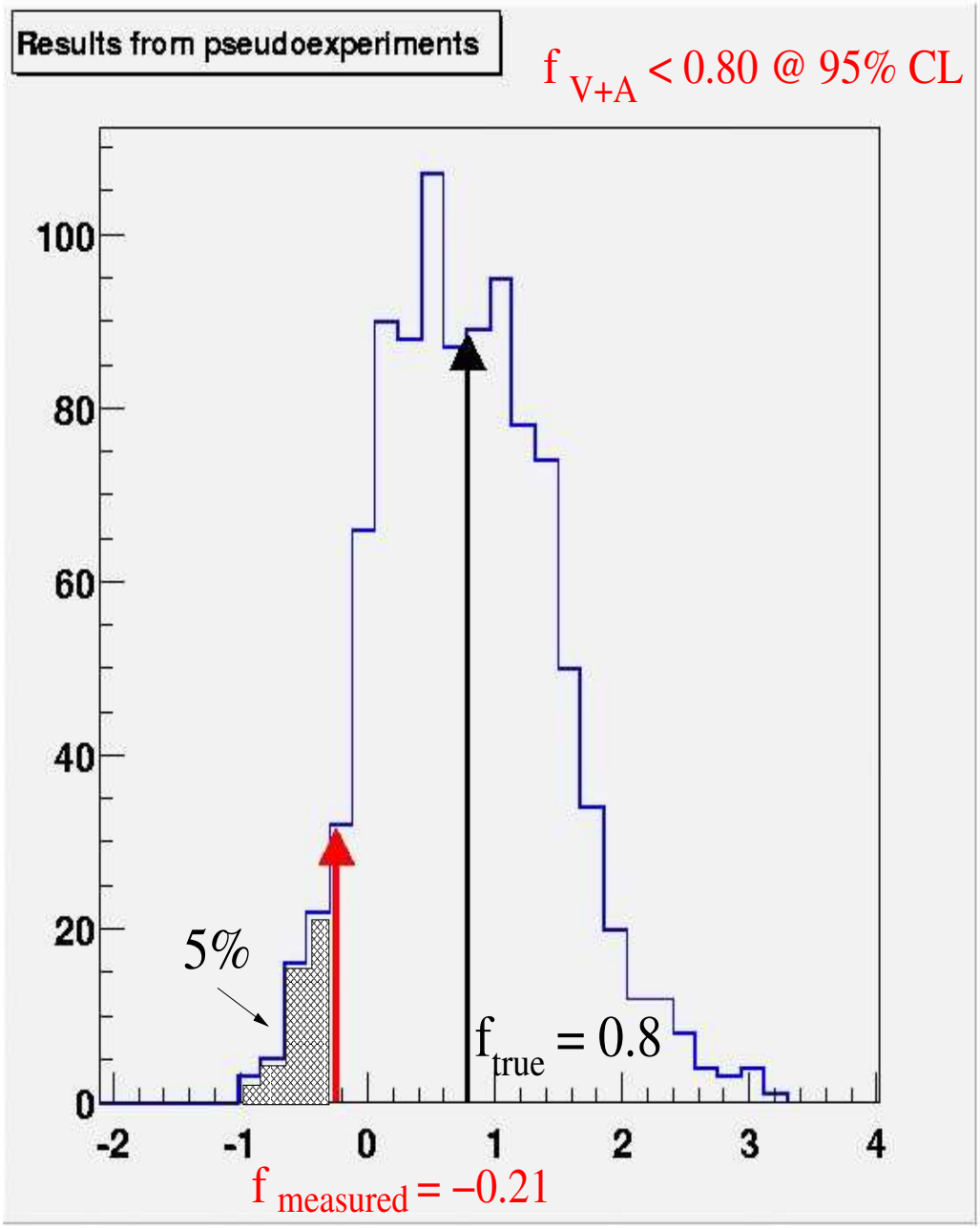

Figure 8.2: Distribution of f_{V+A} from 1000 pseudo-experiments such that 95% of pseudo-experiments had a result greater than $f_{measured}$. The arrows indicate the measured value, -0.21, and the "true" value used in the pseudo-experiments, 0.80, which defines the 95% CL upper limit.

The Frequentist and Bayesian approaches yield very similar answers in the data. The authors disfavor the Bayesian approach since a limit can always be set even in the case of a flat probability distribution (ie, for $f(x) = 1$ in [0,1], $f < 0.95$ @ 95% CL).

Therefore, the final result is that $f_{V+A} < 0.80$ @ 95% Confidence Level.

8.3 Combining with Complementary Observable

Two techniques have been used to search for non-standard weak couplings in top decays at CDF. These searches can be quantified in terms of the fraction of V+A coupling in top decay. It is assumed that the rate for longitudinal W helicity is f_0 = 70%, as is determined by the top mass in relation with the W mass from Equation 5.3. One can relate the fraction of right-handed couplings f_{RH} by

$$f_{RH} = \frac{\Gamma(t \to W^+_{RH} b)}{\Gamma(t \to W^+_{RH} b) + \Gamma(t \to W^+_{LH} b) + \Gamma(t \to W^+_0 b)} \tag{8.2}$$

to the fraction of V+A couplings from Equation 5.4 by

$$f_{V+A} = f_{RH}/(1 - f_0) \tag{8.3}$$

In this analysis, all measurements are in terms of f_{V+A}, whereas the lepton P_T analysis quotes measurements in terms of f_{RH}.

The lepton P_T analysis makes use of the fact that the different spin orientations of the W induce different boosts of the lepton in the W decay, such that for the W^+, $\mathcal{H}$ = +1 yields higher P_T leptons than $\mathcal{H}$ = 0 which are higher than for $\mathcal{H}$ = -1.

This technique has the advantage that it is sensitive mainly to the well-measured P_T of electrons and muons, being sensitive to jet energy uncertainties only in terms of the efficiency for selecting top events based on cuts of jet E_T and $\not\!\!E_{\mathrm{T}}$. Two additional

samples of top events are used in this analysis. One, called the no-tag sample, does not require any b tagged jets. The other sample requires a Soft Lepton Tag (SLT) which tries to identify the b jet by its association with a high P_T electron or muon from semi-leptonic b decay. Because lepton P_T is measured equally well in the non-overlapping b tagged, SLT-tagged, no-tag, and dilepton samples, all of these samples are used in the analysis. The disadvantage of this approach is that the lepton P_T does not take into account the boost it received from the top P_T. For more information about the lepton P_T method, see [20].

The M^2_{l+b} analysis uses a reference frame independent measurement to get a direct measurement of $\psi^\star_l$ since the two are directly related.

$$M^2_{l+b} = 1/2 \cdot (M^2_T - M^2_W)(1 + cos\psi^\star_l) \tag{8.4}$$

There are complications involved in this analysis due to the ambiguity of pairing the lepton with the correct b jet. Also, if the b jet is not explicitly identified, there is the possibility of pairing a lepton with jets from W decay or from gluon radiation. These combinatoric backgrounds are reduced by choosing data samples which explicitly identify b jets either by tagging or by the absence of light quark jets from W decay: SVX double-tagged, SVX single-tagged, and dilepton $t\bar{t}$. In order to make maximal use of the information, all lepton-b pairings are considered, though half of them are incorrect. When there are two possible pairings for a lepton to a b jet, both are considered in the analysis, and the correlation between the pairs is maintained by considering one pairing verses the other pairing in a two-dimensional histogram. One possible problem with this analysis is that the jet energy scale uncertainty could be a large enough systematic that the M^2_{l+b} approach is disfavored. However, the top mass uncertainty and jet energy scale uncertainty are strongly anti-correlated (Section 7.2), therefore reducing the effect of the jet energy scale.

The Run I measurements from the lepton P_T and M^2_{l+b} methods yield similar statistical uncertainties, although the M^2_{l+b} analysis is a bit luckier in having a measurement and uncertainties on the smaller side of those expected from pseudo-experiments. The lepton P_T measurement of f_{V+A} yields a value of 0.37 $\pm$ 0.50 (stat.) $\pm$ 0.2 (sys). The M^2_{l+b} yields a value of $-0.21^{+0.42}_{-0.24}$ (stat.) $\pm$ 0.21 (sys).

8.4 Combining M^2_{l+b} and Lepton P_T

To combine the results, correlations between data samples and systematics must be considered. To combine the statistical and systematic uncertainties of the two approaches, a 3 X 3 covariance matrix is used to handle the correlations between uncertainties from M^2_{l+b} (σ_M), from the correlated lepton P_T measurement using the b tagged and dilepton samples ($\sigma_{L_{COR}}$), and from the uncorrelated SLT and no-tag samples used exclusively in the lepton P_T analysis ($\sigma_{L_{UNC}}$). This covariance matrix, V, can be represented by

$$V = \begin{pmatrix} {\sigma_{L_{COR}}}^2 & \rho_{CM} \cdot \sigma_{L_{COR}} \cdot \sigma_M & \rho_L \cdot \sigma_{L_{COR}} \cdot \sigma_{L_{UNC}} \\ \rho_{CM} \cdot \sigma_{L_{COR}} \cdot \sigma_M & {\sigma_M}^2 & \rho_{UM} \cdot \sigma_{L_{UNC}} \cdot \sigma_M \\ \rho_L \cdot \sigma_{L_{COR}} \cdot \sigma_{L_{UNC}} & \rho_{UM} \cdot \sigma_{L_{UNC}} \cdot \sigma_M & {\sigma_{L_{UNC}}}^2 \end{pmatrix} \tag{8.5}$$

where ρ_{CM} (ρ_{UM}) is the correlation coefficient between results from the M^2_{l+b} and lepton P_T techniques for the correlated (uncorrelated) samples, and ρ_L is the correlation coefficient between results from the correlated and uncorrelated lepton P_T samples. ρ_L is zero for the statistical uncertainties since the samples are non-overlapping, and is one for the systematic uncertainties since these are assumed to impact the measurement in the same way.

Sample	Number of events	
	Lepton P_T	M^2_{l+b}
Dilepton	7	7
B tagged	34	20

Table 8.2: The M^2_{l+b} analysis makes use of the 20 b tagged events from the top mass analysis, while the lepton P_T analysis uses 34 b tagged events from the top cross-section analysis.

8.5 Calculation of Statistical Covariance Matrix

In order to calculate the statistical part of the covariance matrix, it is necessary to know the correlation coefficient ρ_{CM} between measurements of M^2_{l+b} and lepton P_T in the b tagged and dilepton samples. The M^2_{l+b} analysis uses a subset of the b tagged sample used for the lepton P_T analysis since it uses the lower background top mass sample rather than the top cross-section sample. To calculate ρ, pseudo-experiments from Monte Carlo were done to create a two-dimensional distribution of measured values of f_{V+A} for each analysis approach. The M^2_{l+b} pseudo-experiments used 7 dilepton and 20 b tagged events, while the lepton P_T pseudo-experiments used these same 27 events, plus an additional 14 b tagged events (Table 8.2). For the lepton P_T pseudo-experiments, the events were divided into 34-event b tagged and 7-event dilepton samples, and fit to V+A, V−A, and background templates of the same. In the M^2_{l+b} case, the standard analysis divided the 20 b tagged events further into 5-event SVX double-tagged and 15-event SVX single-tagged samples. In this way, ρ takes into account the 14 b tagged events which are not correlated to the M^2_{l+b} analysis. The distribution of pseudo-measurements for lepton P_T verses M^2_{l+b} is shown in Figure 8.3. The correlation coefficient can be

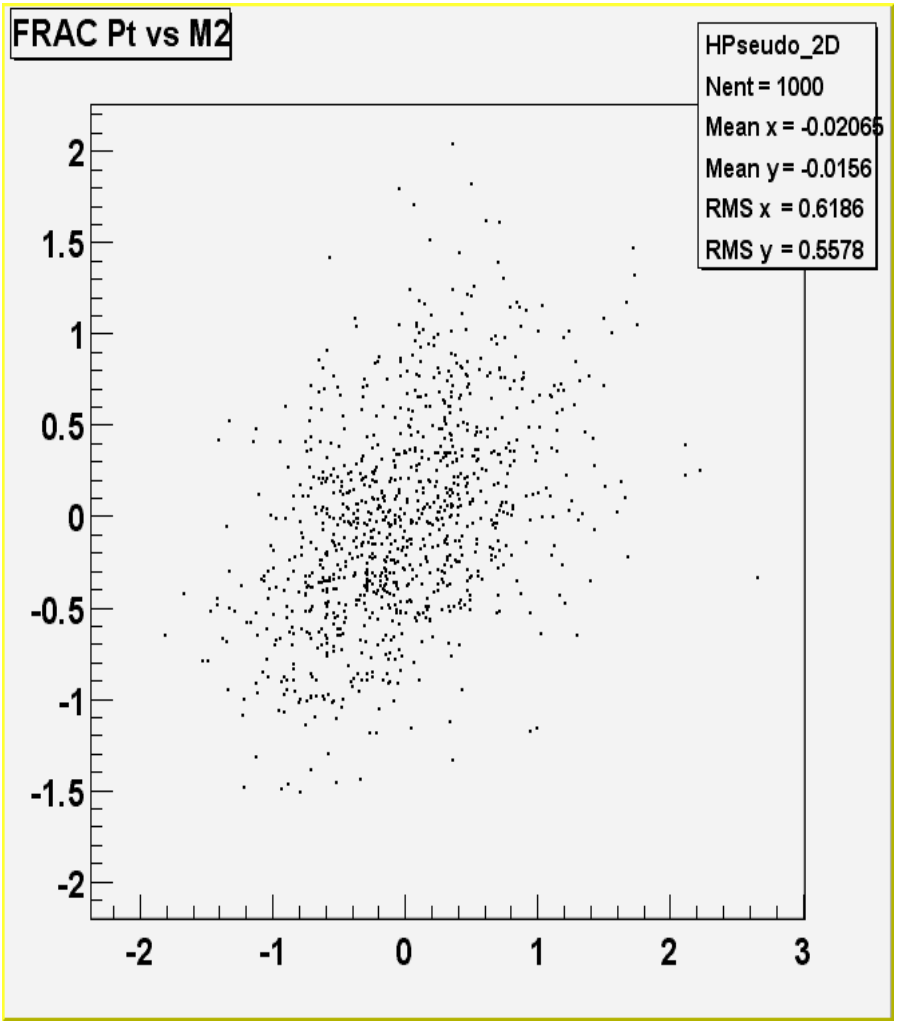

Figure 8.3: The distribution of measured f_{V+A} for the two analysis techniques are shown for 1000 pseudo-experiments.

calculated from this distribution according to:

$$\rho_{LM} = V_{L_{COR}}/\sigma_{L_{COR}}/\sigma_M = 0.44 \tag{8.6}$$

To calculate the 3X3 statistical covariance matrix, it is necessary to separate the uncertainties from the result of the lepton P_T analysis into components from the samples correlated and uncorrelated with the M^2_{l+b} analysis. While the results separated by sample are available for the measurement of the longitudinal component of the W helicity in the lepton P_T analysis, they are not available for the right-handed component which is of concern here. Therefore, to get these contributions, an assumption was made that in the lepton P_T analysis, the relative contribution of each sample to the measurement of the longitudinal helicity component was the same for the right-handed component. The relative weight of the uncertainties from the correlated and uncorrelated data sample of the longitudinal sample was then calculated, and used to determine $\sigma_{L_{COR}}$ and $\sigma_{L_{UNC}}$ by weighting σ_L (see Table 8.3).

Now that ρ, $\sigma_{L_{COR}}$, $\sigma_{L_{UNC}}$ have been determined, as well as σ_M which has a symmetrized value of 0.33, the statistical component of equation 8.5 can be determined.

8.6 Calculation of Systematic Covariance Matrix

The systematics of the two analyses are largely the same. The systematics are compared in terms of shift in f_{V+A} in Table 8.4.

It is assumed that all the systematics are correlated with ρ = 1, except the systematic due to finite Monte Carlo statistics.

		Longitudinal				V+A	
		σ^+	σ^-	$\hat{\sigma}$	relative weight	$\hat{\sigma_L}$	$\hat{\sigma}_{L_{COR,UNC}}$
correlated	SVX	0.46	0.46	0.46	0.66	0.5	0.61
	dilepton	0.57	0.45	0.51			
uncorrelated	SLT	0.87	0.27	0.57	0.34		0.86
	no tag	0.98	0.77	0.875			

Table 8.3: The correlated and uncorrelated components of the V+A measurement using lepton P_T, as is calculated using the weights from the longitudinal measurement.

Summary of Uncertainties		
Systematic uncertainty	M^2_{l+b}	lepton P_T
Top mass	0.19	0.1
Jet energy scale	0.04	0
Background shape	0.05	0.07
Background normalization	0.05	0.03
Gluon radiation	0.05	0.1
B tagging efficiency	0.03	0
Parton distribution functions	0.02	0.07
Monte Carlo statistics	0.01	0.07
Relative acceptance	0.005	0
Total systematic	0.21	0.20

Table 8.4: Summary of uncertainties in terms of shift in measurement of V+A fraction for the two methods.

8.7 Determining Combined Likelihood

The statistical variance V_{stat} and total systematic variance V_{sys} are then summed together into the covariance matrix in equation 8.5. A χ^2 distribution for the combined result is created according to:

$$\chi^2(f) = X^T(f) \cdot V^{-1} \cdot X(f) \tag{8.7}$$

where the components X(f) are the difference between the measurements and the true V+A fraction, f. We assume that the correlated and uncorrelated lepton P_T measurements yield the same value as is the case for the uncertainties outlined in Section 8.5.

$$X(f) = \begin{pmatrix} 0.37 - f \\ -0.21 - f \\ 0.37 - f \end{pmatrix} \tag{8.8}$$

Solving this matrix gives a χ^2 of

$$\chi^2(f) = 7.3137 \cdot f^2 + 1.0306 \cdot f + 1.3499 \tag{8.9}$$

Since the χ^2 distribution corresponds to $-2\log\mathcal{L}$, it can be used to determine the maximum likelihood value and its errors. The solution is -0.07 $\pm$ 0.37.

8.8 Evaluation of Confidence Level

The confidence level of this result can be assigned with Bayesian and Frequentist approaches. Since the result is slightly out of the physical region, a one-sided 95% Confidence Level is used.

The Bayesian approach is to consider the likelihood only in the physical region of

f_{V+A} from [0,1]. We assume a flat prior in f_{V+A}, and find the upper limit of the 95% Confidence Level, f_{UL}, to be the value of f_{V+A} which contains 95% of the area of the likelihood in the physical region.

$$\frac{\int_0^{f_{UL}} L(f)df}{\int_0^1 L(f)df} = 0.95 \tag{8.10}$$

The result is that $f_{V+A} < 0.60$ @ 95% CL.

Our Frequentist approach involves the construction of a Neyman Confidence band [33] which makes no reference to the physical region. Instead, the likelihood is used to determine which true value of f_{V+A} would produce 95% of measurements greater than the experimentally measured value. The result is that $f_{V+A} < 0.61$ @ 95% CL.

The two approaches yield almost the same value. We prefer the Frequentist approach since it is more consistent with the analysis method which allows f_{V+A} to be non-physical. Also, the Bayesian approach will always set an upper limit within the physical region (for a flat probability distribution, $f_{V+A} < 0.95$ @ 95% CL), whereas the Frequentist approach does not have this feature since it determines limits based on the distribution of expected results from measurement which may or may not be physical.

Using the Frequentist approach, we determine that the combined result excludes f_{V+A} = 1 at 99.6 % CL, which corresponds to 2.67 σ.

8.9 Results of Combined Measurement

The combined measurement of f_{V+A} using the lepton P_T and M^2_{l+b} techniques is found to be -0.07 $\pm$ 0.37, so that $f_{V+A} <$ 0.61 @ 95% CL. Statistical and systematic uncertainties in the two measurement techniques, along with their correlations, are taken into

account.

This combined result is an improvement over the previous limit from the M^2_{l+b} technique. Together, the two experimental techniques are able to probe deeply into the nature of the top quark and determine that its physical properties are largely consistent with the Standard Model. With the full Run II data set, a precise measurement of f_{V+A} will become possible.

8.10 Future

Expected statistical and systematic uncertainties are calculated for Run II. Statistical uncertainties are calculated by using pseudo-experiments with sample sizes determined from the CDF Technical Design Report for Run IIA [36] re-scaled to the most recent theoretical cross-section of 7.5 pb [37] (originally 6.8 pb) and Tevatron energy 1.96 TeV (originally 2.0 TeV). Background contributions are considered the same as those expected in Run I. Systematic uncertainties are calculated by scaling the Run I systematics by the improvement in uncertainty between Run I and Run II in terms of the CDF top mass as calculated from the Tev2000 report [38]. The top mass uncertainty and its jet energy scale component are taken for just the CDF top mass, and used to scale the Run I systematics on f_{V+A}, and determine the correlations. The leading systematics and total are shown in table 8.5, and along with the statistical uncertainties in table 8.6. Since the top mass systematic uncertainties are estimated only for 2 fb$^{-}1$, the systematics for this measurement are shown only for this luminosity. Since the top mass uncertainty does not take into account the top mass measurement from $D\emptyset$, this estimation is conservative.

Run 2 expected systematic uncertainties	
Top mass	0.08 *(0.16 w/out jet energy correlation)*
Jet energy scale	0.03 *(0.11 w/out top mass correlation)*
Background normalization	0.05
Background shape uncertainty	0.05
ISR gluon radiation	0.04
FSR gluon radiation	0.03
Total systematic uncertainty	0.11

Table 8.5: Systematic uncertainties determined by scaling the systematics of f_{V+A} for the Run I analysis by the factors obtained by comparing the CDF Run I systematic uncertainties of the top mass to those in expected in 2 fb$^{-}1$ of CDF II data.

Run 2 expected uncertainties		
Luminosity	Stat Error	Syst Error
109 pb^{-1}	0.59	0.21
500 pb^{-1}	0.19	
1000 pb^{-1}	0.14	
2000 pb^{-1}	0.10	0.11

Table 8.6: Statistical uncertainty determined by pseudoexperiments with event samples appropriate to the given luminosty at 1.96 TeV assuming a cross-section of 7.5 pb. Improved systematic uncertainty accounts mainly for better measurements of the jet energy scale and the top mass.

Chapter 9

Conclusions

This thesis presents a search for non-standard weak interactions of the top quark. If present, these would be a hint that the top is important to the weak interaction itself.

Although the Standard Model successfully describes known phenomena, it is expected to fail to explain physics interactions as the energy scale probed by accelerators increases. Clues will be discovered in the frontier energy experiments which will point to a more complete theory which explains the shortcomings of the Standard Model. For instance, it is unexplained why the Standard Model is a V$-$A theory rather than a V$+$A theory, which has the exact opposite asymmetry.

With its uniquely heavy mass, the top quark provides an opportunity to scrutinize Standard Model predictions at the electroweak scale. V$+$A components in top decay may exist due to an exotic particle with right-handed or unbiased couplings mixing with the top quark, slightly altering f_{V+A} from its expected value of zero. Also, the $t\bar{t}$ candidate sample may be contaminated by exotic physics processes which may give the impression that the top has non-standard weak couplings.

This is the first measurement of V$+$A in top decay which provides meaningful limits on this form of the interaction. To achieve this, we first selected events with a high

probability of being $t\bar{t}$ candidates and with minimal ambiguity in identifying the decay products of the W boson. The W from top decay is polarized differently in a V+A theory. To measure this polarization, we use a novel technique of constructing the invariant mass of the lepton and b quark in these events. After including sources of statistical and systematic uncertainties, we find $f_{V+A} < 0.80$ @ 95% Confidence Level (CL). This method sets a better limit than the competing lepton P_T analysis, despite having lower statistics and being susceptable to jet energy scale uncertainties. Combining the two analyses limits $f_{V+A} < 0.61$ @ 95% CL and provides a 99.6 % CL limit that the top does not decay with a pure V+A coupling. The uncertainty in this measurement is dominated by statistics; the dominant systematic uncertainty is from the uncertainty in the top mass.

We examine the potential of future measurements, and determine that with 2000 pb^{-1}, it is reasonable to assume that CDF should measure f_{V+A} with an uncertainty of only 0.15. In this case, the systematic uncertainty, dominated by uncertainties in the top mass, will become the limiting factor in the sensitivity of the measurement.

As statistics improve, it will be useful to measure f_{V+A} separately in the lepton+jets and dilepton decay modes, since non-standard physics with signatures similar to that of $t\bar{t}$ might not have the same effect in each sample. With enough $t\bar{t}$ events, it will also become possible to simultaneously fit for the left-handed, right-handed, and longitudinal components of the W polarization. Future precise measurements of f_{V+A} in top decay will be key steps in testing the Standard Model at its frontier.

Bibliography

[1] Excellent books describing the theory of the Standard Model are *Modern Elementary Particle Physics* by Gordon Kane (Addison-Wesley Publishing Co. 1993) and *Introduction to Elementary Particles* by David Griffiths (John Wiley & Sons, Inc. 1987).

[2] C. F. Kolda and H. Murayama, "The Higgs mass and new physics scales in the minimal standard model," JHEP **0007**, 035 (2000) [arXiv:hep-ph/0003170].

[3] R. M. Harris, C. T. Hill and S. J. Parke, "Cross section for topcolor Z'(t) decaying to t anti-t," arXiv:hep-ph/9911288.

[4] T. Appelquist, H. C. Cheng and B. A. Dobrescu, "Bounds on universal extra dimensions," Phys. Rev. D **64**, 035002 (2001) [arXiv:hep-ph/0012100], and private communication with H. Cheng.

[5] S. D. Holmes, "A Practical Guide To Modern High-Energy Particle Accelerators," FERMILAB-CONF-87-160 *Lectures given at Theoretical Advanced Summer Inst., Santa Fe, N. Mex., Jul 6-24, 1987.*

[6] http://www-bd.fnal.gov/public/.

[7] F. Abe *et al.*, Nucl. Instr. Meth. Phys. Res. A **271**, 387 (1988); D. Amidei*et al.*, *ibid.* **350**, 73 (1994); P. Azzi *et al.*, *ibid.* **360**, 137 (1995).

[8] F. Abe *et al.* [CDF Collaboration], Phys. Rev. D **50**, 2966 (1994).

[9] F. Abe *et al.* [CDF Collaboration], "Observation of top quark production in anti-p p collisions," Phys. Rev. Lett. **74**, 2626 (1995) [arXiv:hep-ex/9503002].

[10] S. Abachi *et al.* [$D\emptyset$ Collaboration], "Observation of the top quark," Phys. Rev. Lett. **74**, 2632 (1995) [arXiv:hep-ex/9503003].

[11] A. Datta, P. J. O'Donnell, Z. H. Lin, X. Zhang and T. Huang, "Effects of Kaluza-Klein excited W on single top quark production at Tevatron," Phys. Lett. B **483**, 203 (2000) [arXiv:hep-ph/0001059].

[12] C. T. Hill, "Topcolor: Top quark condensation in a gauge extension of the standard model," Phys. Lett. B **266**, 419 (1991).

[13] H. J. He and C. P. Yuan, "New method for detecting charged (pseudo-)scalars at colliders," Phys. Rev. Lett. **83**, 28 (1999) [arXiv:hep-ph/9810367].

[14] G. Triantaphyllou, "New physics with mirror particles," J. Phys. G **26**, 99 (2000) [arXiv:hep-ph/9811250].

[15] D. Choudhury, T. M. Tait and C. E. Wagner, "Beautiful mirrors and precision electroweak data," Phys. Rev. D **65**, 053002 (2002) [arXiv:hep-ph/0109097].

[16] K. Fujikawa and A. Yamada, "Test of the chiral structure of the top - bottom charged current by the process b → s gamma," Phys. Rev. D **49**, 5890 (1994).

[17] G. L. Kane, G. A. Ladinsky and C. P. Yuan, Phys. Rev. D **45**, 124 (1992).

[18] G. Guillian, "Top Quark Decay Kinematics in Fully Reconstructed $t\bar{t}$ Events in the e or $\mu + \not{E}_{\mathrm{T}} + \geq 4$ Jet Decay channel", Ph.D. Thesis, University of Michigan (1999).

[19] Private communication with T. Tait.

[20] T. Affolder *et al.* [CDF Collaboration], "Measurement of the helicity of W bosons in top quark decays," Phys. Rev. Lett. **84**, 216 (2000) [arXiv:hep-ex/9909042].

[21] F. Abe *et al.* [CDF Collaboration], "Measurement of the top quark mass and t anti-t production cross section from dilepton events at the Collider Detector at Fermilab," Phys. Rev. Lett. **80**, 2779 (1998) [arXiv:hep-ex/9802017].

[22] T. Affolder *et al.* [CDF Collaboration], "Measurement of the top quark mass with the Collider Detector at Fermilab," Phys. Rev. D **63**, 032003 (2001) [arXiv:hep-ex/0006028].

[23] G. Corcella *et al.*, "HERWIG 6: An event generator for hadron emission reactions with interfering gluons (including supersymmetric processes)," JHEP **0101**, 010 (2001). Both $t\bar{t}$ samples were generated with HERWIG, the latter using a custom version with adjustable W helicity amplitudes.

[24] T. Sjostrand, Computer Physics Commun. 82 (1994) 74. (Pythia version 6.129 used) (http://shakespeare.thep.lu.se/tf2/staff/torbjorn/Pythia.html).

[25] F. Paige, S. Protopopescu, H. Baer, X. Tata, (1997) (http://wwwlapp.in2p3.fr/gdr-outils/GDR/isajet0.html).

[26] F. A. Berends, H. Kuijf, B. Tausk and W. T. Giele, "On The Production Of A W And Jets At Hadron Colliders," Nucl. Phys. B **357**, 32 (1991).

[27] R. Brun and F. Rademakers, Nucl. Instrum. Meth. A **389**, 81 (1997).

[28] R. Barate *et al.* [ALEPH Collaboration], "Search for the standard model Higgs boson at LEP," Phys. Lett. B **565**, 61 (2003) [arXiv:hep-ex/0306033].

[29] L. Demortier, R. Hall, R. Hughes, B. Klima, R. Roser and M. Strovink [The Top Averaging Group Collaboration], "Combining the top quark mass results for run 1 from CDF and D0," FERMILAB-TM-2084.

[30] D. R. Stump, "A new generation of CTEQ parton distribution functions with uncertainty analysis," *Prepared for 31st International Conference on High Energy Physics (ICHEP 2002), Amsterdam, The Netherlands, 24-31 Jul 2002.*

[31] R. S. Thorne, A. D. Martin, W. J. Stirling and R. G. Roberts, "Update of MRST parton distributions," Acta Phys. Polon. B **33**, 2927 (2002) [arXiv:hep-ph/0207067].

[32] K. Tollefson, "A Measurement of the Top Quark Mass", Ph.D. Thesis, University of Rochester (1997).

[33] J. Neyman, Phil. Trans. Royal Soc. London, Series A, **236**, 333 (1937).

[34] See web page: http://root.cern.ch/root/html/TH1.html#TH1:KolmogorovTest.

[35] F. Abe *et al.* [CDF Collaboration], "Kinematics of t anti-t events at CDF," Phys. Rev. D **59**, 092001 (1999).

[36] CDF Collaboration, "The CDF II Detector technical design report / the CDF II Collaboration", Fermilab Pub-96-390-E (1996).

[37] E. L. Berger and H. Contopanagos, "Threshold resummation of the total cross section for heavy quark production in hadronic collisions," Phys. Rev. D **57**, 253 (1998) [arXiv:hep-ph/9706206].

[38] D. Amidei, R. Brock, "Future electroweak physics at the Fermilab Tevatron: report on the tev 2000 Study Group", Fermilab Pub-96-082 (1996).

Appendix A

Acronyms and Symbols Used

HEP (High Energy Physics) is loaded with TLAs (Three Letter Acronyms); so many, that those in HEP forget that they are acronyms. Although each acronym is defined the first time it is used, here is a list of them all in one place:

α Coupling strength of an interaction

B QCD color charge blue; $\bar{B}$ is antiblue

BBC Beam Beam Counters

b bottom quark

C charge

c speed of light

c charm quark

CDF Collider Detector at Fermilab

CEM Central Electromagnetic Calorimeter

CES Central Electromagnetic Shower Detector

CHA Central Hadronic Calorimeter

CFT Central Fast Tracker

CKM Cabbibo-Kobayashi-Maskawa quark mixing matrix

CMU Central Muon Chamber

CMP Central Muon Upgrade

CMX Central Muon Extension

CPR Central Preshower Detector

CP transformation of Charge and Parity

CTC Central Tracking Chamber

D∅ A collider detector at Fermilab in the Tevatron

d down quark

E energy

$\mathbf{E_{cm}}$ Energy of system as viewed in the center of mass reference frame

$\mathbf{E_T}$ Transverse energy of an object in an event. $E_T = E \cdot sin(\theta)$

e electron

FHA Forward Hadronic Calorimeter

FCNC Flavor Changing Neutral Currents

FMU Forward Muon Detectors

FSR Final State Radiation

eV electron Volts

$\mathbf{f_{V+A}} = \frac{\Gamma(t \to W^+_{RH} b)}{\Gamma(t \to W^+_{RH} b) + \Gamma(t \to W^+_{LH} b)}$

G QCD color charge green, $\bar{G}$ is antigreen

GGWIG Herwig Monte Carlo modified to allow right-handed Ws in top decay

GIM Glashow-Illiopoulos-Maiani Mechanism

g gluon

γ photon

$\mathcal{H}$ Helicity

$\hbar$ Planck's Constant which refers to the angular momentum carried by one photon

j unit of spin

IPD Integrated Probability Distribution

ISR Initial State Radiation

LH Left-Handed

LO leading order, as in a first order calculation in a series expansion

$\mathcal{L}$ Likelihood

l lepton

λ_0 Radiation Length

$\lambda\!\!\!^{-}$ refers to wavelength of a particle or wave

M mass

MC Monte Carlo

MNS Maki-Nakagawa-Sakata neutrino mixing matrix

$\not{E}_{\mathrm{T}}$ Missing E_T.

μ muon

NLL next-to-leading-log, as in a next order calculation in a series expansion

ν neutrino

$\nu_{\mathbf{e}}$ electron neutrino

ν_{μ} muon neutrino

ν_{τ} tau neutrino

P parity

P momentum

PDF Parton Distribution Functions

PEM Plug Electromagnetic Calorimeter

PHA Plug Hadronic Calorimeter

$\mathbf{P_T}$ transverse momentum of an object in an event. $P_T = P \cdot sin(\theta)$

$\mathbf{p}$ proton

QED Quantum Electrodynamics, the theory of the electromagnetic interaction.

QCD Quantum Chromo Dynamics, the theory of the strong interaction

QFL CDF Fast Detector Simulation

$\mathbf{Q^2}$ a measure of the momentum transferred in a collision

q quark

R relative efficiency for detecting V$-$A compared to V$+$A

$\mathbf{R}$ QCD color charge red; $\bar{R}$ is antired

RF Radio-Frequency

RH Right-Handed

Run IA data taking at the Tevatron from 1992-1993

Run IB data taking at the Tevatron from 1994-1995

$\sqrt{\mathbf{s}}$ refers to energy available in a collision

SECVTX Secondary Vertex algorithm

SM Standard Model of particles and interactions

SU$_L$(2) symmetry group representing the weak force which has two isospins

SU(3) symmetry group of the strong force which has three colors

SVX Silicon Vertex Detector

$\mathbf{s}$ strange quark

$\mathbf{t}$ top quark

τ tau

U(1) unitary transformation in one-dimension representing QED

u up quark

VTX Vertex Time Projection Chamber

V - A Vector Minus Axial Vector, refers to the combination and type of vectors of the weak theory. The “minus’ means the Axial Vector is left-handed.

V + A Vector Plus Axial Vector, refers to a combination and type of vectors which is not in the weak theory. The “plus” means the Axial Vector is right-handed.

vev Vacuum Expectation Value, refers to the energy level of the ground state of the vacuum

WHA Wall Hadronic Calorimeter

X spatial coordinate

x fraction of total momentum carried by a parton within a proton

$\mathbf{X_0}$ Absorption Length

Appendix B

Units and Prefixes

In particle physics, we use a set of units based on the electron volt, the amount of energy an electron has after being accelerated through a potential difference of 1 volt. We say that energy is measured in terms of eV (or electron Volts). Protons and anti-protons in the Tevatron have energies of 900 GeV (900 billion electron Volts). Momentum is measured in eV/c (c is the speed if light), and mass is measured with eV/c^2. Often times, particle physicists use units where c = 1, and then energy, momentum, and mass are all in units of eV. This convention is used throughout this thesis. Charge is given in units of the charge of an electron, such that the up quark charge is +2/3. Note that stable and free particles have only been found in nature with integer charge. The primary units of this thesis are shown in Table B.1. The prefixes for the units are shown in Table B.2.

Symbol	Unit	Description	Notes
eV	electron Volt	energy	
eV		momentum	eV/c where c = 1
eV		mass	eV/c^2 where c = 1
m	meter	length	
s	second	time	
b	barn	cross-section	equal to 10^{-24} cm^2

Table B.1: Units.

Power	Symbol	Name	Common Name
> 1			
10^6	M	Mega	million
10^9	G	Giga	billion
10^12	T	Tera	trillion
< 1			
10^-3	m	milli	thousandth
10^-6	μ	micro	millionth
10^-9	n	nano	billionth
10^-12	p	pico	trillionth
10^-15	f	femto	quadrillionth

Table B.2: Prefixes for units.

Appendix C

More information

More information about this analysis is available at
http://www.pas.rochester.edu/∼ksmcf/student_theses/ben_kilminster
including:

i A description of the procedure for generating MC samples, simulating and reconstructing them in the CDF Run I software framework, conducting the measurement, and evaluating systematic uncertainties.

ii An explanation of software tools developed for the analysis.

iii The procedure for obtaining the analysis code and this thesis document.

iv Links to publications associated with this thesis.